



This thesis was typeset with  $\text{\LaTeX}$ , using a modified version of the University of California Ph.D. dissertation class file, `ucthesis.cls`. Unless otherwise noted, all figures in this thesis were created by the author using IDL<sup>®</sup> or CorelDraw<sup>®</sup>.

The photo on the cover shows a radiosonde being launched from just below the Paranal Observatory site during one of the PWV measurement campaigns.

REMOTE SENSING OF ATMOSPHERIC WATER VAPOUR  
ABOVE THE CHILEAN ANDES

RICHARD ROBERT QUEREL

B.Sc. in Physics with Honours, University of Waterloo, 2000  
M.Sc. Physics, University of Lethbridge, 2008

A Thesis

Submitted to the School of Graduate Studies  
of the University of Lethbridge  
in Partial Fulfilment of the  
Requirements of the Degree

PHILOSOPHIÆ DOCTOR

in

EARTH, SPACE, AND PHYSICAL SCIENCE

Department of Physics & Astronomy  
University of Lethbridge  
LETHBRIDGE, ALBERTA, CANADA

© Richard Robert Querel, 2010

---

## Dedication

For Cindy.

---

## Abstract

Water vapour is the principle source of opacity at infrared wavelengths in the Earth's atmosphere. In support of site testing for the European Extremely Large Telescope (E-ELT), we have used La Silla and Paranal as calibration sites to verify satellite measurements of precipitable water vapour (PWV). We reconstructed the PWV history over both sites by analysing thousands of archived high-resolution echelle calibration spectra and compared that to satellite estimates for the same period. Three PWV measurement campaigns were conducted over both sites using several independent measurement techniques. Radiosondes were launched to coincide with satellite measurements and provide a PWV reference standard allowing intercomparison between the various instruments and methods. This multi-faceted approach has resulted in a unique data set. Integral to this analysis is the internal consistency provided by using a common atmospheric model.

---

## Acknowledgements

I would like to thank my supervisor, Dr. David Naylor, for taking me on as a student, challenging me with his questions, and for his full support and assistance during my studies. I would also like to thank Dr. Florian Kerber of the European Southern Observatory (ESO) for a great collaboration on the PWV measurement campaigns. The campaigns were supported by ESO in the context of site-testing work for the E-ELT. Dr. Kerber was the lead of that site-testing project. Thanks go to Greg Tompkins for his work with IRMA at home and abroad. While I cannot ignore your lunacy, I can turn the other way. I would also like to thank Brad Gom for his efforts in keeping IRMA afloat and his support of the BTRAM project; Frank Klassen for machining bits of kit for the lunar photometer; Ian Chapman for developing BTRAM; and Mike Dosso for assisting with lunar measurements. Thank you to Regan Dahl for continuing to share his wealth of knowledge about IRMA and everything related to it. Thanks also go to Locke Spencer for always being available to try to answer any question. Thank you to Scott Jones and Gibion Makiwa for proof-reading the final version of this thesis. And finally, I would like to thank all of my collaborators on the PWV measurement campaigns: Arlette Chacón, Dr. Reinhard Hanuschik, Dr. Carlos Guirao, Dr. Alain Smette, Dr. Gianluca Lombardi, Dr. Gaspare Lo Curto, Dr. Joanna Thomas-Osip, Dr. Gabriel Prieto, Dr. Michel Curé, Dr. Marc Sarazin and many others. It certainly was a team effort.

---

# Contents

Dedication	iii
Abstract	iv
Acknowledgements	v
Table of Contents	vi
List of Tables	ix
List of Figures	x
List of Abbreviations	xiii
List of Equations	xvi
<b>1 Introduction</b>	<b>1</b>
1.1 Overview . . . . .	1
1.2 Precipitable water vapour . . . . .	4
1.3 Radiative transfer / Atmospheric modeling summary . . . . .	8
1.3.1 BTRAM summary . . . . .	9
1.4 Focus of my work as reported in this thesis . . . . .	10
<b>2 Site Testing</b>	<b>12</b>
2.1 Introduction . . . . .	12
2.2 Why build a large telescope? . . . . .	13
2.3 Site selection . . . . .	14
2.4 Summary . . . . .	20
<b>3 Introduction to Spectroscopy</b>	<b>21</b>
3.1 Radiative transfer overview . . . . .	21
3.2 Elements of radiometry . . . . .	22
3.3 Introduction to spectroscopy . . . . .	24
3.3.1 Rotational spectroscopy . . . . .	26
3.3.2 Transition energies and frequencies . . . . .	30
3.3.3 Transition intensities and Einstein coefficients . . . . .	33
3.3.4 Intensities and populations . . . . .	36

## CONTENTS

---

3.4	Line shapes . . . . .	42
4	Atmospheric Modeling . . . . .	49
4.1	Overview . . . . .	49
4.2	Atmospheric modeling . . . . .	49
4.3	Atmospheric profiles . . . . .	52
4.4	Radiative transfer . . . . .	55
4.5	Summary . . . . .	62
5	Methods: Radiosondes . . . . .	65
5.1	Introduction . . . . .	65
5.2	Radiosonde analysis . . . . .	70
5.3	Determination of adiabatic lapse rate . . . . .	74
5.4	Determination of $H_{\text{H}_2\text{O}}$ from radiosonde data . . . . .	76
5.4.1	Calculating the partial pressure of water vapour . . . . .	78
5.4.2	Calculating the density of water vapour . . . . .	79
5.4.3	Calculating precipitable water vapour . . . . .	81
5.5	Summary . . . . .	81
6	Methods: Infrared Radiometer . . . . .	83
6.1	IRMA summary . . . . .	83
6.1.1	IRMA hardware . . . . .	84
6.1.2	IRMA advantages . . . . .	87
6.1.3	Calibration . . . . .	88
7	Methods: Satellite Estimates . . . . .	91
7.1	Envisat - MERIS . . . . .	92
7.2	GOES-Imager . . . . .	95
7.2.1	Conversion of radiance to brightness temperature . . . . .	101
7.3	Summary . . . . .	105
8	Methods: Spectral Fitting . . . . .	107
8.1	Overview . . . . .	107
8.2	Introduction . . . . .	108
8.3	MIKE observations of atmospheric water vapour . . . . .	112
8.4	Equivalent width derived PWV . . . . .	113
8.5	Fitting spectral data - Absorption . . . . .	115
8.5.1	Effect of varying resolution . . . . .	123
8.6	Fitting spectral data - Emission . . . . .	124
8.7	Conclusion . . . . .	129
9	History of PWV over La Silla Paranal Observatory from ESO Archival Data . . . . .	131
9.1	Introduction . . . . .	132
9.1.1	Verification of satellite data . . . . .	133
9.2	Results from the archive: La Silla . . . . .	136



CONTENTS

---

9.3 Results from the archive: Paranal . . . . .	142
9.4 Conclusion . . . . .	146
10 Campaign to Measure Water Vapour: La Silla	150
11 Campaign to Measure Water Vapour: Paranal	157
12 Correlation of Methods	164
12.1 Comparison of methods and validation with respect to radiosondes	164
12.2 Comparison with GOES . . . . .	167
12.3 Findings of the PWV campaigns . . . . .	170
12.4 Conclusion . . . . .	171
13 Conclusions	173
Bibliography	178
A Methods: Lunar Absorption Spectrophotometer	186
A.1 Overview . . . . .	186
A.2 Introduction . . . . .	186
A.3 Background . . . . .	187
A.4 Lunar spectrophotometer . . . . .	187
A.5 Design . . . . .	188
A.6 Calibration and operation . . . . .	188
A.7 Data processing . . . . .	192
A.8 Results . . . . .	193
A.9 Further work . . . . .	194
B Fundamentals of Diffraction Grating Spectrometers	196
B.1 Spectrometers . . . . .	196
B.2 Diffraction grating . . . . .	196
B.3 Order . . . . .	198
B.4 Dispersion . . . . .	198
B.5 Spectral resolution and resolving power . . . . .	199
B.6 Free spectral range . . . . .	200
B.7 Blazing . . . . .	200
B.8 MIKE free spectral range . . . . .	201
B.9 Diffraction grating ILS . . . . .	203
C Spectral Fitting Algorithm Source Code	205

---

# List of Tables

3.1	Radiometric quantities and associated units . . . . .	24
3.2	Transition data for CO and its isotopes from the JPL molecular spectroscopy catalogue. . . . .	31
3.3	Water vapour vibrational transitions for the spectral regions measured in this thesis . . . . .	43
5.1	Sample radiosonde data from the NOAA radiosonde archive . . . . .	72
9.1	Mean PWV over La Silla derived from different methods . . . . .	142
9.2	Number of nights (%) when PWV over La Silla was below a given value . .	142
9.3	Mean PWV over Paranal derived from different methods . . . . .	146
9.4	Number of nights (%) when PWV over Paranal was below a given value . .	146
10.1	Summary of data collected during May 2009 PWV measurement campaign at La Silla . . . . .	153
10.2	Summary of instrumentation used during the May 2009 PWV measurement campaign at La Silla . . . . .	154
11.1	Summary of instrumentation used during the PWV measurement campaigns at Paranal . . . . .	160
11.2	Summary of data collected during July/August 2009 PWV measurement campaign at Paranal . . . . .	162
11.3	Summary of data collected during November 2009 PWV measurement campaign at Paranal . . . . .	162
12.1	Correlation between various instruments and radiosondes . . . . .	165

---

# List of Figures

1.1	NASA MODIS plot of mean atmospheric water vapour for March 21, 2006.	7
1.2	Instrument-model-measurement system . . . . .	11
2.1	Simulated atmospheric transmission over Mauna Kea . . . . .	16
3.1	The electromagnetic spectrum and types of transitions associated with each different energy/frequency range . . . . .	27
3.2	A diatomic molecule . . . . .	28
3.3	Detailed rotational spectrum of CO . . . . .	32
3.4	A set of rotational energy levels $E(J)$ . . . . .	33
3.5	A non-linear triatomic molecule . . . . .	38
3.6	Simulated rotational spectrum of H <sub>2</sub> O and its isotopes . . . . .	39
3.7	Energy level diagram for para and ortho H <sub>2</sub> O . . . . .	41
3.8	Doppler, Lorentz and Voigt line profiles . . . . .	47
3.9	Altitude dependence of Doppler, Lorentz and Voigt profiles . . . . .	48
4.1	Input parameters and resources necessary for atmospheric modeling . . . . .	51
4.2	Temperature profile from the U.S. Standard Atmosphere 1976 . . . . .	53
4.3	Pressure profile from the U.S. Standard Atmosphere 1976 . . . . .	53
4.4	Mixing ratios from the U.S. Standard Atmosphere 1976 . . . . .	54
4.5	Depletion of the radiant intensity in traversing an absorbing medium . . . . .	56
4.6	Planck emission from a set of temperatures . . . . .	58
4.7	Simulated atmospheric flux spectrum for PWV = 0.5, 1.0, 2.0 and 4.0 mm.	64
5.1	A Vaisala RS92-SGP radiosonde instrumentation package . . . . .	66
5.2	Radiosonde SkewT-LogP diagram . . . . .	67
5.3	Radiosonde Hodogram . . . . .	68
5.4	Pressure versus altitude data from 3003 radiosondes (10 years) from Antofagasta, Chile. . . . .	73
5.5	Temperature versus altitude data from 3003 radiosondes (10 years) from Antofagasta, Chile. . . . .	73
5.6	Mean temperature versus altitude data derived from 3003 radiosondes launched from Antofagasta, Chile. . . . .	75
6.1	Normalised IRMA instrument response function . . . . .	84
6.2	Optical side of an open IRMA unit . . . . .	85
6.3	IRMA unit installed at Las Campanas Observatory . . . . .	87

LIST OF FIGURES

---

6.4	IRMA sky-dip and calibration data . . . . .	89
7.1	MERIS water vapour bands and typical reflectance for bare soil, vegetation, and snow. . . . .	96
7.2	BTRAM simulated transmission for MERIS water vapour bands at sea-level with PWV = 25 mm. . . . .	97
7.3	Global maximum water vapour amounts determined by MERIS for 2006 . .	97
7.4	Full disk visible image from the GOES-12 spacecraft . . . . .	99
7.5	Full disk moisture channel image from the GOES-12 spacecraft . . . . .	99
7.6	BTRAM simulated emission and transmission for the GOES water vapour band at sea-level with PWV = 25 mm. . . . .	100
7.7	Weighting functions for selected infrared observing channels . . . . .	103
8.1	Transmission spectrum for the atmosphere above the Las Campanas Observatory . . . . .	110
8.2	Screenshot of the BTRAM atmospheric modeling software . . . . .	111
8.3	Algorithm for fitting a simulated spectrum to absorption spectra. . . . .	116
8.4	Simulated water and oxygen lines as compared to echelle measured data . .	118
8.5	BTRAM fit to echelle measured spectrum (several lines) . . . . .	119
8.6	BTRAM fit to echelle measured spectrum (three lines) . . . . .	119
8.7	BTRAM fit to echelle measured spectrum (single line) . . . . .	120
8.8	BTRAM fit to echelle measured spectrum, 700 nm region (dry and wet night)	121
8.9	BTRAM fit to echelle measured spectrum, 800 nm region (dry and wet night)	122
8.10	Equivalent width MIKE PWV versus BTRAM fitted PWV . . . . .	123
8.11	PWV fits with a varying slit width . . . . .	125
8.12	Algorithm for fitting a simulated spectrum to emission spectra . . . . .	126
8.13	CRILES data fitted with a simulated emission spectrum . . . . .	127
8.14	VISIR data fitted with a simulated emission spectrum . . . . .	128
9.1	BTRAM fit to UVES archival data . . . . .	134
9.2	BTRAM fit to FEROS archival data . . . . .	135
9.3	Scatter plot comparing GOES and MERIS PWV over La Silla . . . . .	138
9.4	Scatter plot comparing GOES and FEROS PWV over La Silla . . . . .	139
9.5	La Silla archival PWV time series (FEROS, GOES, MERIS), 2005–2009 . .	140
9.6	La Silla archival PWV time series (FEROS, GOES, MERIS), May to September 2006 . . . . .	140
9.7	La Silla archival PWV time series (FEROS, GOES, MERIS), August 2006 .	141
9.8	Scatter plot comparing GOES and MERIS PWV over Paranal . . . . .	143
9.9	Scatter plot comparing GOES and UVES PWV over Paranal . . . . .	144
9.10	Paranal archival PWV time series (UVES, GOES, MERIS), 2001–2008 . . .	147
9.11	Paranal archival PWV time series (UVES, GOES, MERIS), July to November 2007 . . . . .	147
9.12	Paranal archival PWV time series (UVES, GOES, MERIS), April to June 2004	148
9.13	Paranal archival PWV time series (UVES, GOES, MERIS), May 2004 . . .	148

## LIST OF FIGURES

---

10.1	PWV time series for May 2009 campaign at La Silla and Las Campanas . . .	155
10.2	PWV time series data for May 12, 2009 . . . . .	155
11.1	PWV time series for August 2009 campaign at Paranal . . . . .	159
11.2	PWV time series for November 2009 campaign at Paranal . . . . .	161
11.3	PWV differences between Paranal and Armazones . . . . .	161
12.1	Scatter plots of IRMA and BACHES versus radiosonde derived PWV . . .	167
12.2	Scatter plots of IRMA, CRIRES, UVES and VISIR versus radiosonde derived PWV . . . . .	168
12.3	Scatter plots of GOES versus radiosonde derived PWV for La Silla and Paranal	170
A.1	Simulated water vapour transmission spectrum and lunar filter bands . . .	189
A.2	Simulated lunar photometer response profile . . . . .	190
A.3	Diagram of on- and off-band measurement technique . . . . .	191
A.4	Optical design schematic of the lunar spectrophotometer. . . . .	192
A.5	Interior photo of the lunar spectrophotometer. . . . .	192
A.6	Time series data from lunar photometer showing the filter bands . . . . .	193
A.7	Two minutes of signal from the detector clearly shows that a lunar tracking system would be beneficial. . . . .	194
A.8	Photo of lunar photometer set-up . . . . .	195
A.9	Comparison between radiosonde PWV and measured flux ratios . . . . .	195
B.1	A simple spectrograph . . . . .	197
B.2	Geometry of diffraction for planar wavefronts. . . . .	197
B.3	Diagram of an echelle grating . . . . .	198
B.4	Diagram of the Rayleigh criterion. . . . .	200
B.5	Diagram of a blazed grating. . . . .	201
B.6	MIKE echelle data showing all orders . . . . .	202
B.7	MIKE CCDs quantum efficiency versus wavelength . . . . .	202
B.8	First light echellogram from FEROS . . . . .	203

---

# List of Abbreviations

<b>AIG</b>	Astronomical Instrumentation Group
<b>ALMA</b>	Atacama Large Millimeter Array
<b>ALTAZ</b>	Altitude-Azimuth
<b>ATM</b>	Atmospheric Transmission at Microwaves (atmospheric model)
<b>ATRAN</b>	Atmospheric Transmission (atmospheric model)
<b>ATs</b>	Auxiliary Telescopes
<b>BACHES</b>	BAsic eCHElle Spectrograph
<b>BTRAM</b>	Blue Sky Transmission and Radiance Atmospheric Model
<b>CCD</b>	Charge-coupled device
<b>CRIRES</b>	CRyogenic high-resolution InfraRed Echelle Spectrograph
<b>E-ELT</b>	European Extremely Large Telescope
<b>ELT</b>	Extremely Large Telescope
<b>EM</b>	Electromagnetic
<b>ENSO</b>	El Niño-Southern Oscillation
<b>ESA</b>	European Space Agency
<b>ESO</b>	European Southern Observatory
<b>FASCODE</b>	Fast Atmospheric Signature Code
<b>FEROS</b>	Fiber-fed Extended Range Optical Spectrograph
<b>FITS</b>	Flexible Image Transport System
<b>FPI</b>	Fabry-Pérot interferometer
<b>FTS</b>	Fourier Transform Spectroscopy
<b>FTS</b>	Fourier Transform Spectrometer
<b>GEISA</b>	<i>Gestion et Etude des Informations Spectroscopiques Atmosphériques</i> : Management and Study of Atmospheric Spectroscopic Information
<b>GOES</b>	Geostationary Operational Environmental Satellites

## LIST OF ABBREVIATIONS

---

<b>GMT</b>	Giant Magellan Telescope
<b>GPS</b>	Global Positioning System
<b>GUI</b>	Graphical user interface
<b>HARPS</b>	High Accuracy Radial velocity Planet Searcher
<b>HITRAN</b>	High-resolution transmission molecular absorption database
<b>HWHM</b>	Half-width at half-maximum
<b>IDL</b>	Interactive Data Language
<b>ILS</b>	Instrumental Lineshape
<b>IR</b>	Infrared
<b>IRMA</b>	Infrared Radiometer for Millimetre Astronomy
<b>ISIS</b>	Institute for Space Imaging Science
<b>JD</b>	Julian Date
<b>JPL</b>	Jet Propulsion Laboratory
<b>LBL<sup>2</sup></b>	Line-by-line layer-by-layer
<b>LCO</b>	Las Campanas Observatory
<b>LTE</b>	Local Thermodynamic Equilibrium
<b>LPE</b>	Local Hydrostatic Equilibrium
<b>MERIS</b>	Medium Resolution Imaging Spectrometer
<b>MIKE</b>	Magellan Inamori Kyocera Echelle spectrograph
<b>MJD</b>	Modified Julian Date
<b>MODIS</b>	Moderate Resolution Imaging Spectroradiometer
<b>NASA</b>	National Aeronautics and Space Administration (USA)
<b>NOAA</b>	National Oceanic & Atmospheric Administration (USA)
<b>OAP</b>	Off-axis parabolic (mirror)
<b>ppm</b>	Parts per million
<b>PWV</b>	Precipitable Water Vapour
<b>RFM</b>	Reference Forward Model (atmospheric model)
<b>RH</b>	Relative Humidity
<b>SMA</b>	Smithsonian Millimeter Array
<b>SPICA</b>	Space Infrared telescope for Cosmology and Astrophysics
<b>TMT</b>	Thirty Meter Telescope
<b>USB</b>	Universal Serial Bus

## LIST OF ABBREVIATIONS

---

<b>USSA1976</b>	U.S. Standard Atmosphere 1976
<b>UT</b>	Universal Time
<b>UTs</b>	Unit Telescopes
<b>UTH</b>	Upper Tropospheric Humidity
<b>UVES</b>	Ultraviolet and Visual Echelle Spectrograph
<b>VISIR</b>	VLT Imager and Spectrometer for mid InfraRed
<b>VLT</b>	Very Large Telescope



---

# List of Equations

1.1	Capacitance, parallel plate capacitor . . . . .	7
1.2	Permittivity of a dielectric . . . . .	7
1.3	Parallel plate capacitor with a dielectric . . . . .	7
2.1	Angular resolution . . . . .	14
2.2	Barometric law . . . . .	17
2.3	Scale height . . . . .	17
2.4	Molar mass . . . . .	18
3.1	Beer's Law . . . . .	22
3.2	Schwarzschild equation . . . . .	22
3.3	Planck relation . . . . .	25
3.4	Reduced mass for a linear rigid rotor . . . . .	27
3.5	Moment of inertia . . . . .	28
3.6	Moment of inertia for a simple rigid rotor . . . . .	28
3.7	Angular momentum for a simple rigid rotor . . . . .	28
3.8	Z component of Angular momentum for a simple rigid rotor . . . . .	28
3.9	Rotational energy of a rigid rotor . . . . .	29
3.11	$B$ and $F(J)$ . . . . .	29
3.12	Difference between energy levels . . . . .	30
3.13	Distortion term corrections to $F(J)$ . . . . .	32
3.14	Rate of change of population $N_u$ of state $u$ due to induced absorption . . . . .	34
3.15	Spectral energy density . . . . .	34
3.16	Planck equation . . . . .	34
3.17	Population change due to stimulated emission . . . . .	34
3.18	Population change due to spontaneous emission . . . . .	34
3.19	Equilibrium population change . . . . .	35
3.20	Boltzmann distribution of equilibrium populations . . . . .	35
3.21	Einstein A coefficient . . . . .	35
3.22	Transition moment . . . . .	35
3.23	Einstein B coefficient . . . . .	36
3.24	Boltzmann distribution for energies . . . . .	36
3.25	Ratio of $J^{\text{th}}$ level population to ground state population . . . . .	37
3.28	Population maximum . . . . .	37
3.29	Hamiltonian for a light asymmetric rotor . . . . .	38
3.30	Heisenberg uncertainty principle . . . . .	44
3.31	Doppler effect . . . . .	44

LIST OF EQUATIONS

---

3.32	Doppler broadening line shape . . . . .	45
3.33	Doppler broadening half-width half-maximum . . . . .	45
3.34	Lorentz broadening lineshape . . . . .	46
3.35	Lorentz broadening half-width half-maximum . . . . .	46
3.36	Voigt profile . . . . .	46
4.1	Schwarzschild equation . . . . .	55
4.2	Opacity . . . . .	56
4.3	(Mass) absorption coefficient of a spectral line . . . . .	56
4.4	Planck equation . . . . .	57
4.5	Curtis-Godson approximation . . . . .	59
4.6	Opacity formulation in the LBL <sup>2</sup> approach . . . . .	60
5.1	Adiabatic lapse rate . . . . .	74
5.2	Scale height from measurements . . . . .	77
5.3	Saturation vapour pressure . . . . .	79
5.4	Partial pressure of water vapour . . . . .	79
5.5	Relative humidity . . . . .	79
5.6	Mixing ratio as computed from densities . . . . .	79
5.7	Ideal gas law . . . . .	80
5.8	Ideal gas law with density . . . . .	80
5.9	Density of air . . . . .	80
5.10	Water vapour density . . . . .	81
7.1	MERIS PWV retrieval algorithm . . . . .	94
7.2	GOES channel gain scaling . . . . .	102
7.3	Brightness temperature using an inverted Planck function . . . . .	102
7.4	Brightness Temperature from Radiance . . . . .	102
7.5	Upper Tropospheric Humidity from Brightness Temperature . . . . .	102
7.6	Normalised pressure factor for UTH equation . . . . .	103
7.7	Mixing ratio from UTH . . . . .	104
7.8	GOES derived PWV using mixing ratio . . . . .	104
8.1	PWV from equivalent width . . . . .	114
B.1	Grating equation . . . . .	197
B.2	Grating equation in Littrow configuration . . . . .	198
B.3	Angular dispersion . . . . .	198
B.4	Differentiated grating equation . . . . .	198
B.5	Angular dispersion . . . . .	199
B.6	Linear dispersion . . . . .	199
B.7	Resolving power . . . . .	199
B.8	Resolving power . . . . .	199
B.9	Maximal resolving power . . . . .	199
B.10	Angular width . . . . .	199
B.11	Free spectral range . . . . .	200
B.12	Free spectral range . . . . .	200
B.13	Blaze angle relationship . . . . .	201
B.15	Flux density distribution function for a set of rectangular slits . . . . .	203

---

# Chapter 1

## Introduction

### 1.1 Overview

Developed as a collaboration between the University of Lethbridge and the Herzberg Institute of Astrophysics, the Infrared (IR) Radiometer for Millimetre Astronomy (IRMA) [1] is a light weight and relatively low cost radiometer designed for determining atmospheric water vapour column abundance above high altitude telescope sites around the world. It uses a Mercury Cadmium Telluride (HgCdTe) infrared photoconductive detector<sup>1</sup> to measure the emission from water vapour rotational transitions in a carefully chosen spectral band centred around 20  $\mu\text{m}$ . The total power detected in this band is converted to a column abundance expressed in terms of precipitable water vapour (PWV) using the Blue Sky Spectroscopy Transmission and Radiance Atmospheric Model (BTRAM), an atmospheric model developed by previous members of our research group [2].

IRMA is a compact, reliable instrument with low power consumption, and there-

---

<sup>1</sup>#KMPC19-1-SP, Kolmar Technologies, Inc. <http://www.kolmartech.com>

fore lends itself to applications of atmospheric water vapour monitoring in remote locations. As a result, IRMA has been used by each of the Extremely Large Telescope (ELT) projects to help select their construction sites. Specifically, the Thirty Meter Telescope (TMT) [3] site selection team has chosen Mauna Kea as its site, and the Giant Magellan Telescope (GMT) [4] site selection team has decided to locate the new telescope on a hill adjacent to the Las Campanas Observatory in central Chile.

More recently, we have collaborated with a group of scientists from the European Southern Observatory (ESO) to assist in a set of site characterization and PWV calibration campaigns at their La Silla and Paranal observatory sites. In the context of site testing for their proposed European Extremely Large Telescope (E-ELT) [5], we have made measurements of PWV using several methods in an attempt to verify satellite estimates of the water column. Since satellites offer global coverage and have historical, calibrated data archives, if reliable PWV could be derived from them, it would provide a unique historical data set. For example, to first order, the satellite PWV data could provide information at a remote site, before ground-based testing were to occur. This could prove useful for sites that were undeveloped and extremely remote, and therefore challenging and expensive to deploy personnel and equipment.

My thesis reports on the contributions that I have made to modeling the atmosphere above the test sites, calibrating the IRMA units, devising a fitting algorithm to retrieve PWV from high-resolution echelle spectra, and the design, development and testing of a novel lunar absorption spectrophotometer to measure PWV. Since water vapour dramatically affects the transmission of radiation from astronomical sources, it is essen-

## 1.1. OVERVIEW

---

tial to have accurate, real-time information about the atmospheric water vapour column abundance.

The next generation of large, ground-based telescopes will allow for measurements of greater spatial resolution than was previously possible, but this hinges on having and identifying *good* observing nights. A good observing night would include many of the following features: cloudless, steady temperature, and little or no air movements to minimise turbulence, effects referred to as astronomical seeing. The factor missing from this list is water vapour. The effects of water vapour are essentially negligible at optical wavelengths. What the naked eye might see as a *clear* night at optical wavelengths may actually represent an atmosphere containing a significant amount of PWV, rendering the atmosphere nearly opaque in the infrared region of the spectrum.

Over the course of three PWV measurement campaigns in the Chilean Andes, several months of data from four sites were collected: La Silla<sup>2</sup>, Las Campanas<sup>3</sup>, Paranal<sup>4</sup> and Cerro Armazones. This multi-instrument, multi-facility data set was processed, providing us with a unique, large data set from which to derive statistical information about the sites that would, in part, influence the future location of the E-ELT telescope and the subsequent science that will be performed.

The importance of the site testing process cannot be overemphasized. Due to the large scale of the ELT projects (GMT, TMT and E-ELT), in terms of both the potential for ground-breaking scientific research, and the economics of the projects, their site selection teams require environmental data from candidate sites in order to make the best possible

---

<sup>2</sup>ESO: La Silla: <http://www.eso.org/sci/facilities/lasilla/site/aboutls.html>

<sup>3</sup>Las Campanas Observatory: <http://www.lco.cl/>

<sup>4</sup>ESO: The Very Large Telescope (Paranal): <http://www.eso.org/public/teles-instr/vlt.html>

## 1.2. PRECIPITABLE WATER VAPOUR

---

decision about where to locate the telescopes. As of April 2010, all three large telescope projects have completed their site selection process and efforts have now shifted towards site characterisation.

In the site testing phase, IRMA units were deployed to remote sites to measure PWV as an aid to the site selection process. An IRMA unit can find continued use as a real-time opacity monitor to assist in identifying those nights best suited for performing infrared astronomical observations. Thus, another goal of the PWV campaigns was to validate IRMA in this capacity.

### 1.2 Precipitable water vapour

PWV refers to the depth of liquid water present upon condensing a vertical column of water vapour of unit cross sectional area. Unless otherwise specified, the column is the height of the atmosphere, typically taken from the site location to the top of the atmosphere, which in this application can be taken as 100 km. PWV is a linear parameter with units of millimetres. If 1 mm PWV was condensed over an area of  $1 \text{ m}^2$ , the resulting liquid water would have a mass of 1 kg, since  $1 \text{ m}^3$  of water has a mass of 1000 kg.

Over time, liquid water, like Earth's oceans, comes to an equilibrium at its surface with the concentration of water vapour above it. If there is no motion, this equilibrium will be static. For example, there is water vapour in equilibrium above a steamy cup of tea. If you blow away this water vapour, the concentration will decrease so that *new* molecules of water will evaporate from the liquid and take their place. When the *new* molecules evaporate, they take with them some heat from the liquid. This is the mechanism by which

## 1.2. PRECIPITABLE WATER VAPOUR

---

tea is cooled by blowing on it. If the atmosphere is assumed to be at equilibrium, then the ocean can be considered as a covered cup of water. Over time there will be an equilibrium reached between the water molecules on the ocean surface and the water molecules in the air above the ocean. The amount of water in the air will depend on the temperature of both the ocean and the air. An example of this relationship between ocean temperature and airborne water vapour is seen in the El Niño-Southern Oscillation (ENSO)<sup>5</sup>, where the surface temperature of large areas of the Pacific ocean can increase by as much as 6 K. As the surface temperature of the oceans increases, the quantity of suspended water vapour increases (see saturation vapour pressure in §5.4.1), resulting in shifting weather patterns that can bring widespread drought over one part of the Earth, and heavy rains over another. Through this mechanism, climate is affected on a global scale.

Gaseous water is a small, (0.1–10,000 parts per million (ppm)) but environmentally significant constituent of the atmosphere [6]. The troposphere contains the majority of this water vapour. Besides accounting for most of the Earth's natural greenhouse effect, gaseous water also condenses to form clouds that cool the surface. In general terms, atmospheric water strongly influences, and is strongly influenced by, weather and weather is modified by climate.

The average residence time of water molecules in the troposphere is ~10 days. Water depleted by precipitation is replenished by evaporation from the seas, lakes, rivers and the transpiration of plants, and other biological and geological processes.

The annual mean global concentration of water vapour would yield about 25 mm of liquid water over the entire surface of the Earth if it were to condense. However, the mean

---

<sup>5</sup><http://www.physicalgeography.net/fundamentals/contents.html>

## 1.2. PRECIPITABLE WATER VAPOUR

---

annual precipitation for the planet is on the order of 1 m, which indicates a rapid turnover of water in the air. Figure 1.1 shows the global mean water vapour measured on March 21, 2006, by the MOderate Resolution Imaging Spectroradiometer (MODIS) instrument on the National Aeronautics and Space Administration (NASA) Terra satellite<sup>6</sup>. PWV in the figure ranges from  $\sim 0$ –75 mm, with the highest PWV values measured across the tropics. Measurements by the MODIS instrument cover the entire surface of the Earth every 1–2 days, measuring in over 36 spectral bands.

For demanding submillimetre astronomical applications, PWV should be less than 1 mm. These low levels of PWV are seen in the March 21, 2006 data in Figure 1.1 as the violet regions. Most of the northern hemisphere is violet, not surprising as this is winter/spring in the north, usually accompanied by snow and precipitation. The other regions that stand out are the northern African desert, where winds and dust and lack of high elevation sites make for poor observing conditions. Antarctica offers low PWV conditions but, as will be described later, there are several other factors that make Antarctica a challenging site. Lastly, there is a violet streak running up the west coast of South America. This streak is the Chilean Andes, devoid of precipitation and consisting of largely high and dry conditions, ideal for astronomical observing.

The amount of water vapour in the atmosphere directly affects the permittivity of the air [7]. Thus, one way of measuring relative humidity is to measure the capacitance of a parallel plate system using wet air as the dielectric. Some radiosonde instruments use this method to measure humidity. Capacitance,  $C$ , is defined as the ratio of charge,  $Q$ , to

---

<sup>6</sup>NASA MODIS: <http://modis.gsfc.nasa.gov/index.php>



## 1.2. PRECIPITABLE WATER VAPOUR

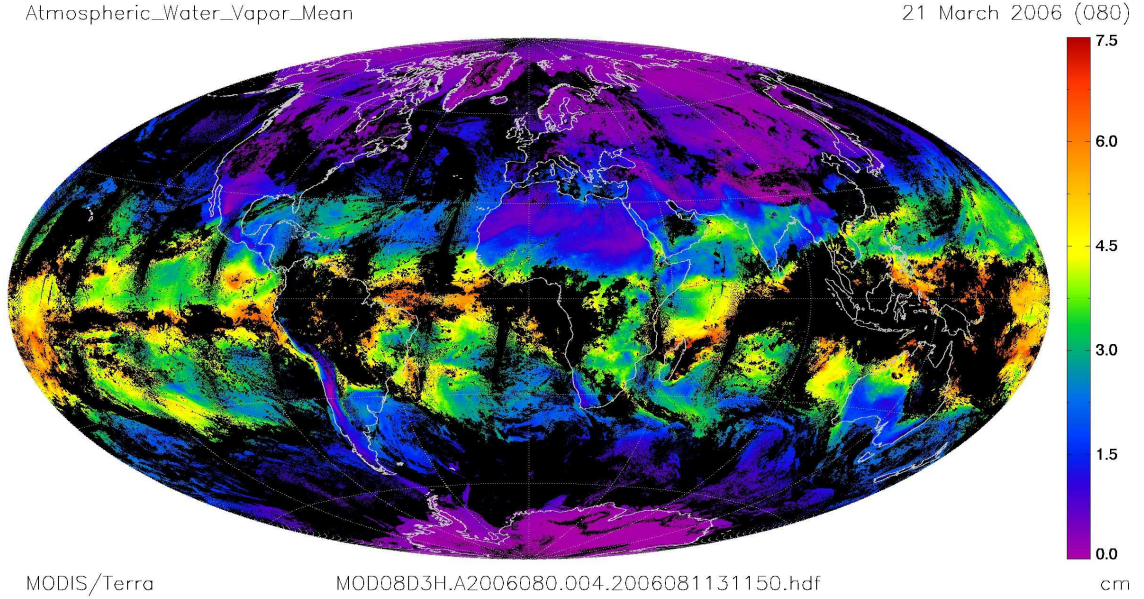


**Figure 1.1:** Mean atmospheric water vapour for March 21, 2006, as measured by the MODIS instrument on the NASA Terra satellite. The black regions represent gaps in the data due to the orbital path of the satellite. They are filled in on subsequent overpasses. Figure courtesy NASA.

the potential between two conductors, a and b,  $V_{ab}$ ,

$$C = \frac{Q}{V_{ab}} = \epsilon_0 \frac{A}{d} \quad [\text{C}] , \quad (1.1)$$

$$\epsilon = K \epsilon_0 \quad [\text{C}^2 \text{ N}^{-1} \text{ m}^2] , \quad (1.2)$$

$$C = K C_0 = K \epsilon_0 \frac{A}{d} = \epsilon \frac{A}{d} \quad [\text{C}] , \quad (1.3)$$

where  $\epsilon_0$  is the permittivity of free space,  $\epsilon_0 = 8.8542 \times 10^{-12} \text{ C}^2 \text{ N}^{-1} \text{ m}^2$  [7]. The capacitance of a parallel-plate capacitor with conductors of equal area  $A$ , and a vacuum separating the plates by a distance  $d$ , is given by Equation 1.1. If the vacuum is replaced with a dielectric, the capacitance increases by a factor  $K$ . The dielectric constant,  $K$ ,

of 1 atmosphere of dry air at 293 K is  $K = 1.00059$ , whereas the dielectric constant for water vapour at 293 K is  $K = 80.4$  [7]. This sizeable difference in  $K$  lends itself to the determination of the quantity of water vapour within a given quantity of air. Thus, using Equations 1.1 and 1.3, it is possible to calibrate and characterise such a device to measure relative humidity. Relative humidity will be discussed further in Chapter 5.

Water vapour has been identified in the atmosphere of a transiting extra-solar planet (HD189733b) by comparing models for the planet's transmitted spectrum to multi-wavelength measurements in the mid-infrared (in this case 3–8  $\mu\text{m}$ ) [8]. If astronomers are to have any hope of making extraterrestrial measurements of water vapour from ground-level observatories, they will first need to have a good understanding of the abundance of water vapour in our own atmosphere. This is the principal reason for having space-based observatories, such as Akari (Astro-F) [9], Herschel [10], the as yet launched Space Infrared telescope for Cosmology and Astrophysics (SPICA) [11] and the Spitzer space telescope [12].

### 1.3 Radiative transfer / Atmospheric modeling summary

Radiative transfer is the study of how energy in the form of electromagnetic (EM) radiation propagates through a medium, in our case through a mixture of gases (the atmosphere). Chapter 3 introduces the underlying principles of radiative transfer that are required to model an atmosphere.

Extracting meaningful results from any remote sounding instrument always involves use of a sophisticated atmospheric model. Atmospheric models tend to come in a variety of forms, the simplest being a plane-parallel, static (non-convective), non-scattering

(containing no aerosols, anthropogenic or naturally occurring) atmosphere with a smooth distribution of matter. All of these constraints may seem to reduce the realism of the model and thus its general applicability. However, they serve to make it simpler and thus faster computationally while maintaining the defining physical features of the system.

Atmospheric models depend upon several parameters including temperature, pressure, adiabatic lapse rate, scale height, mixing ratios, zenith angle and the nature of the radiation input to the atmosphere [13]. For example looking through the atmosphere at the Sun, both the spectrum of the Sun and the absorption spectrum of the atmosphere profile would need to be taken into account.

#### 1.3.1 BTRAM summary

The Blue Sky Transmission and Radiance Atmospheric Model (BTRAM<sup>7</sup>) is a line-by-line radiative transfer model used to simulate the transmission and emission resulting from a user-definable atmosphere. BTRAM was developed by David Naylor and Ian Chapman [2, 13] of the Astronomical Instrumentation Group (AIG) at the University of Lethbridge. It began as a customisable graphical user interface (GUI) with a simplified subset of the geometries available in Fast Atmospheric Signature Code (FASCODE) [14]. FASCODE was written in Fortran and enabled complicated geometries. By simplifying the available geometries and building the model in the Interactive Data Language (IDL<sup>®</sup>)<sup>8</sup>, BTRAM allows for customisable atmospheres based on radiosonde data, or through modifying pre-built profiles, which include: Antarctic Summer, Chajnantor Winter, Mauna Kea, Mid-Latitude Summer, Mid-Latitude Winter, Sub-Arctic Summer, Sub-Arctic Winter,

---

<sup>7</sup>BTRAM Website: <http://blueskyspectroscopy.com/>

<sup>8</sup>IDL: <http://www.itvis.com/idl/>

Tropical, and U.S. Standard. BTRAM uses the HIgh-resolution TRANsmission (HITRAN 2008) spectral line database for molecular line information [15].

#### 1.4 Focus of my work as reported in this thesis

As the fifth graduate student working on the IRMA project, my research builds upon that of previous graduate students. Graeme Smith was involved with the proof-of-concept version of IRMA, used at Mauna Kea [1]. Ian Chapman developed the radiative transfer atmospheric model used in conjunction with IRMA to relate atmospheric flux to PWV [2]. Ian Schofield created the communications and control system using a Rabbit microcontroller to enable the remote operation of the IRMA units [16]. Regan Dahl converted the system from Rabbit over to a PC104 controller. In my Master's thesis, I performed a thorough error analysis of the entire instrument/atmospheric model. Errors associated with internal blackbody temperature measurements were identified and accounted for through implementation of a calibration procedure employing an external calibrated reference blackbody. BTRAM was used to investigate the dependency on retrieved water vapour values as a function of the site-specific model input parameters.

The IRMA instrument, like any radiometer, provides meaningful results only if it is calibrated with respect to a known radiometric source. Once calibrated, the IRMA signal can be converted to atmospheric flux and then PWV through an atmospheric model. Thus, both the instrument and the atmospheric model have associated uncertainties that can propagate through to the final PWV value, as depicted in Figure 1.2.

The work described in this thesis includes three approximately month-long cam-

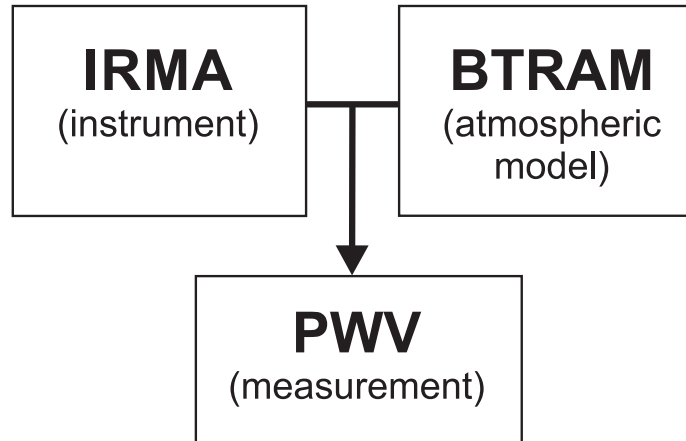


**Figure 1.2:** Measurements of PWV result from the IRMA-BTRAM, instrument/atmospheric model combination. Uncertainty in either the instrument or atmospheric model will propagate through the system resulting in an uncertainty in the PWV measurement.

paigns in Chile to measure PWV. They were undertaken with the goal of verifying satellite estimates of PWV in the context of site testing for the E-ELT. Also described are the variety of methods and instruments used, including spectral fitting described in Chapter 8 and the development of a lunar absorption spectrophotometer described in Appendix A.

The presence of water vapour in the atmosphere severely limits terrestrial astronomy, particularly in the far-infrared and sub-millimetre spectral regions. Sites with low PWV are thus favoured for installation of astronomical instrumentation, as will be discussed in the next chapter.

---

## Chapter 2

# Site Testing

### 2.1 Introduction

The E-ELT project [5] is an ambitious undertaking by the European Southern Observatory and its many member states, to construct the world's largest optical telescope within the next decade. The sheer size of the E-ELT (42-metre diameter primary collecting area) creates obvious design obstacles and, hence, the E-ELT represents a technological milestone in the eventual construction of even larger ground-based telescopes.

My thesis project involved testing sites to determine the best location for the E-ELT. As part of this effort, the Institute for Space Imaging Science (ISIS) at the University of Lethbridge has collaborated with researchers from ESO and the Universidad de Valparaiso's Astroclimatology group to conduct PWV measurement campaigns to study the water vapour and resulting atmospheric opacity at several sites in Chile. The goal was to apply the results to satellite estimates of PWV for the same sites at the same time to hopefully gain valuable insight into the utility of the global data set provided by the satellite

## 2.2. WHY BUILD A LARGE TELESCOPE?

---

measurements. The findings from our PWV campaigns were presented to the Site Selection Advisory Committee, who in turn provided the ESO Council with a preliminary report of its main conclusions in March 2010. These conclusions confirmed that all of the sites examined in the final shortlist (Armazones, Ventarrones, Tolonchar and Vizcachas in Chile, and La Palma in Spain) have very good conditions for astronomical observing, each with its particular strengths. The technical report concluded that “Cerro Armazones stands out as the clearly preferred site, because it has the best balance of sky quality for all the factors considered and can be operated in an integrated fashion with ESO’s Paranal Observatory.” On April 26, 2010, the ESO Council selected Cerro Armazones as the baseline site for the planned 42-metre E-ELT<sup>1</sup>.

### 2.2 Why build a large telescope?

When designing an optical telescope there is a relationship between the diameter of the primary reflecting surface, the wavelength of light being measured, and the maximum spatial resolution provided by the telescope. This relationship is referred to as the angular resolution or diffraction limited performance of a telescope. It determines the maximal spatial resolving power of any image forming device. Resolving power is the ability to measure the angular separation of unique points in an object. In the case of a single telescope, point-like sources separated by an angle smaller than the angular resolution cannot be resolved. The angular resolution  $\theta$  of a single telescope can be approximated by Equation 2.1:

$$\theta \approx \frac{\lambda}{D} \quad [\text{radians}] \quad , \quad (2.1)$$

---

<sup>1</sup>ESO: E-ELT Site Chosen: <http://www.eso.org/public/news/eso1018/>

## 2.3. SITE SELECTION

---

where  $\lambda$  is the wavelength of the observed radiation and  $D$  is the diameter of the telescope's objective or primary reflecting surface. The size of the primary reflecting surface will also determine the telescope's ability to collect photons and, thus, observe weaker, more distant objects.

For near-IR radiation ( $\lambda \sim 1000$  nm, or  $1 \mu\text{m}$ ), a telescope primary mirror diameter of 42 m will give  $\sim 2.4 \times 10^{-8}$  radians of angular resolution. This is equivalent to  $\sim 4.9$  milliarcseconds of angular resolution. To put this angular value into perspective, it would be sufficient to distinguish a 14-point headline (4.8 mm) off a newspaper in Calgary, Alberta, as viewed from Lethbridge, Alberta ( $\sim 200$  km distant)!

In order to achieve high angular resolution at longer wavelengths, the effective diameter of the telescope must be increased proportionately, hence the use of interferometers like the Smithsonian Millimeter Array (SMA) in Hawaii, or the Atacama Large Millimeter Array (ALMA) currently being built on Chajnantor in northern Chile. Equation 2.1 can also be used to calculate the angular resolution of an interferometer. In this case, however, the effective diameter,  $D$ , is replaced by the largest baseline of the interferometric array,  $B$ .

### 2.3 Site selection

The atmosphere is a complex system whose constituents can be divided into two main sets: atoms and molecules that interact with radiation in discrete ways according to the laws of quantum mechanics, and larger condensates such as aerosols, ice crystals, liquid water droplets, dust and soot that can be treated more classically. When these two types of systems are combined (classical and quantum), the complexity of understanding



### 2.3. SITE SELECTION

---

and modeling such an atmosphere becomes readily apparent.

When selecting a site for a ground-based observatory, it is important that ground based sources of light be minimal and that the sky be transparent within the spectral region of interest. Many universities have optical telescopes that were moderately useful 50 years ago. However, with the general expansion of urban landscapes, these same small-scale observatories now find themselves within areas completely overrun with light pollution. Another obstacle to observing is the opacity of the atmosphere itself. Naïvely, air is transparent (zero opacity) to visible light, such that we can see the sun, moon, stars, etc. However, this transparency does not apply to all regions of the electromagnetic spectrum, hence the need for instruments to determine this opacity in regions beyond the limits of human vision. Figure 2.1 is a simulated transmission spectrum for the atmosphere above Mauna Kea with 1 mm PWV over the wavelength range from 0.5 – 1000  $\mu\text{m}$ . Also shown are the measurement bands utilised in the studies to be presented in this thesis.

One of the most important first steps of the E-ELT project was the selection of a site for the location of the telescope. Several sites were short-listed; these included sites in Chile and the Spanish Canary Islands off the coast of Morocco. These sites were studied carefully to determine their scientific quality based upon such factors as winds, average cloud cover, atmospheric turbulence/stability and the resulting astronomical seeing, and water vapour content. The AIG at the University of Lethbridge has developed an infrared radiometer (IRMA) that was employed in this effort as a PWV monitor. Data were collected and analysed to provide an accurate representation of the local atmospheric conditions at several of the potential Chilean sites. The final site, Cerro Armazones, was chosen based

### 2.3. SITE SELECTION

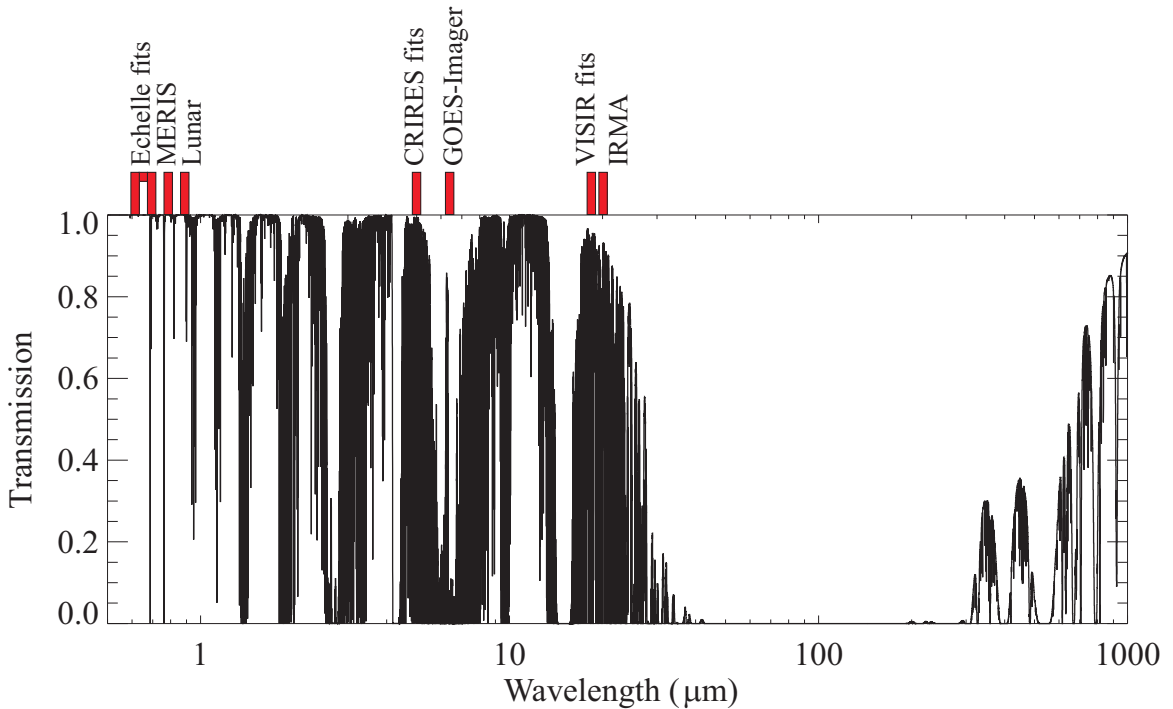


**Figure 2.1:** BTRAM simulated atmospheric transmission over Mauna Kea for  $PWV = 1$  mm;  $\lambda = 0.5\text{--}1000$   $\mu\text{m}$ . There are no transmissive atmospheric windows present for  $PWV = 1$  mm between  $\sim 30\text{--}300$   $\mu\text{m}$  (1–10 GHz). The instrumental measurement bands are plotted above the spectrum.

upon an optimal blend of scientific quality and logistical considerations.

As the optical thickness of the atmosphere increases, more light at a specific frequency will be absorbed, until finally the atmosphere becomes completely opaque, effectively saturated at that frequency. Ideally, we would have nothing (no matter or medium) between us and the light we want to observe. This can be achieved by performing the measurement in space, above the Earth’s atmosphere. There are both technical and economic difficulties associated with this option. Our next resort is to have a ground-based observatory. The atmosphere blankets the Earth’s surface with a thickness of roughly 16 km everywhere (thicker at the equator and thinner at the poles due in part to the Earth’s rotation and to solar insolation). To get a sense of the distribution of the atmosphere with respect to

### 2.3. SITE SELECTION

---

height, 50% of the atmosphere by mass is below 5.6 km, 90% by mass is below 16 km, and 99.99997% by mass is below 100 km [17]. Thus, mountainous regions with base altitudes nearing 5.6 km will be above 50% of the atmosphere, and >90% of the water vapour, which is the dominant source of opacity in the infrared spectral region.

For an atmosphere that is in both local thermodynamic equilibrium (LTE) and local hydrostatic equilibrium (LPE), it can readily be shown that pressure and density decrease approximately exponentially with height, assuming a flat non-revolving Earth, constant gravity, etc. Thus, with higher altitude comes lower pressure, as is observed by finding a continuously thinner atmosphere the further one is from the Earth's surface. The thinner the atmosphere, the better it is for observing purposes, since thin implies lower density and therefore a lower number of molecules per given volume, decreasing the probability of interaction between radiation and matter, resulting in less absorption/emission/scattering of the light. The relationship between pressure and altitude is expressible as the law of atmospheres, also known as the barometric law:

$$\frac{p(z)}{p(0)} = e^{-z/H} \quad , \quad (2.2)$$

where  $p$  is pressure [mbar or Pa],  $z$  is altitude [m], and  $H$  is the scale height [m]. Thus, atmospheric density and pressure decrease by a factor of  $1/e$  every time the altitude increases by one scale height. Scale height,  $H$  [m], is expressed as:

$$H = \frac{k_B T}{m g} \quad [\text{m}] \quad , \quad (2.3)$$

where  $k_B$  is Boltzmann's constant [ $k_B = 1.381 \times 10^{-23} \text{ JK}^{-1}$ ],  $T$  is temperature [K],  $m$  is the mean molecular mass of the air particle [kg], and  $g$  is the acceleration due to gravity

### 2.3. SITE SELECTION

---

[ $\text{ms}^{-2}$ ]. Molecular mass is defined as:

$$m = \frac{M}{N_A} \quad [\text{kg}] \quad , \quad (2.4)$$

where  $M$  is the molar mass [ $\text{kg mol}^{-1}$ ], or atomic mass unit [ $\text{u}$ ], and  $N_A$  is Avogadro's constant,  $6.022 \times 10^{23} \text{ mol}^{-1}$ . By definition, one mole is the amount of substance that contains as many elementary entities as there are atoms in 12 g of carbon-12 [7]. One mole of carbon-12 is 12.00000 grams. The atomic mass unit,  $u$ , is defined as 1/12 the mass of a carbon-12 atom, thus, carbon-12 is also 12.00000  $u$ . For example, the average atomic mass of hydrogen is 1.00794  $u$ , and that of oxygen is 15.9994  $u$ . The molecular mass of water,  $\text{H}_2\text{O}$ , is  $2 \times 1.00794 \text{ u} + 15.9994 \text{ u} = 18.01528 \text{ u}$ . Thus, one mole of water has a mass of 18.01528 g corresponding to a mean molecular mass of  $m = 2.9916 \times 10^{-26} \text{ kg}$  for one molecule of water.

The mean molar mass of dry air is  $0.02896 \text{ kg mol}^{-1}$ . As mentioned above, the mean molar mass of water is  $0.01802 \text{ kg mol}^{-1}$ . If  $T = 260 \text{ K}$ , the average temperature of the atmosphere, then Equation 2.3 results in  $H(\text{dry air}) = 7.6 \text{ km}$ , and  $H(\text{water}) = 12.2 \text{ km}$ . While the theoretical scale height of dry air agrees well with experimental measurements, the scale height of water as determined from radiosonde data in previous studies is  $\sim 0.3$  —  $2.1 \text{ km}$ [18]. This large discrepancy is due to the complexity of water and its ability to co-exist in three phases at atmospheric temperatures.

At infrared wavelengths centred around the  $20 \mu\text{m}$  region, the pure rotational transitions of water molecules are the dominant spectral features observed in our atmosphere [19]. IRMA is designed to measure directly this emission due to water vapour and, via an atmospheric model, infer the line-of-sight column abundance.

### 2.3. SITE SELECTION

---

The Earth offers many locations of extreme climate. A location offering a combination of these extremes would have the most favourable conditions for astronomical observing. For example, a desert might be selected for its local dryness. However, if the desert is at low altitude, there would still be a relatively thick atmosphere overhead, and potentially a high quantity of water vapour above it. Similarly, a location found at high altitude might not be appropriate due to high amounts of precipitation. The Atacama desert is located on a plateau at high elevation in the cold, desolate Andean tableland in northwestern Argentina and adjacent regions of Chile. It has the advantageous combination of being both high and dry.

An extremely cold place, such as Antarctica, also has the benefits of being both very dry and quite high ( $\sim 3000$  m). Antarctica is, in fact, the driest place on Earth since most of the water in the atmosphere above has precipitated. Elevation is no longer a primary concern since there is little water vapour in the atmosphere. There are, however, numerous challenges associated with situating an observatory in Antarctica, not the least of which are the extremely low temperatures, lack of infrastructure, geographical distance from major population centres, and maintenance of structures and equipment in the hostile, almost lifeless, environment. However, the benefits far outweigh the difficulties imposed by the location. In addition to being both high and dry, Antarctica has the added benefit of having 3+ months of continual darkness for observing, albeit with a limited view of the sky. According to the 1994 report edited by M. Burton [20], the Antarctic plateau is the most favourable terrestrial site for astronomical development due to its dark sky, hyper-dry, steady, and clear air, minimal interference from anthropogenic sources, and

geographical considerations. However, the impracticalities persist and the ELT projects have not considered Antarctica as a realistic observatory site.

### **2.4 Summary**

The scientific driver for building a large telescope is to have greater spatial resolution. The atmosphere is partially opaque at infrared wavelengths, depending on the amount of precipitable water vapour present above the site. Sites with qualities that are beneficial to astronomical observing have low PWV and are often found to be at high altitude, thus above a large portion of the atmosphere. The following chapters will briefly introduce radiative transfer theory, spectroscopy and its applications within atmospheric modeling.

---

## Chapter 3

# Introduction to Spectroscopy

### 3.1 Radiative transfer overview

Radiative transfer is defined as the process by which radiation passes through a medium that may contain any combination of scatterers, absorbers, and emitters. While the ancient Greeks began the process of reasoning known today as science, early work on radiative transfer began with Lord Rayleigh's investigations in 1871 on the nature of scattering by air molecules [21]. Simple radiative transfer was first formulated by Schwarzschild in 1906 in his work describing radiative equilibrium of a grey stellar atmosphere under conditions of local thermodynamic equilibrium and local hydrostatic equilibrium [22]. Since that time, sophisticated numerical solutions to radiative transfer problems have been developed, initially for single layer, and single wavelength applications, which are readily extended to a complex multi-layer, multi-chromatic atmosphere.

One of the simplest radiative transfer models is the Schwarzschild equation for a single atmospheric layer with constant pressure, temperature and density, for one specific

### 3.2. ELEMENTS OF RADIOMETRY

---

wavelength, effectively Beer's law with emission taken into account. Beer's law is given as [23]:

$$I = I_0 e^{-\alpha s} \quad [\text{W sr}^{-1} (\text{cm}^{-1})^{-1}] \quad , \quad (3.1)$$

where  $\alpha$  is an absorption coefficient and  $s$  is a path length. As an extension to Beer's law, the Schwarzschild equation is expressed as:

$$L_\sigma = L_\sigma(0) e^{-\tau_\sigma} + B_\sigma(T_s) (1 - e^{-\tau_\sigma}) \quad , \quad (3.2)$$

where  $L_\sigma$  has units of  $[\text{W m}^{-2} \text{sr}^{-1} (\text{cm}^{-1})^{-1}]$  and will be discussed further in Chapter 4.

It is possible to expand this simple model to represent a complex atmosphere where all parameters vary across the height of the atmosphere. This model could include many layers and be computed over many wavelengths. The effects of having multiple absorbers can only be calculated under the assumption that their interactions are independent from each other. Moreover, when determining the spectral emission from a molecule, it is necessary to account for contributions to emission away from the line centre that arise from the line profile.

The following sections will discuss the key points of radiative transfer, an introduction to molecular rotational spectroscopy, the characteristics of spectral line profiles, and the fundamentals of atmospheric modeling as applied to IRMA through the accurate simulation of test measurement sites.

### 3.2 Elements of radiometry

What follows is a brief introduction to the radiometric concepts at work within the BTRAM model. A more thorough development can be found in references [1] and [2].



### 3.2. ELEMENTS OF RADIOMETRY

---

Radiometry is the precise measurement of an amount of electromagnetic radiation detected over a specified wavelength or frequency range expressed as radiant power in Watts. This radiation can be referred to in a variety of ways. Table 3.1 highlights the common radiometric terms and their associated units.

All radiometric quantities can be *spectral*, meaning they are measured per unit wavelength or per unit wavenumber interval, denoted by subscript  $\lambda$  [m] or  $\sigma$  [ $\text{cm}^{-1}$ ], respectively. Wavenumber,  $\sigma$ , as used in this thesis, is  $1/\lambda$  and has units of  $\text{cm}^{-1}$ . The wavenumber was first used in the analysis of atomic spectra by Johannes Rydberg in the 1880s. Fourier Transform Spectroscopy (FTS) was proposed shortly thereafter, but was not fully developed until the 1950s with the advent of computers. Since a Fourier transform performed on data as a function of optical path difference within the interferometer [cm] yields a reciprocal spectrum [ $\text{cm}^{-1}$ ], the wavenumber was found to be a convenient unit for this work. Wavenumber is proportional to inverse wavelength, and thus is the analogue of frequency.

There is a natural progression between the following four radiometric quantities: energy, power, intensity and radiance. The first, spectral power,  $\Phi_\sigma$ , is the spectral energy per unit time [ $\text{W} (\text{cm}^{-1})^{-1}$ ]. Spectral intensity,  $I_\sigma$ , is the spectral power per unit solid angle [ $\text{W sr}^{-1} (\text{cm}^{-1})^{-1}$ ]. Spectral irradiance,  $E_\sigma$ , is the spectral power per unit cross-sectional area [ $\text{W m}^{-2} (\text{cm}^{-1})^{-1}$ ]. Lastly, spectral radiance,  $L_\sigma$ , is the spectral intensity per unit projected source area [ $\text{W m}^{-2} \text{sr}^{-1} (\text{cm}^{-1})^{-1}$ ]. The concept of solid angle,  $\Omega$ , measured in steradians, sr, is used to describe two-dimensional angular spans in three-dimensional space, analogous to the way in which the angle,  $\theta$ , in radians, describes angles in a plane.

**Table 3.1:** Radiometric quantities and associated units

Radiometric Quantity	Symbol	Units
Spectral power	$\Phi_\sigma$	W (cm <sup>-1</sup> ) <sup>-1</sup>
Spectral intensity	$I_\sigma$	W sr <sup>-1</sup> (cm <sup>-1</sup> ) <sup>-1</sup>
Spectral irradiance	$E_\sigma$	W m <sup>-2</sup> (cm <sup>-1</sup> ) <sup>-1</sup>
Spectral radiance	$L_\sigma$	W m <sup>-2</sup> sr <sup>-1</sup> (cm <sup>-1</sup> ) <sup>-1</sup>

A solid angle of  $4\pi$  sr covers all directions in space, i.e., the full sphere.

### 3.3 Introduction to spectroscopy

All methods of measuring water vapour examined in this thesis (apart from radiosondes) determine the water column abundance through measurements of radiation within a given spectral range and subsequent retrieval of PWV using an atmospheric model and instrument dependent algorithm. Spectroscopy is the study of the interaction between radiation and matter (as a function of either wavelength or frequency). I will begin by introducing the reader to fundamental concepts of spectroscopy, radiative transfer and atmospheric modeling. These concepts will then be applied on a case-by-case basis to the individual instruments that I have used in determining PWV in this thesis.

There are multiple ways that a molecule, atom, or ion can absorb and emit electromagnetic radiation, thus producing the measurable and unique spectrum of radiant energy versus frequency (or wavelength). In order of decreasing energy, the physical mechanisms leading to energy transitions include nuclear transitions (radioactivity/gamma radiation), electronic transitions (X-rays, ultraviolet, and visible radiation), vibrational transitions (near-infrared radiation), rotational transitions (far-infrared radiation), and elec-

### 3.3. INTRODUCTION TO SPECTROSCOPY

---

tron/nuclear spin transitions (microwaves, radio waves); see Figure 3.1. The energy associated with rotation of a molecule is much less than the energy associated with vibration. The frequencies at which a molecule will either rotate or vibrate will depend intrinsically on the masses and locations of the atoms in the molecule and the respective force constants in their chemical bonds. Equation 3.3, described below, shows the proportionality relationship between energy and frequency. A higher energy difference translates directly to a higher frequency, and vice-versa.

Spectroscopy is the study of electromagnetic radiation and its frequency dependent interactions with matter. It is a method of determining the chemical composition of materials by looking at their spectra either in emission or absorption. By this method, spectroscopy can be used to determine the composition and physical conditions of distant stars and galaxies. While spectroscopic observations at visible wavelengths can be used to identify atoms, in the case of molecules, the infrared region provides far more powerful diagnostic capabilities due to the complexities of the allowed rotational and vibrational transitions.

Atoms in their ground state can be excited through the addition of unique and discrete amounts of energy. For each of these specific transitions, there will be an associated photon of fixed frequency with exactly the energy required. The same processes also work in reverse. An electron dropping from an upper excited state,  $E_u$ , to a lower state,  $E_l$ , will emit a quantum of energy as a photon of a given frequency, described by:

$$\Delta E_{ul} = E_u - E_l = h \nu = h c \sigma \quad [\text{J}] , \quad (3.3)$$

where  $\Delta E_{ul}$  is the photon energy [J],  $h$  is Planck's constant [ $\text{m}^2 \text{kg s}^{-1}$ ],  $\nu$  is the photon

### 3.3. INTRODUCTION TO SPECTROSCOPY

---

frequency [ $\text{s}^{-1}$ ],  $c$  is the speed of light in a vacuum [ $\text{cm s}^{-1}$ ], and  $\sigma$  is wavenumber [ $\text{cm}^{-1}$ ]. Note that  $c$  should be expressed in  $\text{cm s}^{-1}$  whenever using the wavenumber form of a relationship.

Differences in rates of rotation and vibration serve to separate, spectrally, lighter molecules from heavier ones. For example, a heavy molecule will have a larger reduced mass and thus a larger moment of inertia,  $I$ , resulting in a smaller spacing between adjacent rotational energy levels, i.e., the energy levels will be more densely packed than those of a lighter molecule. Water, being one of the lightest rotators commonly present in our atmosphere, has rotational energy levels with large inter-level spacing, leading to rotational transitions at higher frequencies. Other common atmospheric molecules do not have any measurable rotational transitions at these higher frequencies because the associated states are not populated. Moreover, the observed rotational transitions of water extend to  $500 \text{ cm}^{-1}$  ( $20 \text{ }\mu\text{m}$ ), just below the energy levels where molecules begin to exhibit their vibrational transitions. For this reason,  $20 \text{ }\mu\text{m}$  is an ideal spectral region to measure water vapour. As an aside,  $20 \text{ }\mu\text{m}$  also happens to be near the peak of the Planck curve for temperatures found in the lower atmosphere ( $\sim 250 \text{ K}$ ), as will be discussed in §4.4.

#### 3.3.1 Rotational spectroscopy

The water molecule is an asymmetric top requiring a complex model for spectroscopic analysis [23]. To introduce the concepts of rotational spectroscopy, I will begin with a simple diatomic molecule and build upon that foundation until the model is sufficiently complex. Then, I will show how that model relates to a water molecule. I have chosen carbon monoxide (CO), a simple diatomic molecule possessing rotational transitions, that

### 3.3. INTRODUCTION TO SPECTROSCOPY

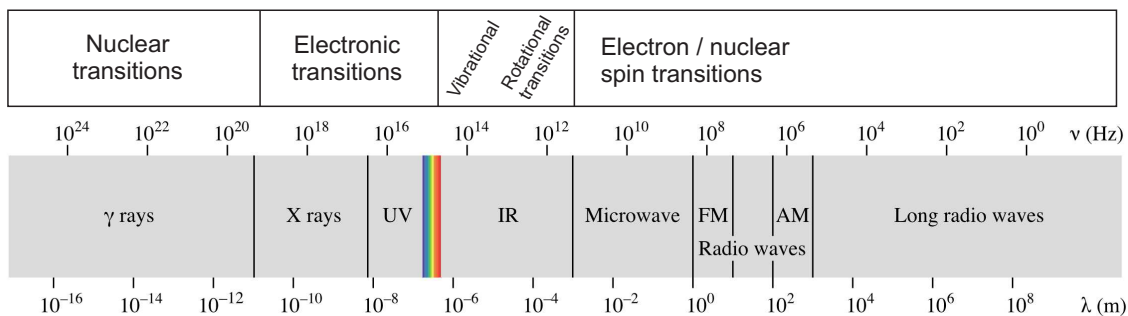


**Figure 3.1:** The electromagnetic spectrum and the types of transitions associated with each different energy/frequency range. Image based on original by Philip Ronan (Creative Commons license).

is present in the Earth's atmosphere. CO is a heteronuclear diatomic molecule, as depicted in Figure 3.2. In quantum mechanics, the simplest approximation for the rotation of a diatomic molecule is obtained through the linear rigid rotor model. The term rigid is used here because it is assumed that the connection between the masses is both inflexible and massless, implying no vibration or significant contribution to the moment of inertia of the system. The reduced mass for a linear rigid rotor is given as:

$$\mu = \frac{m_1 m_2}{m_1 + m_2} \quad [\text{kg}] , \quad (3.4)$$

where  $m_1$  and  $m_2$  are point masses. This model can be used to predict the rotational energy levels,  $E(J)$ , of a diatomic molecule using only the measured atomic masses and their separation. Rotational energy depends primarily on the moment of inertia of the molecular system. The moment of inertia,  $I$ , of any molecule about any axis through the centre of gravity is [24]:

$$I = \sum_i m_i r_i^2 \quad [\text{kg m}^2] , \quad (3.5)$$

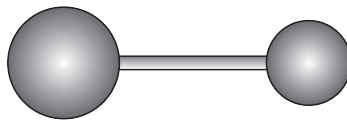


**Figure 3.2:** A diatomic molecule.

where  $m_i$  and  $r_i$  are the mass and distance, respectively, of the  $i^{\text{th}}$  atom with respect to the centre of gravity of the system. For a diatomic molecule, Equation 3.5 reduces to:

$$I = \mu R^2 \quad [\text{kg m}^2] , \quad (3.6)$$

where  $\mu$  is the reduced mass of the molecule and  $R$  is the internuclear separation.

The angular momentum for this simple rigid rotor model is given by [23]:

$$P_J = \sqrt{J(J+1)} \hbar \quad [\text{J s}] , \quad (3.7)$$

where  $J$  is a rotational quantum number ( $J = 0, 1, 2, \dots$ ), and  $\hbar = h/2\pi$  where  $h$  is Planck's constant. Due to the space quantization of rotational angular momentum, the  $z$  component of  $P_J$  is given by [23]:

$$(P_J)_z = M_J \hbar \quad [\text{J s}] , \quad (3.8)$$

where  $M_J = J, J-1, \dots, -J$ . As a result, the degeneracy of each rotational energy level is  $2J+1$ .

It is possible to describe the space- and time-dependence of a non-relativistic, quantum mechanical system using the Schrödinger equation, the quantum mechanical analogue of Newton's second law of motion,  $\vec{F} = m\vec{a} = \frac{d(m\vec{v})}{dt}$ . Solving the Schrödinger equation for the linear rigid rotor system results in a quantised formulation for the rotational energy

### 3.3. INTRODUCTION TO SPECTROSCOPY

---

given by Equation 3.9 [25]:

$$E(J) = \frac{h^2}{8\pi^2 I} J(J+1) \quad [\text{J}] \quad . \quad (3.9)$$

The rotational constant,  $B$ , and term value,  $F(J)$ , are defined as follows:

$$B = \frac{h}{8\pi^2 c I} \quad [\text{cm}^{-1}] \quad , \quad (3.10)$$

$$F(J) = \frac{E(J)}{hc} = B J(J+1) \quad [\text{cm}^{-1}] \quad . \quad (3.11)$$

The rotational constant of a molecule depends solely on the moment of inertia of the molecule. The unique dependence of  $B$  on reduced mass and bond length allows for the identification of differing masses by analysis of subtle differences in the transition frequencies of isotopically substituted species. The isotope with heavier mass will have slightly lower rotational energy levels than its non-isotopic sibling. Through this relation, with a knowledge of the internuclear separation, measurements of  $B$  allow for the precise determination of the reduced mass of a molecule and represent a very powerful structural diagnostic and isotopic identification technique.

Although Equation 3.9 specifies the rotational energy levels in Joules, in practice, frequencies are measured as opposed to energies. For this reason, energy levels,  $E(J)$ , can be converted to term values,  $F(J)$ , using Equation 3.11 with dimensions of either frequency or wavenumber, by dividing  $E(J)$  by  $h$  or  $hc$ , respectively.

The moment of inertia of a molecule,  $I$ , is represented by a tensor of rank 2. Geometrically,  $I$  is defined by three mutually orthogonal axes  $A$ ,  $B$ , and  $C$ , whose origin is at the centre of mass of the molecule. This is referred to as the principal axis system [23]. A

### 3.3. INTRODUCTION TO SPECTROSCOPY

---

diatomic molecule can be oriented in such a way that, due to symmetry, two components of  $I$  are equal, i.e.  $I_A = I_B \neq I_C$ . This symmetry leads to a relatively simple set of rotational transitions, as shown in the simulated spectrum of CO in Figure 3.3. The spectrum shown includes transitions due to CO and three isotopes,  $^{13}\text{C}^{16}\text{O}$ ,  $^{12}\text{C}^{17}\text{O}$ , and  $^{12}\text{C}^{18}\text{O}$ . The transmittance plot was created with BTRAM, using a simulated gas cell of length  $\ell = 5$  m, temperature  $T = 273.15$  K, and pressure  $P = 1$  kPa. The spectral range was set to 25–50  $\text{cm}^{-1}$  (400–200  $\mu\text{m}$ ), with a resolution of 0.0001  $\text{cm}^{-1}$ . Transition data from the Jet Propulsion Laboratory (JPL) molecular spectroscopy catalogue<sup>1</sup> for CO and its isotopes are presented in Table 3.2.

#### 3.3.2 Transition energies and frequencies

Figure 3.4 shows how the rotational energy levels increase (and diverge) with increasing rotational quantum number. The rotational energy levels can also be expressed as wavenumbers by using Equation 3.11. The difference between energy levels when expressed as term values,  $F(J)$ , gives the frequency of the spectral transition,  $\sigma(J + 1 \rightarrow J)$ . The spacing between the transitions is an integer multiple of twice the rotational constant,  $2B$ :

$$\sigma(J + 1 \rightarrow J) = F(J + 1) - F(J) = 2B(J + 1) \quad [\text{cm}^{-1}] , \quad (3.12)$$

Thus, using Equation 3.12 and the  $F(J)$  results above, it is possible to determine the frequency of the spectral transitions. However, one would find that the calculated values are not correct. The reason for the discrepancy between the calculated and measured values is that the initial assumption of a rigid rotor is incorrect. As rotational energy increases, the

---

<sup>1</sup>JPL Molecular Spectroscopy Catalogue: <http://spec.jpl.nasa.gov/>



### 3.3. INTRODUCTION TO SPECTROSCOPY

---

**Table 3.2:** Transition data for CO and its isotopes from the JPL molecular spectroscopy catalogue.

28001 CO									
26.90701	0.00000	-2.6716	2	80.7354	15	-28001	101	7	6
30.74793	0.00000	-2.5590	2	107.6424	17	-28001	101	8	7
34.58767	0.00000	-2.4751	2	138.3904	19	-28001	101	9	8
38.42610	0.00000	-2.4156	2	172.9780	21	-28001	10110		9
42.26305	0.00000	-2.3773	2	211.4041	23	-28001	10111		10
46.09839	0.00000	-2.3581	2	253.6672	25	-28001	10112		11
49.93197	0.00000	-2.3561	2	299.7656	27	-28001	10113		12
29001 C-13-0									
25.72393	0.00000	-2.7187	2	77.1850	15	29001	101	7	6
29.39610	0.00000	-2.6034	2	102.9089	17	29001	101	8	7
33.06719	0.00000	-2.5165	2	132.3050	19	29001	101	9	8
36.73707	0.00000	-2.4535	2	165.3722	21	29001	10110		9
40.40561	0.00001	-2.4115	2	202.1092	23	29001	10111		10
44.07268	0.00001	-2.3881	2	242.5149	25	29001	10112		11
47.73813	0.00001	-2.3816	2	286.5875	27	29001	10113		12
29006 CO-17									
26.22750	0.00000	-2.6982	2	78.6962	15	29006	101	7	6
29.97150	0.00000	-2.5841	2	104.9237	17	29006	101	8	7
33.71438	0.00000	-2.4984	2	134.8952	19	29006	101	9	8
37.45601	0.00000	-2.4369	2	168.6096	21	29006	10110		9
41.19624	0.00001	-2.3965	2	206.0656	23	29006	10111		10
44.93494	0.00001	-2.3748	2	247.2618	25	29006	10112		11
48.67197	0.00001	-2.3702	2	292.1968	27	29006	10113		12
30001 CO-18									
25.62611	0.00000	-2.7226	2	76.8914	15	30001	101	7	6
29.28432	0.00000	-2.6071	2	102.5175	17	30001	101	8	7
32.94147	0.00000	-2.5199	2	131.8018	19	30001	101	9	8
36.59741	0.00000	-2.4567	2	164.7433	21	30001	10110		9
40.25203	0.00001	-2.4143	2	201.3407	23	30001	10111		10
43.90518	0.00001	-2.3906	2	241.5927	25	30001	10112		11
47.55673	0.00001	-2.3837	2	285.4979	27	30001	10113		12

Legend: FREQ, ERR, LGINT, DR, ELO, GUP, TAG, QNFMT, QN', QN''

FREQ: Frequency of the line in  $\text{cm}^{-1}$ .

ERR: Estimated or experimental error of FREQ in  $\text{cm}^{-1}$ .

LGINT: Base 10 logarithm of the integrated intensity in units of  $\text{nm}^2 \text{MHz}$  at 300 K.

DR: Degrees of freedom in the rotational partition function

ELO: Lower state energy in  $\text{cm}^{-1}$  relative to the ground state.

GUP: Upper state degeneracy.

TAG: Species tag or molecular identifier.

QNFMT: Identifies the format of the quantum numbers

QN': Quantum numbers for the upper state.

QN'': Quantum numbers for the lower state.

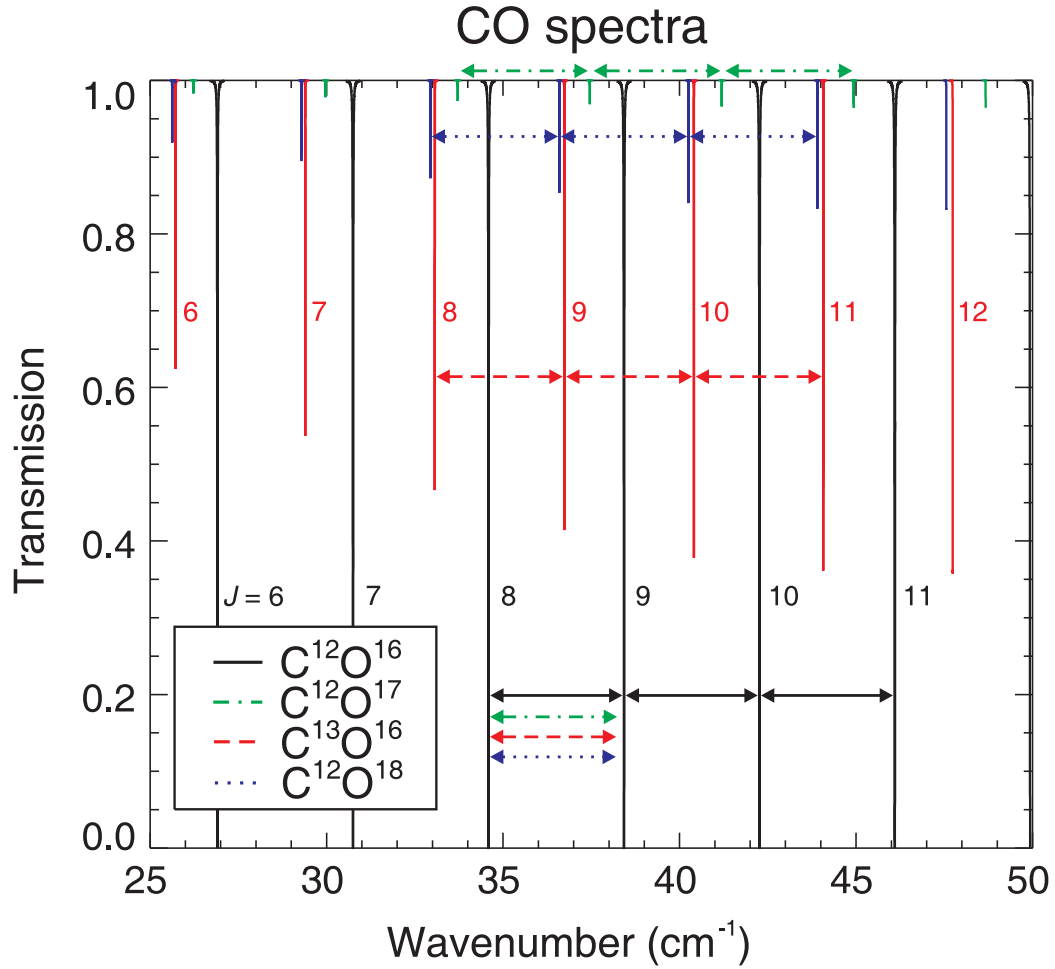


**Figure 3.3:** Detailed rotational spectrum for 1 kPa of CO and its isotopes at 273.15 K, in a 5 m gas cell, for  $\sigma = 25\text{--}50\text{ cm}^{-1}$ , at  $0.0001\text{ cm}^{-1}$  resolution.

bond length varies as a function of rotational energy. Correcting this requires the addition of higher-order distortion terms to the rotational energy expression:

$$F(J) = BJ(J+1) - D(J(J+1))^2 + H(J(J+1))^3 + L(J(J+1))^4 \dots, \quad (3.13)$$

where  $D$ ,  $H$  and  $L$  are distortion constants [23].

The  $2B$  spacing is observed between transitions for the same isotope, shown as the horizontal black, red, blue, and green lines in Figure 3.3. The spacings are different for

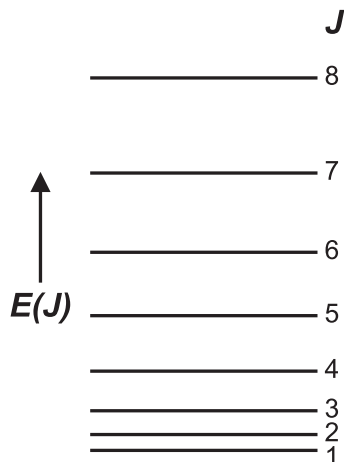


**Figure 3.4:** A set of rotational energy levels  $E(J)$  for increasing rotational quantum number,  $J$ .

each isotope, due to the differences in the rotational constant,  $B$ , for each isotope.

### 3.3.3 Transition intensities and Einstein coefficients

Knowing the frequency at which a rotational transition occurs is only one part of the puzzle. The intensity of each transition must also be known to simulate the spectrum of a given molecule. The transition intensity is proportional to the Einstein  $A_{ul}$  coefficient [23]. Emission and absorption and their relationships with the Einstein coefficients will be discussed in the following section.

There are three radiative processes by which energy can be exchanged between two time-independent states, where  $E_u$  represents an upper excited state, and  $E_l$  represents a lower state. These three processes are induced absorption, spontaneous emission, and induced or stimulated emission. In induced absorption, an atom absorbs a quantum of radiation and is excited from the  $l$  to the  $u$  state. The rate of change of population  $N_u$  of

### 3.3. INTRODUCTION TO SPECTROSCOPY

---

state  $u$  due to induced absorption is expressed as:

$$\frac{dN_u}{dt} = N_l B_{lu} \rho_\sigma(T) \quad [\text{s}^{-1}] \quad , \quad (3.14)$$

where  $B_{lu}$  is an Einstein coefficient and  $\rho_\sigma(T)$  is the spectral energy density whose dependence on wavenumber and temperature is given by [23]:

$$\int \rho_\sigma(T) d\sigma = \int \frac{8 \pi h c \sigma^3}{\exp\left(\frac{h c \sigma}{k_B T}\right) - 1} d\sigma \quad [\text{J m}^{-3}] \quad . \quad (3.15)$$

The spectral energy density function is geometrically related to the Planck function,  $B_\sigma(T)$ , given by Equation 4.4 and to be discussed in Chapter 4, by:

$$\int \rho_\sigma(T) d\sigma = \int \frac{4\pi}{c} B_\sigma(T) d\sigma \quad [\text{J m}^{-3}] \quad . \quad (3.16)$$

Induced or stimulated emission has a similar expression for population change, given by:

$$\frac{dN_u}{dt} = -N_u B_{ul} \rho_\sigma(T) \quad [\text{s}^{-1}] \quad , \quad (3.17)$$

where  $B_{ul}$  is the Einstein coefficient for this process, with  $B_{ul} = B_{lu}$ . Spontaneous emission has no dependence on the spectral energy density term; it is given by:

$$\frac{dN_u}{dt} = -N_u A_{ul} \quad [\text{s}^{-1}] \quad , \quad (3.18)$$

where  $A_{ul}$  is the Einstein coefficient associated with spontaneous emission.  $A_{ul}$  is also related to the natural spectral line broadening mechanism to be discussed in §3.4.

In any given situation all three processes are possible. For a system that has reached equilibrium, the net change in population can be expressed as:

$$\frac{dN_u}{dt} = (N_l - N_u) B_{ul} \rho_\sigma(T) - N_u A_{ul} = 0 \quad [\text{s}^{-1}] \quad , \quad (3.19)$$

### 3.3. INTRODUCTION TO SPECTROSCOPY

---

At equilibrium, the populations of  $N_u$  and  $N_l$  are related through the Boltzmann distribution [26]:

$$\frac{N_u}{N_l} = \frac{g_u}{g_l} \exp\left(-\frac{\Delta E_{ul}}{k_B T}\right) , \quad (3.20)$$

where  $g_u$  and  $g_l$  are the degeneracies of states  $u$  and  $l$ . Through substitution of Equations 3.15 and 3.20 into Equation 3.19, one can express  $A_{ul}$  in terms of  $B_{ul}$ :

$$A_{ul} = 8 \pi h c \sigma^3 B_{ul} \quad [\text{s}^{-1}] . \quad (3.21)$$

Equation 3.21 shows that spontaneous emission increases rapidly relative to induced emission as  $\sigma$  increases. The operation of lasers is based entirely on induced emission. The above equation shows that the process of lasing is more readily achievable for lower frequency radiation. The first lasers were referred to as masers, since they operated at lower, microwave frequencies.

The role of Einstein coefficients in emission and absorption processes have been described, and now I will relate them to transition intensities. This is done through the transition moment matrix element,  $\mathbf{R}^{ul}$ . The transition moment is a vector quantity expressed as:

$$\mathbf{R}^{ul} = \int \psi_u^* \vec{\mu} \psi_l d\tau \quad [\text{C m}] , \quad (3.22)$$

where  $\psi_u$  and  $\psi_l$  are the wavefunctions of the upper and lower states and  $\vec{\mu}$  is the electric dipole moment operator,  $\vec{\mu} \equiv \sum_i q_i \mathbf{r}_i$ , where  $q_i$  is the charge and  $\mathbf{r}_i$  is the position vector of the  $i^{\text{th}}$  particle. Transition intensity is proportional to the transition probability, which is the square of the dipole moment matrix element. This transition probability is also related

### 3.3. INTRODUCTION TO SPECTROSCOPY

---

to the Einstein  $B_{ul}$  coefficient through the following:

$$B_{ul} = \frac{8 \pi^3}{(4 \pi \epsilon_0) 3 h^2} |\mathbf{R}^{ul}|^2 \quad [\text{s}^{-1} \text{ J}^{-1} \text{ m}^3] . \quad (3.23)$$

The intensity of a given transition can thus be traced from  $\vec{\mu}$  to  $|\mathbf{R}^{ul}|^2$  to  $B_{ul}$  and finally to  $A_{ul}$ , the Einstein coefficient associated with spontaneous emission.

Transitions are only allowed for non-zero matrix elements  $\mathbf{R}^{ul}$ , which lead to the well-known selection rules of quantum mechanics. These rotational selection rules state that a molecule must possess a permanent dipole moment ( $\vec{\mu} \neq 0$ ), that  $\Delta J = \pm 1$ , and that  $\Delta M_J = 0, \pm 1$ . However, the selection rule related to  $\Delta M_J$  only increases the degeneracy, as discussed in §3.3.1, in the presence of an external electromagnetic field. Thus, through these selection rules and the above formulations, it is possible to determine which transitions will exist. To determine the relative intensity of the transitions, in addition to the individual line strengths, the relative populations of the corresponding energy levels must be known.

#### 3.3.4 Intensities and populations

The intensity of an emission line depends upon the population and degeneracy of the upper state of the transition. In the general case, the population  $N_i$  of the  $i^{\text{th}}$  level, relative to the ground state  $N_0$ , is given by the Boltzmann distribution, which can be expressed as in Equation 3.20. The Boltzmann distribution for energies is expressed as [26]:

$$\frac{N_i}{N} = \frac{g_i e^{-E_i/k_B T}}{\sum_i g_i e^{-E_i/k_B T}} = \frac{g_i e^{-E_i/k_B T}}{Z} , \quad (3.24)$$

where  $E_i$  is the energy of the  $i^{\text{th}}$  state,  $T$  is temperature,  $g_i$  is the degeneracy of the state, and  $N_i$  is the number of particles at the same  $E_i$  energy level.  $N$  is the total number of

### 3.3. INTRODUCTION TO SPECTROSCOPY

---

particles. The denominator is the partition function  $Z = \sum_i g_i e^{-E_i/k_B T}$ .  $Z$  represents the sum of all states and is used to determine the probabilities of how the particles are partitioned amongst the different possible energies.

Equation 3.24 can be used to determine the population of the  $J^{\text{th}}$  rotational energy level whose degeneracy is  $g_J = 2J + 1$ . The population of the  $J^{\text{th}}$  level relative to the population in the ground state ( $J = 0$ ) results from the ratio of  $N_J$  to  $N_0$ :

$$\frac{N_J/N}{N_0/N} = \frac{g_J e^{-E(J)/k_B T}/Z}{g_0 e^{-E(0)/k_B T}/Z} , \quad (3.25)$$

$$\frac{N_J}{N_0} = (2J + 1) \exp\left(\frac{-\Delta E_{J0}}{k_B T}\right) . \quad (3.26)$$

The factor of  $(2J + 1)$  increases linearly with  $J$ , whereas the exponential term decreases rapidly. The resulting behaviour of the distribution is such that  $N_J/N_0$  increases at low  $J$  values, until the exponential term dominates at higher  $J$  values, asymptotically returning  $N_J/N_0$  to zero. The population has a maximum and, thus, under the assumption of a constant  $A_{ul}$ , a maximal intensity at energy level  $J = J_{\text{max}}$ , with integer value nearest to:

$$\frac{d(N_J/N_0)}{dJ} = 0 , \quad (3.27)$$

leading to

$$J_{\text{max}} = \sqrt{\frac{k_B T}{2hB}} - \frac{1}{2} , \quad (3.28)$$

when  $B$  is expressed in units of frequency. Thus, from Equation 3.26 and the previous section on Einstein coefficients, the relative intensities of spectral lines have been shown to depend almost exclusively on temperature and some fundamental molecular parameters. Of these factors, all are independent of the environment except for temperature.

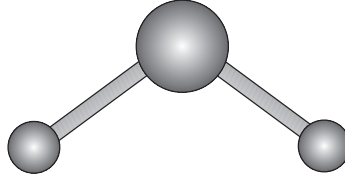


**Figure 3.5:** A non-linear triatomic molecule.

Thus far, only the transitions of a diatomic molecule have been explored and modeled. When description of the system is extended to include triatomic molecules, as shown in Figure 3.5, the equations required become far more complicated. While water would seem to be a relatively simple molecule, the complexities arising from it being a non-linear triatomic molecule are not trivial. The reduced symmetry of a water molecule, expressed as  $I_A \neq I_B \neq I_C$ , results in the complicated set of rotational transitions shown in the simulated water vapour spectrum in Figure 3.6.

The rigid asymmetric rotor Hamiltonian operator can be written as follows:

$$\begin{aligned}
 \hat{H} &= \frac{\hat{J}_a^2}{2I_A} + \frac{\hat{J}_b^2}{2I_B} + \frac{\hat{J}_c^2}{2I_C} \\
 A &= \frac{\hbar^2}{2I_A} \\
 B &= \frac{\hbar^2}{2I_B} \\
 C &= \frac{\hbar^2}{2I_C} \\
 \hbar^2 \hat{H} &= A\hat{J}_a^2 + B\hat{J}_b^2 + C\hat{J}_c^2 \\
 &= \left(\frac{A+B}{2}\right) (\hat{J}_a^2 + \hat{J}_b^2) + C\hat{J}_c^2 + \frac{(A-B)}{2} (\hat{J}_a^2 - \hat{J}_b^2) \\
 &= \left(\frac{A+B}{2}\right) \hat{J}^2 + \left(C - \frac{(A+B)}{2}\right) \hat{J}_c^2 + \left(\frac{A-B}{4}\right) ((\hat{J}^+)^2 + (\hat{J}^-)^2) .
 \end{aligned} \tag{3.29}$$



### 3.3. INTRODUCTION TO SPECTROSCOPY

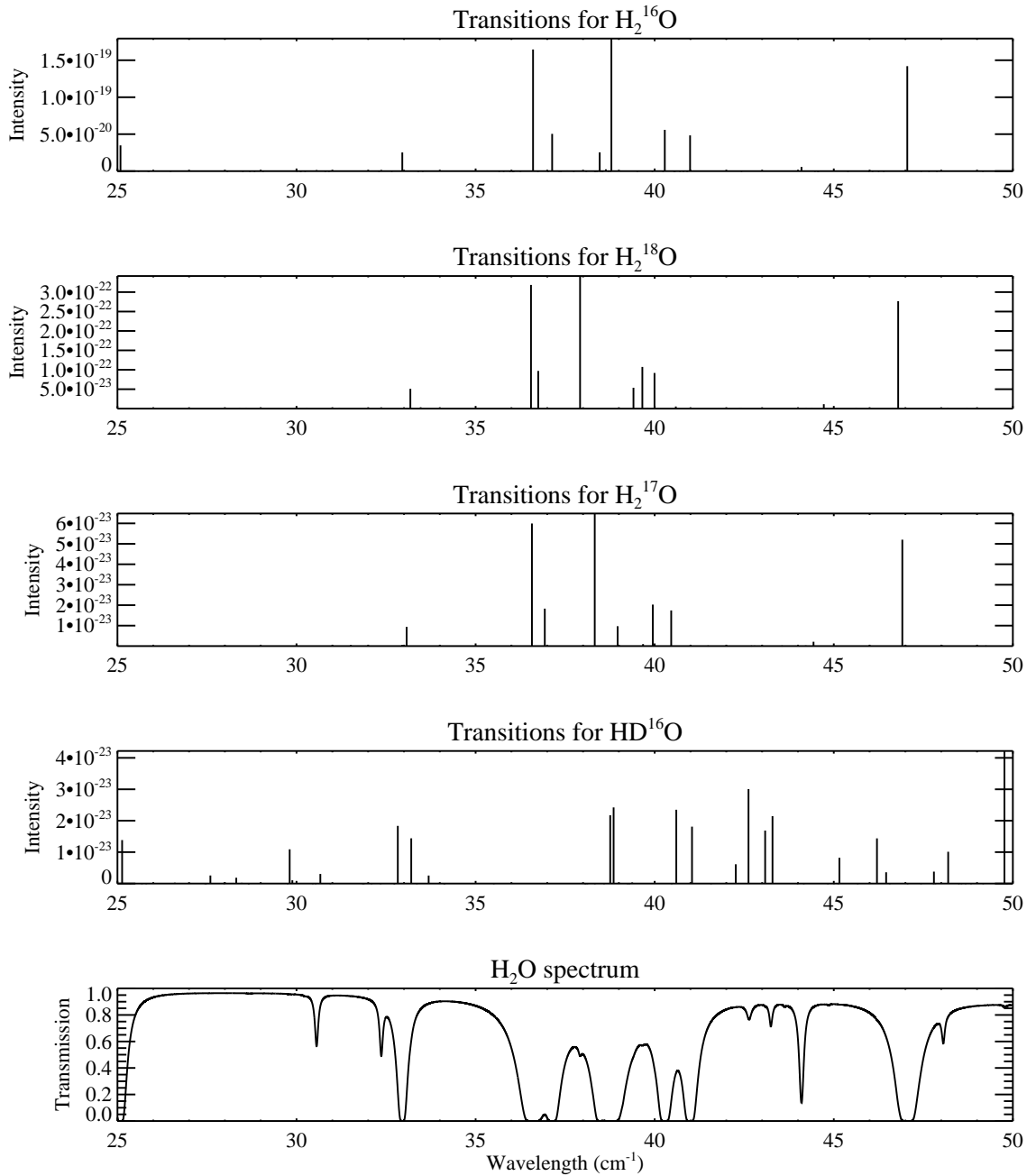


**Figure 3.6:** Simulated rotational spectrum for 10 kPa of  $\text{H}_2\text{O}$  and its isotopes at 273.15 K, in a 0.1 m gas cell, for  $\sigma = 25\text{--}50 \text{ cm}^{-1}$ , at  $0.001 \text{ cm}^{-1}$  resolution. The top panels show the transition line centres and intensities for  $\text{H}_2\text{O}$  and its isotopes, in units of  $\text{cm}^{-1}/(\text{molecule cm}^{-3})$  at 296 K. The intensities include the natural isotopic abundances.

Equation 3.29 illustrates the complexities that arise from the asymmetries in the water molecule (or any other asymmetric top). The chaotic arrangement of lines that result from the relationship is apparent from the energy level diagram of ortho- and para-H<sub>2</sub>O shown in Figure 3.7. Ortho- and para- refer to the two types of spin isomers of the hydrogen present in a water molecule: paramagnetic ortho-H<sub>2</sub>O if the nuclear spins of the two protons are parallel, and non-magnetic para-H<sub>2</sub>O if the nuclear spins are anti-parallel [27]. Carbon monoxide does not exhibit these ortho/para properties due to its relatively large mass, as compared to the light water molecule.

While in principle you can calculate from first principles the transition spectrum for a linear molecule, for a complex asymmetric top, these calculations become far more challenging, as shown by the Hamiltonian for water in Equation 3.29. It is due to this complexity that BTRAM [13] and other models do not attempt to determine the frequencies or line strengths for water vapour rotational transitions from first principles. Instead, they rely upon the necessary frequency and line strength information catalogued in molecular databases such as HITRAN [15], Gestion et Etude des Informations Spectroscopiques Atmosphériques: Management and Study of Atmospheric Spectroscopic Information (GEISA) [28] or JPL. Table 3.3 outlines the rotational and ro-vibrational water vapour transitions and associated bands that are the source of the water vapour features measured by the various instruments used in this thesis [29].

### 3.3. INTRODUCTION TO SPECTROSCOPY

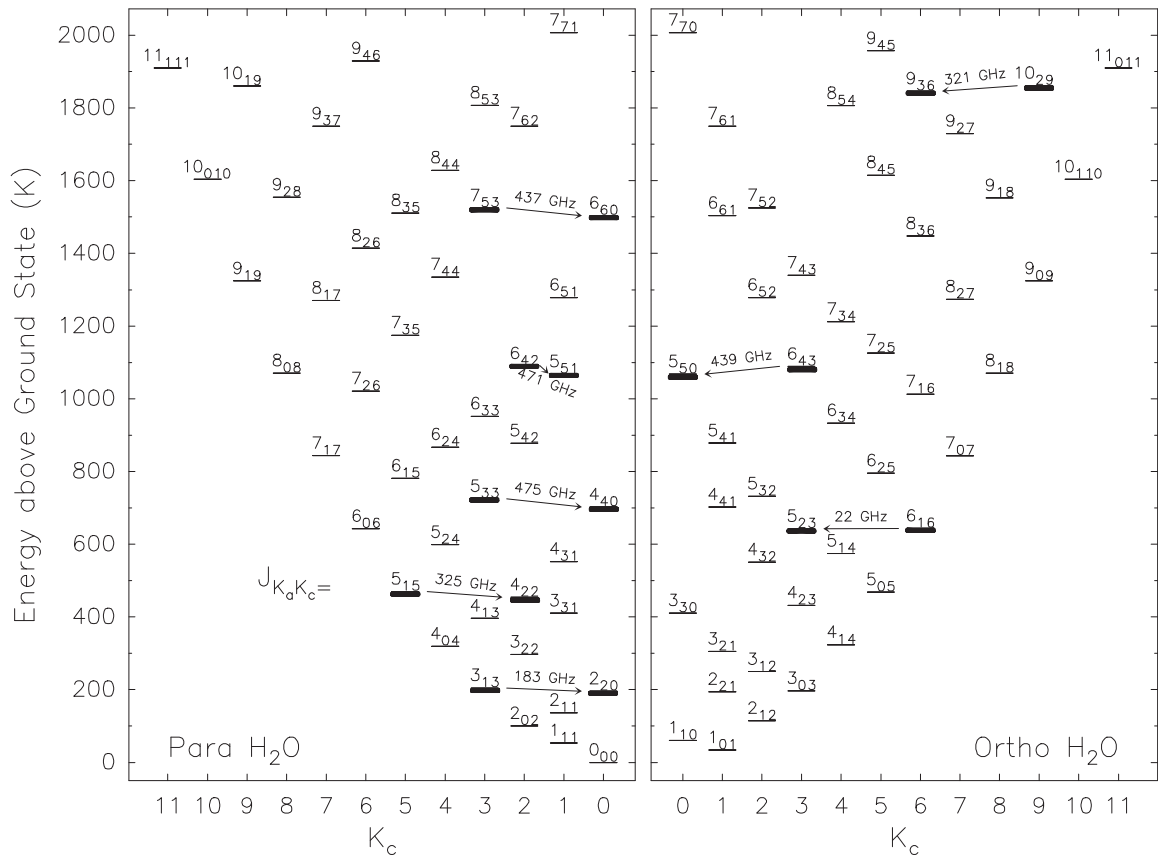


**Figure 3.7:** Energy level diagram for para H<sub>2</sub>O (left) and ortho H<sub>2</sub>O (right). Upper and lower levels of known maser lines appear in bold, are connected by arrows and have the rounded transition frequency (in GHz) indicated [30].

In summary, the frequencies of rotational transitions for a simple molecule can be calculated using the kind of analysis described above, but, in practice, researchers choose instead to use molecular databases put together by teams of molecular spectroscopists. While these databases give the centre frequency of the transition, the emission occurs over a range of frequencies determined by environmental conditions, notably the temperature and pressure of the gas being studied. This broadening and the resulting spectral line profile are described in the following section.

#### **3.4 Line shapes**

When measuring an emission or absorption line with a spectrometer, many factors determine the shape of the observed line. These include natural characteristics, features of the physical environment (temperature and pressure), and instrumental effects. Ideally, a molecule would emit all of its energy at a single frequency. However, in reality, there are a number of factors that result in this emission being spread over a range of frequencies. Experimentally, absorption or emission features with infinitesimal line-widths are not observed. What are observed are continuous line profiles with well-defined line shapes.

Lineshape functions can be of two general types: homogeneous and inhomogeneous. A homogeneous lineshape occurs when all molecules in the system are interacted with equally and thus have identical lineshapes, resulting in a Lorentzian profile. Inhomogeneous lineshapes are created by a set of molecules with lineshapes arising from non-identical interactions, resulting in a Gaussian profile [23].

Apart from instrumental effects, the three physical processes that determine the

### 3.4. LINE SHAPES

---

**Table 3.3:** Water vapour vibrational transitions for the spectral regions measured in this thesis. The centre of each spectral region is given in both wavelength and wavenumber. The upper and lower vibrational quantum numbers are given, and each transition is expressed as a combination of the fundamental vibrational modes,  $\nu_1$ ,  $\nu_2$  and  $\nu_3$ .

Wavelength range ( $\mu\text{m}$ )	Wavenumber range ( $\text{cm}^{-1}$ )	Upper	Lower	
<b>Pure rotational transitions</b>				
$\sim 20.00$	$\sim 500$	0 0 0	0 0 0	
$\sim 19.45$	$\sim 514$	0 0 0	0 0 0	
<b>Ro-vibrational transitions</b>				
$\sim 6.75$	$\sim 1481$	0 1 0 0 2 0	0 0 0 0 1 0	$\nu_2$ $2\nu_2 - \nu_2$
$\sim 5.03$	$\sim 2000$	0 0 1 0 1 0 0 2 0	0 1 0 0 0 0 0 1 0	$\nu_3 - \nu_2$ $\nu_2$ $2\nu_2 - \nu_2$
$\sim 0.94$	$\sim 10638$	0 2 2 0 4 1 1 0 2 1 2 1 2 0 1 3 0 0	0 0 0 0 0 0 0 0 0 0 0 0 0 0 0 0 0 0	$2\nu_2 + 2\nu_3$ $4\nu_2 + \nu_3$ $\nu_1 + 2\nu_3$ $\nu_1 + 2\nu_2 + \nu_3$ $2\nu_1 + \nu_3$ $3\nu_1$
$\sim 0.90$	$\sim 11111$	0 0 3 1 0 2 2 0 1 3 0 0	0 0 0 0 0 0 0 0 0 0 0 0	$\nu_3$ $\nu_1 + 2\nu_3$ $2\nu_1 + \nu_3$ $3\nu_1$
$\sim 0.72$	$\sim 13889$	0 2 3 1 2 2 2 0 2 2 2 1 3 0 1 3 2 0 4 0 0	0 0	$2\nu_2 + 3\nu_3$ $\nu_1 + 2\nu_2 + 2\nu_3$ $2\nu_1 + 2\nu_3$ $2\nu_1 + 2\nu_2 + \nu_3$ $3\nu_1 + \nu_3$ $3\nu_1 + 2\nu_2$ $4\nu_1$
$\sim 0.65$	$\sim 15385$	0 3 3 2 3 1 3 1 1 3 3 0 4 1 0	0 0 0 0 0 0 0 0 0 0 0 0 0 0 0	$3\nu_2 + 3\nu_3$ $2\nu_1 + 3\nu_2 + \nu_3$ $3\nu_1 + \nu_2 + \nu_3$ $3\nu_1 + 3\nu_2$ $4\nu_1 + \nu_2$

### 3.4. LINE SHAPES

---

shape of a line resulting from radiative transitions are natural broadening, broadening due to temperature, and broadening due to pressure. The most fundamental of these mechanisms is natural broadening. This is a quantum mechanical property due to the Heisenberg uncertainty principle, expressed as [23]:

$$\Delta E \Delta t \geq \frac{\hbar}{2} \Rightarrow \Delta t \geq \frac{\hbar}{2\Delta E} \Rightarrow \Delta t \geq \frac{1}{4\pi \Delta\nu}, \quad (3.30)$$

This fundamental principle states that the product of the energy-time uncertainty cannot be below a fundamental constant. The implication here is that an uncertainty in the time-occupation of an energy level, the lifetime, is directly translated into an uncertainty in that energy level. This  $\Delta E$  is equivalent to  $\Delta\nu$  through Equation 3.3. Thus, a finite duration necessitates a spectral spread. The mean value of this duration is the inverse of the Einstein  $A_{ul}$  coefficient introduced in §3.3.3. All spectral lines have this intrinsic shape called natural broadening. However, typical halfwidths of natural broadening for rotational transitions are on the order of  $10^{-14} \text{ cm}^{-1}$ , which is challenging to measure in practice and can be neglected [24].

The sources of broadening that must be considered in atmospheric modeling are due to environmental conditions, namely temperature and pressure. Doppler broadening is due to the statistical distribution of velocities of the atoms (or molecules) in the gas emitting radiation. Depending on whether the motion of each atom is towards or away from the observer, the associated photon it emits will either be red- or blue-shifted by the Doppler effect, expressed as [24]:

$$\sigma = \sigma_0 \left(1 - \frac{v}{c}\right)^{-1} \quad [\text{cm}^{-1}], \quad (3.31)$$

where  $\sigma$  is the measured frequency,  $\sigma_0$  is the actual frequency,  $v$  is the velocity of the atom,

### 3.4. LINE SHAPES

---

and  $c$  is the speed of light. Since the atomic velocities will exhibit a Maxwell-Boltzmann distribution, there will be a spread to  $\sigma$ , i.e., a spectral broadening. The higher the gas temperature, the wider the distribution of atomic velocities, thus the broader the emitted spectral line. Since each atom will have a unique velocity and thus emit unique frequency photons, the overall effect of Doppler broadening is said to be inhomogeneous, resulting in the Gaussian line shape given by [24]:

$$f_D(\sigma - \sigma_0) = \frac{1}{\alpha_D} \sqrt{\frac{\ln 2}{\pi}} \exp \left[ -\ln 2 \left( \frac{\sigma - \sigma_0}{\alpha_D} \right)^2 \right] \quad [\text{cm}^{-1}] \quad , \quad (3.32)$$

$$\alpha_D \equiv \sigma_0 \sqrt{\frac{2 \ln 2 \, k_B T}{m c^2}} \quad [\text{cm}^{-1}] \quad , \quad (3.33)$$

where  $\sigma$  is frequency,  $\sigma_0$  is frequency of the line centre, and  $\alpha_D$  is the Doppler half-width at half-maximum (HWHM).

The other environmental factor that affects the line shape is pressure. Molecules in an atmosphere are not isolated and, therefore, will collide with other molecules (or the boundary of the container if being studied in a gas cell). Collisions broaden the spectroscopic linewidths by shortening the lifetime of the excited states. Again, this uncertainty in the time-occupancy of the energy levels (duration) translates to a spectral spread as it does for the natural broadening mechanism. This effect is homogeneous since, at equilibrium, all molecules are assumed to experience collisions caused by equal pressures and thus have an identical pressure-broadened lineshape for a particular transition [23]. It is characterised by the Lorentz profile given by:

$$f_L(\sigma - \sigma_0) = \frac{1}{\pi} \frac{\alpha_L}{(\sigma - \sigma_0)^2 + \alpha_L^2} \quad [\text{cm}^{-1}] \quad , \quad (3.34)$$

$$\alpha_L \equiv \frac{1}{2\pi\tau} \quad [\text{cm}^{-1}] \quad , \quad (3.35)$$

where  $\alpha_L$  is the Lorentz HWHM and  $\tau$  is the average lifetime of the excited state. The Lorentz width is only proportional to  $\tau^{-1}$ ; no other physical factors are involved.

The fundamental difference between the Doppler and Lorentz profiles is in the shape of the wing structure, shown in Figure 3.8. The Doppler profile has a relatively large amplitude with narrow wings, while the converse is true for the Lorentz profile.

The Doppler and Lorentz line profiles both represent particular properties of the atmosphere. Each of them is dominant under different conditions. Lorentz dominates at lower altitudes (see Figure 3.9), where pressure is higher and Doppler dominates at higher altitudes, where pressure is much lower.

To accommodate both the effects of temperature and pressure, the Voigt profile is frequently used [23]. The Voigt profile is a convolution of the Doppler and Lorentz profiles expressed as:

$$f_V(\sigma - \sigma_0) = \frac{1}{\alpha_D} \sqrt{\frac{\ln 2}{\pi}} \frac{y}{\pi} \int_{-\infty}^{\infty} \frac{\exp(-t^2)}{y^2 + (x - t)^2} dt \quad [\text{cm}^{-1}] \quad , \quad (3.36)$$

where the ratio of the Lorentz to Doppler widths is  $y = \frac{\alpha_L}{\alpha_D} \sqrt{\ln 2}$  and  $x = \frac{\sigma - \sigma_0}{\alpha_D} \sqrt{\ln 2}$  is related to the wavenumber scale in units of Doppler width. At the high pressure limit ( $y \rightarrow \infty$ ) or low pressure limit ( $y \rightarrow 0$ ), the Voigt profile asymptotically follows the Lorentz or Doppler profiles, respectively, as can be seen from its behaviour in Figure 3.9. The figure shows how the Voigt approximates the Lorentzian and Doppler profiles in the regions where each dominates.

Finally, the impact of the spectrometer itself needs to be considered when designing



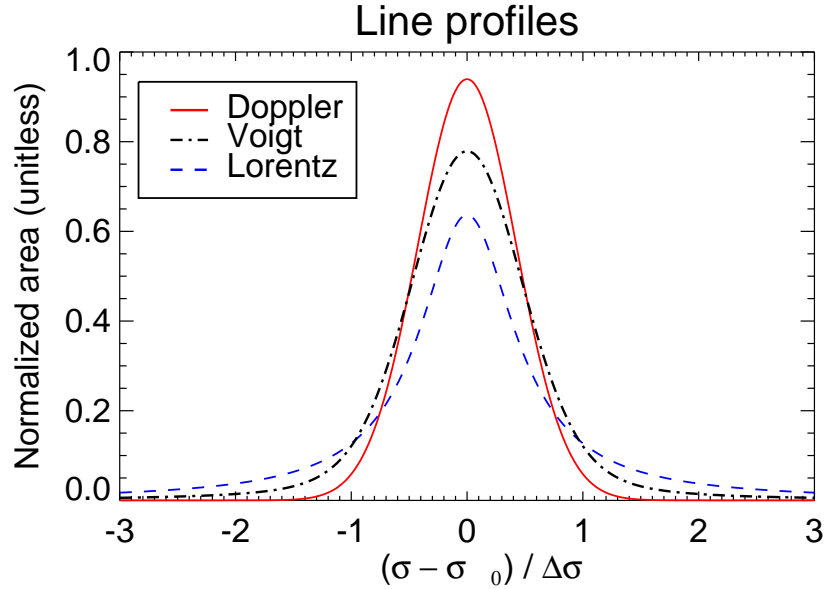


**Figure 3.8:** Doppler, Lorentz and Voigt profiles with normalised area and equal half-widths. The example Voigt profile represents an intermediate set of environmental conditions between the two extremes of temperature dependence and pressure dependence, represented by the Doppler and Lorentz profile respectively.

an experiment to measure the atmospheric emission spectrum. For example, measurement with a diffraction grating will add a Gaussian-like instrumental line profile to the measurement (see Appendix B), a Fabry-Perót interferometer (FPI) adds an Airy instrumental line profile [32], and a Fourier Transform Spectrometer (FTS) adds a sinc profile to the measurement [33].

In summary, both the environmental conditions and the instrumental effects must be taken into account when modeling or retrieving spectral information from observed spectra. Line modeling requires knowledge of how and when each specific process dominates. Conversely, through high-resolution measurements of an isolated spectral line profile, it is possible to deduce some of the physical conditions ( $P$ ,  $T$ ,  $\rho$ ) of the emitting region in question.

### 3.4. LINE SHAPES

---

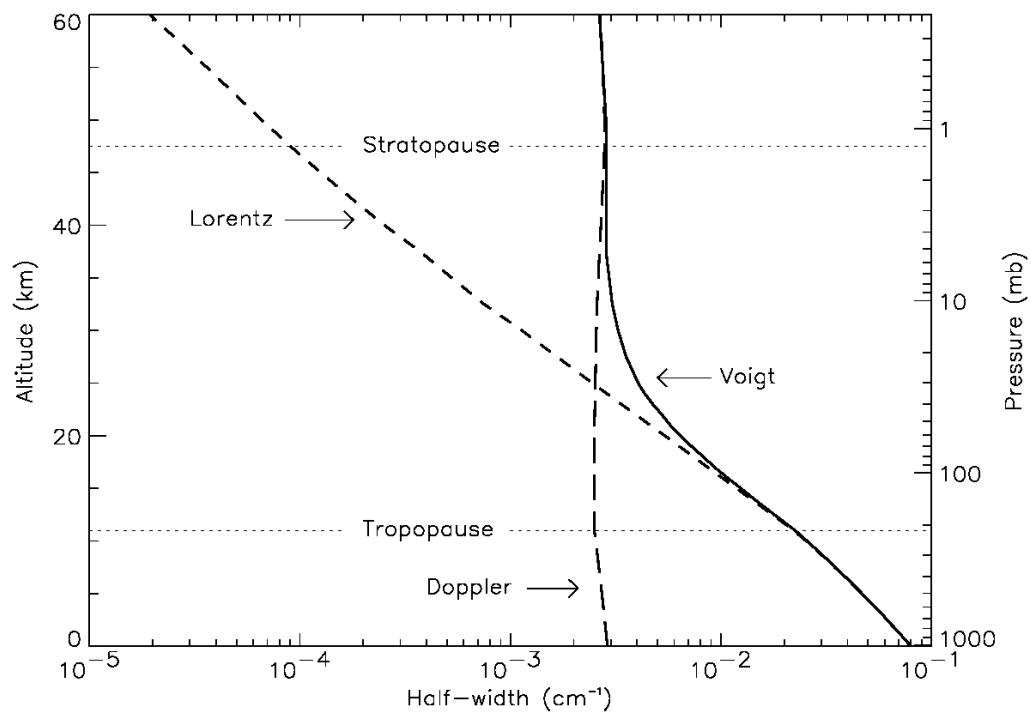


**Figure 3.9:** Approximate altitude dependence from 0–60 km of the Doppler, Lorentz and Voigt half-widths for the 1976 U.S. Standard Atmosphere [6]. Figure from Larar *et al.*, 2002 [31].

---

## Chapter 4

# Atmospheric Modeling

### 4.1 Overview

Atmospheres are complex ensembles of molecules at varying pressures and temperatures. However, it is possible to simplify the description of the physical properties of the system through the use of some reasonable assumptions. In virtually all atmospheric models, the atmosphere is assumed to be in local hydrostatic equilibrium and local thermal equilibrium, which implies no net vertical motion, essentially a static atmosphere with the molecules well-mixed.

### 4.2 Atmospheric modeling

As our understanding of the dynamic processes that shape our environment grows, the better is our position to predict, enact positive change, and prepare for the inevitabilities of the weather within our environment. Atmospheric modeling is an integral aspect of this process.

Detailed atmospheric modeling became possible with the advent of computers, particularly with the US military and their simulation software FASCODE [14]. The purpose of FASCODE was to identify the characteristic spectral signatures of possible exhaust trails of aircraft, rockets, or missiles, with the intention of identification as friend or foe. Thus, there was a need to understand the backdrop against which they were trying to identify these specific features, which led to the birth of modern atmospheric modeling.

In order to accurately model an atmosphere, many details must be known about its structure and composition. The necessary inputs to a generic atmospheric model are shown in Figure 4.1. Ideally, the best atmospheric profile is that obtained from a locally launched radiosonde at the time of your observations. But, these are only launched from specific locations and usually at non-ideal times. The next best thing is to create a representative profile through a statistical analysis of radiosonde data as described in §4.3. Once the molecular abundances of the species contributing to emission are known for a particular parcel of atmosphere, their spectral transitions can be calculated as described in Chapter 3. This calculation requires parameters from a molecular database such as the transition frequency, line strengths, air-broadened half-widths, and self-broadened half-widths. These parameters are contained in several large databases, including HITRAN [15], GEISA [28] and JPL. An example of the format from the JPL catalogue is given in Table 3.2. To put the scale of these databases into context, HITRAN 2008 Version 13.0 [15] contains 2,713,968 spectral lines for 39 molecules including all of their principal isotopes. All physical quantities and data for these spectral lines are documented for a temperature of 296 K and must be adjusted for typical atmospheric temperatures.

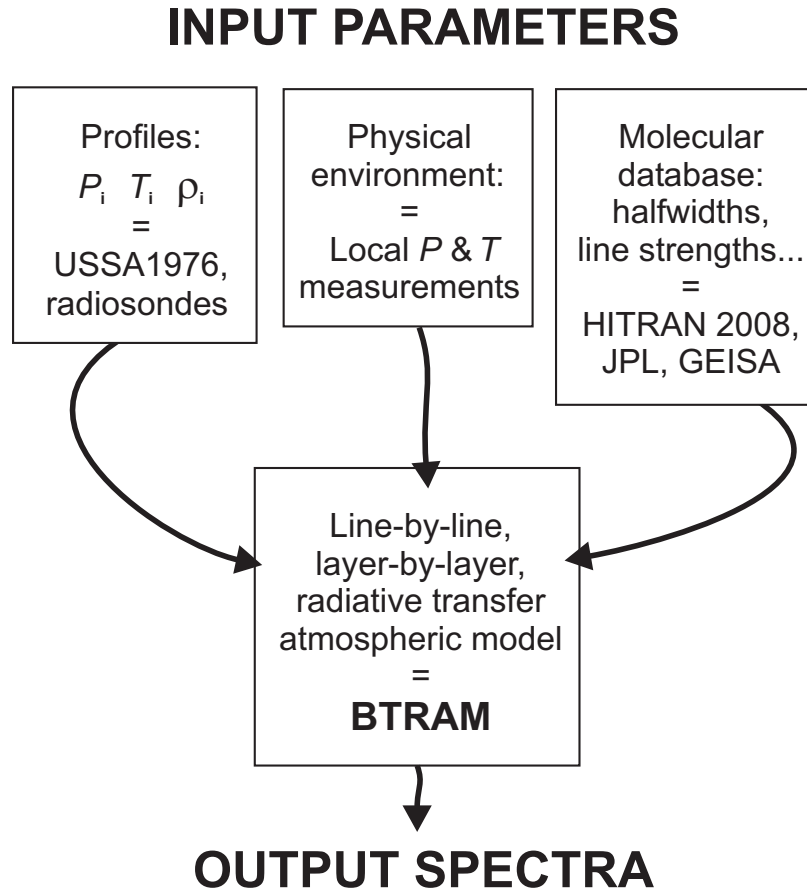


**Figure 4.1:** Input parameters and resources necessary for atmospheric modeling.

Armed with these three sets of information, the local physical environment, atmospheric profiles, and the molecular database, it is possible to construct a realistic representation of the atmosphere above any given location on the Earth.

The relations governing local hydrostatic and thermal equilibrium were discussed in Chapter 2: the barometric law (Equation 2.2) and that of scale height (Equation 2.3). Hydrostatic equilibrium occurs when compression due to gravity is balanced by a pressure gradient force in the opposite direction. When hydrostatic and thermal equilibrium are assumed, atmospheric processes become easier to model.

### 4.3 Atmospheric profiles

As described in §1.3.1, the atmospheric model used in this thesis is based upon the BTRAM code which was developed and is maintained by the Astronomical Instrumentation Group at the University of Lethbridge.

One of the most commonly used set of atmospheric profiles and parameters is the U.S. Standard Atmosphere 1976 (USSA1976). The USSA1976 temperature profile for Earth is shown in Figure 4.2, and the pressure and constituent profiles are shown in Figures 4.3 and 4.4, respectively. Included in the profile are the mass mixing ratio of  $\text{N}_2\text{O}$ ,  $\text{O}_2$ ,  $\text{CO}_2$ ,  $\text{CH}_4$ ,  $\text{H}_2\text{O}$ ,  $\text{CO}$ , and  $\text{O}_3$ . While  $\text{N}_2$  is the most abundant gas in the atmosphere it is not included in this list since it is a homopolar molecule, and therefore does not possess a permanent electric dipole moment, nor any significant rotational transitions and hence has no relevant effect on opacity. Although, the same can be said of  $\text{O}_2$ , unlike  $\text{N}_2$  it possesses a weak magnetic dipole moment, which, because of the abundance of oxygen, results in transitions that are visible in the sub-millimetre spectral region [34].

While these profiles do show the general features of the atmosphere, they do not represent the conditions experienced on high altitude mountain sites and, thus, the need for site-specific profiles. One mean atmospheric profile cannot be expected to cover the range of conditions (regional, seasonal) experienced on the Earth, and for this reason FASCODE was distributed with a set of seasonally specific profiles for a variety of latitudes. The list of profiles is given in §1.3.1.

While this has improved matters, these generic profiles do not represent specific

### 4.3. ATMOSPHERIC PROFILES

---

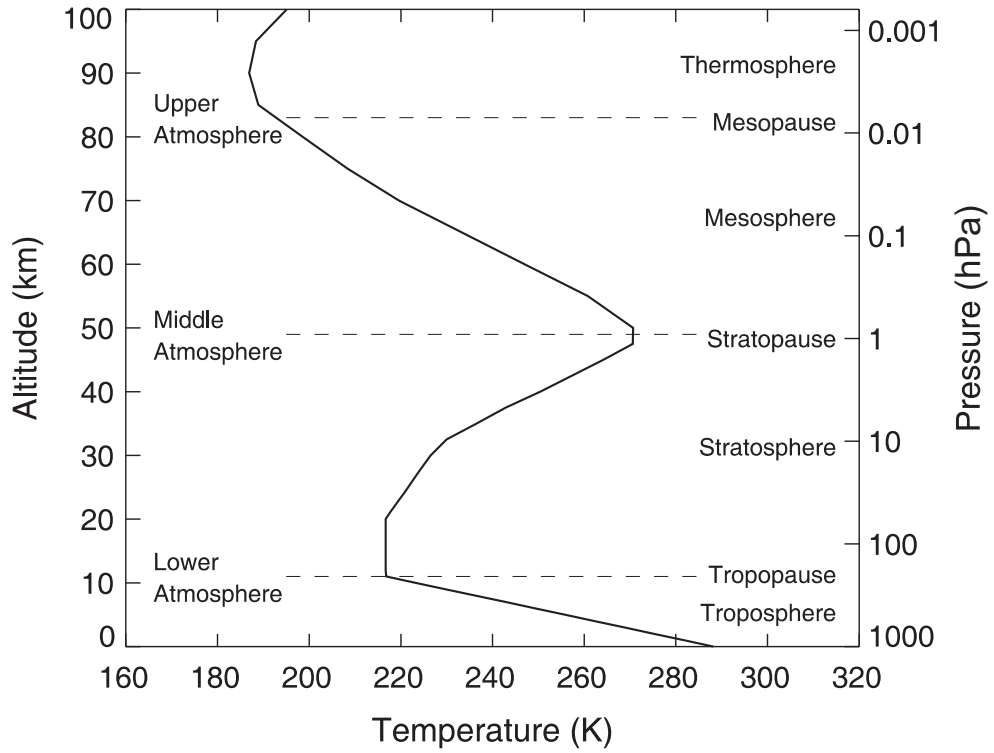


Figure 4.2: Temperature profile from the U.S. Standard Atmosphere 1976 [6]

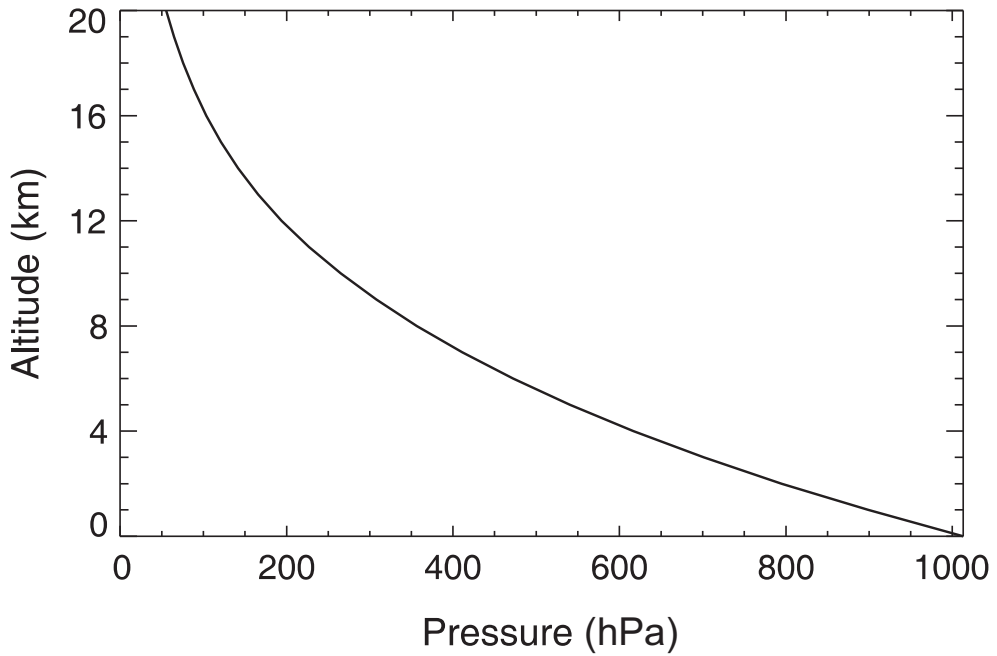
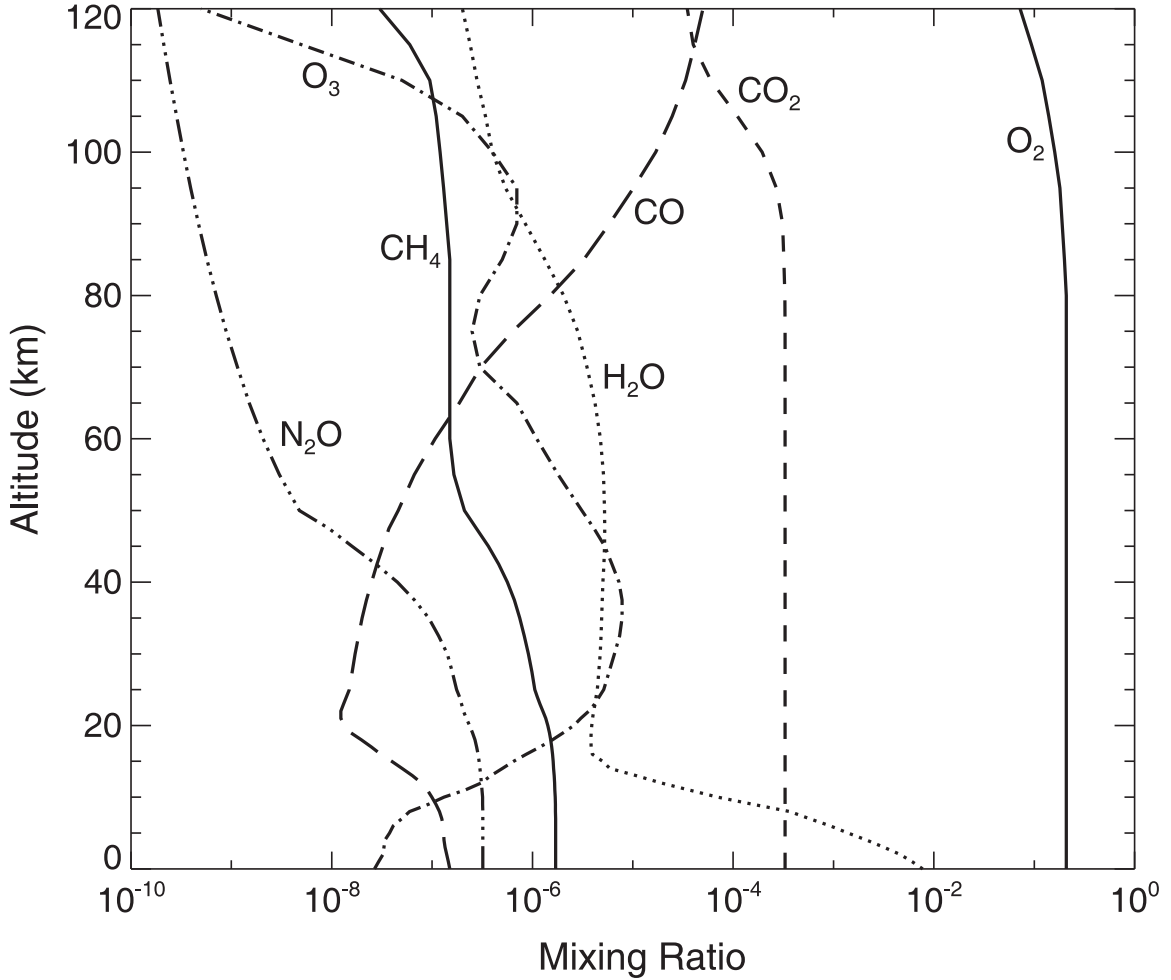


Figure 4.3: Pressure profile from the U.S. Standard Atmosphere 1976 [6]



**Figure 4.4:** Representative vertical mixing ratios from the U.S. Standard Atmosphere 1976 [6]

locations to a sufficiently high level of accuracy as is demanded in astronomical observations. If astronomers want to understand the faint emissions from distant galaxies they have to understand the spectral signature of the Earth's atmosphere at least at the level sufficient to understand the astronomical observation. For example, it would only be possible to discern a signal-to-noise of 1% from a distant object if the uncertainty in the atmosphere itself was understood to better than 1%.

Thus in our PWV measurement campaign, we decided to launch radiosondes from



the mountaintops to provide us with the best representation of the atmosphere at the time of the tests.

#### 4.4 Radiative transfer

As mentioned in §3.1, the simplest example of radiative transfer involves one layer composed of a single species, at constant  $P$  and  $T$ , irradiated by energy of a single frequency. From this simple foundation, the more complex form of a multi-layer, multi-wavelength, multi-species atmospheric model can be created, as is the case with BTRAM [13].

Figure 4.5 represents the general case of a single layer of well-mixed atmospheric medium with incident frequency-dependent radiation,  $I_\sigma(0)$ , from a source on the left. As it passes through the atmospheric medium it will be modified by  $dI_\sigma$  over the interval  $ds$ . This modification can take the form of frequency specific absorption by the atmosphere, thereby reducing the incident radiation at those select frequencies. Or the modification can come from frequency specific emission from the atmosphere, thereby adding to the incident radiation at select frequencies. After this modification, the radiation leaves the atmosphere at  $s_1$  and the observer on the right measures the outcoming radiation as  $I_\sigma(s_1)$ . Thus, the resulting radiation exiting the atmosphere will be a combination of the absorption modified incident radiation and the emission of the atmosphere itself. The process outlined in Figure 4.5 is described by the Schwarzschild equation (Equation 3.2) which can be expanded as the following [35]:

$$L_\sigma(s_1) = L_\sigma(0) e^{-\tau_\sigma(s_1,0)} + \int_0^{s_1} B_\sigma(T_s) e^{-\tau_\sigma(s_1,s)} k_\sigma \rho ds \quad . \quad (4.1)$$

This formulation assumes no scattering and pure blackbody emission. The first part of the

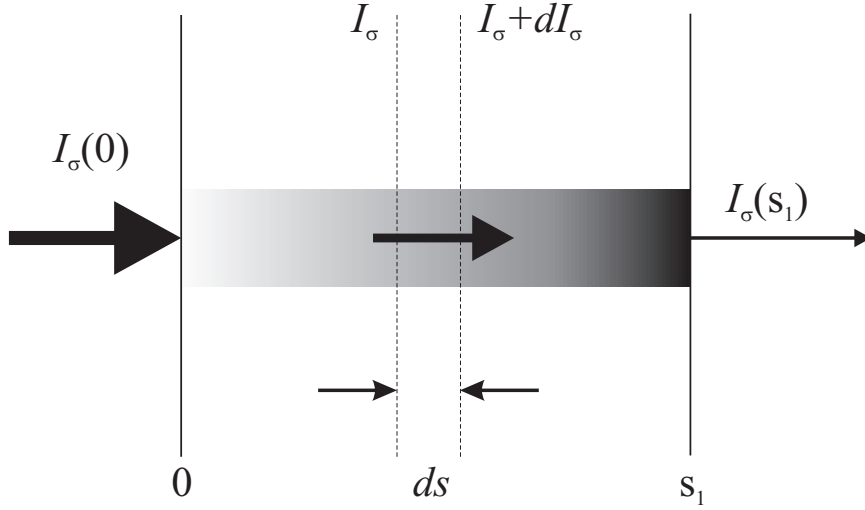


**Figure 4.5:** Depletion of the radiant intensity in traversing an absorbing medium

equation represents the absorption due to the atmosphere over the interval  $s = [0, s_1]$ . This absorption is expressed here as a fractional transmission,  $e^{-\tau}$ , where  $\tau$  is opacity, defined as:

$$\tau_{\sigma}(s_1, 0) = \int_0^{s_1} \sum_i k_{\sigma_i} \rho_i ds \quad , \quad (4.2)$$

where the integration range represents the extent of the medium, and the summation over  $i$  accounts for the  $i$  different atmospheric molecular species being included. The frequency dependent absorption coefficient is  $k_{\sigma}$ . The density of the absorber is given by  $\rho$ . Thus, the opacity of any given medium is expressed as the integral over the depth, or distance through a medium, of the product of the absorber abundance and the absorption coefficient.

The (mass) absorption coefficient of a spectral line can be expressed as:

$$k_{\sigma} = S f(\sigma - \sigma_0) \quad [\text{m}^2 \text{ kg}^{-1}] \quad , \quad (4.3)$$

where  $S$  is the integrated absorption coefficient, or line strength, defined as  $S = \int_0^{\infty} k_{\sigma} d\sigma$ ,

$\sigma_0$  is the line center, and  $f(\sigma - \sigma_0)$  is the normalised broadening profile discussed in §3.4.

In Figure 4.5, the increasing opacity of the medium is depicted as the gradually darkening band that starts as transparent, and ends at the right as black (opaque). The relative transmissions of the radiation in this simple case are shown graphically as the thickness of the arrows. Again, the amplitude of the incident radiation is high, gradually decreasing to the small amount of out-going radiation.

The second part of the Schwarzschild equation, Equation 4.1, represents the emission due to the atmosphere itself. The  $B_\sigma(T_s)$  term represents atmospheric blackbody radiation. Blackbody radiation, described by the Planck function, refers to the spectral distribution of radiation emitted from matter at a given temperature [23]:

$$B_\sigma(T) = \frac{2 h c^2 \sigma^3}{\exp\left(\frac{h c \sigma}{k_B T}\right) - 1} \quad [\text{W m}^{-2} \text{ sr}^{-1} (\text{cm}^{-1})^{-1}] \quad (4.4)$$

Figure 4.6 shows the Planck curve for several temperatures. While these curves are continuous, in the case of emission from a gas, the Planck curve merely provides the maximal envelope that saturated emission could reach at any given frequency for any given temperature. The actual frequency dependent emission will be determined by the environmentally driven line broadening conditions as discussed in §3.3.

It is instructive to view Equation 4.1 for two limiting cases: the optically thin case,  $\tau \approx 0$ , and the optically thick case,  $\tau \gg 1$ . Expansion of the integral in Equation 4.1 results in a  $(1 - e^{-\tau})$  term. For the case where the atmosphere is optically thin, the opacity terms would be negligible implying little absorption or emission. Thus, in this case where the atmosphere is optically thin one essentially sees right through it.

In the case where the atmosphere is optically thick, the opacity term is large

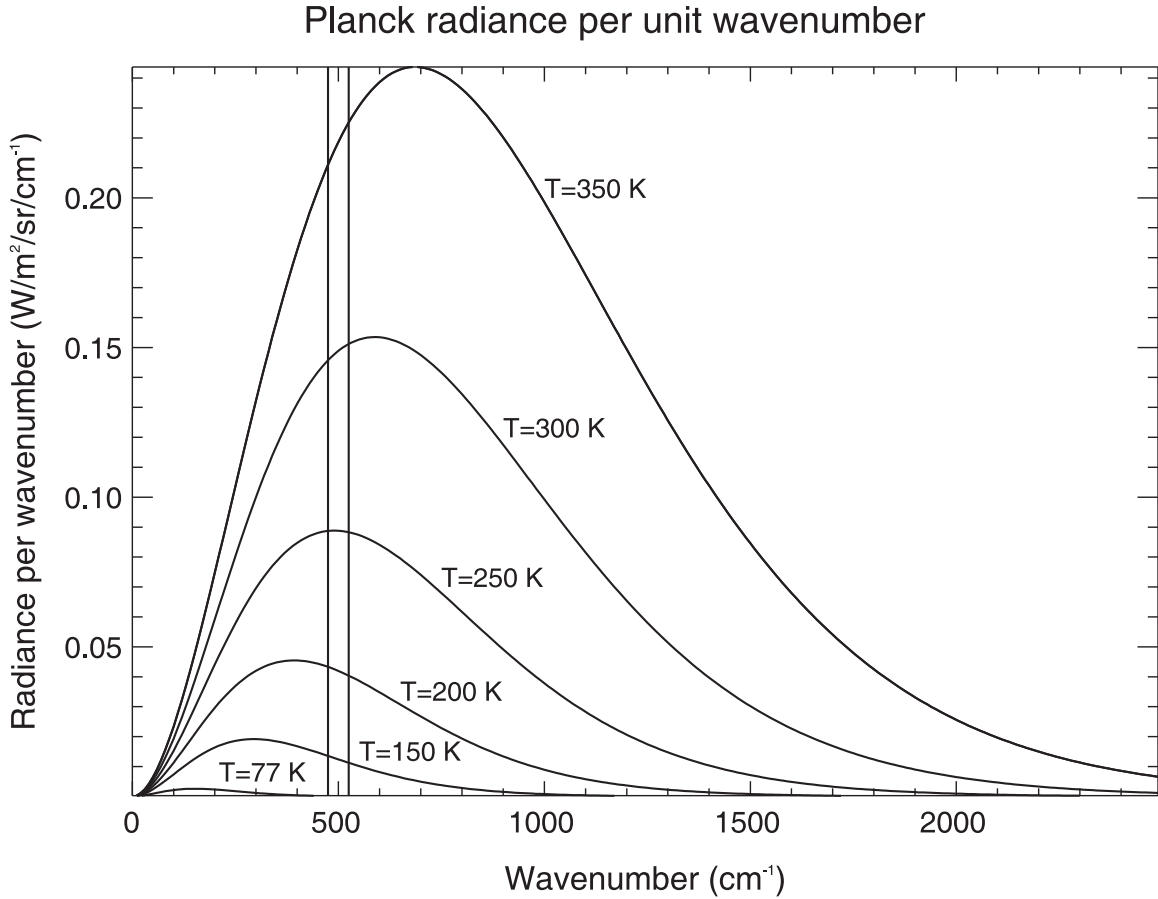


**Figure 4.6:** Planck (blackbody) emission between 0 and 2500  $\text{cm}^{-1}$  for a set of temperatures. The curve for  $T = 250 \text{ K}$ , which corresponds to an average value for effective sky temperature, peaks near  $500 \text{ cm}^{-1}$ , the spectral region IRMA is designed to operate in.

( $\tau \gg 1$ ), and the fractional transmission term,  $e^{-\tau}$ , goes to zero. The contribution from the  $I_{\sigma}(0)$  term in Equation 4.1 is reduced to zero, meaning that all incident radiation is absorbed by the atmosphere. Due to this large opacity, the only radiation visible to the observer would be that originating from within the atmosphere itself, which would take the form of the Planck curve,  $B_{\sigma}(T)$ , in this limiting, optically thick case.

Using Equation 4.1, it is now possible to model the radiative transfer within an atmosphere. The analysis up to now has dealt with a single layer. Is it possible to model

#### 4.4. RADIATIVE TRANSFER

---

an entire atmosphere by breaking it up into a series of layers where the output of one layer becomes the input to the next. Mean values for the physical properties of each layer can be applied so as to accurately represent the simplified layer. Imagine a column of atmosphere in thermal and hydrostatic equilibrium, as described in §2.3. The atmosphere is first divided into horizontal layers containing unique temperatures, pressures, and abundances of molecules. This process is further simplified through application of the Curtis-Godson approximation [36]. The approximation states that for a fixed path length through a medium the path-dependent pressure,  $P(z)$ , can be represented by the mean pressure,  $\bar{p}$  over that path length, defined by:

$$\bar{p} = \frac{\int pc\rho dz}{\int c\rho dz} \quad [\text{Pa}] \quad , \quad (4.5)$$

where  $c$  is the fractional concentration (by mass) of absorber, also known as a mass mixing ratio. This equation effectively weights the pressure according to the density of the absorber as a function of altitude.

Using Equation 4.1, one calculates the radiation leaving a layer in terms of the radiation incident upon the layer and the radiation emitted from the material in the layer itself. Through the process of summing the cumulative radiation over the full span of layers, and all frequencies, the total radiation-matter interaction of the atmosphere can be simulated. This is referred to as the spectral line-by-line, atmospheric layer-by-layer (LBL<sup>2</sup>) method.

The only fundamental difference from a single layer atmosphere to a multi-layer atmosphere is that one needs to keep track of incident radiation on each layer and how it changes as it propagates through the system. Starting from the top of the atmosphere

and working down towards the surface can be summarised as follows. The top-most layer is assumed to have no incoming radiation, i.e.  $I_0 = 0$ . For example in the case of IRMA, which operates at a wavelength of  $\sim 20 \mu\text{m}$  ( $500 \text{ cm}^{-1}$ ), in reality there is very little radiation coming from objects other than the sun or moon and thus  $I_0$  can be set to zero. The ubiquitous cosmic background radiation can also be ignored because it peaks at microwave frequencies, well outside the measurement range of the HgCdTe photoconductive detector in the IRMA instrument.

To summarise, the model atmosphere is divided into discrete elements referred to as layers. Each layer has a temperature profile, pressure profile, and molecular abundance distribution. Using the Curtis-Godson approximation, mean values can be determined for each of these parameters specific to each layer. The model is created by stepping through the atmosphere, layer by layer, and calculating the frequency dependent absorption, or opacity due to each absorbing species in the system. These frequency dependent opacities are then summed across all layers. The ability to sum opacities rather than multiplying transmittances results in faster computation. Consider the example of two layers of atmosphere, given by  $I_1$  and  $I_2$ , with input radiation  $I_0$ :

$$\begin{aligned}
 I_1 &= I_0 \exp(-\tau_1) \\
 I_2 &= I_1 \exp(-\tau_2) \\
 I_2 &= I_0 \exp(-\tau_1) \exp(-\tau_2) \\
 I_2 &= I_0 \exp(-[\tau_1 + \tau_2]) \\
 &\vdots \\
 I_N &= I_0 \exp\left(-\sum_i^N \tau_i\right)
 \end{aligned}
 \tag{4.6}$$

Equation 4.6 shows the computational value of using the opacity formulation for a LBL<sup>2</sup> approach. As the frequency-dependent opacity of each layer is computed, it is literally added to the stack of previously computed opacities, until the total contribution from all atmospheric layers over all frequencies have been tabulated. The resulting spectrum is the cumulative absorption and emission of all spectral transitions occurring within the region being mapped. This is the process used in virtually all line-by-line, layer-by-layer, radiative transfer atmospheric models.

When modeling a given spectral range, all contributions from adjacent spectral lines must be individually calculated and included. This is known as the line-by-line method. The wings of the spectral line profile contribute to all spectral lines falling within the wing profile. This wing size overlap is generally taken to be 25 wavenumbers, beyond which the contribution has been found to be minimal [2]. Considering that there may be thousands of lines within a given region this process quickly becomes computationally intensive. Fortunately, today, computers have the processing power and memory available for this task, allowing high resolution spectra of a multi-layer atmosphere, over a useful wavelength range, to be computed on a standard desktop computer in a matter of minutes. For example, using BTRAM on a 3 GHz processor, computing a transmission spectrum from 500–1000 nm, at a resolution of 0.01 nm, over 37 layers, takes  $\sim 4$  minutes. A transmission spectrum from 715–730 nm at a resolution of 0.001 nm takes  $\sim 80$  seconds. An emission spectrum from 19–21  $\mu\text{m}$  at a resolution of 0.001  $\mu\text{m}$  takes  $\sim 30$  seconds. However, when the process is extended to creating an entire atmospheric flux lookup table for IRMA in the form of a data cube, the iterative process can take several hours depending on the parameter

space of the table.

It is important to note that line-by-line, layer-by-layer computationally intensive methods are not the only ways to simulate the radiative transfer through an atmosphere. Before computers were sufficiently advanced, there were clever analytical methods used to tackle these problems. One such method is called the correlated- $k$  distribution [37]. It gives information about the values of the  $k_\nu$  absorption coefficients over the band. It is a statistical approach that can be useful if all that is desired is information about the entire band. It can not give detail about specific absorption features, since they are lost in the statistical results. However, recall that instruments in the near-past did not have anywhere near the resolution available in instruments today. Simply predicting or being able to analyse the qualities of an entire band was more than sufficient at the time. The notion of producing a detailed model at that time was more of an academic exercise than something useful to try to compare with experimental data.

### 4.5 Summary

This chapter has reviewed some key elements of radiative transfer theory which are embodied in the atmospheric modeling program BTRAM [13]. Our group developed BTRAM to model the atmosphere for specific locations including Mauna Kea, and several sites in Chile, Mexico, and Antarctica. BTRAM is a line-by-line/layer-by-layer atmospheric radiative transfer model based on the HITRAN 2008 molecular database [15]. When studying an atmosphere at relatively high resolution, the differences between using a generic representative model, and a site-specific model based on local radiosonde data, are readily



## 4.5. SUMMARY

---

apparent. Thus, site-specific, simulated atmospheric flux or transmission are necessary if one is testing a model to identify, and minimise, any systematic effects introduced by the model.

The process of creating flux-to-PWV models requires the creation of data cubes. These data cubes are created through a batch processing mode that has been implemented in BTRAM. Figure 4.7 shows the simulated atmospheric flux above Mauna Kea for a PWV range of 0.5–4 mm across the frequency range of an IRMA detector/filter assembly. The water emission lines begin to reach the Planck envelope at relatively low PWV. IRMA is thus most sensitive to low PWV because the variation in flux with respect to PWV decreases as the water vapour lines saturate.

As discussed elsewhere, the impetus for developing BTRAM was to simulate site-specific atmospheres. It does so by using customised atmospheric profiles. Through the statistical analysis of radiosondes, as described in Chapter 5, I have produced a series of site specific profiles for use with BTRAM.

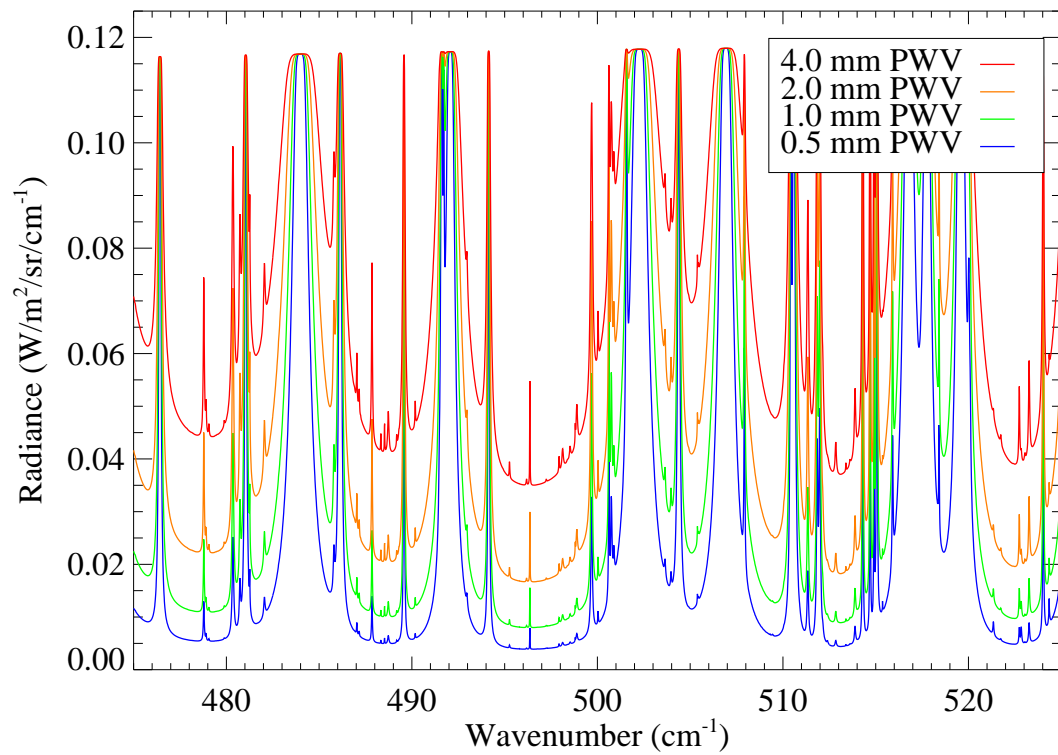


**Figure 4.7:** Simulated atmospheric flux spectrum above Mauna Kea for PWV = 0.5, 1.0, 2.0 and 4.0 mm over the operational frequency range of an IRMA unit. The water emission lines begin to saturate to the Planck envelope at relatively low PWV. IRMA is most sensitive below this saturation limit.

---

## Chapter 5

# Methods of Measuring Water

## Vapour: Radiosondes

### 5.1 Introduction

A radiosonde is considered the gold standard for the direct measurement of water vapour as its sensors are lifted up through the atmosphere by a helium-filled balloon. A radiosonde consists of a balloon-borne suite of meteorological instruments that perform *in situ* atmospheric measurements of pressure, temperature, wind speed, and dew point or relative humidity at altitudes up to 20–30 km [38]. A helium-filled balloon carries an instrumentation payload skyward while data are telemetered to a ground-station.

The radiosondes used in this study, built by the Finnish company, Vaisala Inc<sup>1</sup>, an example of such an instrument package is shown in Figure 5.1. The water vapour measurement is made using a proprietary sensor that measures relative humidity. This device

---

<sup>1</sup>Vaisala Radiosonde RS92. Vaisala Inc. <http://www.vaisala.com/weather/products/rs92.html>

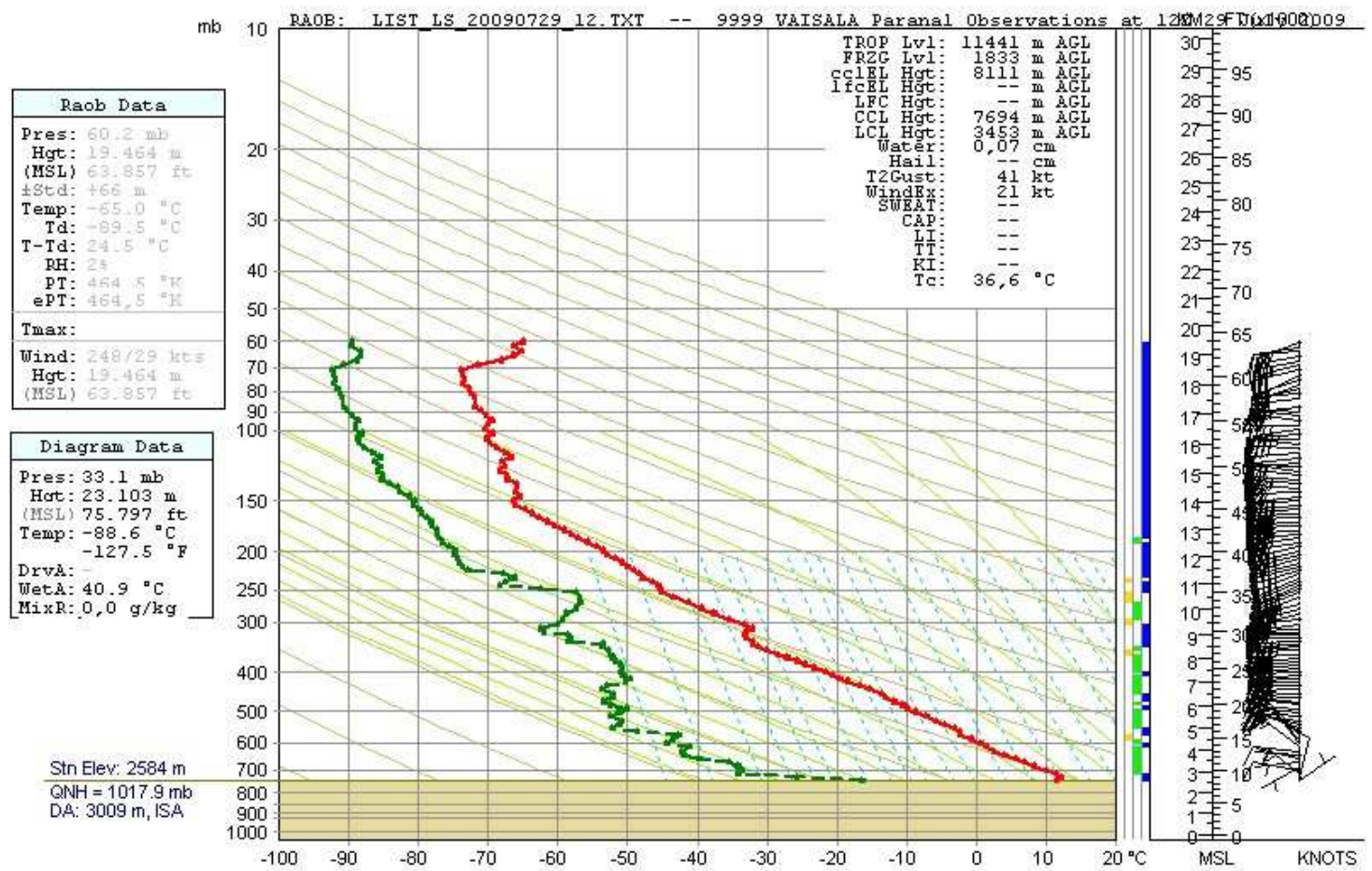


**Figure 5.1:** A Vaisala RS92-SGP radiosonde instrumentation package. The unit is approximately  $220 \times 80 \times 75$  mm, weighing typically 250 g. Image courtesy of Vaisala Inc.

is a thin-film capacitor, heated twin sensor. Its two independent sensors alternate between a measuring and a heating mode; this serves to minimise any ice or liquid accumulation on the sensors while it passes through clouds or particularly wet conditions.

An example of the data produced by a radiosonde is shown as a SkewT-LogP plot in Figure 5.2. An optional Global Positioning System (GPS) receiver allows for the recording of spatial location as well. Figure 5.3 shows the recorded flight path of the radiosonde whose data were shown in Figure 5.2. From these data, pressure versus altitude, or temperature versus altitude plots can be constructed, allowing adiabatic lapse rate and scale height of water to be determined, described further in §5.3 and §5.4.

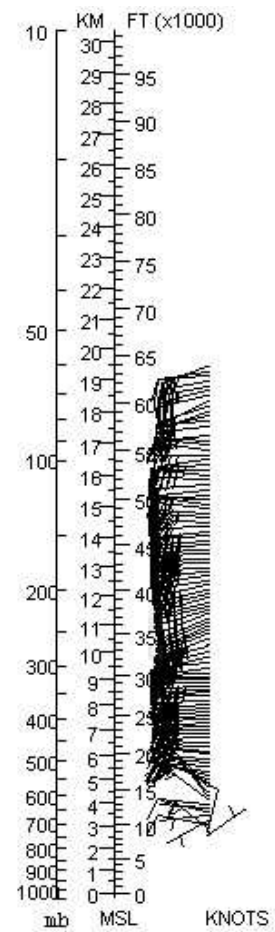
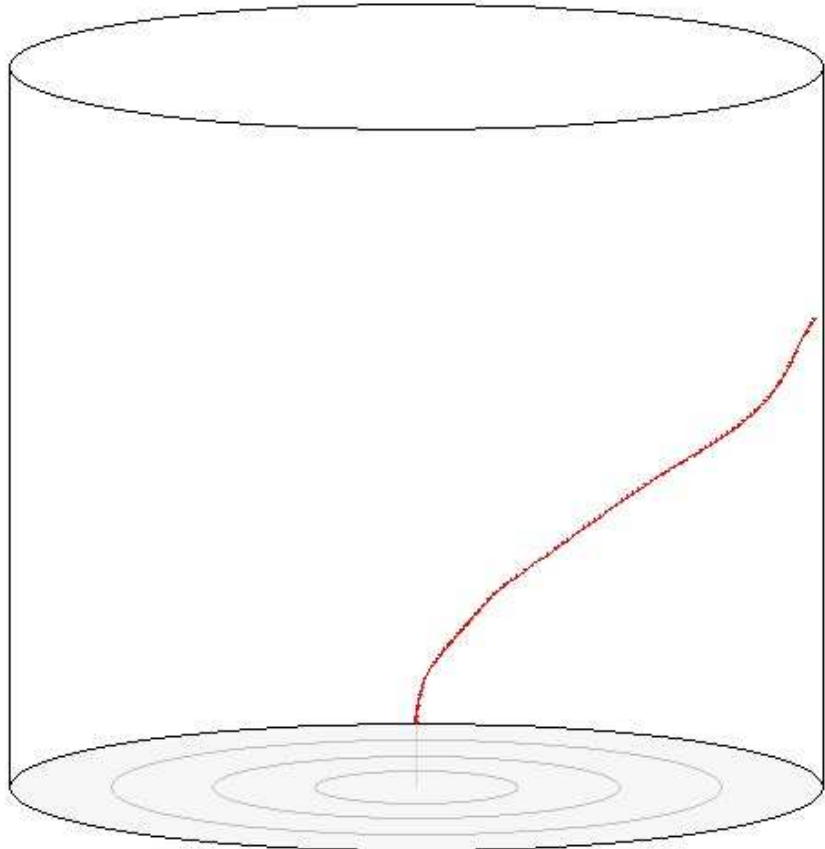
Since radiosondes are the accepted standard for measuring atmospheric conditions



RAOB Config #1:

**Figure 5.2:** A standard method of plotting radiosonde data is through a SkewT-LogP Diagram. The abscissa is temperature in degrees Celsius (°C) and the ordinate is altitude, given in both kilometres (km) and feet (FT). This coordinate system allows for the direct presentation of vertical profiles of atmospheric temperature (red line (right)) and dew point temperature (green line (left)).

HODOGRAM  
 3-D Trajectory Diagram  
 20 Kilometer Intervals  
 Vertical Tilt: 76  
 Azimuth View: 360  
 Auto-Rotation



RAOB Config #1:

**Figure 5.3:** A hodogram is a type of plot used to display motion. The path of the radiosonde is traced as the red curve. The base is oriented so north is the far edge of the circle. Each concentric circle represents a 20 km interval. This particular balloon traveled to  $\approx 80$  km towards the east at a near constant rate. Wind direction information is depicted as the arrows to the far right (again, most of these show a prevailing wind directed east-ward).

## 5.1. INTRODUCTION

---

such as temperature, pressure and humidity they provide the best data for developing site-specific atmospheric models. While radiosondes are launched regularly from major airports around the world, usually twice a day, at 0h and 12h Universal Time (UT), they are rarely above astronomical sites of interest. These radiosonde launches do however create a network of global coverage, whose vast data archives allow statistical analyses to be performed. These publicly available radiosonde data are a useful resource to anyone studying the Earth's atmosphere. The more that can be known about the atmosphere above a specific geographical location, the more accurate the resulting model. For the Chilean sites being studied, the closest radiosonde launch location is Antofagasta, Chile (Lat:  $-23^{\circ}25' 48.0''$ , Long:  $-70^{\circ}25' 48.0''$ ). The approximate distance from Antofagasta to the Paranal observatory site and potential E-ELT site, Cerro Armazones, is  $\sim 130$  km. During the PWV measurement campaigns, comparisons were made between the profiles from the Antofagasta radiosonde launches and those launched at Paranal. The contemporaneous profiles were similar in nearly every instance. This brings up the question of applicability of the radiosonde data. Is 130 km close enough to be physically meaningful? It is hoped that since the radiosonde data is within a few hundred kilometers it should represent the gross characteristics of the region. For instance, the radiosondes launched twice daily from Hilo International Airport, Hawaii are  $\sim 50$  km away from the observatory locations on Mauna Kea. However as the balloons are carried aloft they pass through the extremely humid tropical atmosphere before they encounter the inversion layer and may carry humidity with them that would bias their measurements. Even with these uncertainties with systematic errors and radiosonde trajectories, a model based on *local* launch data is still expected to

## 5.2. RADIOSONDE ANALYSIS

---

be superior to a mean profile. Moreover, since radiosondes are launched daily, it is possible to look at seasonal variations and long-term trends.

All remote sounding instruments require an accurate instrument model, atmospheric model, and retrieval algorithm to properly interpret measurements. The accuracy of PWV measurements depend both on the accuracy of the experiment itself, and the accuracy of the atmospheric model. Any error in the model will propagate through to the final PWV measurement value. For this reason it is necessary to understand the sensitivity in the retrieved PWV to any error in the input parameters, for example base temperature or lapse rate. Since, in general, there will be no real-time radiosonde data describing the atmosphere at the instant a PWV measurement is made, it is necessary to rely on a statistical approach using data from numerous radiosondes. In previous work [18], I accessed the archival radiosonde data for Hilo and Antofagasta, and used them to calculate statistically representative input parameters and profiles for use in our atmospheric model.

### 5.2 Radiosonde analysis

As part of my previous work with the TMT site testing campaigns, I accessed the National Oceanic & Atmospheric Administration (NOAA) database of global radiosondes<sup>2</sup> and reprocessed their raw data from first principles to create site-specific atmospheric models, and determine the resulting PWV sensitivity of the model in terms of input parameter uncertainty. The NOAA website radiosonde database is accessible to the public. Technical documents are also available online that detail the radiosonde data formats and the database itself [39]. The radiosonde data available from the NOAA site contain pressure

---

<sup>2</sup>NOAA/ESRL Radiosonde Database Access: <http://www.esrl.noaa.gov/raobs/>



## 5.2. RADIOSONDE ANALYSIS

---

[mbar], height [m], temperature [ $^{\circ}\text{C}$ ], dew point [ $^{\circ}\text{C}$ ], wind direction [degrees], and wind speed [ $\text{m s}^{-1}$ ]. Wind information is not required in this analysis. An example of typical raw radiosonde data is shown in Table 5.1.

Figures 5.4 and 5.5 show data from 3003 daily radiosondes launched from Antofagasta, Chile, spanning August 1998 through to May 2007. Both figures show the complete set of radiosonde data over this period, as well as the mean  $\pm$  the standard deviation. Figure 5.4 is the mean pressure profile, with  $\sigma_P = 2.75$  hPa (or 0.3% of atmospheric pressure). Figure 5.5 is the mean temperature profile, with  $\sigma_T = 3.59$  K (or 1.3% of typical base atmospheric temperatures). The pressure profile follows the theoretical exponential decay as expected; the data, mean, and standard deviation are almost indistinguishable on the scale shown. The temperature profile has a significantly larger spread across the data set, yet for the most part the data are still well behaved. Since the two daily radiosondes are launched at 8 a.m. and 8 p.m. local-time, the variation between them is minimal and so I chose to use an average profile for the launch region. The multi-year data set can be subdivided into seasonal sets or even monthly sets. No significant difference has been found between the multi-annual mean and the mean values derived from any subset of the data.

Though the vast amount of regional radiosonde data which is statistically processed may, to first-order, seem to solve the puzzle of characterising the environment around a site, there remains the challenge of knowing how the error in each parameter is propagated. How does the uncertainty in each parameter contribute to the eventual determination of flux and subsequently PWV? These parameters include ambient temperature, ambient pressure, adiabatic lapse rate, and the scale height of water vapour. Base temperature and pressure

## 5.2. RADIOSONDE ANALYSIS

---

**Table 5.1:** Sample radiosonde data from the NOAA radiosonde archive.

1	2	3	4	5	6	7
LINTYP						
			header lines			
254	HOUR	DAY	MONTH	YEAR	(blank)	(blank)
1	WBAN#	WMO#	LAT D	LON D	ELEV	RTIME
2	HYDRO	MXWD	TROPL	LINES	TINDEX	SOURCE
3	(blank)	STAID	(blank)	(blank)	SONDE	WSUNITS
			data lines			
9	PRESSURE	HEIGHT	TEMP	DEWPT	WIND DIR	WIND SPD
:						
:						
254	12	7	AUG	2007		
1	99999	85442	23.43S	70.43W	120	32767
2	100	160	86	33	32767	3
3		SCFA			32767	ms
9	1004	120	106	73	360	15
4	1000	149	104	60	55	10
4	925	792	50	43	160	31
5	924	801	48	39	32767	32767
5	918	855	118	-182	32767	32767
5	914	892	158	-242	32767	32767
5	892	1098	156	-294	32767	32767
5	874	1271	184	32767	32767	32767
4	850	1509	178	32767	130	51
4	700	3132	76	32767	60	26
5	692	3226	74	32767	32767	32767
4	500	5800	-135	-595	275	82
5	458	6458	-189	-629	32767	32767
4	400	7450	-249	-669	275	247
5	374	7935	-269	-679	32767	32767
4	300	9490	-389	-639	275	442

Note: data points with values of 32767 indicate no data, and both atmospheric temperature and dew point are recorded in tenths of degrees.

## 5.2. RADIOSONDE ANALYSIS

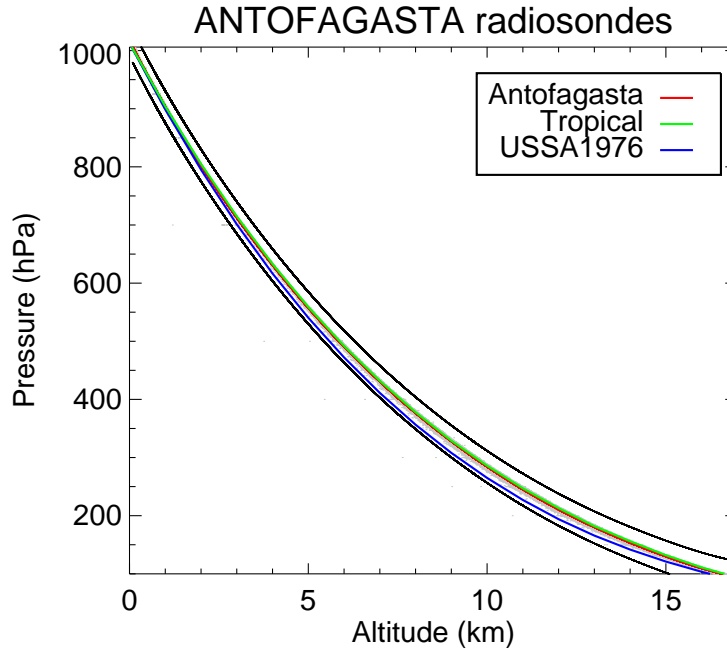


**Figure 5.4:** Pressure versus altitude data from a set of 3003 radiosondes spanning approximately a 10 year period launched from Antofagasta, Chile. Raw radiosonde data points are plotted in grey and the mean of these data in red. The  $\pm$  standard deviation curves are plotted in black and scaled by  $10\times$  for clarity. The pressure profiles from both the FASCODE Tropical (green curve) and U.S. Standard Atmosphere 1976 (blue curve) are also shown for comparison.

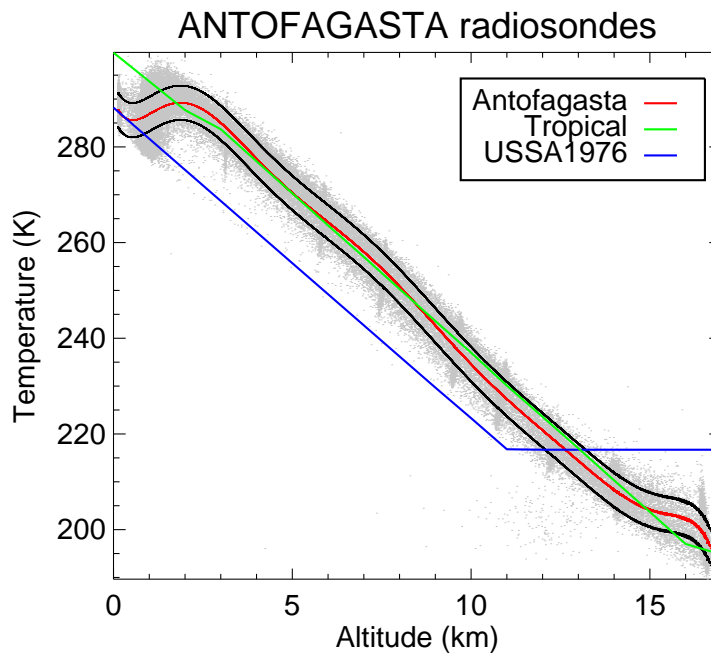


**Figure 5.5:** Temperature versus altitude data from a set of 3003 radiosondes spanning approximately a 10 year period launched from Antofagasta, Chile. Raw radiosonde data points are plotted in grey, the mean of these data in red, and the  $\pm$  standard deviation in black. The temperature profiles from both the FASCODE Tropical (green curve) and U.S. Standard Atmosphere 1976 (blue curve) are also shown for comparison.

### 5.3. DETERMINATION OF ADIABATIC LAPSE RATE

---

can be measured to fairly high precision ( $\Delta T = \pm 0.1$  K,  $\Delta P = \pm 0.5$  hPa) with locally installed meteorological towers, and thus are of little concern here. Adiabatic lapse rate can be determined from the slope of a temperature versus altitude plot of data provided by an individual radiosonde, or statistically derived mean of the data, as shown in Figure 5.6. The linear relationship between temperature decrease and elevation increase is valid from the surface of the Earth through to the tropopause (the temperature inversion boundary where the troposphere is decoupled from the stratosphere). The altitude of the tropopause varies according to latitude, having heights ranging from  $\sim 8$  km at the poles to  $\sim 18$  km over the western equatorial Pacific due to the rotation of the Earth and the different amounts of solar radiation incident on the Earth [36].

#### 5.3 Determination of adiabatic lapse rate

The term adiabatic refers to a reversible thermodynamic process that occurs without gain or loss of heat and without a change in entropy. Adiabatic lapse rate,  $\Gamma$ , is the rate of decrease of temperature with increase in altitude [40], given by:

$$-\frac{dT}{dz} = -\left(\frac{T_2 - T_1}{z_2 - z_1}\right) = \frac{g}{c_p} = \Gamma \quad [\text{K m}^{-1}] , \quad (5.1)$$

where  $c_p$  is the specific heat capacity of air at constant pressure [ $\text{J kg}^{-1} \text{K}^{-1}$ ] and  $g$  is the acceleration due to gravity, where  $g = 9.81 \text{ ms}^{-2}$ . For dry air at 273 K,  $c_p = 1005.7 \pm 2.5$  [ $\text{J kg}^{-1} \text{K}^{-1}$ ], resulting in a calculated lapse rate of  $\Gamma = -9.75 \pm 0.02 \text{ K km}^{-1}$ . Measured lapse rates are much less than this with typical values ranging from  $\sim -5$  to  $-7 \text{ K km}^{-1}$ . This difference is sometimes referred to as the wet adiabat, as opposed to the dry adiabat component; the atmosphere should get colder faster, but it does not. All measured lapse

### 5.3. DETERMINATION OF ADIABATIC LAPSE RATE

---

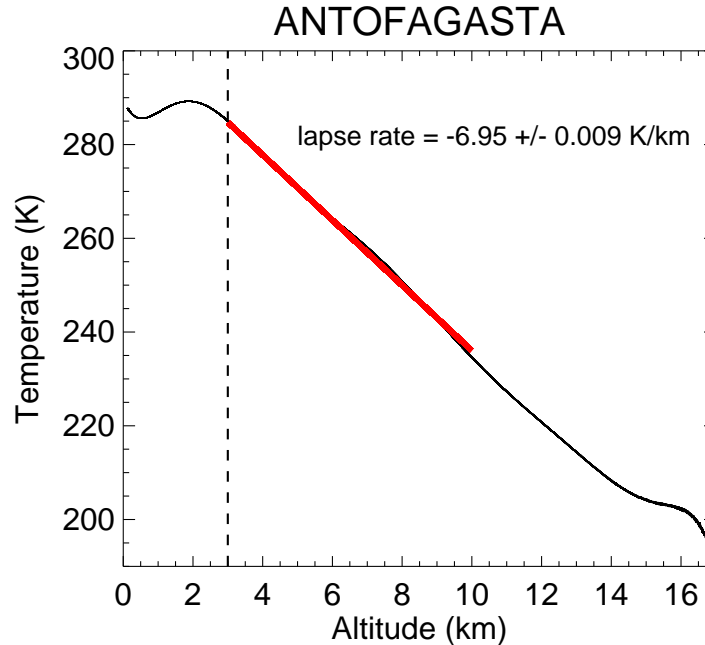


**Figure 5.6:** Mean temperature versus altitude data set derived from 3003 radiosondes launched from Antofagasta, Chile. The temperature data from 3 – 10 km was fitted to a line, resulting in a value for the lapse rate of  $\Gamma = -6.95 \pm 0.01$  K/km. The dotted line denotes the base elevation.

rates are lower than the theoretical  $\Gamma \approx -10$  K km<sup>-1</sup> due solely to having a condensable substance mixed into the atmosphere. Water exists in different phases (gas, liquid, and solid) over the temperature range occurring in our atmosphere. Unlike, N<sub>2</sub> and O<sub>2</sub> which do not condense and precipitate in our atmosphere, water does have this property. As elevation increases and the atmosphere gets colder, a critical point is reached at which water vapour will condense and form dimers and eventually droplets of water (or ice crystals). As water condenses and goes through a phase transition, the energy associated with the transition is released back into the atmosphere as latent energy. This serves to warm the atmosphere, effectively allowing it to keep its heat at higher altitudes than possible if it were dry, thus the reason why  $\Gamma_{\text{measured}} > \Gamma_{\text{theoretical}}$ .

#### 5.4. DETERMINATION OF $H_{\text{H}_2\text{O}}$ FROM RADIOSONDE DATA

---

Adiabatic lapse rate can be measured directly from statistically averaged radiosonde data, as shown in Figure 5.6 for the set of Antofagasta radiosondes resulting in an adiabatic lapse rate measurement of  $\Gamma = -6.95 \pm 0.01$  K/km. While this value for lapse rate may not represent the exact lapse rate in effect at the time of the PWV measurement, it is reasonable to assume that the lapse rate obtained from averaging a set of over 3000 spatially and seasonally representative radiosondes is statistically close enough for our purposes.

#### 5.4 Determination of $H_{\text{H}_2\text{O}}$ from radiosonde data

Scale height,  $H$ , as discussed in §2.3, is the interval of height in which the pressure/density of the atmosphere decreases by a factor of  $1/e$  [36]. While the actual distribution of atmospheric water vapour is in constant flux,  $H_{\text{H}_2\text{O}}$  describes the mean distribution of water vapour within the atmosphere.

An important distinction needs to be made between the scale height of the atmosphere and the scale height of water vapour. They both result in a similar decrease in pressure/density but have radically different values. The scale height of the atmosphere is  $\sim 8$  km, as calculated in §2.3, while the scale height of water vapour found in the literature ranges from  $\sim 1.0$ – $2.5$  km. The reason for the difference between the two scale heights (atmospheric and water vapour) is the same reason a difference exists between  $\Gamma_{\text{measured}}$  and  $\Gamma_{\text{theoretical}}$ . Again, it is the presence of water vapour and its propensity to condense that creates the difference. The atmosphere is primarily composed of  $\text{N}_2$  ( $\sim 78\%$  by volume) and  $\text{O}_2$  ( $\sim 21\%$  by volume), both of which are well-mixed and present in their gas phase

#### 5.4. DETERMINATION OF $H_{\text{H}_2\text{O}}$ FROM RADIOSONDE DATA

---

throughout the entire atmosphere. The water in our atmosphere exhibits more complicated behaviour due to its existence in three phases.

As mentioned above, scale height is a decrease in pressure or density with respect to increase in altitude. Therefore, to determine scale height, the partial pressure of water vapour,  $P_{\text{water}}$ , and the density of water vapour,  $\rho_{\text{water}}$ , must first be expressed as a function of altitude. The raw radiosonde data provides values for pressure,  $P$ , temperature,  $T$ , dewpoint temperature,  $D$ , and altitude,  $Z$ . From these values, it is possible to determine the partial pressure of water vapour, and subsequently the density of water vapour. Once density has been calculated, scale height can be determined by satisfying the following equality:

$$\rho_{\text{water}}(h + H) = \frac{\rho_{\text{water}}(h)}{e} . \quad (5.2)$$

This equality, based on the equation for scale height, Equation 2.2, states that the density at height  $h + H$  is equal to the density at height  $h$  divided by  $e$ . Thus,  $H$  is the height interval required to decrease density by a factor of  $1/e$ , the definition of scale height.

Once the density,  $\rho_{\text{water}}(h)$  is known, multiplication by an interval of height results in a water vapour column density with units  $\text{kg m}^{-2}$ . These units are functionally equivalent to the linear units of PWV expressed in mm.

When  $H$  is determined using the column density relationship in Equation 5.2, it is important to recall that radiosondes are often launched from elevations far below the observatory locations. For example, Hilo airport launches radiosondes at sea level, but the base elevation of Mauna Kea is  $\sim 4200$  m. While there are data allowing the calculation of  $H$  for elevations below 4200 m, the purpose of the study is to determine the scale height

## 5.4. DETERMINATION OF $H_{\text{H}_2\text{O}}$ FROM RADIOSONDE DATA

---

above the site. Therefore the base density used in the calculation is the density at the observing site.

In a prior study [18], I showed that the noise budget for retrieved PWV is relatively insensitive to ambient pressure, ambient temperature and adiabatic lapse rate, due to their input uncertainties all being well defined, and relatively small. However, since the scale height of water vapour is derived and subject to a wider possible range of values than any other parameter being studied, it is the primary source of larger uncertainties in PWV. Therefore, any attempt at successfully modeling the atmosphere above any site is limited by the uncertainty of the scale height of water vapour and its potential fluctuations over time.

### 5.4.1 Calculating the partial pressure of water vapour

To calculate the partial pressure of water vapour,  $P_{\text{water}}$ , it is necessary to introduce the concept of saturation, or equilibrium, vapour pressure. As the amount of water vapour in the air increases, there reaches a point of saturation, beyond which the addition of more water vapour is not possible, and precipitation occurs. This point of saturation is dependent on the dew point for conditions in question. The dew point temperature,  $D$ , for a parcel of air at a constant pressure is the temperature at which water vapour will condense and form drops of liquid water, or ice crystals if the dew point is below the freezing point of water.

An empirical expression for equilibrium vapour pressure,  $e_s(T)$ , with 0.3% accuracy over the temperature range  $-35\text{ }^\circ\text{C} \leq T \leq 35\text{ }^\circ\text{C}$  is given as [41]:

$$e_s(T) = 6.112 \times \exp\left(\frac{17.67 \times T}{T + 243.5}\right) \quad [\text{mb}] \quad , \quad (5.3)$$



#### 5.4. DETERMINATION OF $H_{\text{H}_2\text{O}}$ FROM RADIOSONDE DATA

---

where  $T$  is the temperature of the gas [ $^{\circ}\text{C}$ ]. If the atmosphere were saturated, both temperatures would be equal,  $T = D$ . The relation for partial pressure of water vapour,  $P_{\text{water}}$ , is given by:

$$P_{\text{water}} = e_s(D) \quad [\text{mb}] , \quad (5.4)$$

where  $D$  is the dew point temperature. A useful indicator known as the relative humidity index, is based on the ratio of the saturation vapour pressures computed at  $T$  and  $D$ . Relative humidity, RH [%], is expressed as:

$$\text{RH} = \frac{e_s(D)}{e_s(T)} \times 100\% \quad [\%] . \quad (5.5)$$

where  $T$  is atmospheric temperature, and  $D$  is the dew point temperature. At RH = 100%, the atmosphere is saturated with water vapour and precipitation is likely to occur.

##### 5.4.2 Calculating the density of water vapour

The vertical distribution of any atmospheric component can be expressed as a mass mixing ratio profile. The mass mixing ratio for water vapour is defined as the ratio of water vapour mass to dry air mass within a given volume [36]. Since the mass-to-mass ratio is being computed within an equal volume, it is equivalent to a density-to-density ratio  $\left(\frac{m_1}{V} : \frac{m_2}{V} \equiv \rho_1 : \rho_2\right)$ . Thus, the mass mixing ratio can be computed with densities for each atmospheric layer and expressed as:

$$\text{Mixing ratio} = \frac{\rho_{\text{water}}(z)}{\rho_{\text{air}}(z)} , \quad (5.6)$$

where  $z$  goes from the base elevation to the top of the atmosphere. Since water vapour is primarily constrained to the troposphere, and the radiosonde database had little data

#### 5.4. DETERMINATION OF $H_{\text{H}_2\text{O}}$ FROM RADIOSONDE DATA

---

above 16 km, the generic latitude-based profiles from FASCODE were used from 16–54 km, the top of our model.

Having calculated the partial pressure of water vapour in the previous subsection, it is possible to use that quantity to determine the density of water vapour through an application of the ideal gas law. According to the ideal gas law:

$$PV = N k_B T \quad [\text{J}] \quad , \quad (5.7)$$

where  $P$  is pressure [Pa],  $V$  is volume [ $\text{m}^3$ ],  $N$  is the number of molecules,  $k_B$  is the Boltzmann constant [ $\text{J K}^{-1}$ ], and  $T$  is the absolute temperature [K]. If density,  $\rho$ , is defined as a number density equal to  $N/V$ , then Equation 5.7 becomes:

$$P = \rho k_B T \quad [\text{Pa}] \equiv [\text{N m}^{-2}] \quad . \quad (5.8)$$

To calculate the density of air,  $\rho_{\text{air}}$ , for a given parcel of atmosphere, Equation 5.8 can be re-expressed as:

$$\rho_{\text{air}} = \frac{P_{\text{atm}} - P_{\text{water}}}{k_B T} \times \frac{M_{\text{air}}}{N_A} \quad [\text{kg m}^{-3}] \quad (5.9)$$

where  $M_{\text{air}}$  is the molecular mass of dry air [ $\text{kg mol}^{-1}$ ],  $N_A$  is Avogadro's number [ $\text{mol}^{-1}$ ],  $P_{\text{atm}}$  is atmospheric pressure [Pa],  $P_{\text{water}}$  is the partial pressure of water [Pa],  $k_B$  is the Boltzmann constant [ $\text{J K}^{-1}$ ], and  $T$  is atmospheric temperature within the parcel [K]. When performing any of these calculations it is important to be aware of the units being used. Some formulations use pressure in millibars, others use the SI unit of Pascals, whereas others use temperatures expressed in Celsius rather than Kelvin. When calculating  $\rho_{\text{air}}$  using Equation 5.9, the pressure parameter is  $P_{\text{atm}} - P_{\text{water}}$ . This is because the air density being calculated is not that of the air in its entirety, but that of dry air (without any water

## 5.5. SUMMARY

---

content). Thus the need to subtract the partial pressure due to water,  $P_{\text{water}}$ . Water vapour density can also be determined using a re-expression of Equation 5.8:

$$\rho_{\text{water}} = \frac{P_{\text{water}}}{k_B T} \times \frac{M_{\text{water}}}{N_A} \quad [\text{kg m}^{-3}] , \quad (5.10)$$

where  $M_{\text{water}}$  is the molecular weight of water.

### 5.4.3 Calculating precipitable water vapour

Now that the density of water vapour,  $\rho_{\text{water}}$ , in a given parcel has been computed, to determine the column density of the water, also expressible as PWV, simply multiply the density by the height of the layer. As mentioned in §5.4, 1 kg m<sup>-2</sup> of water vapour will have a depth of 1 mm if condensed. PWV is being used here to represent the column abundance in one layer. PWV can also refer to the total column abundance of water vapour, i.e. integrated over all layers. On average there is ~ 25 mm of PWV distributed above the entire surface of the Earth. Since this amount of water decreases exponentially with altitude, shown by Equation 2.2, therein lies the fundamental reason to use high altitude sites for observatories.

## 5.5 Summary

Using the methods described above it is possible to use radiosonde data to create a regionally representative atmospheric model for any site on Earth. Temperature and pressure profiles can be created directly from the raw radiosonde data. Determination of adiabatic lapse rate and scale height of water vapour have been demonstrated using first principle calculations and statistical methods. The key parameters that drive the

## 5.5. SUMMARY

---

atmospheric model have been analysed in terms of how their variation affects resulting PWV output from the model. It was shown that the derived PWV is most sensitive to the assumed scale height of water vapour. This scale height is difficult to measure in real-time and, thus, I used a statistically derived mean value from the radiosonde data.

---

## Chapter 6

# Methods of Measuring Water Vapour: Infrared Radiometer

### 6.1 IRMA summary

The AIG at the University of Lethbridge, under the supervision of Dr. David Naylor, has been developing IRMA radiometers that use a novel technique for measuring precipitable water vapour. IRMA is a simple infrared radiometer that measures a narrow range of the spectrum centred around  $20\ \mu\text{m}$  ( $500\ \text{cm}^{-1}$ ,  $15\ \text{THz}$ ) (shown in Figure 6.1). The benefits of this region are that it contains primarily rotational spectral features of water vapour [19] and little else, so, to first order, the integrated flux over this narrow band can be attributed to emission from water molecules.

There are two main applications for the IRMA radiometer: one is as a real-time phase-delay monitor for sub-millimetre astronomy, to allow for phase correction of interferometric telescope data due to induced atmospheric effects [1, 2], the other is as a sky opacity

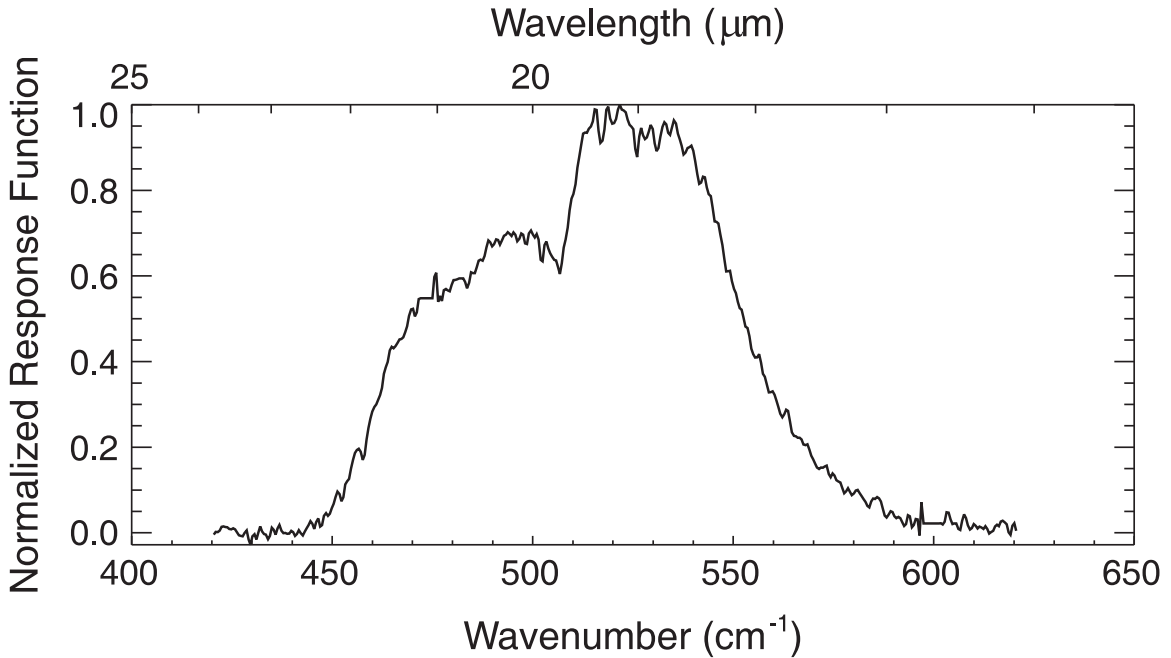


**Figure 6.1:** Normalised IRMA instrument response function as measured at 77 K using an ABB Bomem FTS. The profile is the end-to-end instrument response (the convolution of the filter transmission profile, transmission of the anti-reflection coated ZnSe window, and the photodetector response over the given spectral range).

monitor for use in infrared astronomy. This thesis focuses on the opacity monitoring aspect of the instrument.

### 6.1.1 IRMA hardware

IRMA has gone through several major design modifications since its proof-of-concept in December, 1999. These include integrating a Stirling-cycle cooler<sup>1</sup>, shown in Figure 6.2, to replace the liquid nitrogen wet cryostat required to cool the detector. External computer control was eliminated by employing a PC104 embedded computer<sup>2,3</sup>. A rabbit micro-controller<sup>4</sup> has also been used to control the altitude-azimuth (ALTAZ) hardware in

<sup>1</sup>Honeywell Hymatic, Redditch, Worcestershire, UK., <http://www.hymatic.co.uk/>

<sup>2</sup>WinSystems, Inc., <http://www.winsystems.com>

<sup>3</sup>Advanced Micro Peripherals Ltd., <http://www.ampltd.com/>

<sup>4</sup>Rabbit Semiconductor, <http://www.rabbitsemiconductor.com/>



**Figure 6.2:** Photo of the optical side of the IRMA instrument. The shutter/internal blackbody is open. Components including the detector assembly, the cooler controller, chopper wheel, and paraboloid mirror can be seen from this side of the unit. The far side (not pictured) houses the electronics.

basemount and forks attached to the radiometer unit. These allow the unit to be pointed in any direction, and for the unit to be inverted (parked) if inclement weather is forecasted.

The IRMA instrument consists of a  $35 \times 22 \times 19$  cm box weighing approximately 28 kg. Inside this box, the HgCdTe detector is placed in a vacuum vessel that is cooled using a compact, low power consumption Stirling cycle cooler, to its operating temperature of  $\sim 70$  K, increasing the measurement sensitivity. The incident astronomical signal is passband-filtered and then divided by a five-segment chopper blade to provide a 455 Hz chopped signal to the electronics, controlled by a small PC104 microcomputer. The sky is viewed via a 100 mm f/1 90° off-axis parabolic (OAP) mirror through an opening in the top of

the instrument [42]. The opening can be sealed during bad weather by a lid mechanism that includes an attached black body for instrument calibration. The IRMA box can be attached directly to a telescope and aligned with the main telescope beam to be used as a phase correction tool for radio interferometric data [43].

In addition to its uses in phase correction, IRMA can also be used as a real-time IR opacity monitor. It is this functionality that will be further described in this thesis. To function as an opacity monitor, IRMA is mounted between the upright forks of a robotic ALTAZ mount. The ALTAZ mount allows the unit to be arbitrarily pointed, adding the ability to perform skymaps and skydips, the former referring to 2-D rotation across all degrees of azimuth and elevation, whilst skydips refer to movement along the elevation axis only. These functions can be run from a remote computer, which then logs the data in daily files. Periodic calibrations are performed by observation of an internal blackbody source at two temperatures: one at ambient temperature and then a second at an elevated temperature.

Since February 2005, an IRMA has been measuring PWV levels in Chile at the Gemini South site on Cerro Pachón (Lat:  $-30^{\circ}14' 26.7''$ , Long:  $-70^{\circ}44' 12.1''$ , Alt: 2722 m) with a second unit added at the nearby Las Campanas observatory (Lat:  $-29^{\circ}0' 54.0''$ , Long:  $-70^{\circ}41' 32.0''$ , Alt: 2380 m) in August 2005 (shown in Figure 6.3). In early 2007 data collection started with three IRMA units at three locations for the TMT project site testing effort [44]. In 2009, IRMA units were used as the back-bone of three measurement campaigns done in collaboration with ESO in the context of site-testing for the E-ELT. The results from these campaigns will be discussed in Chapters 9, 10 and 11.





**Figure 6.3:** An IRMA unit installed at the Las Campanas Observatory. The Magellan telescopes are shown in the background (right).

I present here a description of the features of the IRMA units that enable them to operate in remote, unattended locations in the Chilean desert.

### 6.1.2 IRMA advantages

The advantages of a  $20\ \mu\text{m}$  radiometer for measuring water vapour are as follows: the peak of the Planck curve for typical atmospheric temperatures occurs at  $20\ \mu\text{m}$  ( $500\ \text{cm}^{-1}$ ) shown in Figure 4.6. As identified by Naylor *et al.* [19] the  $20\ \mu\text{m}$  atmospheric window contains primarily rotational transitions of water vapour, and therefore the integrated flux across the band provides a sensitive measure of water vapour. In its original development, IRMA was designed to function as a phase-delay monitor for radio-telescope arrays. Another common method of measuring water vapour is through the use of a heterodyne receiver

tuned to the 183 GHz emission line of water vapour. Unfortunately this system requires a local oscillator which has the potential of causing significant interference with the radio measurements. Since IRMA is a passive radiometer it causes no interference. IRMA also has the added benefits of being self-contained, robust, and remotely controllable.

### 6.1.3 Calibration

Since the IRMA radiometer is effectively a sensitive thermometer, its measurements are highly influenced by its local environment. Temperature sensors are distributed around the unit, across the cooler, near the electronics and inside the optical pathway housing in an attempt to quantify the thermal characteristics of the radiometer while it is operating. Utilising the real-time temperatures from within the unit, a method has been developed [18] to minimise the effects of stray thermal radiation, i.e. mirror spill-over, gradients due to ambient temperatures and wind loads, and from the cooler, controller and electronics themselves.

To first-order, the detector is linear with respect to incident flux, so a two-point calibration (ambient and warm load) is used. The controllable protective lid contains a resistive heating element on its underside (facing the off-axis parabolic mirror). In a calibration cycle, the lid is closed and the detector measures the lid at ambient, before the heater is turned on, and the warming and subsequent cooling of the lid are recorded by the detector, until the lid is finally reopened. This wave shape is shown as the curve beginning at 04:30 UT in Figure 6.4.

This ambient-warm method has also been employed using a larger, external black-body that can be placed above the IRMA unit. In this way the same calibration load can

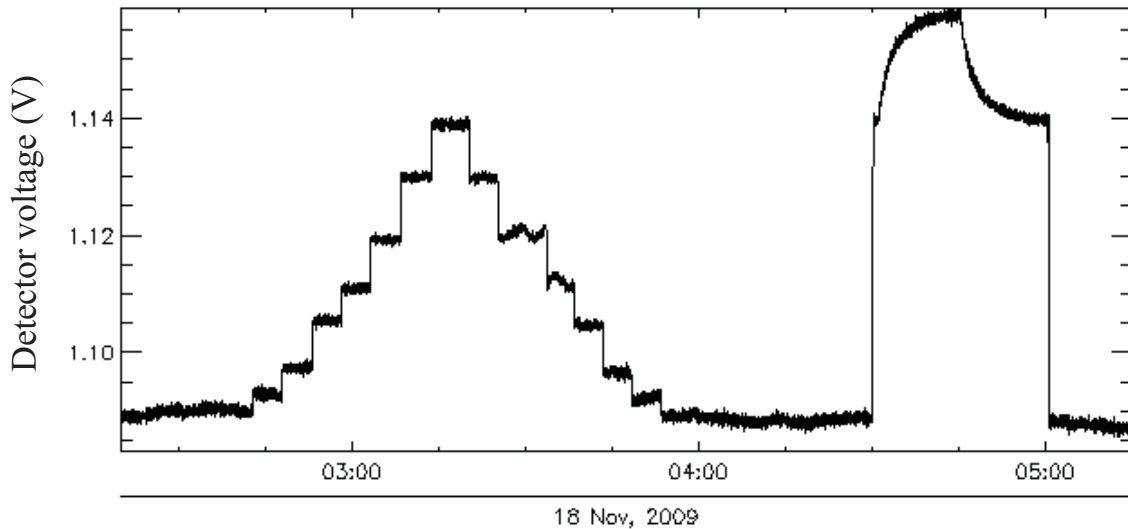


**Figure 6.4:** Raw IRMA data showing a  $15^\circ$  incremental sky-dip from zenith to the horizon and back to zenith (left), and a standard 30-minute calibration routine that measures the heated inner-side of the lid at ambient, warmed, and then passively cooled back to ambient (right). The data shown are the detector voltage versus time in hours.

be heated to a designated temperature and positioned above several IRMA units in sequence, allowing them to see the common load and providing a common reference standard to calibrate their respective signals. After application of the calibration algorithm, each unit can be made to retrieve the same effective flux from the measurements of the common calibration source [18].

Finally, a useful process to further test and reduce the differences between the retrieved IRMA PWV values is the skydip. A skydip refers to the act of tipping the radiometer from zenith through to the horizon, which, due to a longer effective path length through the atmosphere and under the assumption of a plane-parallel homogeneous atmosphere, allows the radiometer to measure an increasing range of PWV. The stair-step curve in Figure 6.4 shows the signal voltage resulting from a sky-dip starting at zenith through

## 6.1. IRMA SUMMARY

---

to the horizon and back to zenith in steps of  $15^\circ$ . When two or more radiometers perform a simultaneous sky-dip in the same direction it allows each to see a large variation in water column abundance under nearly-identical environmental conditions. This results in a data set that is useful for intercomparing the incident fluxes and subsequent PWV values retrieved by co-located IRMA units.

---

## Chapter 7

# Methods of Measuring Water

## Vapour: Satellite Estimates

Measurements of water vapour using satellite observations offer the possibility of global coverage and decades of archived data to allow for a historical survey of the weather statistics above a site to be characterised. The applicability of satellite determined PWV values as a potential aid to the selection of candidate sites is an important topic [45] and will be described in this chapter. One important goal of this study was to compare satellite estimates of PWV with a variety of simultaneous ground-based methods that included radiosondes launched from the observation site. Data from two satellite platforms have been examined in this study: GOES-Imager<sup>1</sup> and Envisat-MERIS<sup>2</sup>, each of which will be examined separately. While data from the Moderate Resolution Imaging Spectroradiometer (MODIS) aboard the NASA Terra and NASA Aqua satellites were available, when exam-

---

<sup>1</sup>GOES project science website: <http://goes.gsfc.nasa.gov/>

<sup>2</sup>ESA Earthnet: ENVISAT: <http://envisat.esa.int/>

ined, there was nearly a factor of two difference between the MODIS derived PWV values and all others measurements during a given time period. I contacted our collaborators, the Valparaíso group, since they regularly use MODIS retrievals, but they were not able to explain the existence of the scaling factor present in the processed data. For this reason the MODIS data were not incorporated into our study.

### 7.1 Envisat - MERIS

The Environmental Satellite, Envisat, is a sun-synchronous, polar-orbiting, Earth-observing satellite built by the European Space Agency (ESA) and launched on March 1, 2002. Envisat carries nine instruments that each measure various features of the atmosphere, land, water and ice, respectively, employing a variety of measurement techniques. Being sun-synchronous, Envisat is in a low Earth orbit, at an average altitude of 800 km, with an inclination of  $98.5^\circ$  and orbital period of  $\sim 100$  minutes. These orbital conditions provide global sampling with high temporal coverage at the poles and the ability to revisit an equatorial site in  $\sim 2-3$  days.

One of the nine dedicated Earth-observing instruments aboard Envisat is the Medium Resolution Imaging Spectrometer (MERIS)<sup>3</sup> [46]. MERIS measures reflected sunlight off the Earth's surface and atmosphere. Its primary mission had been to measure ocean colour (i.e. measurement of photosynthetic potential by detection of phytoplankton (algae), water quality, coastal erosion and extended pollution areas), but has since had its scope of objectives expanded to include both atmospheric and land surface related studies [46]. MERIS operates as a spectrometer over the visible and near-infrared spectral range, 390–

---

<sup>3</sup>MERIS Product Handbook: <http://envisat.esa.int/handbooks/meris/>

1040 nm, but only 15 spectral bands are output in bandwidths that can be programmed between 2.5–30 nm. The total water vapour content data product for MERIS claims a PWV range of 1–70 mm with an over-land accuracy of  $\pm 1.6$  mm ( $\pm 2.6$  mm above water surfaces) [47]. In the full resolution mode each pixel has an instantaneous field of view of  $0.019^\circ$ , with nadir spatial sampling of 260 m across track and 290 m along track (nominally 300 m). The reduced resolution mode used for large-scale studies has a nadir sampling of  $\sim 1.04$  km across track by 1.2 km along track (nominal resolution of 1.2 km) [48]. For our study, colleagues at ESO provided us with the total water vapour content measurements as processed from reduced resolution data.

Since MERIS was designed to study surface reflectance, a sun-synchronous orbit is critical to its operations because time-of-day effects can be controlled by observing the same location under similar illumination conditions on every pass, although time-of-year effects also need to be accounted for. MERIS scans the surface of the Earth through a push-broom method in which the linear charge-coupled device (CCD) arrays provide spatial sampling in the across-track direction (the broom head), while the motion of the satellite provides scanning in the along-track direction. With a  $68.5^\circ$  field-of-view around nadir, and a swath width of 1150 km, MERIS achieves global coverage every 3 days (in equatorial regions). Polar regions are visited more frequently due to the convergence of orbits.

The downside of this polar orbital configuration is that Envisat only passes over the Chilean study sites every 2–3 days. The overfly time in this region is  $\sim 13:50$ – $14:50$  UT, producing a sparse data set of day-time only measurements, which at first glance may seem of limited value when interested in a night-time study of PWV. However, the historical

archive of data does allow for comparison with day-time GOES data and allows for the possible inference of night-time values from measured day-time trends.

Water vapour column abundances are retrieved from the MERIS data using the signal ratio between channels 14 and 15, centred at 890 and 900 nm respectively, each with a 10 nm bandwidth. The general form of this algorithm is given by [47]:

$$W = k_0 + k_1 \log\left(\frac{L_{Ch15}}{L_{Ch14}}\right) + k_2 \log^2\left(\frac{L_{Ch15}}{L_{Ch14}}\right) \quad [\text{mm}] , \quad (7.1)$$

where  $W$  is the total water vapour column expressed as PWV,  $L_{Ch14}$  and  $L_{Ch15}$  are the radiances measured by MERIS channels 14 and 15, and  $k_0$ ,  $k_1$  and  $k_2$  are regression coefficients. This algorithm is based on the assumption that a logarithmic relationship between absorber mass and extinction exists, (Beer's law), expressed previously as Equation 3.1. This relationship assumes monochromatic radiation in a non-scattering atmosphere with unsaturated absorption, implying the linear/weak regime approximation is applicable. The quadratic term in Equation 7.1 is introduced as an empirical correction to the simple model.

The regression coefficients are derived by inverting results from a radiative transfer model and depend on observation geometry. Surface pressure is required in order to model the pressure broadening effects on water vapour absorption. Moreover it has been found that a correction involving the signal from channel 10 (753 nm) is necessary when the surface albedo of channels 14 and 15 differ by  $> \pm 1\%$  [47]. Figure 7.1 shows the MERIS water vapour measurement bands and the typical reflectance for bare soil, vegetation and snow. Figure 7.2 shows the simulated transmission expected for  $\text{PWV} = 25$  mm at sea-level in the 890 and 900 nm pass-bands. Once the radiance ratio is corrected, it can be passed through



the water vapour retrieval algorithm. Figure 7.3 shows the global maximum mean water vapour abundances as determined by MERIS for 2006.

### 7.2 GOES-Imager

A second source of PWV data used in our analysis is from one of the Geostationary Operational Environmental Satellites (GOES), more specifically the Imager instrument aboard GOES-12. The GOES satellites are operated by the National Oceanographic and Atmospheric Administration. They provide support for meteorological research and weather forecasting.

Unlike the Envisat spacecraft that is in low Earth orbit, the GOES satellites are located high above the surface of the Earth at  $\sim 36,000$  km. At this altitude, the satellites orbit at a speed that is approximately equal to the rate of rotation of the Earth, which effectively renders them motionless with respect to the surface of the Earth. This geostationary vantage point allows the satellite to stare continuously at the Earth which is useful for remote sensing and meteorological applications. While they are not able to provide global coverage, the evolution of clouds or storms can be recorded in real-time giving scientists valuable information about the atmosphere and its processes.

At the time of this writing there are four GOES satellites in operation, two of which are positioned in on-orbit storage. GOES-11 is operating as GOES-West; located at  $135^\circ\text{W}$  over the Pacific Ocean. GOES-12 is operating as GOES-East, located at  $75^\circ\text{West}$  over the Amazon River. Figure 7.4 shows a GOES-12-Imager full-disk visible channel image. Political boundaries have been superimposed onto the image. The United States as well

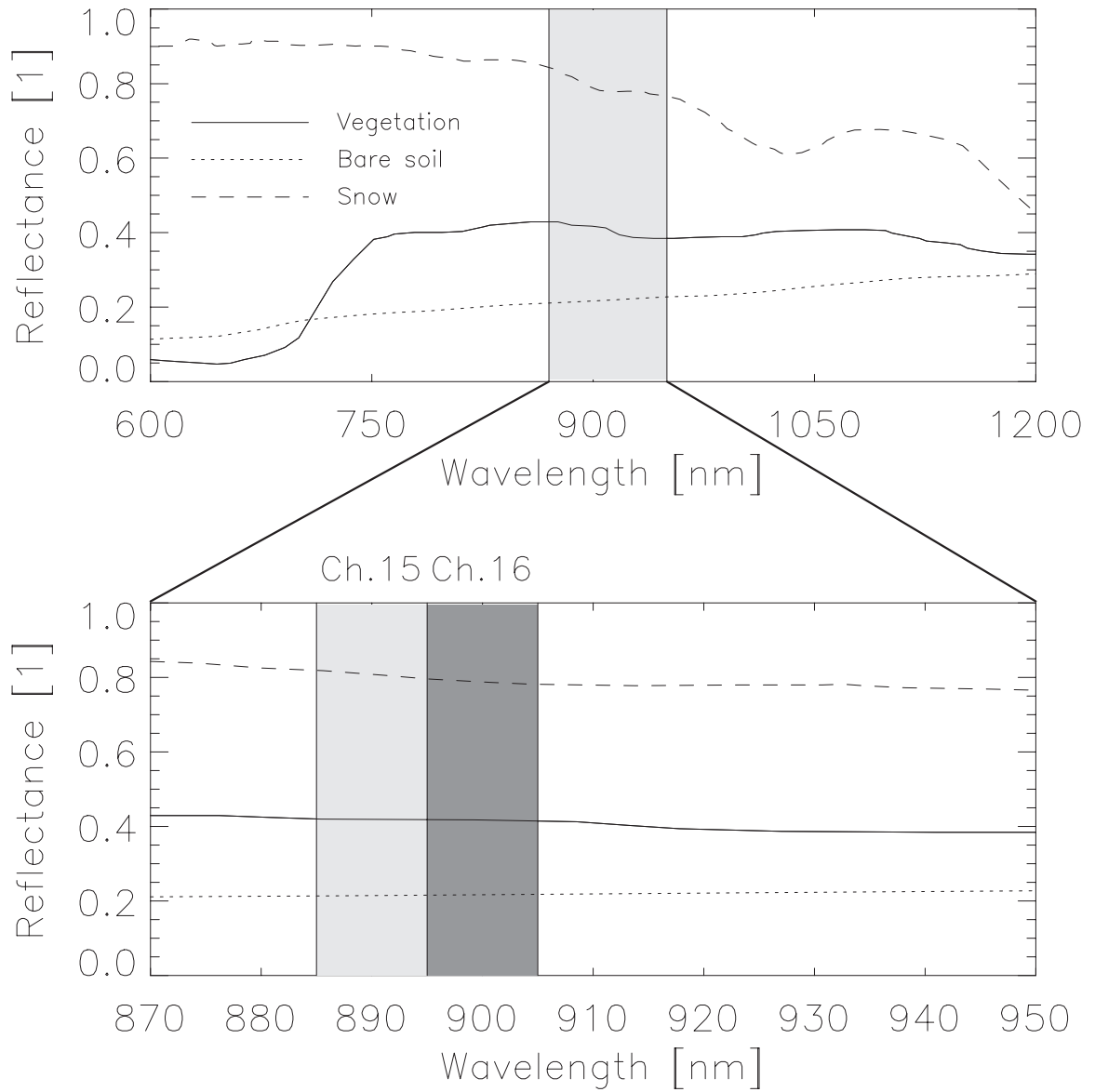


**Figure 7.1:** MERIS water vapour bands (bottom) and typical reflectance for bare soil, vegetation, and snow (top) [47].

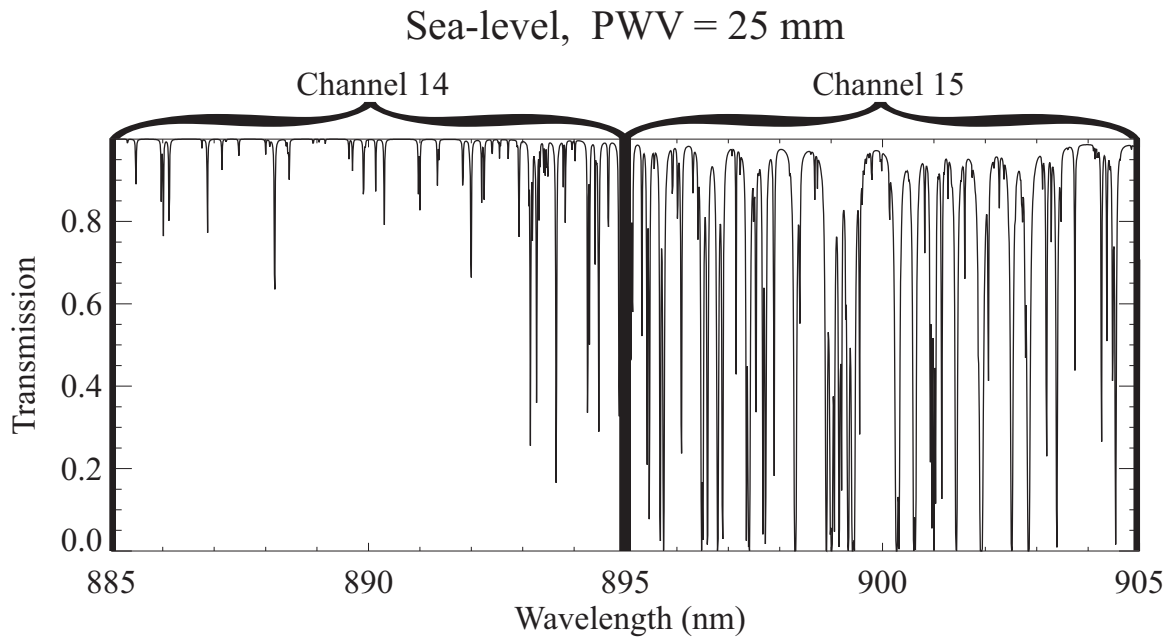


**Figure 7.2:** BTRAM simulated transmission for MERIS water vapour bands at sea-level with PWV = 25 mm.

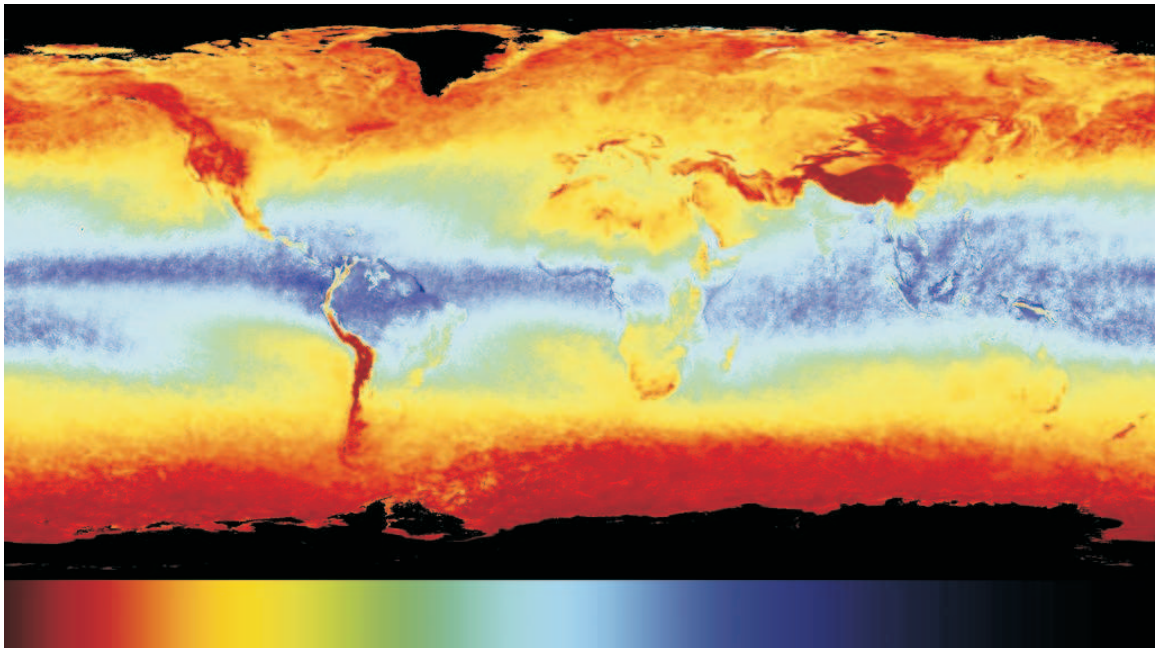


**Figure 7.3:** Global maximum water vapour amounts determined by MERIS for 2006. The scale, shown on the bottom of the image, goes from red (low PWV) to blue (high PWV). The scale is approximately 0–70 mm PWV. (Image credit: European Space Agency. All rights reserved.)

## 7.2. GOES-IMAGER

---

as southern Canada are visible in the upper left of the image. GOES-12 provides the U.S. with most of its weather information. Figure 7.5 shows a GOES-12-Imager full-disk moisture channel image. Clouds are visible in the image. The dry Atacama desert is visible as the dark patch in northern Chile.

GOES-12-Imager data measurements are taken every 3 hours (02:45, 05:45, 08:45, 11:45, 14:45, 17:45, 20:45 and 23:45 UT). These data are available approximately 1.5 hours after scan time [49]. Numerical meteorological forecast model data provides the profiles used to calculate the water content of the regions not probed by the satellite measurement. These simulated data consist of the daily model output runs initialised with 00UT and 12UT real-world data.

Water vapour is determined through passive remote sensing at different wavelengths. GOES-12, as well as the other GOES satellites, is equipped with an imager and a sounder. Using data from its five channel imaging radiometer, PWV can be determined through the comparison of two channels: the  $6.7 (\pm 0.25) \mu\text{m}$  water vapour channel and the  $10.7 (\pm 0.5) \mu\text{m}$  infrared window channel<sup>4</sup>. Figure 7.6 shows the simulated emission and transmission expected through the atmosphere at sea-level with  $\text{PWV} = 25 \text{ mm}$ . Figure 7.7 shows the weighting functions for different infrared channels. These wavelength dependent, pressure distributed weighting functions are a method of assigning influence to each channel according to the pressure(s) at which each is most dominant. For example, in Figure 7.7 the weighting function for the  $6.7 \mu\text{m}$  channel indicates that it is most sensitive to emission by the water vapour layer between  $300\text{--}600 \text{ hPa}$ <sup>5</sup> (equivalent to  $\sim 4.4\text{--}9 \text{ km}$ ). The emission

---

<sup>4</sup>NOAASIS: GOES Imager: <http://noaasis.noaa.gov/NOAASIS/ml/imager.html>

<sup>5</sup>1 hectopascal (hPa)  $\equiv$  100 Pa  $\equiv$  1 millibar.

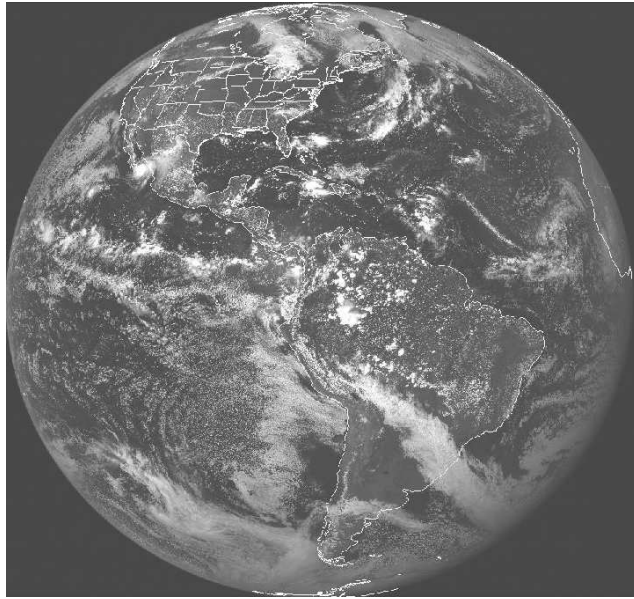


**Figure 7.4:** Full disk visible image from the GOES-12 spacecraft. This image was taken at  $0.65 \mu\text{m}$ . North America is visible in the upper left, while South America, specifically Chile, is roughly centred (left-right) in the bottom quarter of the image. (Image credit: NOAA. All rights reserved.)

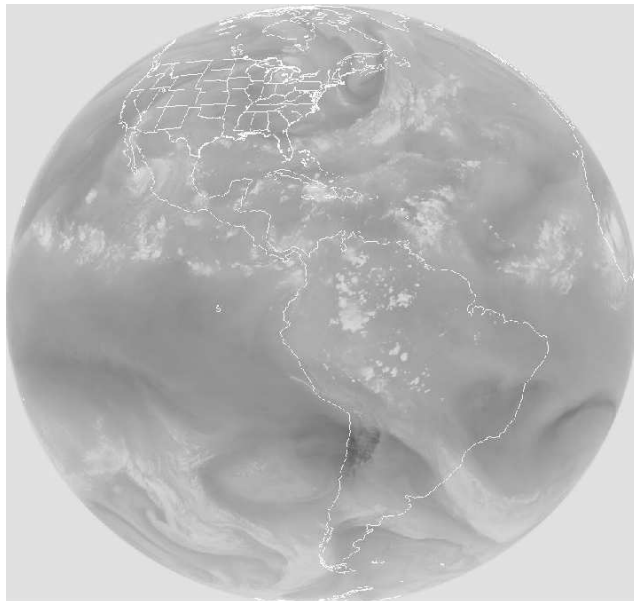


**Figure 7.5:** Full disk moisture channel image from the GOES-12 spacecraft. This image was taken at  $6.75 \mu\text{m}$ . Clouds and circulation patterns are visible. A particularly dark patch implying low water vapour can be seen over the northern Andes in Chile's Atacama Desert. (Image credit: NOAA. All rights reserved.)

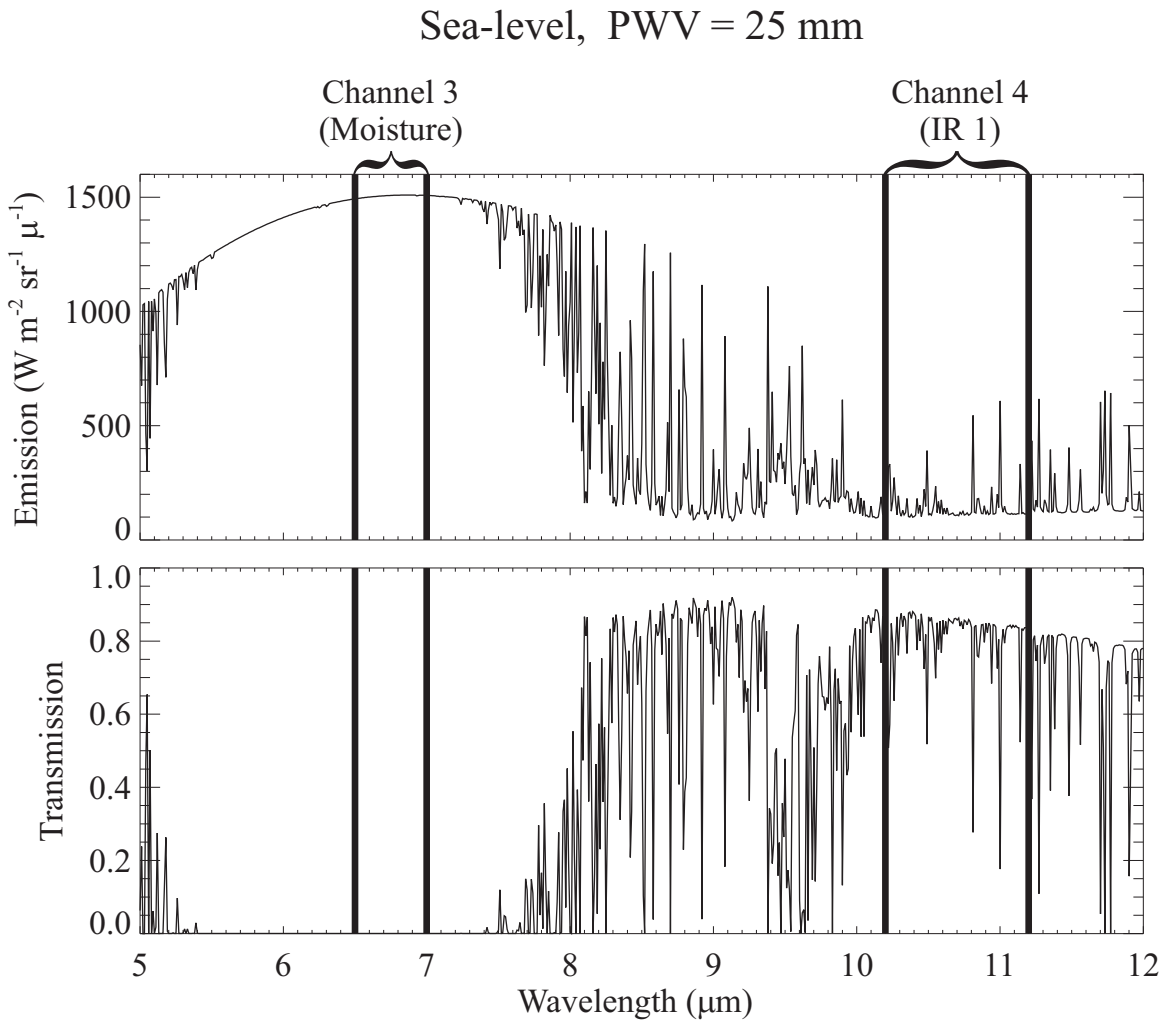


**Figure 7.6:** BTRAM simulated emission and transmission for the GOES water vapour band at sea-level with PWV = 25 mm, using the US Standard atmospheric profile 1976, with a base temperature of 300 K and a base pressure of 1000 hPa.

specific to this layer will depend on the abundance of water vapour and its temperature. Temperature can be set according to an *a priori* model or representative radiosonde measurement, thus leaving emission as a function of column abundance alone. As stated above, the 6.7  $\mu\text{m}$  channel is located near the centre of a strong water absorption band. Under clear sky conditions, this channel is primarily sensitive to relative humidity averaged over a layer in the upper troposphere [50].

### 7.2.1 Conversion of radiance to brightness temperature

To use the satellite derived radiance measurements for meteorological purposes the radiances need first be converted to brightness temperatures [51]. Brightness temperature or effective temperature is a quantity used to standardise and compare radiant sources. It compares the emission of a grey body to the emission of a black body in thermal equilibrium with its environment at a given frequency  $\sigma$ . The temperature of the equivalently radiating black body is known as the brightness temperature.

The emissivity of land, water and clouds is nearly unity at infrared wavelengths [52]. Therefore, the temperature determined from the radiance of the 10.7  $\mu\text{m}$  channel is a direct measurement of the temperature of the emitting surface. Thus, if clouds are present, this becomes a measurement of the top of the clouds, which poses some challenges in discriminating between clear and cloudy skies.

A calibrated radiance is determined from the raw counts through the simple application of a bias scaling factor and a first order gain scaling factor as follows:

$$L = (X - b)/m \quad [\text{W m}^{-2} \text{ sr}^{-1} (\text{cm}^{-1})^{-1}] \quad , \quad (7.2)$$

where  $L$  is radiance,  $X$  is the raw count value and  $m$  and  $b$  are the calibration gain and offset respectively.

Brightness temperature can be calculated from the radiance using an inverted version of the Planck function (given earlier in Equation 4.4):

$$T = \left( \frac{hc}{k_B} \right) \frac{\sigma}{\ln \left( 1 + \frac{2hc^2\sigma^3}{B_\sigma(T)} \right)} \quad [\text{K}] \quad . \quad (7.3)$$

$$T_{\text{eff}} = \frac{C_2\sigma}{\ln \left( 1 + \frac{C_1\sigma^3}{L} \right)} \quad [\text{K}] \quad . \quad (7.4)$$

where  $T_{\text{eff}}$  is the effective temperature [K],  $\sigma$  is the central wavenumber of the channel [ $\text{cm}^{-1}$ ], and  $C_1$  and  $C_2$  are radiation constants:  $C_1 = 1.191 \times 10^{-5} [\text{W m}^{-2} \text{sr}^{-1} \text{cm}^4]$  and  $C_2 = 1.439 [\text{cm K}]$ . Again, as above, to convert effective temperatures to actual temperatures, a channel dependent calibration gain and offset would be applied. These bias/scaling factors account for the variations in the inverse Planck function across the spectral pass-band of each channel. The difference between  $T$  and  $T_{\text{eff}}$  increases with temperature but is typically on the order of 0.1 K and thus negligible for most calculations.

To retrieve PWV, the 6.7  $\mu\text{m}$  brightness temperature can be converted to an upper tropospheric humidity value (UTH). UTH is a measure of the relative humidity within an atmospheric layer extending from 300–600 hPa. A semi-empirical relationship has been derived between UTH and the 6.7  $\mu\text{m}$  channel brightness temperature [49, 52, 54, 55, 56].

$$\text{UTH} = \frac{\exp(a + bT)}{\cos(\theta) p_0} \quad , \quad (7.5)$$

where  $\theta$  is the satellite viewing zenith angle (or Earth latitude being observed),  $a$  and  $b$  are the slope and intercept of a least-square fit to the regression line as defined by an empirical



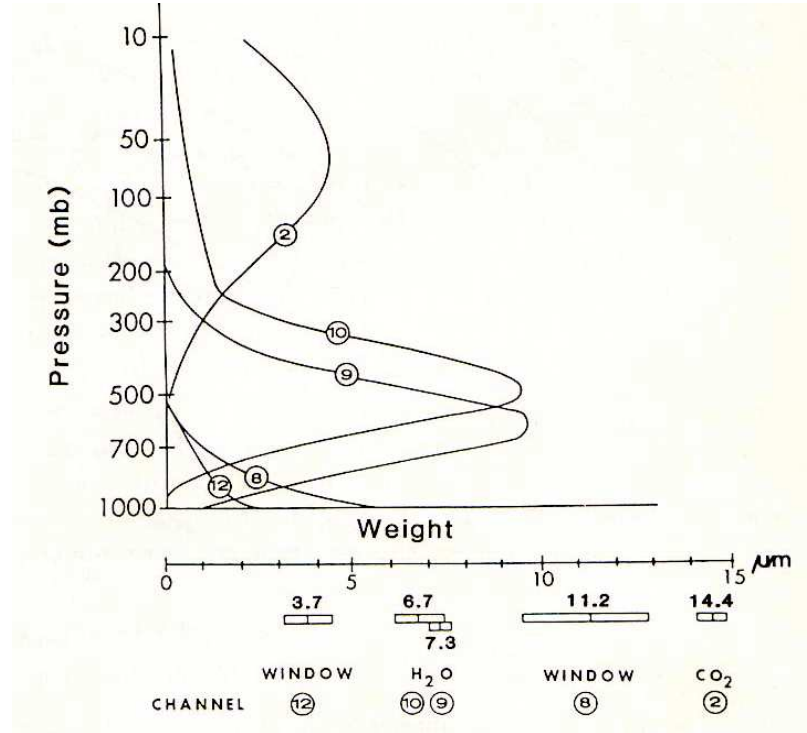


Figure 7.7: Weighting functions for selected infrared observing channels [53].

relationship and  $p_0$  is the normalised pressure variable. This relationship is applicable to clear regions (when no clouds are present). The regression fit parameters are seasonally dependent and obtained from a look-up table. The normalised pressure variable is defined as:

$$p_0 = \frac{p(T = 240\text{K})}{300} \quad , \quad (7.6)$$

where  $p$  is the pressure where atmospheric temperature is 240 K. The factor  $p_0$  is used to account for the vertical shifting of the weighting function peak as the temperature varies: it increases for warm airmasses and decreases for cold airmasses.

The final step is to convert the UTH value to PWV. As mentioned above, UTH is a measure of the relative humidity between 300–600 hPa. Thus, for this pressure range the

relative humidity is set to the UTH. Using this relative humidity and the saturation mixing ratio,  $x_s$  (computed using independent measures of upper-air temperature and pressure), it is possible to calculate the mixing ratio,  $x$ , subdivided arbitrarily in a number of pressure levels as the saturation mixing ratio data allows.

$$x = \text{UTH} \times x_s \quad . \quad (7.7)$$

This still leaves a large information gap for the mixing ratios at pressures outside the range 300–600 hPa. Since the satellite cannot measure water vapour outside this range it is necessary to introduce assumptions or complementary data to proceed. Radiosonde data shows that very little water vapour is found or expected at atmospheric pressures below 300 hPa. To determine the water vapour content from the surface up to 600 hPa, some extrapolation is required. Among the methods commonly used are linear extrapolation from the surface values, using predicted profiles from a forecast model, or, using contemporaneous radiosonde data. The mixing ratio at 100 hPa is set to zero and values between 100–300 hPa are linearly interpolated. The surface relative humidity and temperature are used to derive a surface mixing ratio (at approximately 750 hPa for Paranal). In our analysis, the moisture profile from the radiosondes is scaled to the 600 hPa value from the satellite derivation. Armed with information about the temperature profile,  $x_s$  can be computed for all altitudes and then  $x$  is calculated using Equation 7.7. PWV is calculated from  $x$  using the following equation [52]:

$$\text{PWV} = \frac{1}{g} \int_{P_{\text{surface}}}^{P_{100}} x \, dP \quad [\text{mm}] \quad , \quad (7.8)$$

where  $x$  is the mixing ratio,  $dP$  is the incremental pressure change [Pa], and  $g$  is the

### 7.3. SUMMARY

---

acceleration due to gravity [ $\text{m s}^{-2}$ ]. This gives PWV in units of  $\text{kg m}^{-2}$  equivalent to mm of water.

Most of the water vapour in the atmosphere resides in the bottom few kilometres, often below an inversion layer that serves to cap off the moist air, and separate it from the drier air above. Mixing ratios above and below an inversion layer will be different. Any assumptions about linearity of mixing ratio distributions will necessarily break-down upon passing through an inversion layer. If, however, the site in question is above an inversion layer, as is the case for most astronomical observatories, then mixing ratio distributions are more readily predictable.

While satellite derived PWV has less certainty for regions of lower elevation, they can be used to probe the middle and upper atmosphere to find regions with low PWV. The driest sites within these geographical areas would then most often be found at the highest elevations.

### 7.3 Summary

GOES-Imager and Envisat-MERIS derived PWV each have benefits and drawbacks. For example, GOES-Imager provides good temporal resolution – one full Earth disk observation every 3 hours – but offers only limited spatial resolution ( $12 \times 12$  km). Moreover, the GOES imaging radiometer cannot measure water vapour directly but instead derives it based on an empirical relationship between brightness measurements at 6.5 and  $10.7 \mu\text{m}$  (a water vapour emission band and an IR window, respectively). This approach is sensitive to temperature effects. On the other hand, the MERIS spectrometer directly

### 7.3. SUMMARY

---

measures water vapour lines between 890 and 900 nm with a spatial resolution of  $1.2 \times 1.2$  km, however, due to its polar orbit it passes over sites in Chile only every 2–3 days, always around 14:30 UT, thus providing only day time measurements. A resolution of 1 km is beneficial when the climatological conditions change rapidly with local orography. In the analysis of satellite derived PWV in this thesis I have used the reduced data products after they were processed through their respective standard pipelines. For more information about the instruments please refer to their respective references.

---

## Chapter 8

# Methods of Measuring Water

## Vapour:

## Spectral Fitting

### 8.1 Overview

The determination of PWV through spectral fitting has formed a large part of this PWV campaign. In this chapter I will describe an automated method I developed to fit a simulated atmospheric spectrum to either a measured absorption or emission spectrum.

As discussed in Chapter 3, ground based infrared astronomical measurements are limited by atmospheric opacity which is primarily due to water vapour. Observations of a star with a featureless continuum spectrum, such as a white dwarf, provide a direct measurement of the atmospheric absorption along the line-of-sight to the star. The resulting spectrum can be iteratively fitted to model atmospheric spectra to retrieve PWV. For

atmospheric emission, a similar process is used, whereby a simulated emission spectrum is again fitted to the processed data to quantify the amount of water vapour necessary to produce the measured emission. These two algorithms and examples of their results will be described in this chapter.

### **8.2 Introduction**

This fitting work began as a way of obtaining independent calibration points that could be used as a reference for the IRMA radiometers. While the IRMA units have been shown to provide accurate PWV measurements in a relative sense (i.e. when two co-located IRMA units are measuring the same patch of sky), their calibration in terms of retrieving absolute PWV values has remained a significant challenge. In an attempt to remedy this issue, researchers at Las Campanas observatory began to compare IRMA derived PWV to the PWV values extracted from standard star calibration measurements taken with the Magellan Inamori Kyocera Echelle (MIKE) [57] spectrograph mounted on the Clay Magellan 6.5-m telescope. Several rapidly rotating A and B type stars with magnitudes between 4–6 were designated as calibration targets as they are expected to have few photospheric features in the wavelength range being studied, and their distribution across the sky made certain that a star near to the zenith (low airmass) could be selected as a calibration target. PWV measurements with MIKE are routinely made once per night under clear sky conditions. While impractical for constant monitoring of the PWV, it does provide an excellent tool for verifying the calibration of other instruments.

The method of analysis adopted by the MIKE team was to carefully select a few

isolated, weak lines known to be due to atmospheric water vapour, and determine the abundance by using the equivalent width method and a simple, single layer atmosphere [58, 59].

In an attempt to improve the accuracy of the PWV values derived from these spectra, I devised an automated method of fitting over a thousand weak and strong, isolated and blended, water vapour lines. In the case that errors are random, this should lead to an increase in accuracy by an order of magnitude.

The BTRAM radiative transfer and atmospheric modeling program has been used to generate a theoretical transmission spectrum of the atmosphere above the Las Campanas Observatory. The results are shown in Figure 8.1 for the wavelength range 600–1000 nm, which is part of the red channel of MIKE. The upper plot shows the absorption due to atmospheric water vapour alone for a column abundance of 1 mm PWV. The lower plot shows the equivalent spectrum containing the principal constituents responsible for absorption in this range (mostly CO<sub>2</sub> and O<sub>2</sub>), but excluding water vapour. Examination of these plots shows that there are several regions where water vapour can be isolated for analysis. In this study we have selected the regions delineated by the vertical lines. A screenshot of BTRAM is shown in Figure 8.2

An algorithm was developed in the IDL<sup>®</sup> programming environment using a least-squares fitting routine [60] with the relevant source code given in Appendix C. This algorithm was able to fit the echelle spectra and found that the previously used, simpler method was underestimating PWV by ~25% [61]. The source of this discrepancy has since been identified as resulting from using the natural log of the line flux, which Brault *et al.* [58]

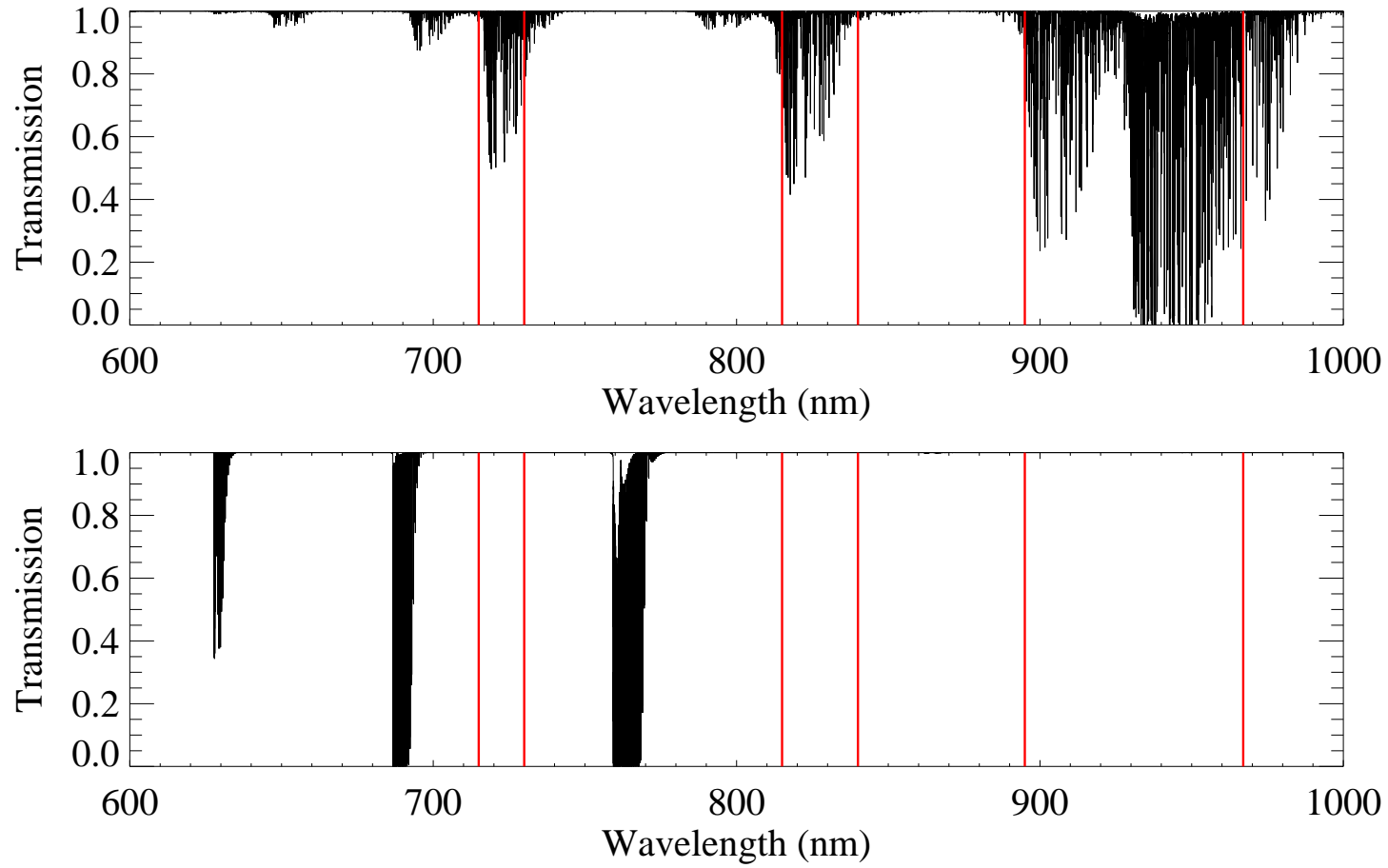


**Figure 8.1:** Transmission spectrum produced by BTRAM for the atmosphere above the Las Campanas Observatory. The upper plot shows the transmission spectrum for water vapour alone (PWV = 1 mm). The lower plot shows the transmission due to all other significant atmospheric constituents, which for this wavelength region are CO<sub>2</sub> and O<sub>2</sub>, and no water vapour. The red vertical bars delineate three regions used for fitting to the echelle data.



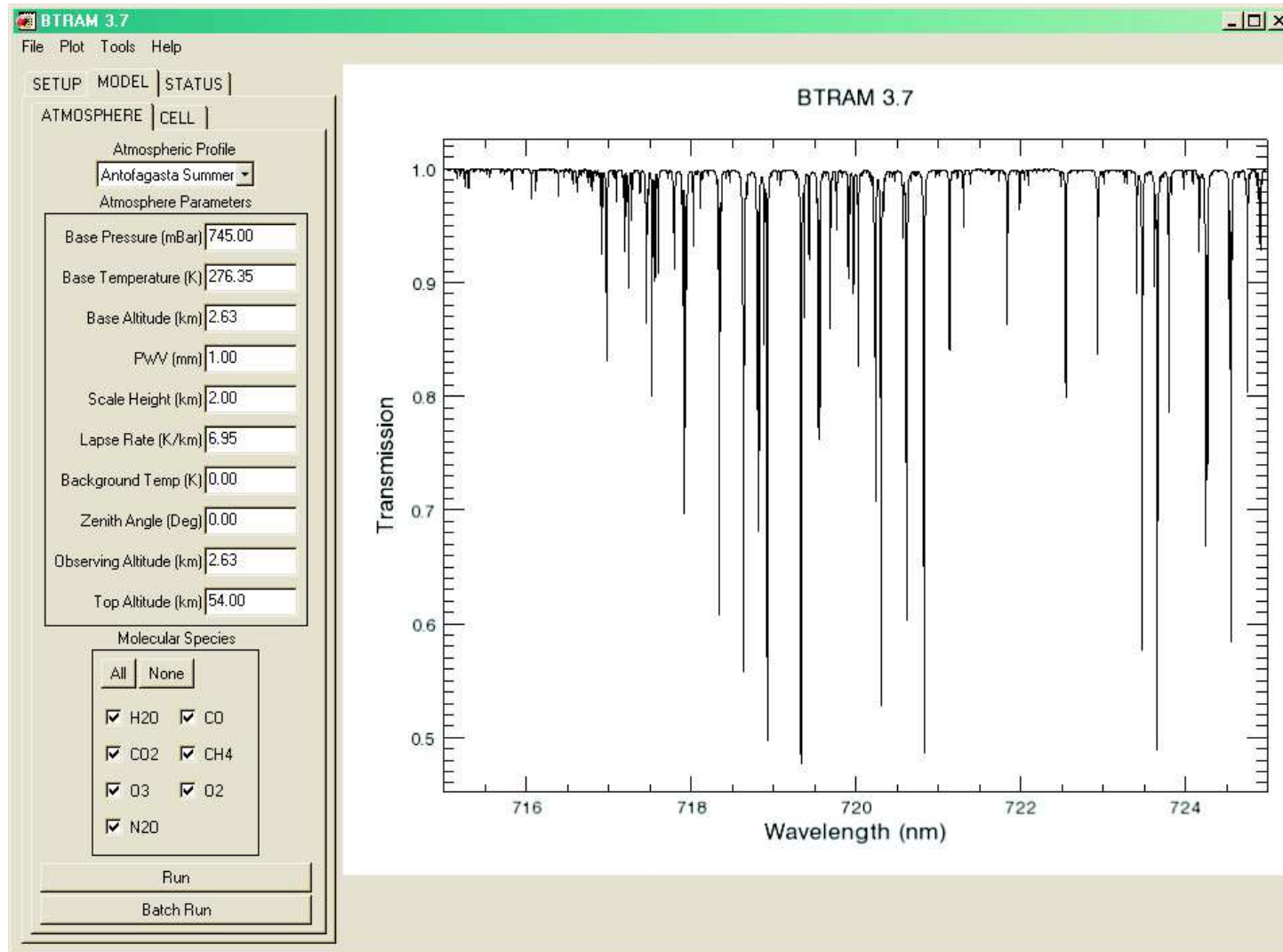


Figure 8.2: Screenshot of the BTRAM atmospheric modeling software.

had claimed as a quick method for obtaining PWV for lines with central depths less than 50%. The discrepancy is essentially eliminated when line strengths and the equivalent width method are applied to the spectra [62].

#### **8.3 MIKE observations of atmospheric water vapour**

In the following study, the BTRAM radiative transfer and atmospheric modeling program was used to generate a theoretical transmission spectrum of the atmosphere above the Las Campanas Observatory which forms the basis for comparison with MIKE observations.

Extracting meaningful results from a remote sounding instrument involves the use of a sophisticated atmospheric model. The uncertainty of the retrieved PWV depends not only on the accuracy of the measurement, but also on the accuracy of the model. The simplest model consists of a plane-parallel, single layer atmosphere defined by a limited set of parameters: pressure, temperature, density and mixing ratios. More complex models involve many layers in which the full radiative transfer from the top of the atmosphere to the observer is computed on a line-by-line, layer-by-layer basis [2]. The multi-layer approach allows one not only to account for the distribution of individual constituent profiles, but also variations in the physical characteristics of the atmosphere, such as temperature, pressure, adiabatic lapse rate and scale height. Although several atmospheric modeling programs exist, i.e. Atmospheric Transmission at Microwaves (ATM)<sup>1</sup>, Atmospheric TRANsmission (ATRAN)<sup>2</sup>, FASCODE [14], Reference Forward Model (RFM)<sup>3</sup>, to name a few, in general

---

<sup>1</sup>Atmospheric Transmission at Microwaves, <http://damir.iem.csic.es/PARDO/atm.html>

<sup>2</sup>ATRAN, <http://atran.sofia.usra.edu/cgi-bin/atran/atran.cgi>

<sup>3</sup>Reference Forward Model, <http://www.atm.ox.ac.uk/RFM/>

only a limited set of atmospheric profiles are available. Unfortunately few of these profiles are well-suited to sites of astronomical interest. This provided the impetus for our group to develop a site-specific atmospheric radiative transfer model called BTRAM [2]. While BTRAM uses the standard HITRAN 2008 database [15], it allows the user to fine tune the model to a specific geographical location using whatever meteorological data are available (e.g. radiosondes, see Chapter 5).

A serendipitous bi-product of MIKE spectra is that they provide a simultaneous measure of the many absorption lines due to atmospheric water vapour. Since these transitions have high excitation energies, the derived column abundances are less sensitive to the atmospheric model used in the retrieval process because the levels are not populated at the typical temperatures of the atmosphere.

#### 8.4 Equivalent width derived PWV

MIKE provides simultaneous coverage over two wavelength ranges, the *blue* channel (320–480 nm) and the *red* channel (440–1000 nm) [57]. Since the majority of the water vapour transitions occur in the *red* channel, I focused exclusively on the data from this range. In order to resolve the individual water vapour lines in this wavelength range, a resolving power,  $R$ , greater than 10,000 is required. MIKE typically operates at  $R = 31,000$ , which allows for a more accurate determination of lineshape and continuum.

Thomas-Osip *et al.* [59] used the Brault method to determine PWV from MIKE spectra. In the Brault method [58], the PWV is determined from a measurement of the integrated area under a weak, isolated absorption line and the knowledge of the relevant

#### 8.4. EQUIVALENT WIDTH DERIVED PWV

---

molecular parameters of the specific line (line strength, lower energy transition and frequency) from a molecular database such as HITRAN, and an assumed mean temperature of the atmosphere.

In the case of an optically thin spectral line, the PWV can be computed directly from the equivalent width of a line:

$$W = \int \left(1 - \frac{I(\lambda)}{I_0}\right) d\lambda \rightarrow N \int \sigma_\lambda d\lambda = N \sigma_0 \Delta\lambda, \quad (8.1)$$

where  $W$  is equivalent width [nm],  $I(\lambda)/I_0$  is the transmission,  $N$  is the column density [molecules  $\text{cm}^{-2}$ ],  $\sigma_\lambda$  is absorption cross-section [ $\text{cm}^2$ ], and  $\sigma_0$  is the mean cross-section [ $\text{cm}^2$ ] averaged over the bandwidth  $\Delta\lambda$  [nm]. Thus, given  $\sigma_0$  and a measurement of the equivalent width of the line it is possible to retrieve the column density  $N$ , which is essentially the Brault method.

In practice, since the molecular parameters are expressed in terms of frequency (wavenumbers), the equivalent width equation, 8.1, is often recast in terms of frequency.

Since 1 mm of water vapour corresponds to a column abundance of  $N_{\text{H}_2\text{O}} = 3.346 \times 10^{21}$  [molecules  $\text{cm}^{-2}$ ], the PWV can be derived from the equivalent width as follows:

$$\text{PWV} = \frac{W}{S(T) \times N_{\text{H}_2\text{O}}} \quad [\text{mm}], \quad (8.2)$$

where  $S(T)$  is the line strength at the assumed mean temperature of the atmosphere [ $\text{cm}^{-1}/(\text{molecule cm}^{-2})$ ], and the equivalent width must be expressed in frequency units [ $\text{cm}^{-1}$ ].

The advantage of this technique is in its simplicity, since it is based on only five parameters. The principle disadvantage of the method is that it requires weak and isolated

lines to correctly identify the continuum ( $I_0$  in equation 8.1) from which the equivalent width is derived. Moreover, the signal-to-noise ratio of weak lines is inherently inferior to that of stronger lines, resulting in higher uncertainties in derived PWV.

In this study I have applied BTRAM to the wavelength range accessible to MIKE. A comprehensive fitting of the complex manifold of water vapour lines has been used to determine more accurately the column abundance of water vapour. These results have been compared to the simple, single line technique used by Thomas-Osip *et al.* [59], and are presented in the next section.

### 8.5 Fitting spectral data - Absorption

The method employed to fit the theoretical BTRAM spectrum to the MIKE data involved the following steps, outlined in Figure 8.3. The MIKE data were reduced using the standard pipeline<sup>4</sup>. The final data product of the pipeline is a multispec Flexible Image Transport System (FITS) file containing spectra for the sky, the object, calibration lamp data, flattened-flat or blaze, and the spectra divided by the flattened flat, or relative fluxing. Each of these is present for every diffraction order of the MIKE observation. After ingesting the MIKE data, the algorithm must remove the continuum. The wavelengths at which the continuum will be evaluated are determined by first examining the regions of the BTRAM spectrum that have absorption less than 0.2%. These corresponding regions are then mapped onto the MIKE data and taken to be representative of the continuum at those wavelengths. A low order polynomial is fitted to the continuum and subsequently removed, resulting in a normalised transmission spectrum.

---

<sup>4</sup>MIKE Pipeline: <http://www.ociw.edu/Code/mike/>

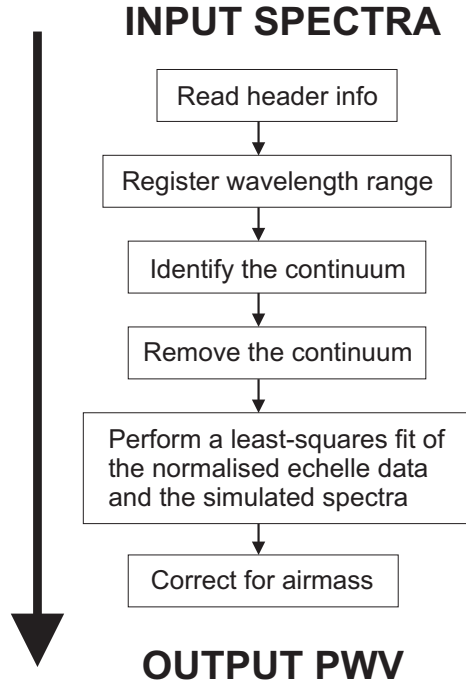


**Figure 8.3:** Algorithm for fitting a simulated spectrum to absorption spectra.

The theoretical atmospheric transmission spectrum is iteratively fitted to the normalised MIKE spectrum using the non-linear least-squares Levenberg-Marquardt algorithm [63]. Fit parameters include PWV, Gaussian half-width, and a wavelength-dependent shift. In order to avoid recomputing the full model at every iteration, I chose to work in opacity space and converted the 1 mm PWV theoretical absorption spectrum into opacity. The opacity spectrum could then be linearly scaled by the fitting algorithm, and then converted back into a transmission spectrum. The relationship between opacity and transmission is given as  $T = e^{-\tau}$ , where  $\tau$  is opacity. The desired output parameter from the fit is PWV. In order to allow an instrumental lineshape to be taken into account, the theoretical transmission spectrum is computed at a higher resolution than the MIKE data (0.001 nm as compared to  $\sim 0.005$ – $0.015$  nm). The resulting spectrum is convolved with a Gaussian

## 8.5. FITTING SPECTRAL DATA - ABSORPTION

---

profile to represent the instrumental lineshape of the echelle spectrograph. The Gaussian half-width is one of the fitting parameters in the minimization routine. In order to account for the varying dispersion across the echelle spectrograph, and the difference between air and vacuum wavelengths, a wavelength-dependent shift is fitted in the narrow regions under study. An example of such a fit is given in Figure 8.4, showing how both atmospheric water vapour and oxygen lines were effectively identified and removed from measured data.

An iterative fitting procedure was developed that minimised the difference between the simulated and measured spectra. As expected, MIKE data are broadened due to its effective instrumental lineshape (ILS). To mimic this effect, a simple Gaussian profile was applied to the high-resolution BTRAM output. Figures 8.5, 8.6 and 8.7 show fitting results for a measurement from September 23, 2007. Each of the plots contains the raw MIKE data (black), the high resolution BTRAM spectra (dashed line), the Gaussian convolved fitted BTRAM spectra (red), and a residual to demonstrate the overall quality of each fit. To first-order, through an examination of the minimal fitting residuals, a Gaussian function appears to be an adequate approximation to the MIKE ILS .

A comparison of the MIKE data and the best-fit BTRAM data for two spectral ranges, 715–730 and 813–838 nm, are shown in Figures 8.8 and 8.9 for both a dry night (left column) and wet night (right column). The top graphs in each figure show a 10 nm range of the 700 and 800 nm windows respectively. The middle and bottom plots show two different zoomed regions of the upper plots, each 2 nm wide. In each plot the upper trace is the MIKE data, the middle trace is the fitted BTRAM data displaced for clarity, and the bottom trace shows the residual difference between the MIKE and BTRAM data. There is

## 8.5. FITTING SPECTRAL DATA - ABSORPTION

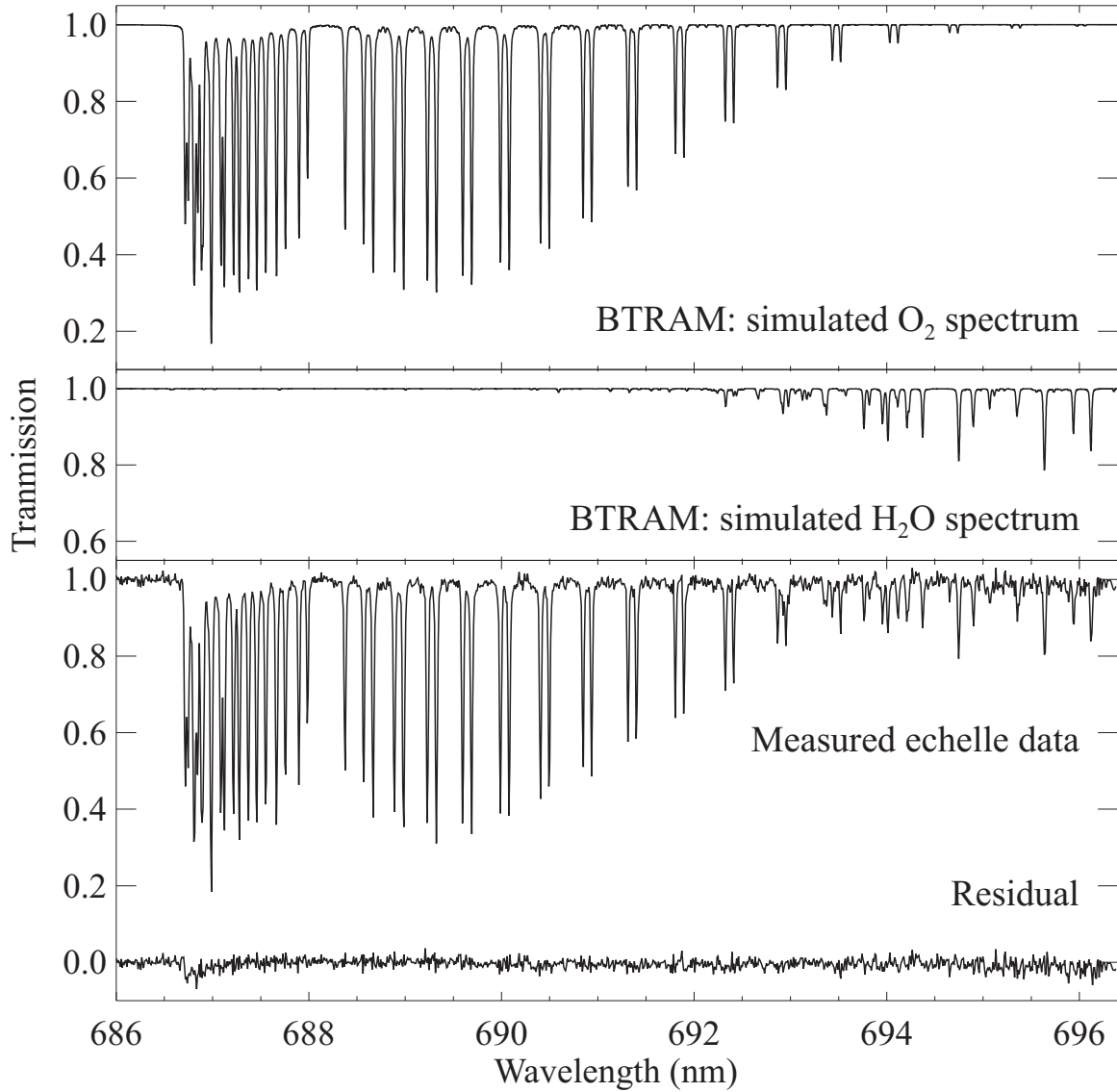


**Figure 8.4:** Simulated water and oxygen lines as compared to echelle measured data. The top two curves are the simulated spectra of water vapour and oxygen, respectively. The third curve is normalised echelle data from the MIKE instrument. The bottom curve is the residual after removing all the water lines and oxygen lines from the echelle data. All curves are shown to the same scale. The process works well except for saturated regions where it is difficult for the fitting algorithm to determine the continuum.



## 8.5. FITTING SPECTRAL DATA - ABSORPTION

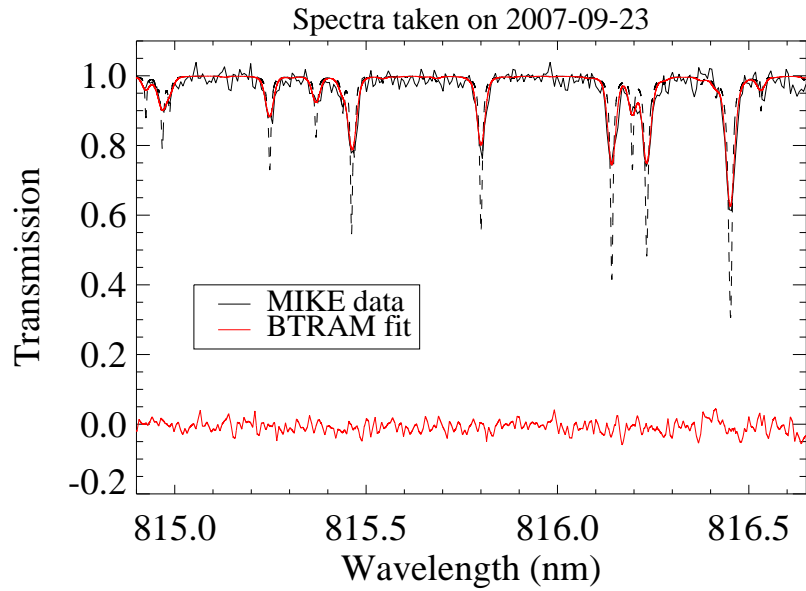


**Figure 8.5:** Raw MIKE data (black), simulated BTRAM spectra (dashed), and best fit Gaussian instrumental lineshape convolved BTRAM spectra (red) for several water vapour lines. The residual is shown to the same scale.

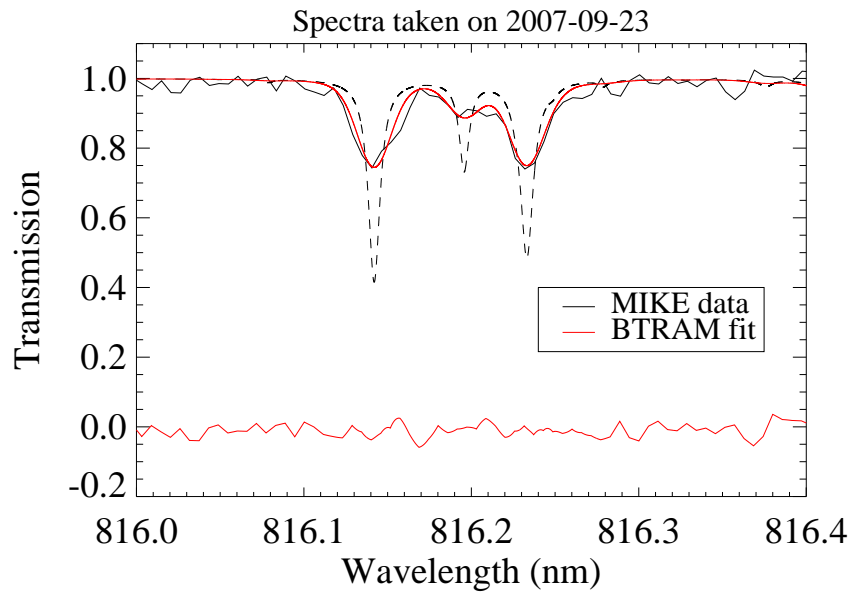


**Figure 8.6:** Raw MIKE data (black), simulated BTRAM spectra (dashed), and best fit Gaussian instrumental lineshape convolved BTRAM spectra (red) for three water vapour lines. The residual is shown to the same scale.

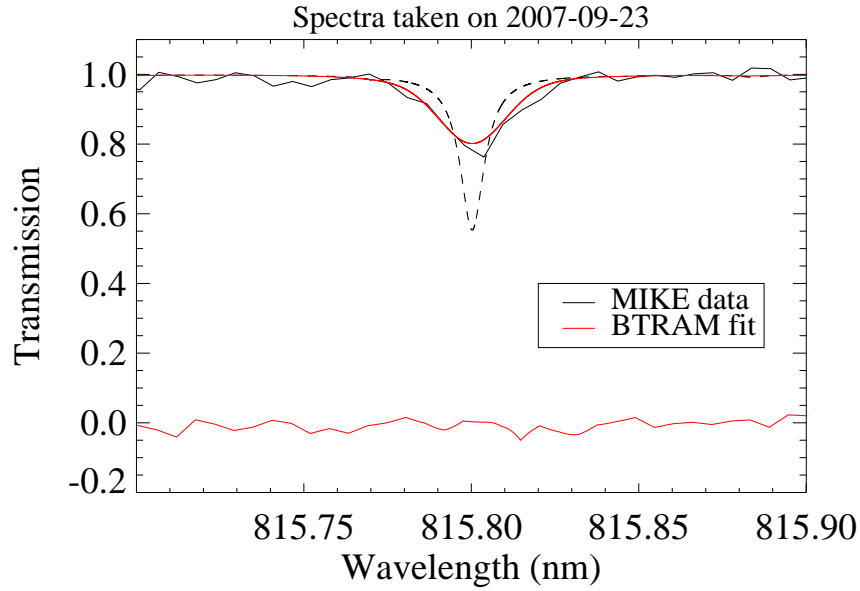


**Figure 8.7:** Raw MIKE data (black), simulated BTRAM spectra (dashed), and best fit Gaussian instrumental lineshape convolved BTRAM spectra (red) for a single water vapour line. The residual is shown to the same scale.

seen to be excellent agreement across the complex manifold of water vapour lines observed by MIKE. It can also be seen that the signal to noise in the 700 nm band is superior to that observed in the 800 nm band. Instrumental artifacts become apparent in the 900 nm band, making removal of the continuum more challenging. For this reason derivation of water vapour using the 900 nm band has not been included in the current analysis.

A comparison of the analysis of the MIKE data using the simple, single layer atmospheric model and the more complex BTRAM atmospheric model is shown in Figure 8.10. PWV values derived by fitting BTRAM are plotted for 5 spectral windows: 715–725, 725–730, 813–821, 822–824 and 830–838 nm. The MIKE derived PWV, using the equivalent width method described in Section 8.4, is limited to the analysis of at most 15 weak and isolated lines. By comparison the BTRAM derived PWV is the result of fitting both strong

## 8.5. FITTING SPECTRAL DATA - ABSORPTION

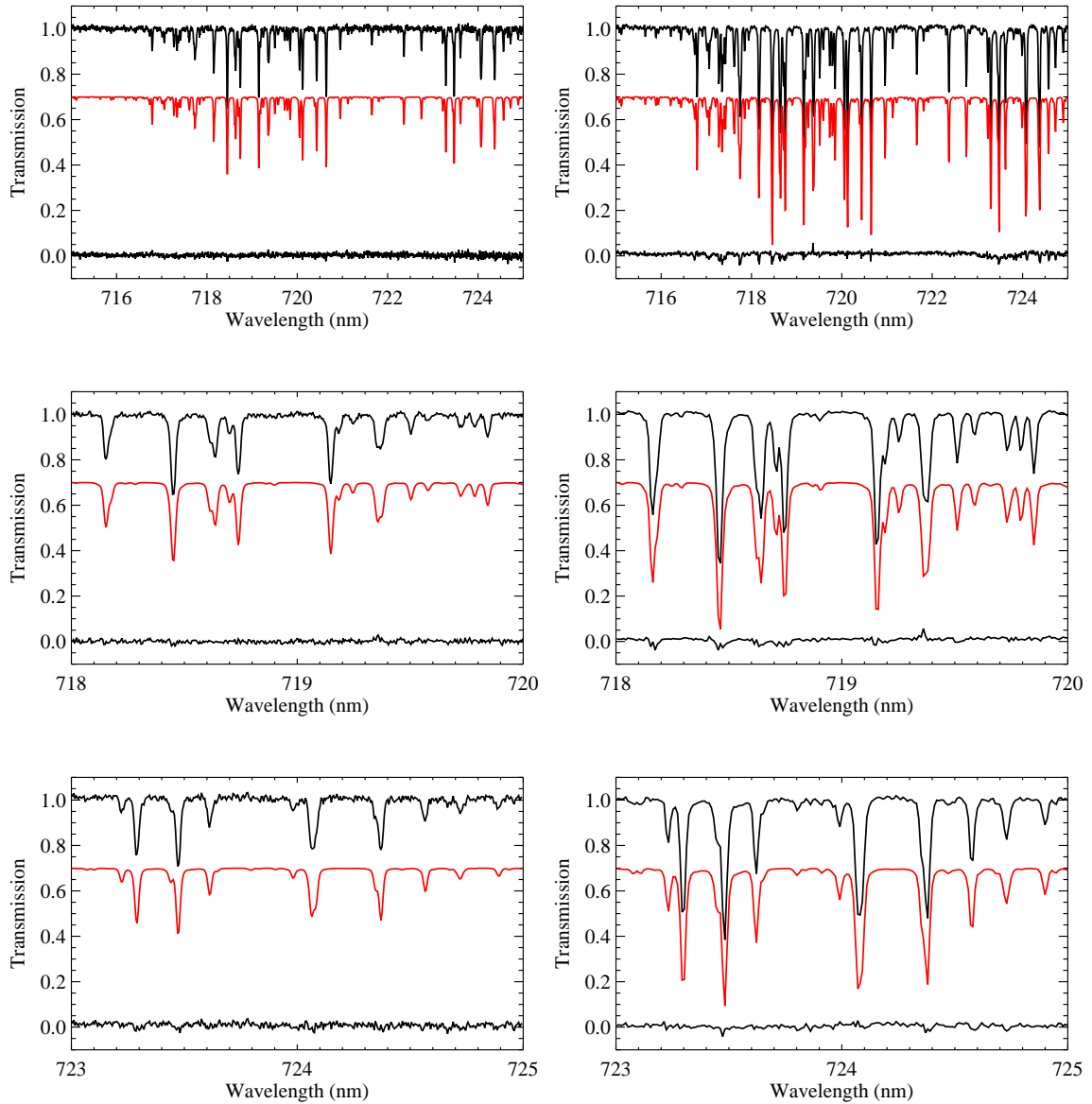


**Figure 8.8:** Transmission plots of MIKE data and the corresponding fitted BTRAM data over the 700 nm region for a dry night (PWV  $\sim 1.5$  mm), left column, and a wet night (PWV  $\sim 4.8$  mm), right column. The upper trace is the MIKE data, the middle trace is the fitted BTRAM data displaced for clarity, and the bottom trace shows the residual difference between the MIKE and BTRAM data.

## 8.5. FITTING SPECTRAL DATA - ABSORPTION

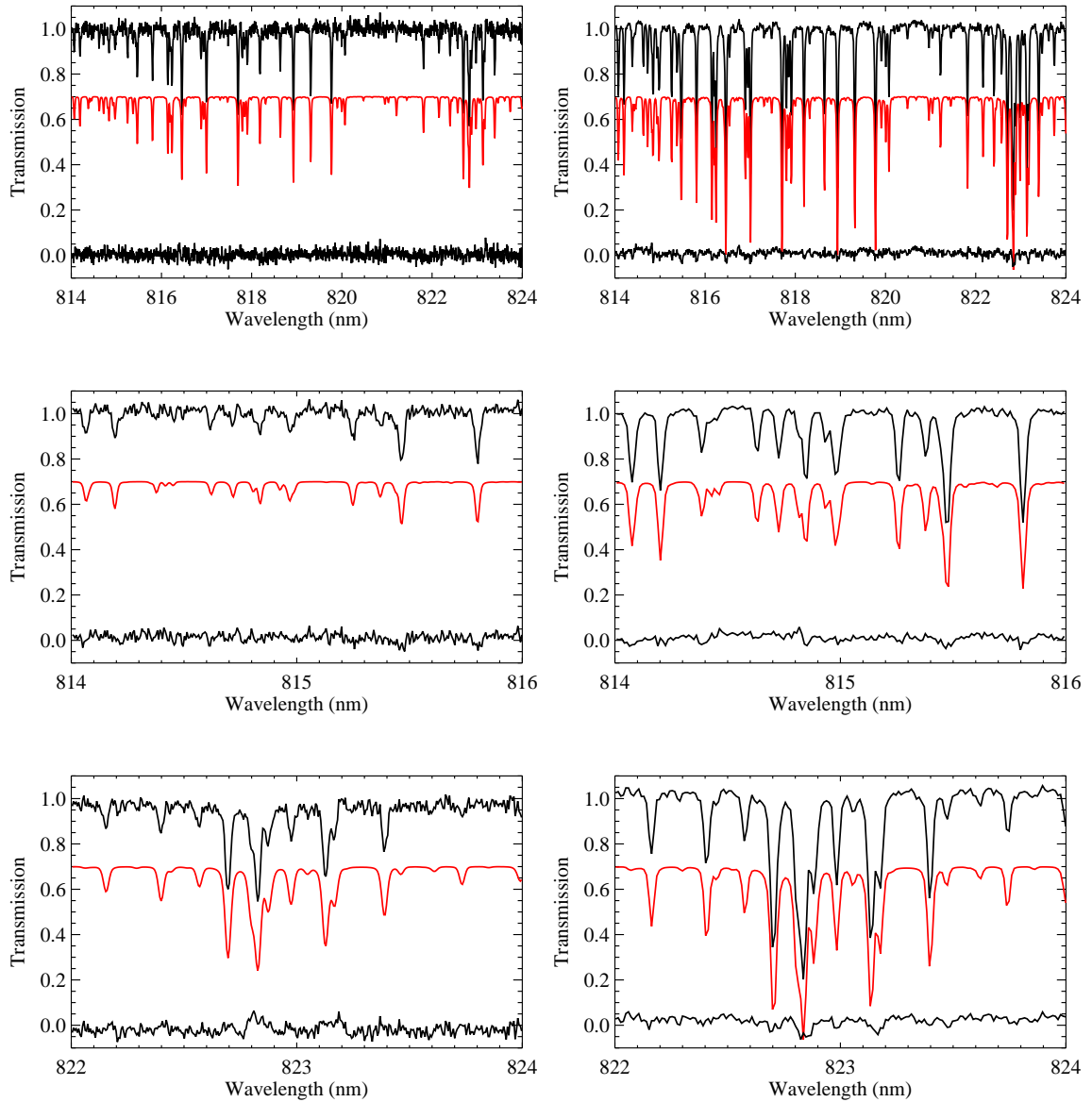


**Figure 8.9:** Transmission plots of MIKE data and the corresponding fitted BTRAM data over the 800 nm region for a dry night (PWV ~ 1.5 mm), left column, and wet night (PWV ~ 4.8 mm), right column. The upper trace is the MIKE data, the middle trace is the fitted BTRAM data displaced for clarity, and the bottom trace shows the residual difference between the MIKE and BTRAM data.

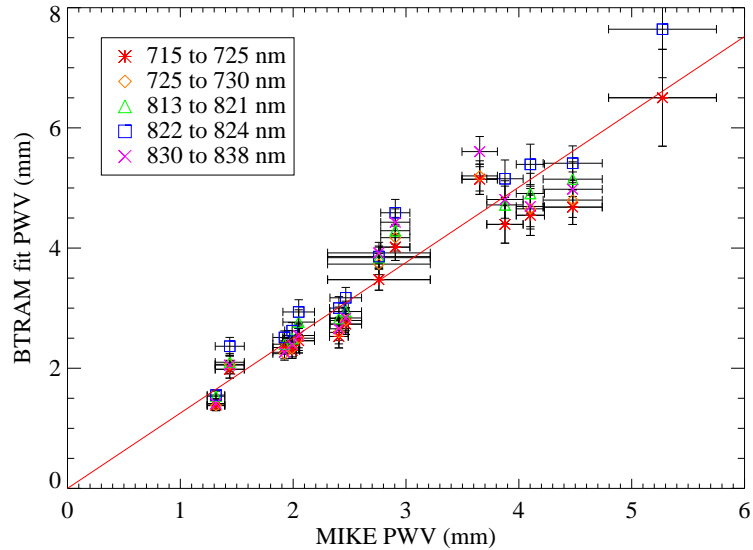


**Figure 8.10:** Equivalent width MIKE PWV versus BTRAM fitted PWV for the Las Campanas Observatory site. 5 wavelength ranges (715–725, 725–730, 813–821, 822–824 and 830–838 nm) have been fit. The best-fit slope to these data is 1.25. The error plotted on the equivalent width derived values is the standard deviation of PWV computed for a set of weak lines. The BTRAM fit derived PWV errors are the standard deviation of the fitted PWV values computed for each of the 5 spectral windows.

and weak lines, either isolated or blended, over a complex manifold which includes over 1100 lines. The derived PWV values from multi-line fitting yields wetter values than those derived from the simpler approach by a factor of  $1.253 \pm 0.063$ . In this analysis we have weighted equally the data from the 700 and 800 nm regions, however the 800 nm region has lower signal-to-noise. As mentioned above, the discrepancy was due to the use of log-Flux in their simplified model. This has since been corrected in their processing algorithm [62].

### 8.5.1 Effect of varying resolution

In the data and analysis that will be presented in Chapters 9, 10, 11 and 12, I will be comparing several different instruments with widely varying resolutions (10,000 – 100,000). It is important to note that these differences in resolution do not affect the fitting

algorithm. Just as the equivalent width method results in a correct value due to the area of the absorption feature being conserved, the results of the fitting algorithm should be no different with varying resolution. Thus, no matter the shape of a single absorption line, whether deep and narrow, or shallow and wide, if the absorption cross-section is of equal area, the extracted PWV will remain constant. For example, the Basic Echelle Spectrograph (BACHES) instrument, which operated at  $R \sim 15,000$ , would measure very broad features, while the Ultraviolet and Visual Echelle Spectrograph (UVES), a higher resolution instrument with  $R > 40,000$ , could resolve the absorption lines. An important step in the algorithm is the Gaussian convolution of the simulated spectrum, used to approximate the ILS, to better match the measured data. A convolution with a normalised function will not change the area of the absorption feature, and this is critical, as it relates back to equivalent width.

To further test this notion, while observing with UVES under conditions of stable seeing, the slit-width was set to 0.3, 0.5, 1.0, 2.0, 5.0 and 10.0 arcseconds over a one hour period with measurements taken every 1–2 minutes. Figure 8.11 shows the results of this experiment. Fitted PWV did not change dramatically while the effective resolution of the input spectra was varied. Also plotted are the airmasses of the two stars observed during this period, HR 5987 and HR 6141.

### **8.6 Fitting spectral data - Emission**

The signal being measured in an emission spectrum is primarily due to the atmosphere, although some contribution from the instrument is also to be expected. The

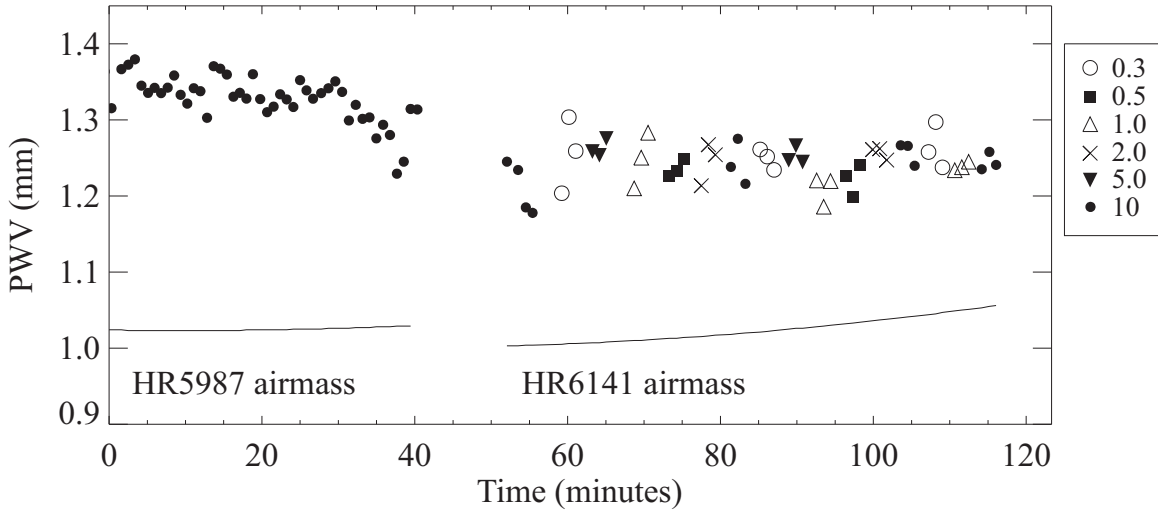


**Figure 8.11:** Fitted PWV values for measurements made under stable seeing conditions with a varying slit width. The legend values denotes slit width. Also plotted are the stars being observed and their respective airmasses.

primary difference between fitting to an absorption spectrum and an emission spectrum is that the continuum is not as well-defined. The base-line continuum in an emission spectrum cannot be assumed to mean zero emission. This fact makes the fitting process less robust than in the transmission case. A flow-chart of the algorithm is shown in Figure 8.12.

The iterative fitting process in the case of an emission spectrum is as follows: ingest a spectrum, read the header, determine the wavelength range and interval, and normalise the vertical scale (emission). Next a fitting is performed to a series of pre-processed simulated spectra ranging from 0 – 20 mm PWV (or a realistic maximal PWV specific to the observing environment). Perform a least squares fit between the measured emission spectrum and the first of the set of simulated emission spectra, with the following free fitting parameters being applied to the simulated spectrum: halfwidth of a Gaussian function, gain and offset. Store the  $\chi^2$  of the residual and the fit parameters for that simulated spectrum. Repeat the process for the next simulated spectrum, and continue through the entire set of spectra.

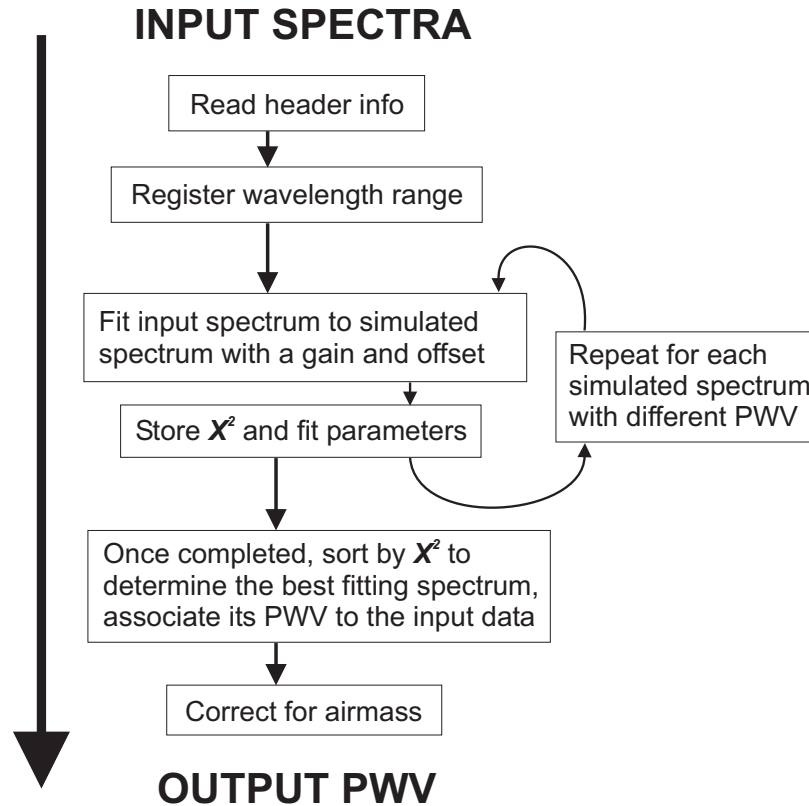


Figure 8.12: Algorithm for fitting a simulated spectrum to emission spectra.

Once completed, sort the list of simulated spectra by their *goodness of fit*,  $\chi^2$  parameter. This list then defines which simulated spectrum best represents the measured spectrum, and the PWV that was used to create said spectrum can be applied to the measured spectrum with some confidence. Associating errors from such a method is a challenging problem. One cannot simply extract a physically meaningful uncertainty in PWV from the statistical  $\chi^2$  value, although it might be possible to estimate a range.

The Cryogenic high-resolution InfraRed Echelle Spectrograph (CRIRES) [64] and the VLT Imager and Spectrometer for mid Infrared (VISIR) [65] are infrared facility instruments at Paranal. Periodically, short integration measurements of atmospheric emission are



## 8.6. FITTING SPECTRAL DATA - EMISSION

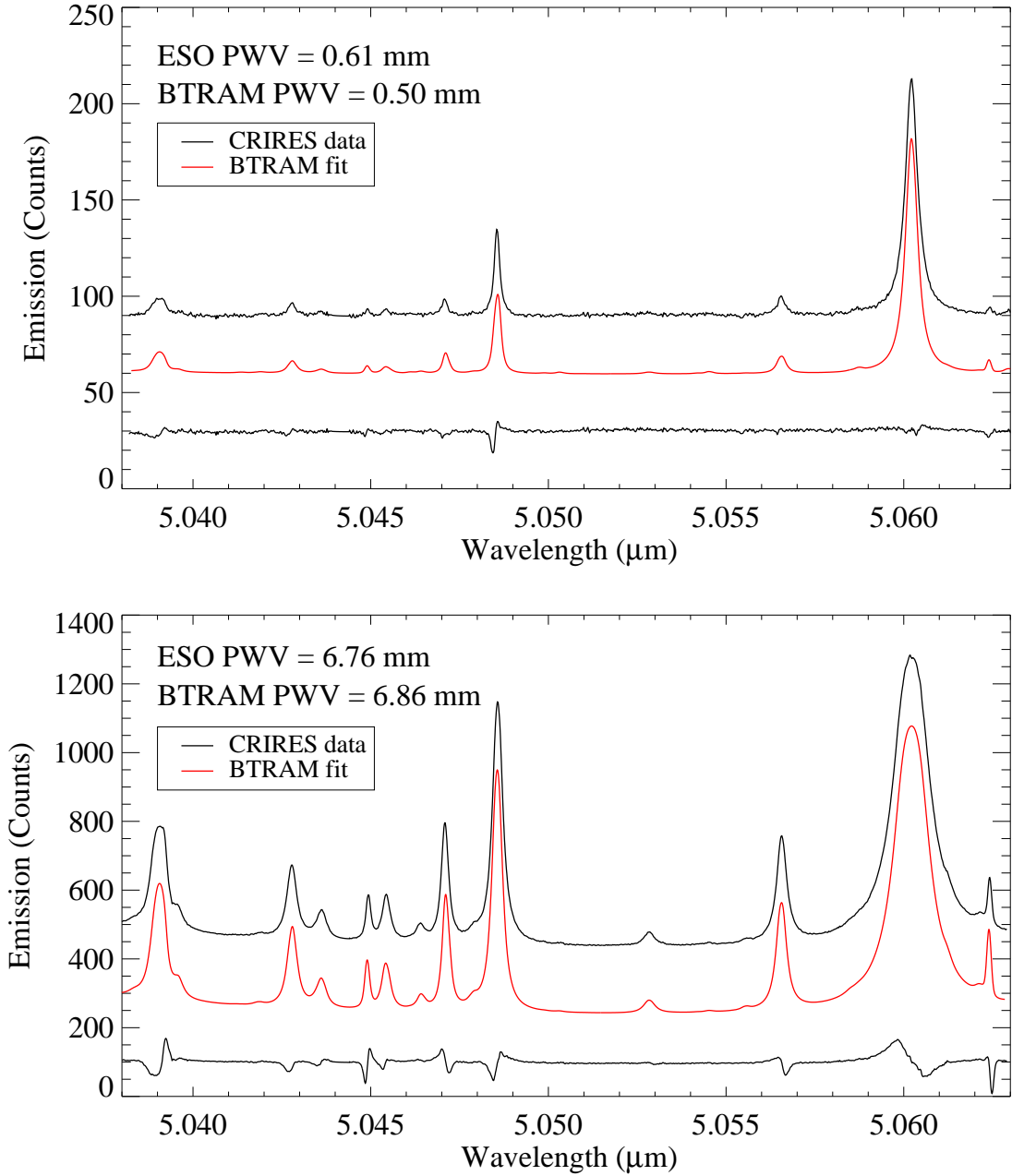


**Figure 8.13:** CRIRES data fitted with a simulated emission spectrum. The CRIRES data (black), the BTRAM fitted model (red) and a residual are all plotted to the same scale. The upper plot is a dry night (PWV  $\approx$  0.5 mm), and the lower plot is a wet night (PWV  $\approx$  6.8 mm). The model and residual have been offset for clarity.

## 8.6. FITTING SPECTRAL DATA - EMISSION

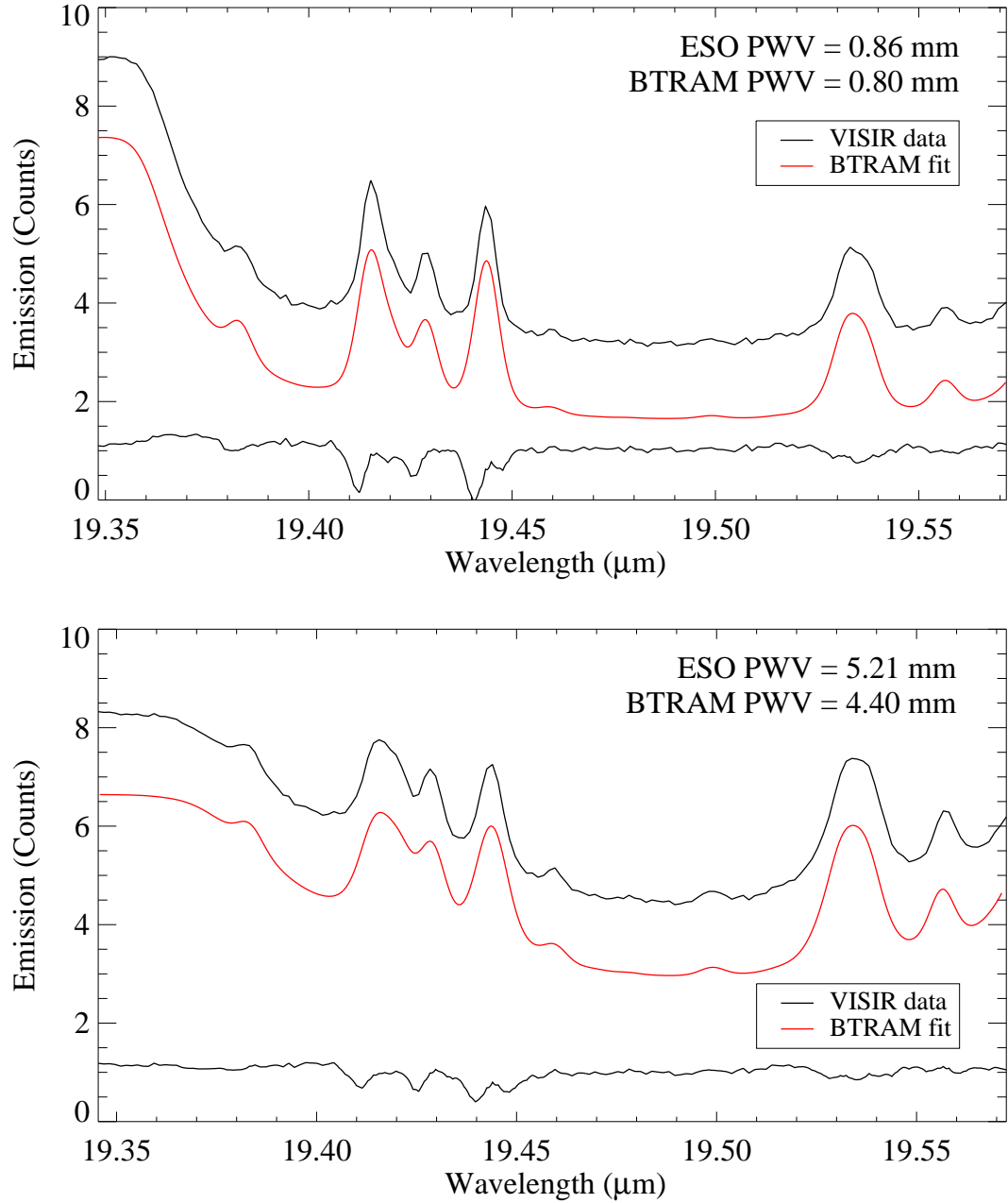


**Figure 8.14:** VISIR data fitted with a simulated emission spectrum. The VISIR data (black), the BTRAM fitted model (red) and a residual are all plotted to the same scale. The upper plot is a dry night (PWV  $\approx$  0.8 mm), and the lower plot is a wet night (PWV  $\approx$  4.4 mm). The model and residual have been offset for clarity.

## 8.7. CONCLUSION

---

performed while these instruments are active and the telescopes are parked at zenith (and no other significant infrared radiating objects are in the line-of-sight). I was provided with emission spectra from CRIRES and VISIR to attempt to extract PWV using our BTRAM model. The CRIRES spectra cover the wavelength range 5.038–5.063  $\mu\text{m}$ , while the VISIR spectra are from 19.35–19.57  $\mu\text{m}$ . Figure 8.13 shows a dry and wet measurement from CRIRES, and Figure 8.14 shows similarly fitted measurements from VISIR. Both sets of plots show the raw measurement (black), the fitted model (red) and a residual to the same scale. The model and residual have been offset for clarity. ESO has a pipeline that processes CRIRES and VISIR spectra to determine PWV<sup>5</sup> [66]. The ESO retrieval algorithm uses the RFM model and the Tropical atmospheric profile from FASCODE. The reported PWV values on Figures 8.13 and 8.14 are those determined by the ESO routine and the BTRAM algorithm, respectively. It is interesting to note that in our analysis of the campaign data, VISIR routinely reported wetter PWV by  $\sim 20\%$ . This may be in part due to their model/profile combination, since BTRAM derived PWV estimates from VISIR were systematically lower by approximately 10%.

### 8.7 Conclusion

It has been demonstrated through an exhaustive analysis of over 1000 water vapour lines in visible and near-infrared spectrograph measurements that it is possible to determine the column abundance of atmospheric water vapour to high precision. When comparing different methods and instruments it is advantageous to use the same atmospheric model in the retrieval process. In this case, the atmospheric model developed by our group, BTRAM,

---

<sup>5</sup>ESO: PWV measurements, <http://www.eso.org/sci/facilities/paranal/sciops/CALISTA/pwv/data.html>

## 8.7. CONCLUSION

---

served as the common model.

A strong correlation was found between the water vapour lines present in the MIKE data and the simulated water vapour spectrum produced with BTRAM. In a previous study of 14 nights of MIKE data it has been shown that PWV derived from the data using the single layer model and equivalent width method underestimates the water vapour abundance by  $\sim 25\%$  when compared to that derived using the multi-layer, multi-line BTRAM fitting approach. This has recently been identified as a problem inherent to using log-Flux for semi-saturated lines [62].

Since this study was undertaken, the process has been streamlined and applied to thousands of re-processed spectra from the ESO archive. In the context of site testing work for the E-ELT, I processed calibration standard star measurements from the Fiber-fed Extended Range Optical Spectrograph (FEROS) [67] ( $\sim 1700$  spectra spanning 4 years; 5 GB of data) and UVES [68] ( $\sim 1500$  spectra spanning 7 years, 600 MB of data) to extract PWV and create a historical record above the La Silla and Paranal observatory sites. All of these spectra were processed in a matter of hours on a standard desktop PC. These historical data and the resulting trends are presented in Chapter 9.

---

## Chapter 9

# History of PWV over La Silla

# Paranal Observatory from ESO

# Archival Data

In this chapter I describe the historical analysis of ESO archival data to extract PWV from routine echelle spectrograph calibration measurements of standard stars. I performed the fits to all of the echelle spectra using BTRAM and the algorithm described in Chapter 8. The extracted PWV were compared to the PWV estimated using satellite data from the Envisat-MERIS [46] instrument and the Imager on the GOES spacecraft. These data were processed and provided to us by Dr. Marc Sarazin (ESO). I present seasonal means of PWV over La Silla and Paranal and a comparison of the satellite estimates versus the PWV values determined from the echelle fits.

## 9.1 Introduction

In the interest of creating a historical data set of the PWV over the La Silla Paranal Observatory, several years of high resolution archival spectra were processed using the spectral fitting approach described in Chapter 8.

In the method, many lines covering several atmospheric bands can be used simultaneously to achieve a global fit between a measured high-resolution spectrum and a simulated manifold of water vapour lines.

As a precursor to the full analysis, I was provided with a small set (<50) of echelle spectra in order to show that the echelle fitting method could indeed be used to analyse the full archival set of calibration star measurements. After successfully demonstrating the fitting method, colleagues at ESO, namely Drs. Lo Curto and Hanuschik, sifted through the archive to extract the flux standard calibration observations for the FEROS [67] (at La Silla) and UVES [68] (at Paranal) high-resolution spectrographs. These archival data were specifically reprocessed to provide the fitting algorithm with a homogeneous set of spectra using validated master calibration files<sup>1</sup>.

To study the seasonal variations of PWV over the La Silla site, I analysed ~1700 FEROS flux standard calibration observations covering the period from 2005–2009. For the Paranal site, I analysed ~1500 UVES spectra covering the period from 2001–2008. Figures 9.1 and 9.2 show examples of these fitting results for UVES and FEROS, for dry and wet conditions. These flux standard spectra of white dwarves have nearly flat and featureless stellar continua making them particularly well suited for this study. The standard star ob-

---

<sup>1</sup>The UVES reprocessed data set: <http://www.eso.org/observing/dfo/quality/reproUVES/processing.html>

servations are performed at a relatively high spectral resolution ( $R \sim 40,000$ ). The number of useable spectra from both instruments could be increased by including science observations as well, however, stellar features represent a significant complication to the extraction of PWV values. Analysis of science data would require the careful selection of targets, for example only stars with temperatures  $>10,000$  K, to minimise the number of photospheric lines; thus we limited our sample to observations of calibration standard stars.

For the analysis with BTRAM, a mid-latitude profile modified with site-specific archival radiosonde data from Antofagasta has been employed. Since the distribution of water vapour is highly time dependent this profile represents a median distribution. It is expected that the median is more applicable to Paranal, which is located  $\sim 110$  km from Antofagasta, while less representative for La Silla, which is  $\sim 625$  km distant. In all cases the distribution of water vapour, usually expressed in terms of a scale height, is the dominant source of uncertainty.

### 9.1.1 Verification of satellite data

The FEROS and UVES flux standard star archival data sets are essential in establishing a statistical relationship between the ground-based data and the satellite data taken with the imager on the geostationary GOES satellite and the MERIS spectrometer onboard the sun-synchronous Envisat, situated in a low Earth orbit. Calibration and validation of space-borne instruments is usually achieved using ground based observations, the goal being to render the satellite data more accurate by characterising systematic effects between instruments and techniques.

As is shown in the next two sections, despite the large difference in spatial and

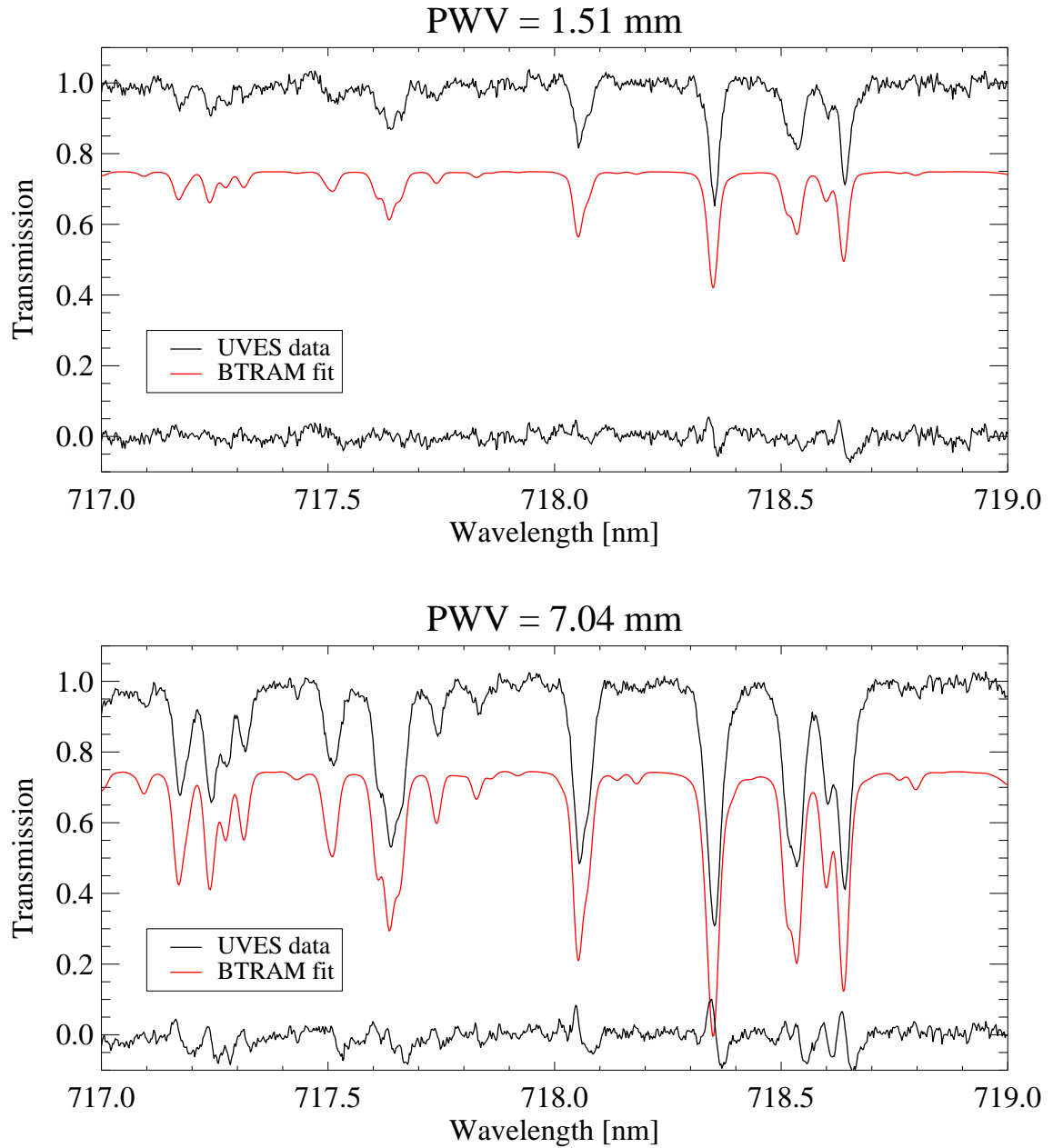


**Figure 9.1:** Sample fit of the PWV model to UVES archival data. Every line present in this spectrum is due to water vapour. Observations of a standard star during a night with lower PWV (2003-07-26) and a night with high PWV (2003-02-19). The model spectrum has been shifted downwards for clarity. The line centres in the model have been shifted to match those of the measurement. The bottom trace shows the residual to the same scale. The uncertainty in the PWV retrieved from the fit is estimated at 10–20%.



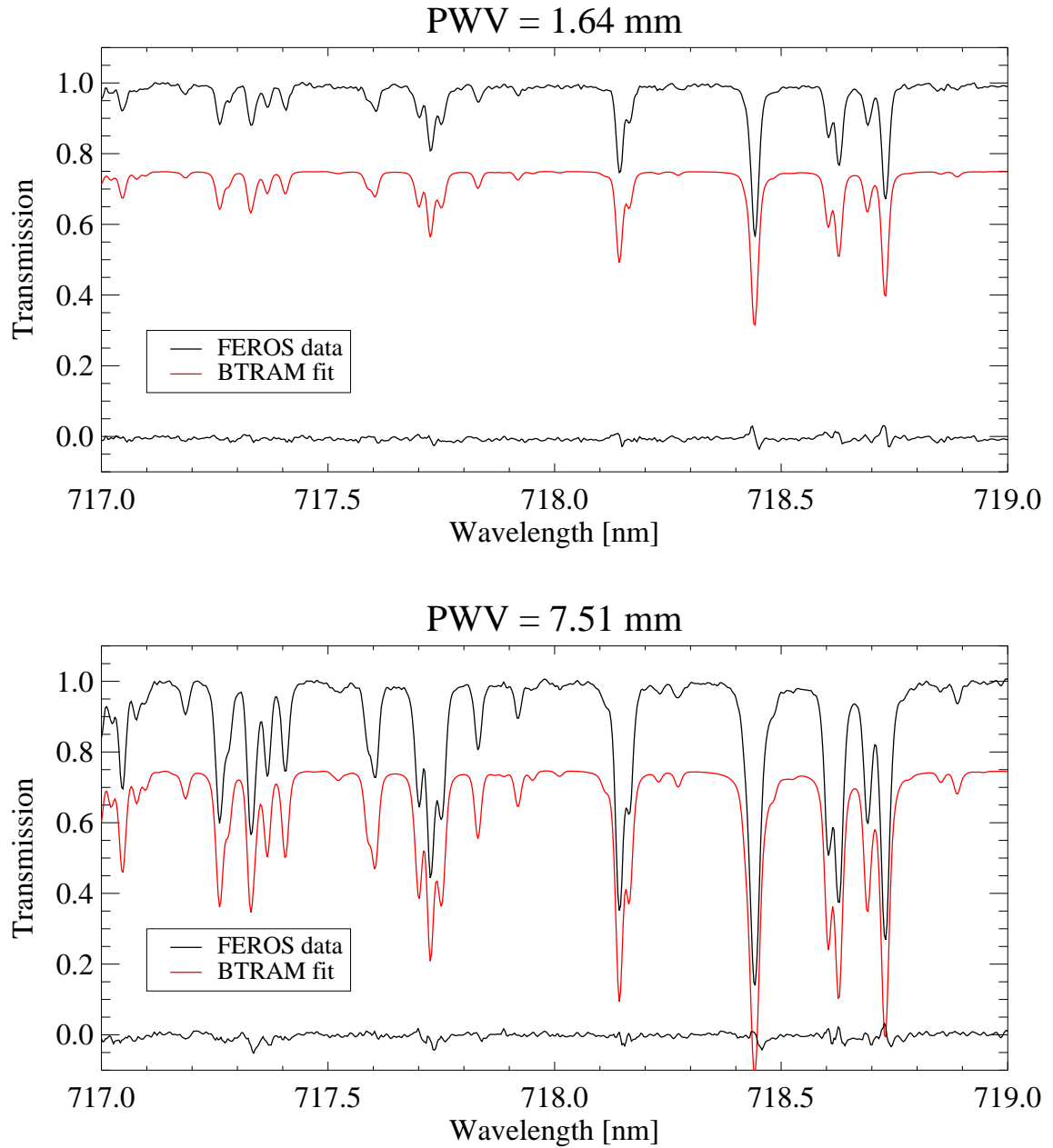


**Figure 9.2:** Sample fit of the PWV model to FEROS archival data. Every line present in this spectrum is due to water vapour. Observation of a standard star during a night with lower PWV (2005-10-13) and a night with high PWV (2005-10-20). The model spectrum has been shifted downwards for clarity. The line centres in the model have been shifted to match those of the measurement. The bottom trace shows the residual to the same scale. The uncertainty in the PWV retrieved from the fit is estimated at 10–20%.

temporal resolution, there is general agreement between the water vapour derived by the two satellites [45]. However, as discussed in Chapter 7, it should be noted that there is an approximate factor of 100 reduction between the GOES footprint and the MERIS footprint, and another factor of 18,000 reduction between the MERIS footprint and the collection area of a typical 10 m telescope. This overall factor of 1.8 million between the area sampled by GOES and the area observed by a telescope illustrates the challenge in comparing their retrieved PWV values. The larger areas will necessarily include regions around the observatories. Since these regions are low-lying and wetter, their retrievals will tend to be biased to higher PWV values. Notwithstanding this limitation, the FEROS and UVES archival data provide ideal data sets to compare ground and space-based measurements.

### **9.2 Results from the archive: La Silla**

When comparing the PWV values derived from the FEROS archival spectra and the satellite data one has to keep in mind that these approaches are different in a number of important aspects. In the ground-based case, the observations sample a very small volume of the atmosphere – a single line-of-sight towards a star. The satellite-borne instrument is nadir-viewing, recording an average of the PWV over its field-of-view, representing many square kilometres which may contain lakes, fields, roads, etc. Also, the ground-based telescopes benefit from using a well-defined stellar continuum as a background source, while the satellites rely on sunlight reflected by the Earth (MERIS) or emission from the atmosphere (GOES). FEROS and MERIS determine PWV from absorption lines in the near-IR (0.7 – 1.0  $\mu\text{m}$ ), while GOES measures brightnesses in the thermal IR (water vapour emission

at 6.5  $\mu\text{m}$  and an IR window at 10.7  $\mu\text{m}$ ). Regardless of the methodology used, in all cases a model of the Earth's atmosphere (which includes pressure, temperature and density profiles) is required to derive PWV.

In an attempt to quantify these qualitative time-series plots I have created correlation plots between GOES and MERIS and GOES and UVES/FEROS (for Paranal and La Silla, respectively). No plot comparing MERIS with UVES/FEROS is possible as MERIS measurements are exclusively performed during daytime. Since it is impossible to control when the satellite measurements were made, the only option is to allow for a reasonable window when the measurements will overlap and then compare those values. Figures 9.3 and 9.4 show the correlation between GOES:MERIS and GOES:FEROS, respectively, for time windows of GOES  $\pm$  0.5 hours, 1.0 hours, 1.5 hours and 2.0 hours. While there is some qualitative agreement as seen in the time-series figures, there is little quantitative agreement as should be expected from the asynchronous measurements over differing footprints. The coefficient of determination ( $R^2$ ) is reported on each correlation figure. A value of  $R^2 = 1$  implies a fully linear relationship between the data points, while  $R^2 = 0$  would indicate no linear relationship. The correlation values of  $R^2 < 0.5$  for GOES:MERIS and  $R^2 < 0.25$  for GOES:FEROS show this relatively poor agreement. The GOES:MERIS plot shows that GOES has a wet bias, albeit to a lesser degree (this might be due to a comparison of daytime values with marginally higher PWV). The spread in both data sets show that the satellites seem to both over- and under-estimate PWV in roughly equal measure.

An example of the agreement between the FEROS, GOES and MERIS PWV derivations in the form of a time series diagram is given in Figure 9.5<sup>2</sup>. Expanded sections

---

<sup>2</sup>Times are plotted as Modified Julian days (MJD). The Julian date (JD) is the interval of time counted

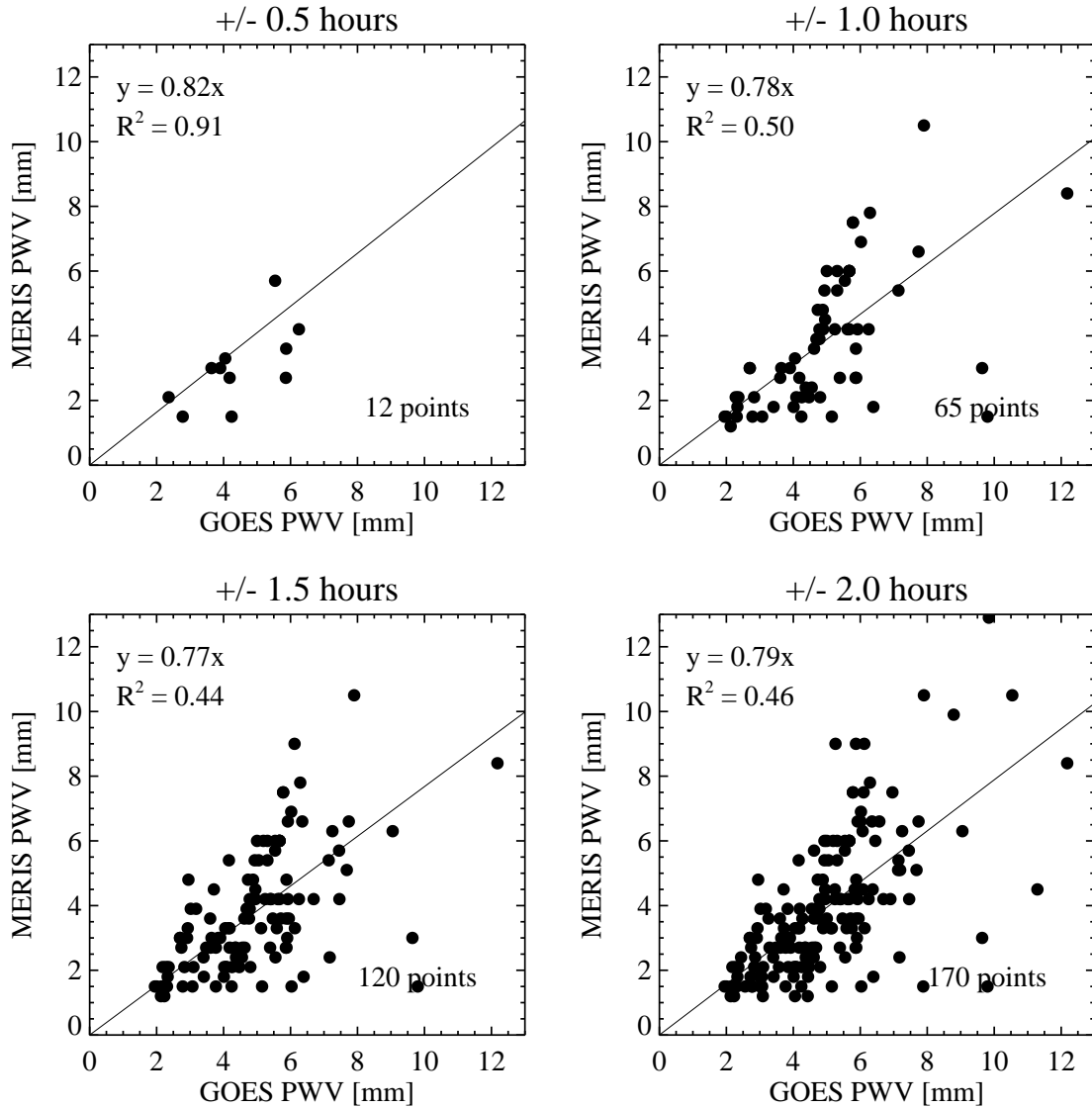


**Figure 9.3:** Comparison of the PWV data from GOES and MERIS over La Silla. To make the correlation possible, a window of comparison is necessary. The upper left plot shows the MERIS data that align with GOES measurement times  $\pm 0.5$  hours. The other plots depict a  $\pm 1.0$ ,  $\pm 1.5$  and  $\pm 2.0$  hour window. The number of data points used in each plot is shown to the lower right. Uncertainties are not plotted but have been included in the analysis.

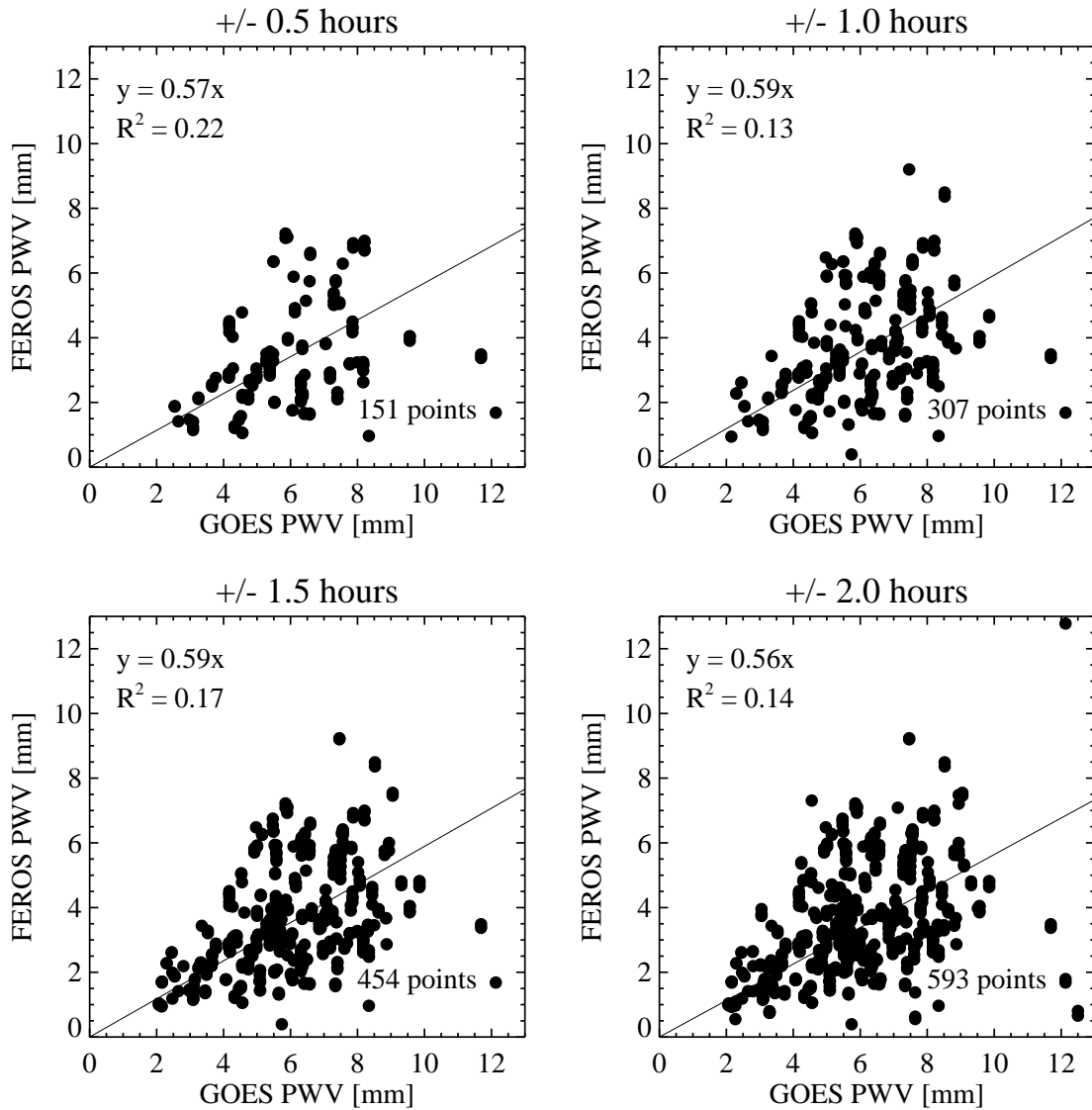


**Figure 9.4:** Comparison of the PWV data from GOES and FEROS over La Silla. To make the correlation possible, a window of comparison is necessary. The upper left plot shows the FEROS data that align with GOES measurement times  $\pm 0.5$  hours. The other plots depict a  $\pm 1.0$ ,  $\pm 1.5$  and  $\pm 2.0$  hour window. The number of data points used in each plot is shown to the lower right. Uncertainties are not plotted but have been included in the analysis.

## 9.2. RESULTS FROM THE ARCHIVE: LA SILLA

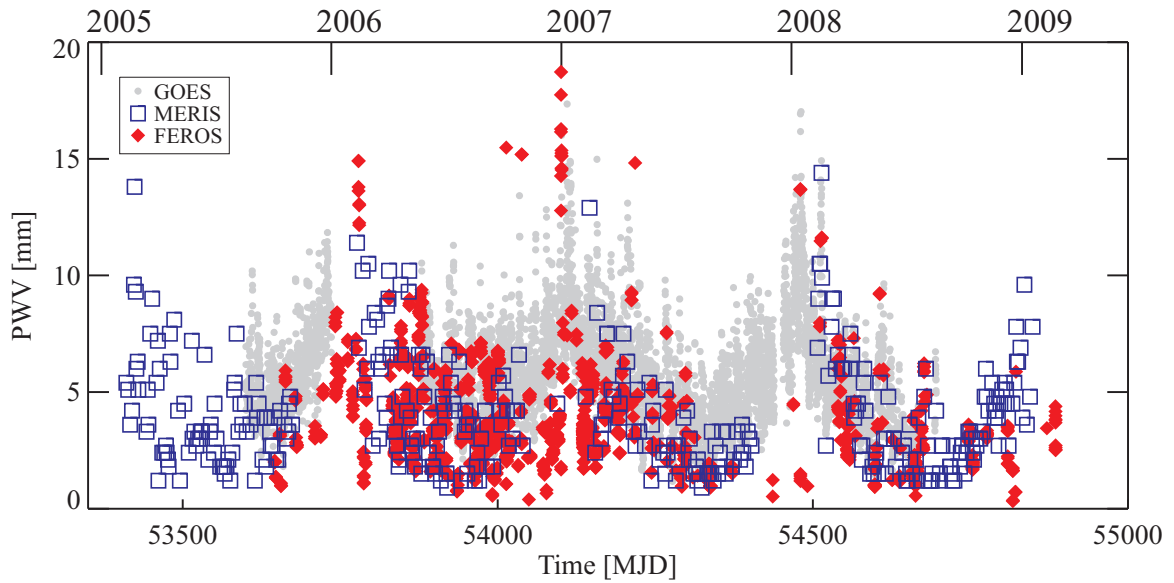


**Figure 9.5:** Comparison of PWV data derived from FEROS archival data and satellite data for the period 2005–2009. Pronounced seasonal variations are evident.

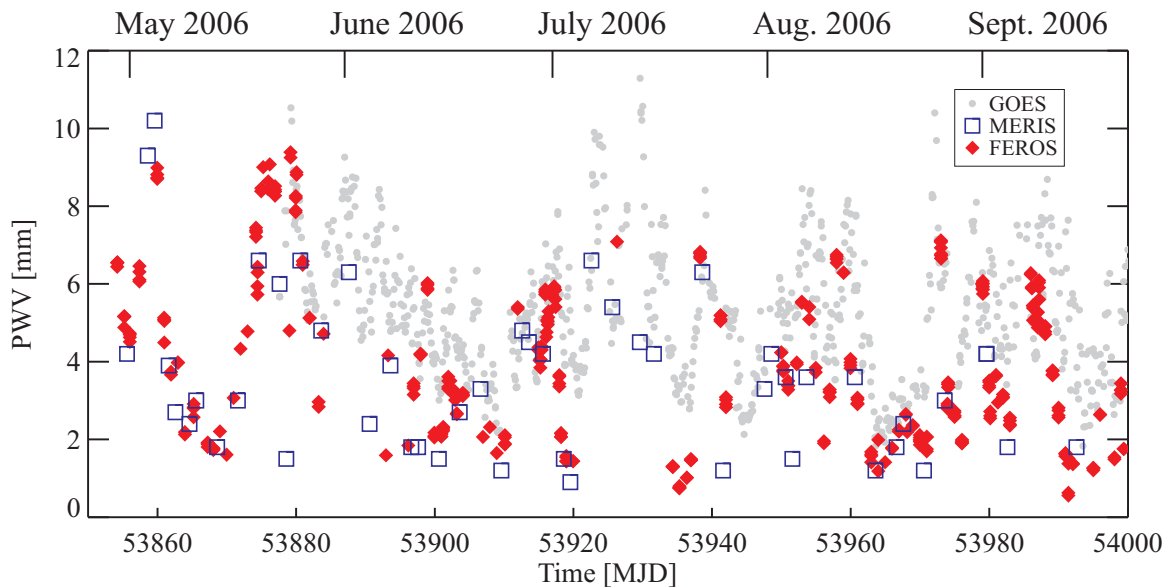


**Figure 9.6:** Comparison of PWV data derived from FEROS archival data and satellite data for May to September 2006.

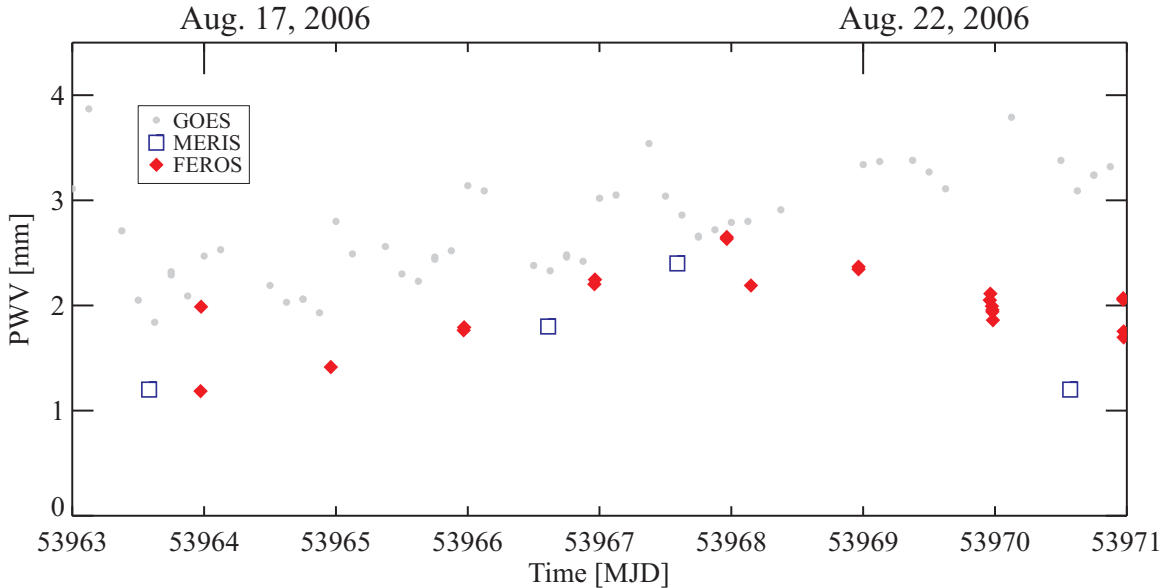


**Figure 9.7:** Comparison of PWV data derived from FEROS archival data and satellite data for August 2006.

of the archival time series are shown in Figures 9.6 and 9.7. A mean winter PWV value of  $3.2 \pm 1.8$  ( $3.9 \pm 2.4$  mm year-long mean) has been derived for La Silla from the FEROS data. These values are similar to those reported by Thomas-Osip *et al.* at nearby Las Campanas observatory [62]. GOES-imager retrieved PWV are consistently higher than those derived from the MERIS instrument. The primary reason for this difference most likely arises from the larger,  $12 \times 12$  km, spatial resolution of the GOES measurement which must include lower altitude and therefore wetter regions in the vicinity of the observatory site. This is reflected in the higher derived GOES estimates given in Table 9.1 and correspondingly, to the lower fraction of low PWV nights given in Table 9.2. The superior agreement between the MERIS and FEROS derived mean PWV is most likely due to the smaller footprint of

---

in days and fractions of days since January 1, 4713 BC Greenwich noon, in the Julian proleptic calendar. Midnight, January 1, 2010 is then expressed as JD 2455197.5. Introduced by the Smithsonian Astrophysical Observatory in 1957 to save space in limited computer memory,  $\text{MJD} = \text{JD} - 2400000.5$ , which shifts the epoch to midnight, November 17, 1858. Midnight, January 1, 2010 is MJD 55197.

### 9.3. RESULTS FROM THE ARCHIVE: PARANAL

**Table 9.1:** Mean PWV over La Silla derived from different methods. The overall mean as well as seasonal means are shown.

Instrument	Mean PWV $\pm$ Standard deviation [mm]				
	Winter	Spring	Summer	Fall	All
GOES-Imager	4.3 $\pm$ 1.7	5.8 $\pm$ 1.6	7.6 $\pm$ 2.3	5.1 $\pm$ 1.8	5.7 $\pm$ 2.2
MERIS	3.0 $\pm$ 1.4	4.0 $\pm$ 2.4	4.2 $\pm$ 2.4	3.5 $\pm$ 1.7	4.0 $\pm$ 2.3
FEROS	3.2 $\pm$ 1.8	3.3 $\pm$ 1.9	5.1 $\pm$ 3.3	4.1 $\pm$ 2.1	3.9 $\pm$ 2.4

**Table 9.2:** Number of nights within the 4-year time period (expressed as a percentage) when the PWV over La Silla was less than or equal to a given value.

Instrument	$\leq 1$ mm [%]	$\leq 1.5$ mm [%]	$\leq 2$ mm [%]
GOES-Imager	0.0	0.5	3.1
MERIS	0.8	11.2	17.2
FEROS	4.0	11.7	22.5

the MERIS observations.

### 9.3 Results from the archive: Paranal

A mean winter PWV value of  $1.9 \pm 1.3$  ( $2.7 \pm 2.2$  year-long mean) has been derived for Paranal from the UVES data, see Table 9.3. As with the La Silla mean PWV values, the relatively large standard deviations in the year-long values are primarily due to seasonal variations. While less pronounced at Paranal than for the lower, La Silla site, these variations are still present in the data. These seasonal variations are stable over the seven years of data analysed, with periods of high PWV occurring during the southern summer months when the site is partially affected by the *invierno altiplánico* (also known as the Bolivian Winter).



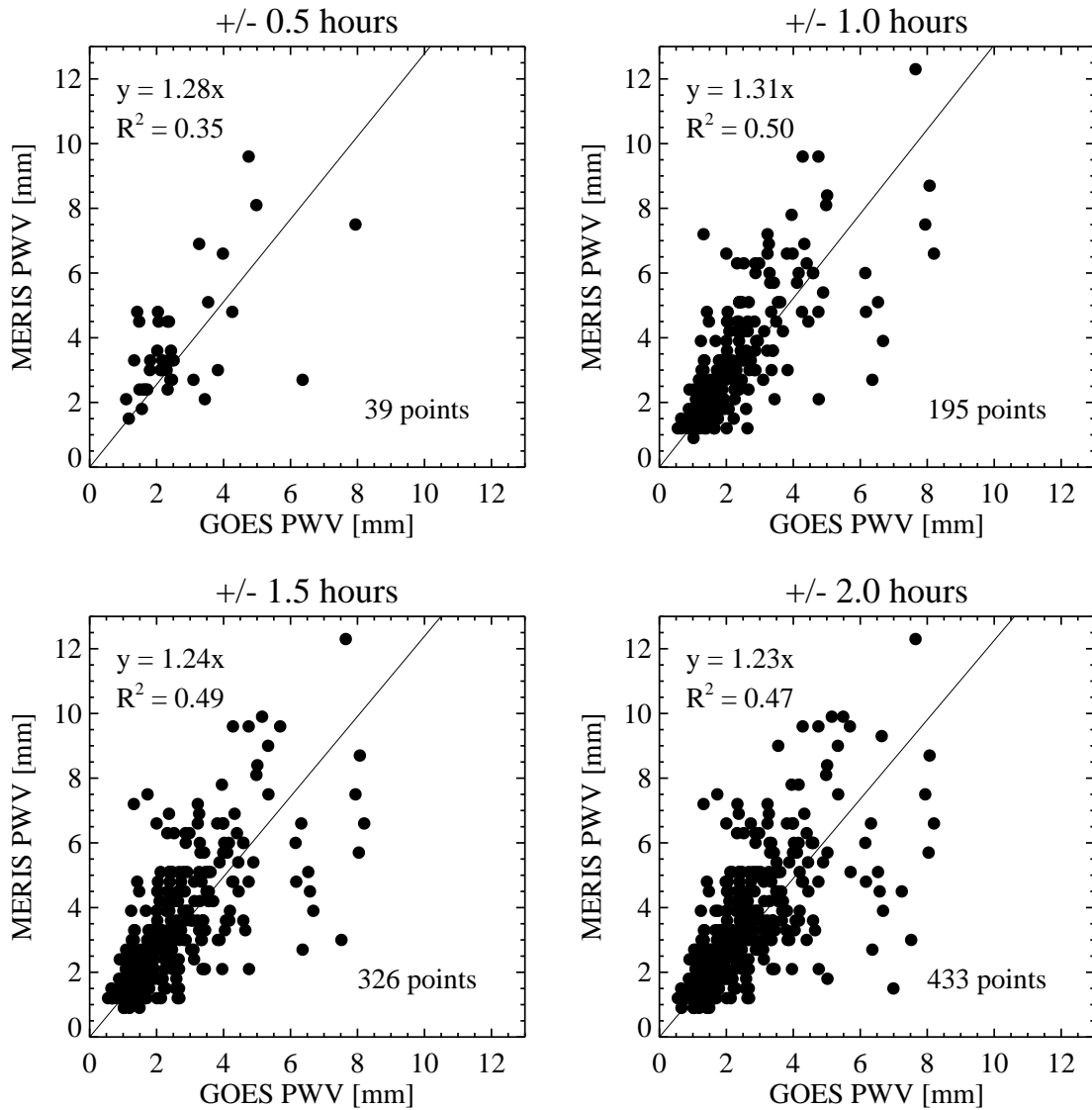


**Figure 9.8:** Comparison of the PWV data from GOES and MERIS over Paranál. To make the correlation possible, a window of comparison is necessary. The upper left plot shows the MERIS data that align with GOES measurement times  $\pm 0.5$  hours. The other plots depict a  $\pm 1.0$ ,  $\pm 1.5$  and  $\pm 2.0$  hour window. The number of data points used in each plot is shown to the lower right. Uncertainties are not plotted but have been included in the analysis.

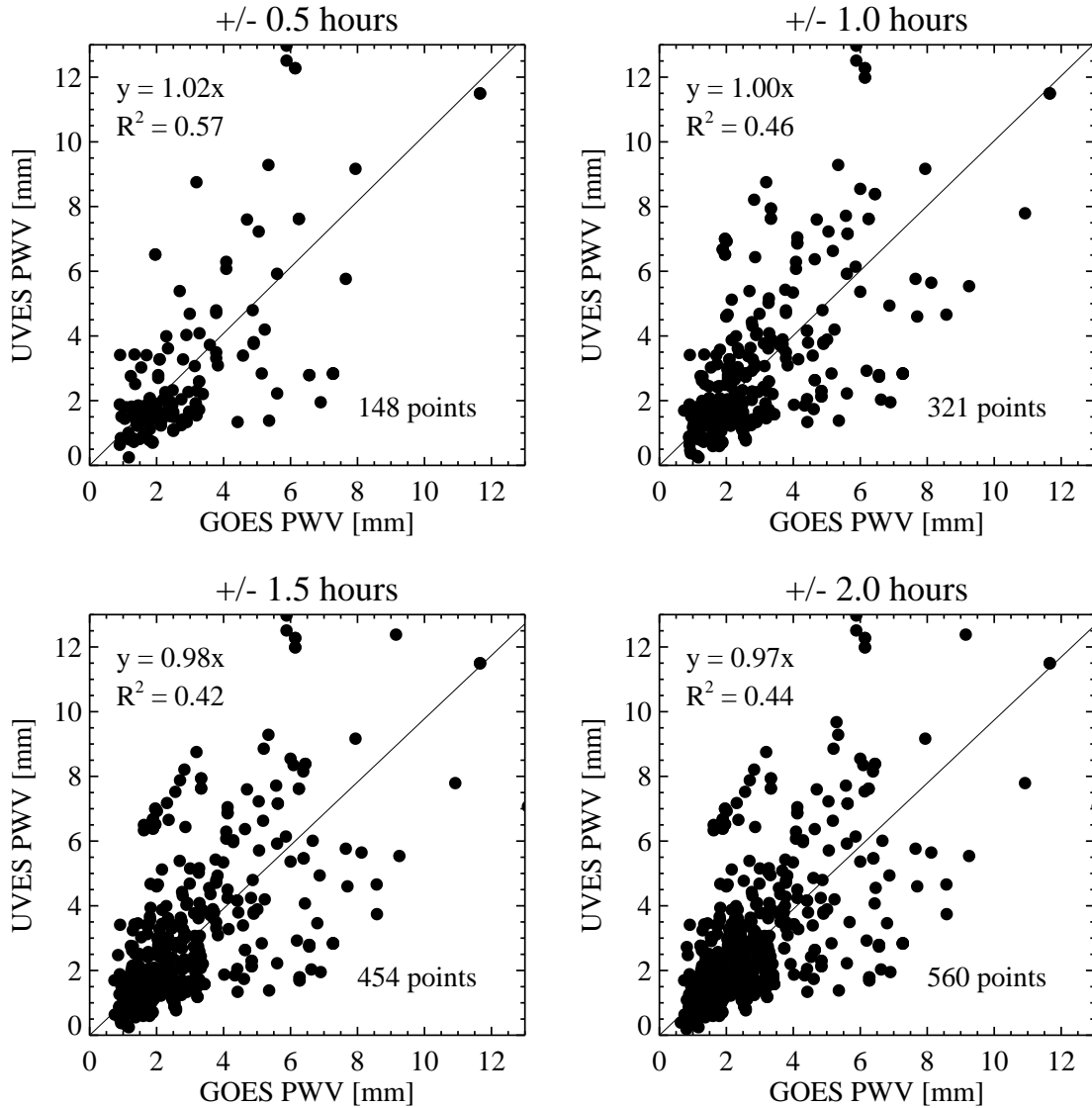


**Figure 9.9:** Comparison of the PWV data from GOES and UVES over Paranal. To make the correlation possible, a window of comparison is necessary. The upper left plot shows the UVES data that align with GOES measurement times  $\pm 0.5$  hours. The other plots depict a  $\pm 1.0$ ,  $\pm 1.5$  and  $\pm 2.0$  hour window. The number of data points used in each plot is shown to the lower right. Uncertainties are not plotted but have been included in the analysis.

As described in the La Silla section above, correlation plots between GOES and MERIS and GOES and UVES have been produced using the same procedures. Figures 9.8 and 9.9 show the correlation between GOES:MERIS and GOES:FEROS, respectively, for the same time windows described above. Again, while there is some qualitative agreement as seen in the time-series figures, there is little quantitative agreement as should be expected from the asynchronous measurements over differing footprints. The correlation values of  $R^2 < 0.5$  for GOES:MERIS and  $R^2 < 0.5$  for GOES:UVES show this relatively poor agreement. Unlike the La Silla data set, the Paranal GOES:MERIS plot shows that MERIS overestimates PWV by  $\sim 20\text{--}30\%$  under dry conditions. The GOES:UVES plot shows that GOES typically derived a higher PWV (i.e. has a wet bias). There is seen to be a wide spread in this correlation which illustrates that satellite measurements cannot be used to provide PWV for any one given night, but, due to the evenness of the spread, on average their data can provide a statistically representative picture of the PWV above a given site.

The UVES data is not fully representative of the conditions over Paranal due to a dry-bias in the measurements. Standard star observations are only performed under clear sky conditions. GOES data has a full-year mean of  $2.8 \pm 1.8$  mm, while MERIS data has a higher PWV of  $3.3 \pm 2.0$  mm. Given the significant differences in the measurement techniques employed in this analysis (transmission, emission; thermal, near-infrared) the agreement is remarkable. MERIS is seen to systematically overestimate PWV under dry conditions, leading to a wet bias in its mean value. It can be seen from Figures 9.10, 9.11, 9.12 and 9.13 that the GOES retrieved PWV are consistently higher than those derived from the MERIS instrument. The primary reason for this difference most likely arises from the

## 9.4. CONCLUSION

---

**Table 9.3:** Mean PWV over Paranal derived from different methods. The overall mean as well as seasonal means are shown.

Instrument	Mean PWV $\pm$ Standard deviation [mm]				
	Winter	Spring	Summer	Fall	All
GOES-Imager	2.1 $\pm$ 1.0	2.3 $\pm$ 1.1	4.3 $\pm$ 2.5	2.9 $\pm$ 1.5	2.8 $\pm$ 1.8
MERIS	2.4 $\pm$ 1.1	2.8 $\pm$ 1.4	5.1 $\pm$ 2.4	3.7 $\pm$ 2.0	3.3 $\pm$ 2.0
UVES	1.9 $\pm$ 1.3	2.2 $\pm$ 1.4	4.9 $\pm$ 3.4	2.7 $\pm$ 1.5	2.7 $\pm$ 2.2

**Table 9.4:** Number of nights within the 8-year time period (expressed as a percentage) when the PWV over Paranal was less than or equal to a given value.

Instrument	$\leq 1$ mm [%]	$\leq 1.5$ mm [%]	$\leq 2$ mm [%]
GOES-Imager	10.8	32.7	53.8
MERIS	1.4	16.8	27.4
UVES	13.3	31.5	46.9

larger,  $12 \times 12$  km, spatial resolution of the GOES measurement which must include lower altitude and therefore wetter regions in the vicinity of the observatory site. This is reflected in the higher derived GOES estimates given in Table 9.1. The superior agreement between the MERIS and UVES derived mean PWV values is most likely due to the smaller footprint of the MERIS observations.

### 9.4 Conclusion

This analysis demonstrates the legacy value and utility of archival data. The historical comparison to satellite data would not have been possible without a well-maintained and accessible repository of measurements.

Given the significant differences between ground and space-based measurement

#### 9.4. CONCLUSION

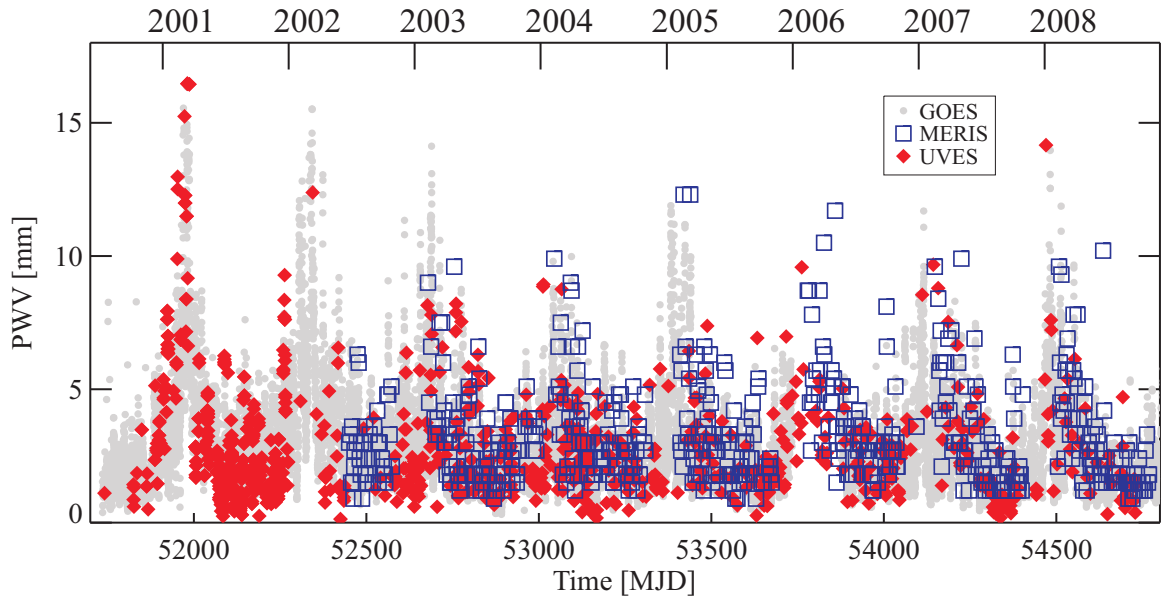


**Figure 9.10:** Comparison of PWV data derived from UVES archival data and satellite data for the period 2001–2008. Pronounced seasonal variations are evident.

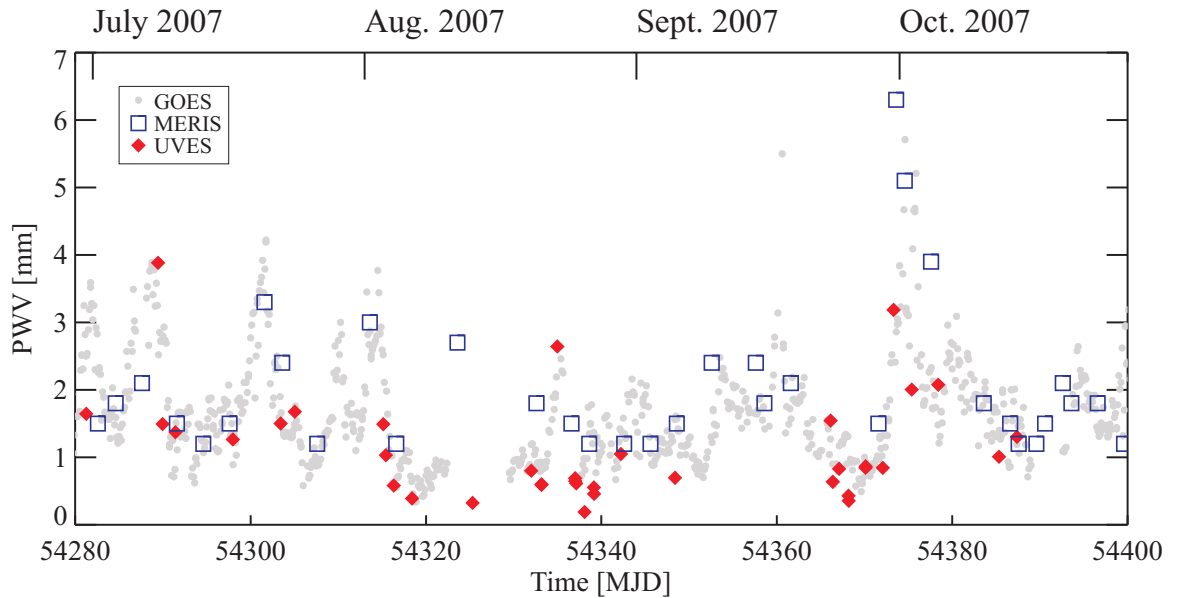


**Figure 9.11:** Comparison of PWV data derived from UVES archival data and satellite data for July to November 2007.

## 9.4. CONCLUSION

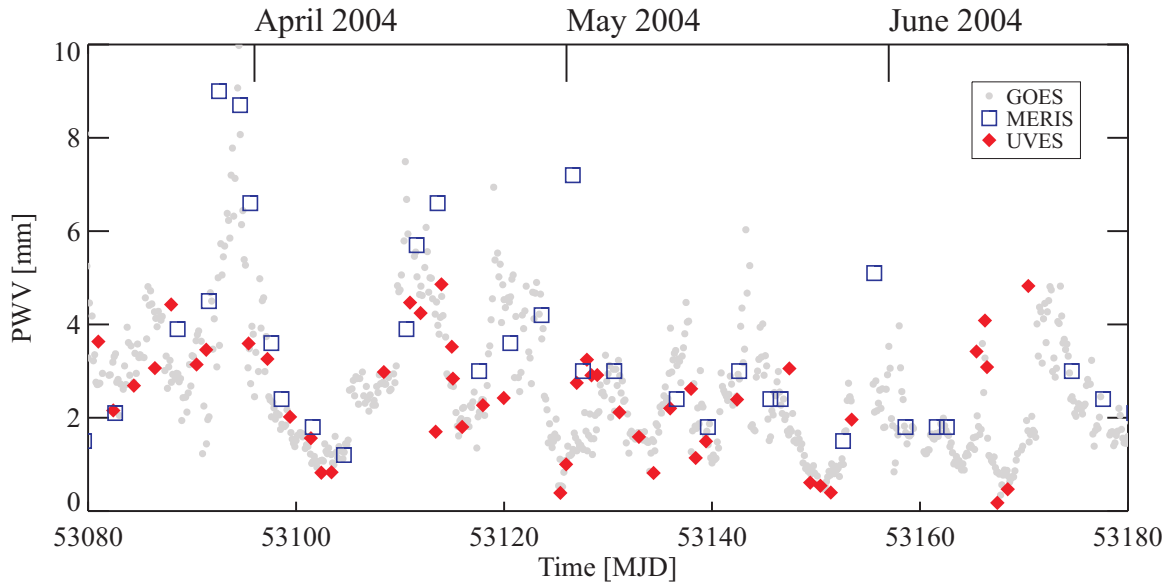


**Figure 9.12:** Comparison of PWV data derived from UVES archival data and satellite data for April to June 2004.

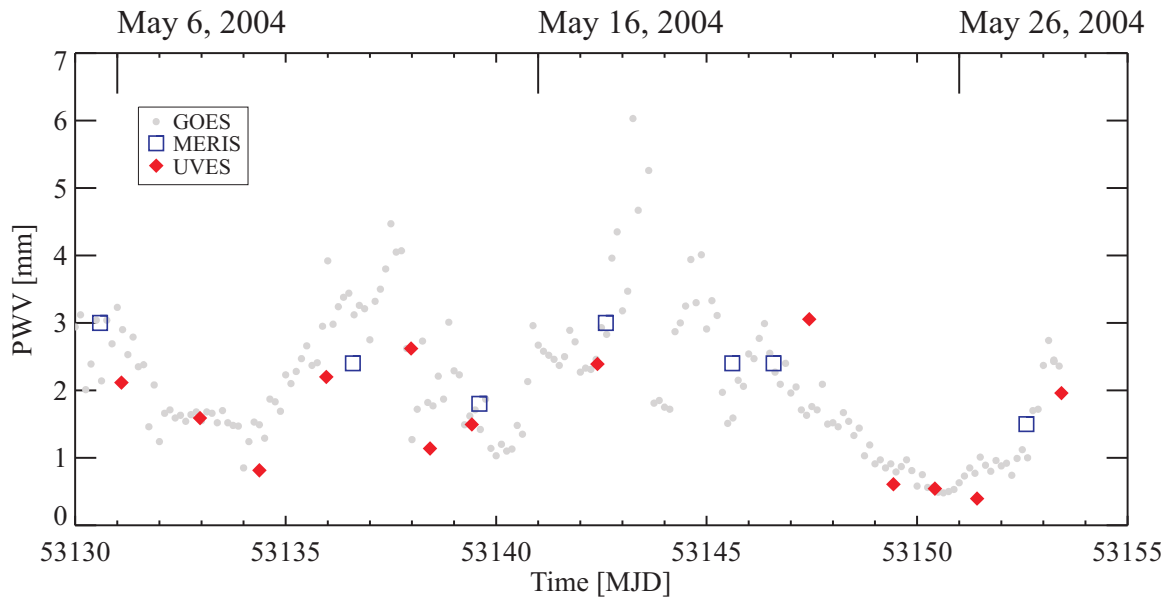


**Figure 9.13:** Enlarged section of Figure 9.12. Note the excellent agreement between all three data sets and specifically between UVES and GOES at very low PWV values.

#### 9.4. CONCLUSION

---

techniques, particularly in spatial and temporal coverage, the degree of agreement found in our study is quite remarkable. In all cases, except for those rare times for which simultaneous radiosonde launches exist, all retrieval methods are based upon a mean atmospheric profile. Since the scale height and distribution of water vapour is time dependent, all results based on archival data can be affected by systematic errors of up to 20% as a consequence of having used a median profile in their retrieval. Even with this caveat it is important to note that when comparing the results presented in this thesis, no zero-point offsets or scaling factors have been applied to the individual data sets.

The results of the archival analysis have highlighted a number of potential sources of systematic error which can be traced directly to temporal and spatial variations of the atmospheric path under study. This provided the impetus for a series of dedicated campaigns to measure PWV over La Silla and Paranal to be described in the following two chapters.

---

## Chapter 10

# Campaign to Measure Water

## Vapour: La Silla

In support of site testing for the European Extremely Large Telescope [5], we have used La Silla and Paranal as calibration sites to verify satellite measurements of PWV. To this end, dedicated measurement campaigns have been conducted over both sites and Las Campanas Observatory through a collaboration between the University of Lethbridge, scientists from the European Southern Observatory, and the Giant Magellan Telescope [4] site test team at LCO.

Several independent measurement techniques were used in this study. Continuous measurements were obtained using IRMA [42] infrared radiometers at 20  $\mu\text{m}$ . PWV was also retrieved from spectra covering the wavelength range from the visible to the infrared using a small, commercially available spectrometer (BACHES [69]) and several facility instruments (FEROS [67], HARPS (High Accuracy Radial velocity Planet Searcher) [70] and



---

MIKE [57]; CRIRES [64], UVES [68], VISIR [65] and X-Shooter [71]) through fitting their data to simulated atmospheric spectra generated using BTRAM. To assist in the validation of the IRMA units, a prototype 4-band lunar absorption spectrophotometer was developed, operating at  $\sim 0.94 \mu\text{m}$ , and had its utility validated during these campaigns.

Local meteorological data were provided by a series of radiosonde launches timed to coincide with satellite overpasses. The radiosondes provided in situ measurements of PWV, and time and location specific atmospheric profiles. Together, this multi-faceted approach has resulted in a unique data set. Integral to this analysis is a site specific atmospheric radiative transfer model (BTRAM), common to all retrieval schemes.

The objectives of these PWV measurement campaigns were to:

1. Assess variation of PWV with air mass through optical spectroscopy;
2. Measure temporal variability of PWV over extended periods ( $>4$  h) and at high cadence ( $<5$  min) with optical spectroscopy and IR radiometers in parallel;
3. Obtain contemporaneous profiles of water vapour distribution using radiosondes;
4. Assess spatial variations by means of parallel observations from two adjacent sites (La Silla and LCO) with optical spectroscopy and IR radiometers;
5. Collect data over a period of at least 1 week; and,
6. Compare and contrast the results from the different ground-based measurements with satellite data.

This chapter summarises the first of three water vapour measurement campaigns undertaken in Chile during May, August and November 2009.

The first of three water vapour measurement campaigns was conducted at the La Silla site of the ESO La Silla Paranal Observatory during the period May 3–15, 2009 [72]. The La Silla facilities are situated at the southern end of the Atacama desert in central

---

Chile, some 600 km north of Santiago de Chile. La Serena is the nearest transportation hub to the La Silla site, located approximately 160 km to the South-West. In addition, contemporaneous measurements were obtained by the Las Campanas Observatory, located  $\sim 30$  km to the north of the La Silla site. Details of the instruments used in this campaign and the data available for analysis are given in Tables 10.1 and 10.2.

The schedule of the radiosonde launches was carefully aligned with times of GOES observations as well as the daily radiosonde launch at Antofagasta airport. The full launch schedule had been authorised four weeks in advance by the Chilean airspace authority. Permission was re-confirmed by telephone 15 minutes prior to each launch. Details of the radiosonde campaign are described in Chacón *et al.* [73]. Figure 10.1 presents the time-series data from the La Silla measurement campaign. Expanded regions corresponding to the vertical bands of the upper plot are shown in middle and lower plots.

Despite some bad weather all campaign goals have been completed. The PWV values encountered during the period were always moderate to high (2–12 mm) in an astronomical sense, as was to be expected for the site at this time of the year. The data set presented in Table 10.2 is unique both in terms of quality and quantity because it allows one to compare and contrast nine independent instruments and four different methods. Given the diversity of the instruments and techniques employed, it is perhaps somewhat surprising that there exists a high degree of correlation between them, which suggests that the determination of PWV could benefit from such a multi-modal approach.

The results of the La Silla campaign are displayed as a time-series in Figure 10.1. The qualitative agreement and overall trends followed by the instruments are clearly illus-

---

**Table 10.1:** Summary of the PWV campaign conducted at La Silla / Las Campanas during May 3–15, 2009.

Instrument	Period	Data Collected
<b>La Silla</b> (Lat: $-29^{\circ}15' 15.0''$ , Long: $-70^{\circ}44' 22.0''$ , Alt: 2400 m)		
Radiosondes	May 5–15	17/20 launches; $\sim 1.5$ h each, up to 20–25 km
BACHES [69]	May 4–15	9.5/12 nights; 375 spectra, cadence $\sim 15$ min
FEROS [67]	May 6, 7	0.9/2 nights; 319 spectra, cadence minutes
HARPS [70]	May 8, 9	2/2 nights; 978 spectra, cadence minutes
IRMA 11 [42]	May 3–15	Nightly coverage; $\sim 168$ hours, cadence seconds
IRMA 12	May 3–15	Nightly coverage; $\sim 179$ hours, cadence seconds
Lunar photometer	May 5–15	$\sim 1500$ scans, cadence seconds
<b>Las Campanas</b> (Lat: $-29^{\circ}0' 54.0''$ , Long: $-70^{\circ}41' 32.0''$ , Alt: 2380 m)		
IRMA 1	Continuous	Nightly coverage; $\sim 124$ hours, cadence seconds
MIKE [57]	May 9, 10, 14	2.5/3 nights; 1449 spectra, cadence $< 30$ sec.

trated in the enlarged segments of the time-series and will be discussed in further detail in Chapter 12 which focusses on the correlation between these various instruments.

While making simultaneous measurements at the La Silla and Las Campanas observatories (located  $\sim 30$  km apart), temporal and spatial differences were expected and indeed observed. Each site had continuous PWV monitoring provided by an IRMA radiometer, and this was supplemented with high cadence measurements by HARPS (La Silla) and MIKE (LCO). The difference in elevation between LCO and La Silla is negligible ( $\sim 20$  m), thus any error associated with the input parameters to the model will not be important, implying that any observed differences were in fact real. For example, in Figure 10.2 at MJD 54963.2, a distinct peak is present in the IRMA 1 data (located at LCO; solid grey circles) while no such feature exists in the IRMA 11 data (solid black circles, located

**Table 10.2:** Summary of the instrumentation used during the dedicated PWV campaign conducted at the La Silla site and Las Campanas Observatory during May 3–15, 2009.

Instrument	Type	Location	Wavelength (used)	Spectral resolution	Data product	Comments
<b>La Silla</b> (Lat: $-29^{\circ}15' 15.0''$ , Long: $-70^{\circ}44' 22.0''$ , Alt: 2400 m)						
Vaisala RS92	Radiosonde	near Schmidt telescope	n/a	n/a	Atmospheric pro- file of tempera- ture, dew point; PWV	In-situ measure- ment ascent to $\sim 20\text{--}25$ km; $\sim 1.5$ h; at 0/6/12 UT
IRMA 11 & 12	IR radiometer	near Schmidt telescope	20 $\mu\text{m}$	n/a	flux; PWV	autonomous units
BACHES	Echelle spectrometer	ESO 1-m tele- scope	400–900 nm; (710–730 nm)	R=18,000	Optical/Near-IR spectrum; PWV	Small, commer- cially available spectrometer
FEROS	Echelle spectrometer	MPG/ESO 2.2 m tele- scope	350–920 nm; (710–730 nm)	R=48,000	Pipeline reduced spectrum; PWV	
HARPS	Echelle spectrometer	ESO 3.6 m telescope	368–691 nm; (650.5–652.5 nm)	R=100,000	Pipeline reduced spectrum; PWV	
Prototype	4-band lunar absorp- tion spectrophotometer	ESO 1-m tele- scope	850, 900, 950, 1000 nm	n/a		
<b>Las Campanas</b> (Lat: $-29^{\circ}0' 54.0''$ , Long: $-70^{\circ}41' 32.0''$ , Alt: 2380 m)						
IRMA 1	IR radiometer	Alcaino peak	20 $\mu\text{m}$	n/a	flux; PWV	autonomous units
MIKE	Echelle spectrometer	Magellan Clay telescope	320–1000 nm; (710–730 nm)	R > 30,000	Pipeline-reduced spectra; PWV	

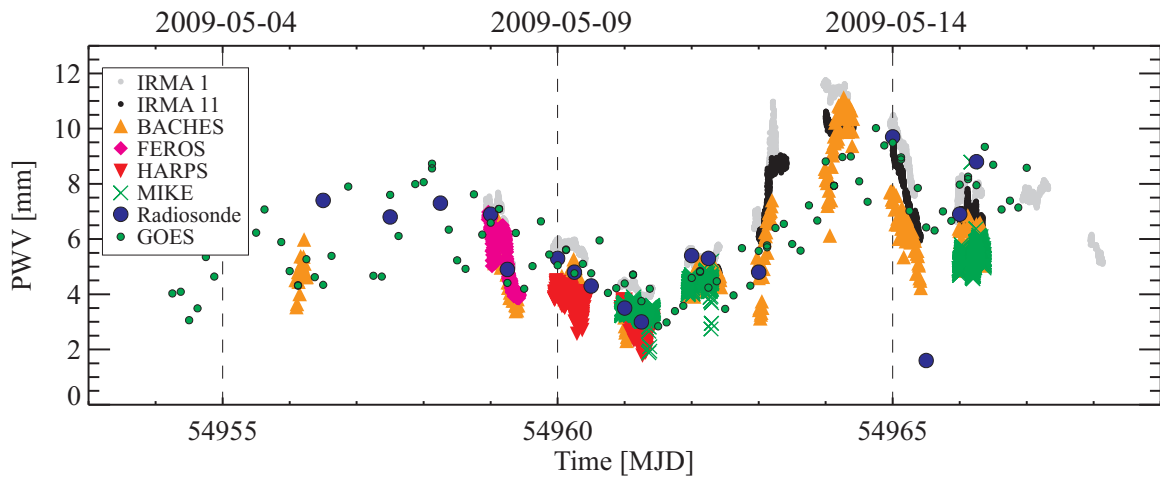


**Figure 10.1:** Time-series PWV data derived from the various methods during the PWV campaign on La Silla and Las Campanas during May 2009. IRMA 1 and MIKE are located at Las Campanas, while all other instruments are at La Silla. GOES satellite data has been overplotted for comparison.

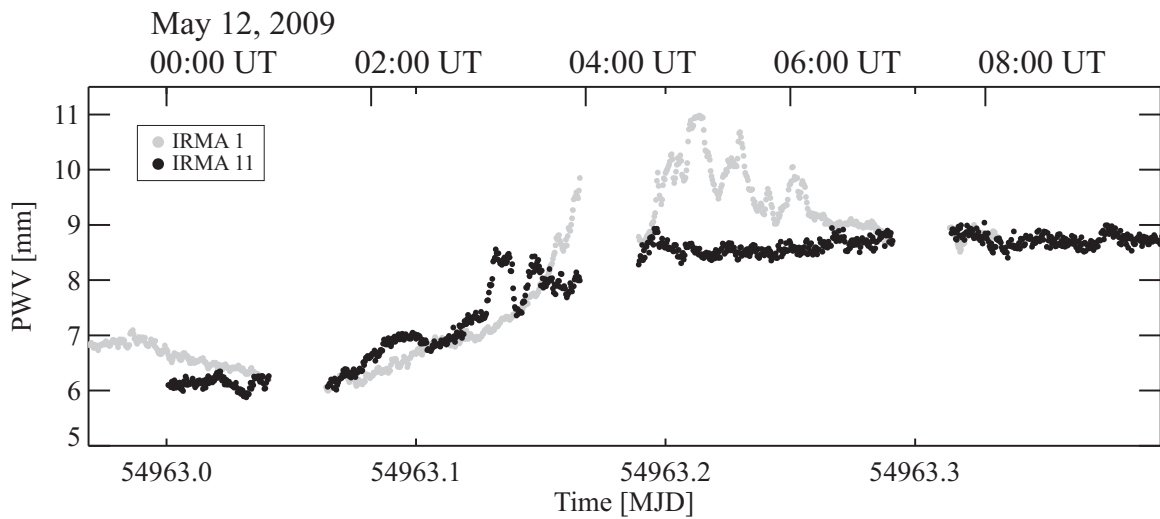


**Figure 10.2:** PWV data from IRMA 1 and IRMA 11 for May 12, 2009. IRMA 11 was at La Silla, while IRMA 1 was at Las Campanas. The time-series shows the high variability in PWV that can occur within the 30 km separation between the two sites.

---

at La Silla).

The PWV measurement campaign conducted at La Silla/Las Campanas was the first of three campaigns. While providing us with valuable data, it also served to highlight some of the challenges associated with a multi-modal approach. In July 2009, we returned to Chile for the second PWV campaign, this time in Northern Chile at the Paranal site. In November 2009, we visited Paranal for the final PWV measurement campaign. These two campaigns will be discussed in the next chapter. In Chapter 12, I will present the correlation between the various instruments and methods from data obtained over the three campaigns.

---

## Chapter 11

# Campaign to Measure Water

## Vapour: Paranal

As a natural follow-up to the measurement campaign at La Silla, two more campaigns were undertaken at the Paranal site in July/August and November 2009. This chapter summarises these two campaigns.

Two dedicated campaigns to measure PWV were conducted on Paranal during the periods July 31–August 10 and November 9–20, 2009 [74]. Descriptions of the instruments used in each campaign are given in Table 11.1. Summaries of the observations and data volume are presented in Tables 11.2 and 11.3. As previously stated, the goal of the campaigns was to operate several instruments contemporaneously in order to get independent measurements of PWV over a period of more than one week. The August and November time-frames were selected in an attempt to investigate seasonal variations. Simultaneous IRMA [42] measurements were made at Cerro Armazones, which is  $\sim 30$  km in-land from

---

Paranal and approximately 400 m higher. Armazones was one of the candidate sites for the E-ELT [5].

Cerro Paranal is located in northern Chile and is home to ESO's Very Large Telescope (VLT). The VLT consists of four identical 8.2 m diameter telescopes, known as Unit Telescopes (UTs), and three smaller Auxiliary Telescopes (ATs). These telescopes may be used in three different modes including an independent telescope mode, a combined coherent mode (or VLT Interferometer mode) and a combined incoherent mode.

The campaign at Paranal benefitted from many of the lessons learned during the prior campaigns. Scheduling of observations was optimised to maximise the number of parallel observations in order to intercompare the various instruments and methods. Two IRMA units were operated in parallel on Paranal and Armazones, respectively for five nights (shown in Figure 11.3). Data analysis was also optimised, making maximum use of ESO pipeline data reduction.

During the two campaigns on Paranal an unprecedented, seven independent instruments were used to derive PWV in an astronomical context resulting in a unique data set. Parallel coverage by more than one instrument has been achieved over extensive periods. Careful coordination with the launch schedule of the radiosondes has allowed us to compare individual methods with respect to the accepted standard in atmospheric sounding. Weather conditions have been good through most of the campaigns with some periods of high cirrus. PWV on Paranal varied between 1–4 mm, with some periods as low as 0.5 mm, giving ample opportunity to sample the range of interest to IR astronomy, namely 0–2 mm, shown in Figures 11.1 and 11.2. The excellent time coverage provided by the



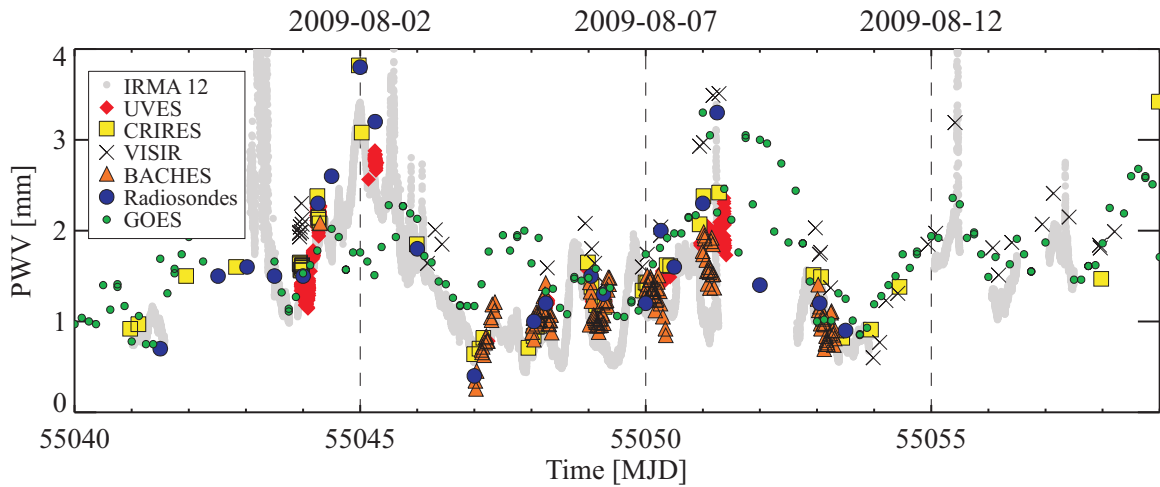


**Figure 11.1:** Time-series PWV data derived from the various methods during the PWV campaign on Paranal in July and August 2009. The sharp peaks of high PWV correspond to periods with some cloud cover. GOES satellite data has been overplotted for comparison.

various instruments has removed the temporal variations associated with the atmosphere. The results, which are presented in Chapter 12, show that agreement down to the order of 0.1 mm is found in many instances.

Calibration of the IR radiometers had been improved by performing synchronised scans from zenith to the horizon, so-called sky dips. The increased line-of-sight through the atmosphere results in an effective increase in the observed PWV column by nearly an order of magnitude ( $1.5 \text{ mm PWV} \Rightarrow 15 \text{ mm PWV}$ ). When performed with two radiometers looking at the same region of the sky in parallel, excellent cross-calibration can be achieved. In our case the improved calibration resulted in agreement between IRMA 11 and 12 at the 0.25 mm level over the range of 1–4 mm PWV.

For 5 days and nights two IRMA units were located on Paranal and Armazones shown in Figure 11.3. Based on the analysis of radiosonde profiles and the observations

**Table 11.1:** Summary of the instrumentation used during the PWV campaign conducted at the Paranal site and Cerro Armazones during July 31–August 10, and November 9–20, 2009.

Instrument	Type	Location	Wavelength (used)	Spectral resolution	Data product	Comments
<b>Paranal</b> (Lat: $-24^{\circ}37' 38''$ , Long: $-70^{\circ}24' 17''$ , Alt: 2635 m)						
Vaisala RS92	Radiosonde	launched 50 m below observing platform	n/a	n/a	Atmospheric profile of temperature, dew point; PWV	In-situ measurement ascent to $\sim 20$ – $25$ km; $\sim 1.5$ h; at 0/6/12UT
IRMA 11 & 12 [42]	IR radiometer	Paranal & Armazones	$20 \mu\text{m}$	n/a	integrated flux; PWV	autonomous units
BACHES [69]	Echelle spectrometer	Site-testing telescope	400–900 nm; (710–730 nm)	R=18,000	Optical spectrum; PWV	Small, commercially available spectrometer
CRIRES [64]	Echelle spectrometer	Nasmyth platform, UT 1	950–5000 nm; (5038–5063 nm)	R=100,000	Pipeline reduced spectrum; PWV	ESO PWV pipeline
VISIR [65]	Mid-IR spectrometer	Nasmyth platform, UT 3	8–13 & 16.5–24.5 $\mu\text{m}$ ; (19.34–19.66 $\mu\text{m}$ )	R=150–30000; used R=4500	Pipeline reduced spectrum; PWV	ESO PWV pipeline
UVES [68]	Echelle spectrometer	Nasmyth platform, UT 2	350–1000 nm; (710–730 nm)	R=20,000–100,000	Pipeline reduced spectrum; PWV	ESO PWV pipeline
Prototype 4-band lunar absorption spectrophotometer		Site testing telescope	850, 900, 950, 1000 nm	n/a		
<b>Armazones</b> (Lat: $-24^{\circ}35' 51''$ , Long: $-70^{\circ}11' 47''$ , Alt: 3064 m)						
IRMA 11 & 12	IR radiometer	Paranal & Armazones	$20 \mu\text{m}$	n/a	integrated flux; PWV	autonomous units

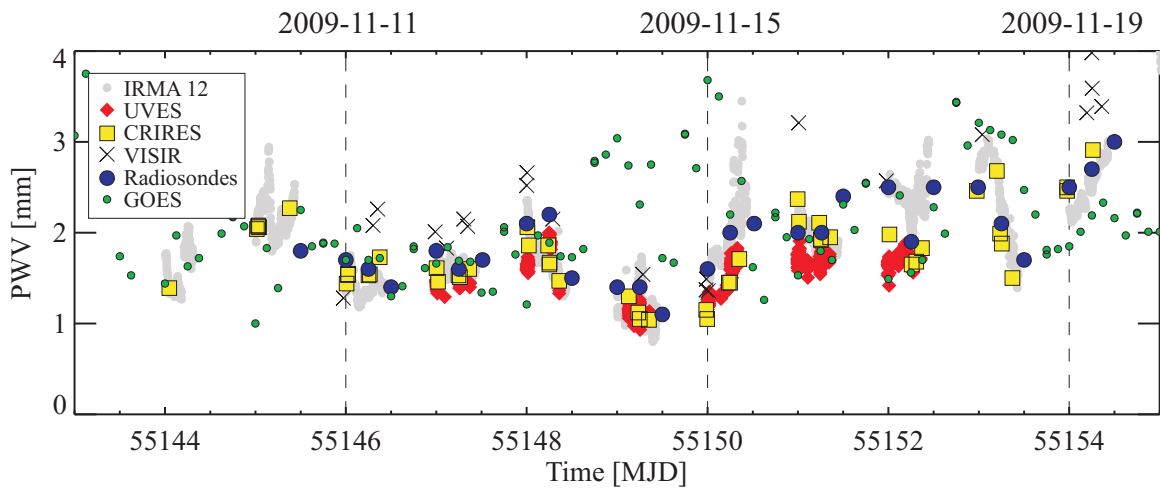


**Figure 11.2:** Time-series PWV data derived from the various methods during the PWV campaign on Paranal in November 2009.

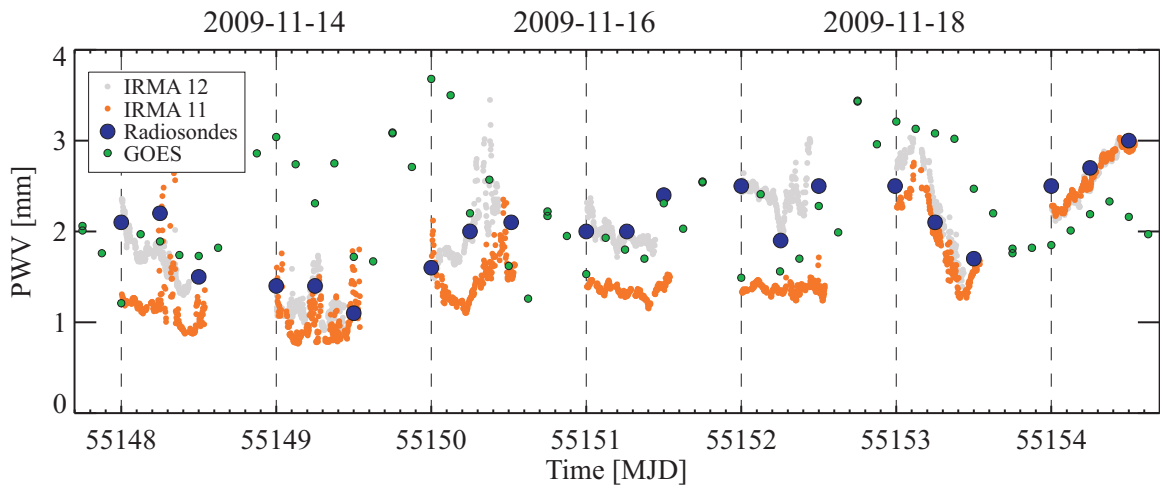


**Figure 11.3:** Natural variations in the offsets between Paranal and Armazones. Time-series PWV data of radiosondes and IRMA units located on Paranal and Armazones. IRMA 11 (black circles) was located on Armazones and systematically measured lower PWV. When it was moved back to Paranal on November 18, 2009, the offset in measured PWV disappeared.

**Table 11.2:** Summary of the PWV campaign conducted at Paranal and Armazones during July 31–August 10, 2009.

Instrument	Period	Data Collected
BACHES	Aug. 1–10	142 spectra, cadence 15–30 min
UVES	July 31–Aug. 8	10.5 h, 474 spectra cadence up to 30s
VISIR	July 31–Aug. 16	46 spectra
CRIRES	July 29–Aug. 15	53 spectra
IRMA 11	July 29–Aug. 10	~150 h; cadence seconds
IRMA 12	Aug. 3–8	~50 h each on Paranal & Armazones, cadence seconds
Radiosondes	July 29–Aug. 10	23/23 launches; ~1.5 h each, up to 20–25 km
Lunar photometer	Aug. 1–7	55 scans, cadence seconds

**Table 11.3:** Summary of the PWV campaign conducted at Paranal and Armazones during November 9–20, 2009.

Instrument	Period	Data Collected
UVES	Nov. 11–17	11 h, 450 spectra cadence up to 30s
VISIR	Nov. 10–21	25 spectra
CRIRES	Nov. 9–21	60 spectra
IRMA 11	Nov. 8–19	~120 h Paranal, ~85 h on Armazones; cadence seconds
IRMA 12	Nov. 9–20,	~200 h Paranal, cadence seconds; left operating
Radiosondes	Nov. 9–19	29/29 launches; ~1.5 h each, up to 20–25 km

conducted at both sites we find an average offset of  $0.3 \pm 0.2$  mm, which is consistent with the difference in altitude between these sites; although one cannot rule out the importance of local variations. The largest offset observed is around 1 mm and it seems to be lowest at low PWV. Note that both methods - radiosondes and IR radiometers - are near their limiting accuracies in this PWV regime. During site testing work for the Thirty Meter Telescope, Otarola *et al* derived PWV from surface weather data; they found a mean value

---

of 2.9 mm for Armazones [44]. While it is possible in principle to derive PWV from the ground data from P, T, Humidity and an assumed profile, as described by Otarola *et al.*, these values were 0.8 mm greater than what we found, which shows that such an approach is greatly over-simplified and prone to error.

In the next chapter I will present correlation statistics and scatter plots in order to perform a quantitative comparison of the instruments and methods used in the three PWV measurement campaigns.

---

## Chapter 12

# Correlation of Methods

In this Chapter I present the results from correlating the different methods and instruments used in the three PWV measurement campaigns.

### 12.1 Comparison of methods and validation with respect to radiosondes

As has been noted, radiosondes are the accepted standard method for atmospheric sounding. Other methods for determining an atmospheric parameter by remote sensing are usually referenced to data provided with radiosonde launches. We have followed this accepted approach in our efforts to evaluate the utility of different methodologies in the measurement of PWV.

A quantitative analysis of the PWV data from the La Silla and Paranal campaigns allows for a comparison of the PWV determined by each specific instrument to that obtained by the radiosonde. Figure 12.1 shows two examples of such correlations. The left panel shows the correlation between an IRMA radiometer and the radiosonde PWV retrievals. A

## 12.1. COMPARISON OF METHODS AND VALIDATION WITH RESPECT TO RADIOSONDES

**Table 12.1:** Comparison of various methods with radiosondes. Shown is the wavelength range of the instrument, the number of points in the correlation, the PWV range, the best-fit slope of a line through the origin, the coefficient of determination  $R^2$ , and the adopted accuracy used in our analysis.

Instrument	$\lambda$	#	PWV [mm]	Slope	$R^2$	Adopted accuracy
BACHES	710–850 nm	26	0.3 – 10.0	0.82	0.94	15%; $\geq 0.3$ mm
UVES	710–850 nm	29	0.4 - 3.3	0.84	0.79	15%; $\geq 0.3$ mm
CRIRES	5038–5063 nm	40	0.8 - 2.9	0.91	0.72	15%; $\geq 0.3$ mm
VISIR	19.3–19.7 $\mu\text{m}$	20	1.1 - 3.1	1.10	0.65	20%; $\geq 0.3$ mm
IRMA (all)	20 $\mu\text{m}$	57	0.4 - 10.0	0.97	0.93	5%; $\geq 0.25$ mm
GOES (La Silla)	6.7, 10.7 $\mu\text{m}$	17	3.0 - 10.0	0.97	0.12	25% $\geq 0.5$ mm
GOES (Paranal)	6.7, 10.7 $\mu\text{m}$	52	0.4 - 4.0	0.95	-0.76	25% $\geq 0.5$ mm

near unity slope is found over a PWV range of  $\sim 3$ –10 mm. Within the accuracies of the methods we find good agreement ( $R^2=0.85$ ). This is despite the fact that IRMA samples a pencil-beam at zenith, whilst the radiosonde samples along its arbitrary ascent vector.

The right panel of Figure 12.1 shows the relationship between the BACHES spectrometer derived PWV values and the simultaneous radiosonde retrievals of PWV. Again, a PWV range of  $\sim 3$ –10 mm was sampled and a good correlation ( $R^2=0.94$ ) is observed. Even with its lower spectral resolution ( $R < 15,000$ ) and 1-m telescope, BACHES derived PWV values were comparable to the results derived from all of the high resolution ( $R = 100,000$ ) facility spectrographs used in our study.

In general, a high degree of correlation is found between optical, IR and radiosonde derived PWV. Moreover, since all retrievals require an atmospheric model, our analysis advantageously, brings an internal consistency by using the same model (BTRAM).

The two Paranal campaigns resulted in a larger data set for the intercomparison of instruments and methods. The absolute accuracy of PWV derived from radiosondes is

## 12.1. COMPARISON OF METHODS AND VALIDATION WITH RESPECT TO RADIOSONDES

---

an important issue in this context. In the literature, an absolute accuracy of 5% overall is reported and  $\sim 15\%$  in very dry conditions [75, 76]. One also has to keep in mind that a radiosonde samples data along its trajectory which carries it to about 20–25 km altitude over the course of about an hour traveling a horizontal distance of up to 80–150 km. As explained in Chapter 5, PWV is derived from the profile for the whole column although water vapour is concentrated in the lower few kilometers. Hence the radiosondes and astronomical spectrographs are not sampling the same column of air and full agreement between retrieved PWV values is not to be expected.

A total of 70 radiosondes have been successfully launched during the two campaigns on La Silla and Paranal. Since the balloon ascends at a rate of a few m/s only a small window of about 30–60 minutes is available to conduct meaningful parallel observations with other methods. For a stand-alone high time resolution monitor such as IRMA this is relatively easy to achieve, while for instruments on the VLT careful planning and flexibility are essential.

As seen in Figures 12.1 and 12.2, there is a high degree of correlation between the PWV derived from radiosonde data and that measured by other methods. IRMA data, available from both Paranal and La Silla, is well defined over the PWV range 0.5–10 mm with a correlation slope very close to one and a minimal zero-point offset. It is pleasing to see that the retrieved PWV values from each instrument are in agreement when instrument specific error bars are accounted for. This validates the decision to use an external blackbody source in the calibration schema of IRMA, a point discussed in my M.Sc. thesis [18]. For the astronomical spectrographs on Paranal the correlation between instruments and radiosondes



## 12.2. COMPARISON WITH GOES

---

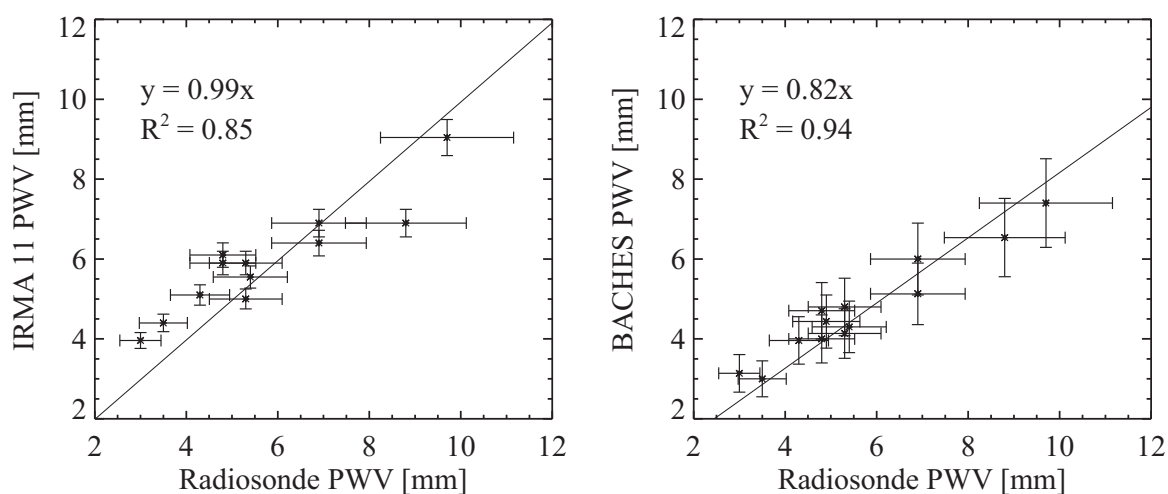


**Figure 12.1:** Left plot is a comparison of PWV data derived using an IR radiometer (IRMA) and the atmospheric profile recorded by radiosonde launches. The right plot is a comparison of PWV derived by fitting an atmospheric model to the BACHES optical spectrometer with PWV measured using radiosonde launches.

shown in Figure 12.2 holds over a range of PWV from 0.5–4 mm. Since all methods involve the same atmospheric model, BTRAM, the fact that we see such broad agreement across a wavelength range spanning from 0.7–20  $\mu\text{m}$ , demonstrates that the algorithms used within BTRAM are sound.

### 12.2 Comparison with GOES

GOES derived PWV values are found to be in reasonable agreement with radiosonde values, as shown in Figure 12.3. The numerical correlation values shown in Table 12.1 are excellent, fully consistent with the findings from both the FEROS and UVES archival data. Although we have shown that there tends to be a wet bias due to their larger footprints, satellite data can still be used successfully for characterisation of sites in terms of PWV provided a substantial time base is available and the environment is homogeneous

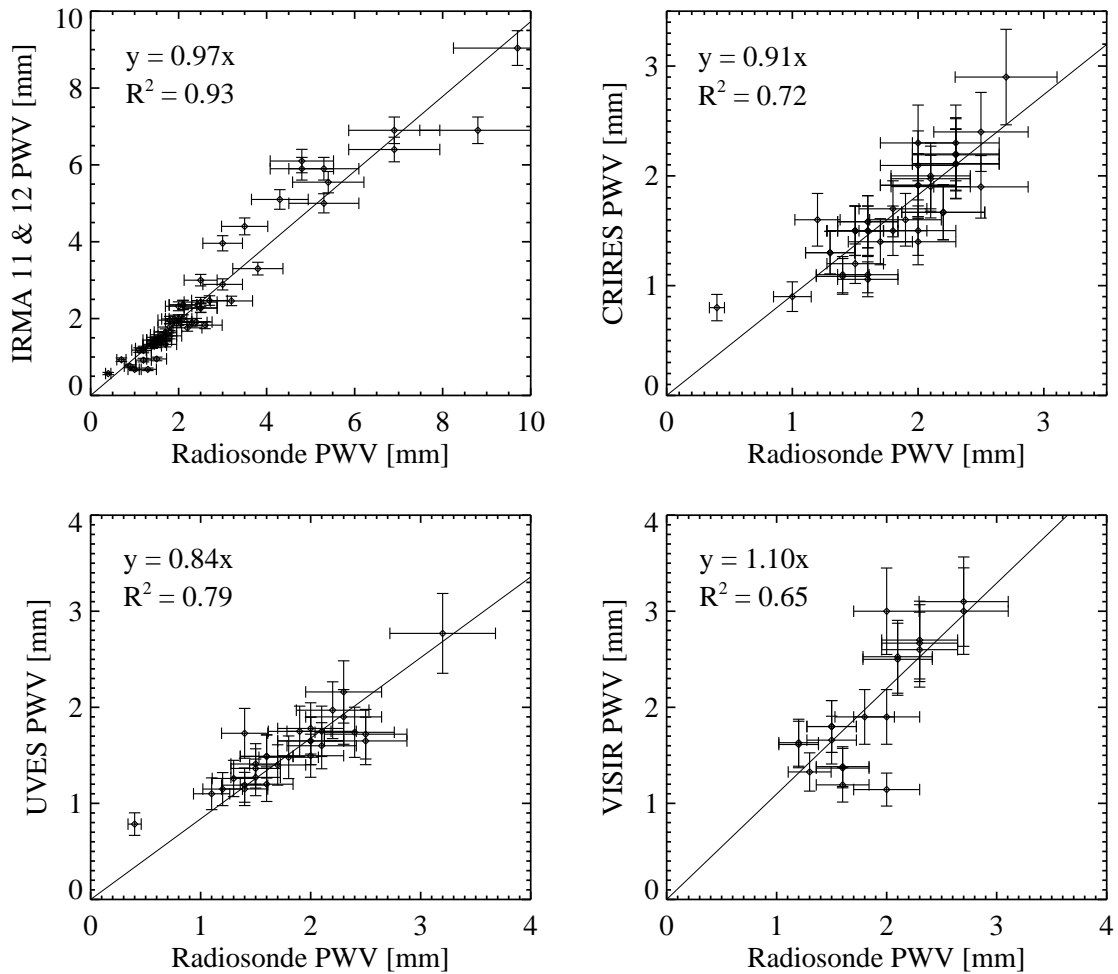


**Figure 12.2:** Correlation between radiosondes and radiometers and spectrograph-derived PWV. Upper left plot compares IRMA radiometers ( $20\ \mu\text{m}$ ) with radiosondes. Upper right plot compares the CRIRES mid-IR instrument ( $5\ \mu\text{m}$ ) with radiosondes. Lower left plot compares the UVES echelle instrument ( $0.7\ \mu\text{m}$ ) with radiosondes. Lower right plot compares VISIR mid-IR instrument ( $20\ \mu\text{m}$ ) with radiosondes. The IRMA:radiosonde correlation is the best ( $R^2 = 0.93$ ) and covers nearly three times the PWV range as that shown in the other panels.

as is the case for Northern Chile. Both these conditions are fulfilled for Paranal and good agreement between GOES and other methods is found.

The La Silla campaign was the first of three PWV measurement campaigns. Some nights with poor weather conditions and thus reduced observation times resulted in a limited set of high resolution spectra for correlation with concurrent radiosonde data. As described above the discrepancy between the FEROS archival PWV and GOES PWV values may be attributable to its limited spatial resolution. GOES is found to both over- and underestimate PWV depending on atmospheric conditions and the actual distribution of water vapour.

Closer inspection of the data taken during the campaigns on both La Silla (high to moderate PWV) and Paranal (low PWV) shows that GOES values can deviate significantly from radiosonde results, shown in the right panel of Figure 12.3. This is also born out in a numerical sense once the precondition of a zero intercept is lifted. The distribution for the Paranal data show a curious butterfly pattern in which both over- and under-estimations of PWV by GOES cancel such that a naïve regression with intercept zero mimics a linear correlation. Similarly, comparison between IRMA – which is a very good proxy for radiosondes data (see Figure 12.2) – and GOES data in the period August/September 2009 show only a very weak correlation.

We conclude that GOES measurements are not suitable to derive PWV with the accuracy required for use in observatory operations such as scheduling observations based on PWV constraints. There are two principle reasons for this: the limited spatial resolution of GOES observations and the use of a median profile to approximate the actual distribution of atmospheric water vapour by the retrieval scheme described in Chapter 7. This effect is

### 12.3. FINDINGS OF THE PWV CAMPAIGNS

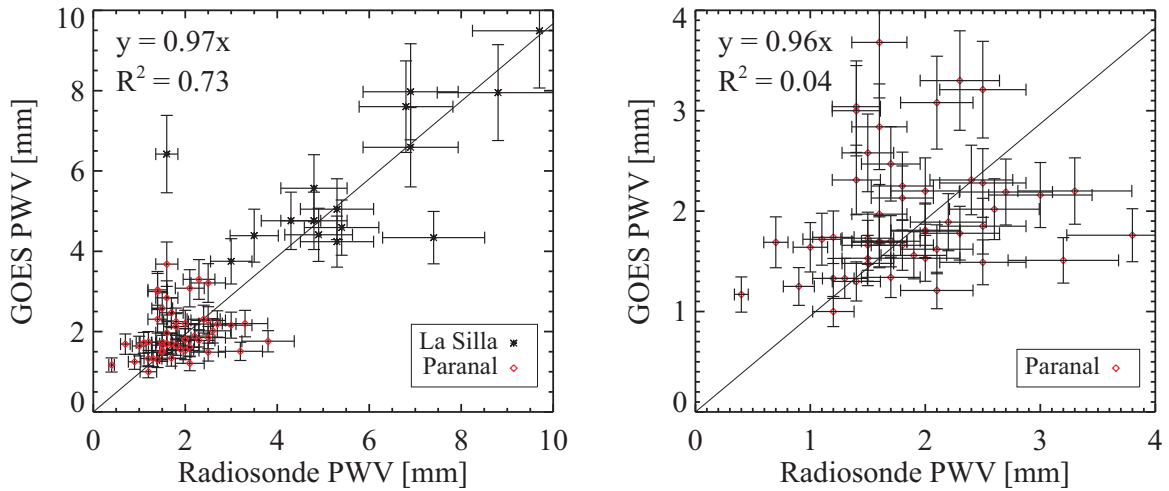


**Figure 12.3:** Comparison of PWV data derived using GOES data and the atmospheric profile recorded by radiosonde launches. The left plot includes data from La Silla and Paranal, and the right plot only includes data from Paranal. The “butterfly” in the right plot indicates that GOES routinely over- and under-estimates PWV, if the radiosonde-derived PWV is taken to be an accurate measure.

even more pronounced for a site like La Silla where wetter regions are present in the same GOES footprint.

### 12.3 Findings of the PWV campaigns

The primary result from the intercomparison of various instruments during the three Chilean campaigns conducted in 2009 is that all instruments are measuring PWV and to first-order they are returning similar values,  $\pm 1$  mm PWV. Using radiosondes as the reference we find that agreement with the infrared radiometer IRMA is excellent providing results that are indistinguishable within the associated errors. Moreover, IRMA provides information of the air mass directly above the observatory. The internal precision of the infrared radiometer data is about 3% while the accuracy is estimated at 5%, but not better than 0.25 mm. Relative agreement between two co-located IRMA units is extremely good

## 12.4. CONCLUSION

---

on time scales of a few seconds to several hours.

The internal precision of PWV data from optical and infrared spectroscopy is about 7% whereas accuracy is estimated to be about 15–20% but not better than 0.3 mm. Quantitative agreement between the individual ground-based remote sensing techniques and in-situ measurements (radiosondes) is very good (10–20%). Evidence for structure in the spatial distribution of water vapour in the sky – at the few 0.1 mm level – can be directly seen as temporal variations in the observations of a transit instrument (IRMA) as well as variations in the PWV found for pointed observations (optical spectroscopy).

### 12.4 Conclusion

The PWV history over La Silla and Paranal has been reconstructed using several years of archival FEROS and UVES data. We have extracted PWV values from these spectra using the BTRAM atmospheric model. In addition, dedicated PWV measurement campaigns have been conducted at both sites, enabling the intercomparison of various astronomical spectrographs covering a wavelength range of 0.6–20  $\mu\text{m}$  with respect to locally launched radiosondes. Satisfactory agreement has been found for all methods with the IRMA radiometers delivering the best accuracy combined with the highest time resolution.

The annual mean PWV for Paranal has been derived at  $2.7 \pm 2.2$  mm, which, since there is a dry-bias to the data set, (UVES measurements were not made on cloudy nights) is in good agreement with the GOES PWV estimates of  $2.8 \pm 1.8$  mm for the same 8-year period. Based on our analysis, Paranal can be used as a reference site for Northern Chile. Comparison of concurrent IRMA measurements performed on Paranal and

## 12.4. CONCLUSION

---

Armazones revealed a PWV offset of 0.3 mm (lower on Armazones) which can be attributed to the altitude difference of  $\sim 400$  m.

The goals of the PWV measurement campaigns have been met in full. The results of this study have been communicated to the Site Selection Advisory Committee contributing directly to the site selection process for the future E-ELT.

From analysis of archival data and the results from the campaigns we have shown that PWV can be successfully monitored by several methods. Indeed, PWV values for Paranal are now routinely monitored using spectra taken with CRIRES, UVES, VISIR and X-shooter. We conclude that PWV should be used as a constraint in planning observations. Steps to this end are planned for the immediate future at Paranal observatory. For the E-ELT, a stand-alone high time resolution PWV monitor will be an essential part of the infrastructure in order to optimise the scientific output of the operations. Observatories are moving towards the realistic goal of real-time monitoring of PWV to optimise observatory scheduling.

---

## Chapter 13

# Conclusions

The goal of my thesis was to explore various ways of evaluating the best sites for conducting infrared astronomy. Since water vapour is the principal source of opacity at infrared wavelengths, my thesis has focused on using as many measurement methods as were available. Extending the work of my M.Sc. thesis, which used an infrared radiometer for site testing campaigns, it was clear that other simultaneous measurements of water vapour were necessary to gain confidence in the techniques employed. That led me into a whole new field of optical telescopes and high resolution spectrometers. Previous researchers had used the equivalent width method with a single isolated line to determine PWV from such high resolution spectra. I expanded the analysis of these spectra from the fitting of a single line to simulating a complex manifold of lines due to atmospheric water vapour.

In this thesis, I have presented results from three campaigns to measure atmospheric water vapour above four Chilean sites using data from nine ground based instruments and two satellites together with contemporaneous launches of radiosondes from the

---

sites.

While each independent method of measuring water vapour yielded reasonable values for PWV, it quickly became evident that a means of tying them all together was necessary. Radiosondes, being the gold standard of atmospheric research, were the desired source of data for this intercomparison. However, radiosondes are routinely launched from airports, but seldom from mountain tops. This provided the impetus for a campaign approach in which a scheduled series of radiosondes were launched from both the La Silla and Paranal observatory sites, while other water vapour measuring instruments were operating.

The radiosonde derived PWV values provided the reference data set for comparison not only with other ground based measures but also simultaneous satellite data to which we gained access. While satellite estimates of PWV have been shown to have limited utility for immediate, local determination of PWV, they do offer global, archived sets of data that become statistically representative of a site when a significant period of time is analysed.

The adopted strategy was to use as many independent techniques and instruments as available, spanning nearly three orders of magnitude in wavelength and ten orders of magnitude in spatial footprint. When one considers this vast parameter space, it is reassuring that each of the various methods paints a similar picture of the sky when an adequate set of data is available to perform a meaningful statistical analysis.

Another aspect of the study that quickly became evident was that each instrument has a particular niche where it is best suited. For instance, satellite data are ideal for a first-order survey of a region, since the spread inherent in the data averages out over long-enough periods of time and can provide a general sense of the water vapour characteristics



---

above a given region of interest. Satellite data would never be used as a substitute for real-time, local measurements, but they do have their value in providing a historical, seasonal and synoptic perspective. Similarly, while one would never dedicate a 10-m telescope and million dollar instrument to measuring telluric water vapour, those very facilities are ideally suited to provide instantaneous measurements that can be used as calibration points.

IRMA is an ideal real-time water vapour monitor, able to measure at sub-second intervals which holds great promise as a means of optimising the use of a large telescope for mid-infrared astronomical observations. Calibrating IRMA is, however, challenging, and having access to point measurements, as produced by a facility echelle instrument, are invaluable. To this end, I designed and built a simple lunar absorption spectrophotometer that could serve this purpose, based upon the same spectral lines used with the echelle study, but with a simpler band approach. Although this measurement technique can only work when the moon is visible, it is still useful. See Appendix A for more details.

In this study, the multi-modal nature of the approach is unique. This work represents the first comprehensive study that attempts to draw together such a vast array of independent data and bring internal consistency through the use of a single atmospheric model. While I am indebted to the many colleagues that have assisted in acquiring access to the archival data and organising the logistics during the three measurement campaigns in Chile, it was my algorithms that were instrumental to the data analysis. An integral part of this study, which sets it apart, are the large number of radiosondes launched directly from the observatory test sites during our three campaigns. A high degree of correlation between radiosonde data and the other methodologies has been found. When one considers the fact

---

that the different techniques cover the wavelength range of  $0.6 - 20 \mu\text{m}$ , it is remarkable that such agreement exists.

This study has also demonstrated the importance and legacy value of archival data. The historical comparison to satellite data would not have been possible without well-maintained and accessible repositories of measurements. Several archival data sets were used in this study: spectrograph data from FEROS (5 years) and UVES (7 years), radiosonde data from the NOAA archives (9 years), and GOES-Imager (8 years) and Envisat-MERIS (6 years) data from their respective archives. With the computing power available in a desktop computer and an advanced software model such as BTRAM, data-mining these archives is straightforward and within the reach of any suitably equipped student or researcher.

Future work might be to expand the echelle fitting and include science targets of the echelle spectrometer. This would require the more careful selection of regions where photospheric contamination is minimal. Regardless, I have demonstrated the importance of routine standard calibration in the analysis.

I have shown that the use of ground-based instruments dedicated to monitoring the atmosphere is feasible and has the potential to add value to observatory scheduling operations for major telescopes. Since the real operating costs of a major astronomical telescope are thousands of dollars per hour and observing times are competitive, it is essential that scheduling be optimised. Real-time monitoring of PWV is useful as an operational tool (short-term) and for site characterisation and testing (long-term). Measurements of spectrophotometric standard stars have been demonstrated to be good tools for monitoring the PWV over the facilities using existing instrumentation. A continuous monitoring of PWV

---

using this method (ideally once per day) would allow for the generation of a long-term data set that could help to characterise the site and serve as a baseline for understanding the climatology of other sites.

Finally, since our work was in support of the site-testing efforts of the European Extremely Large Telescope, it is worth noting that on April 26, 2010, it was announced that Cerro Armazones had been selected as the candidate site for the future E-ELT.

---

# Bibliography

- [1] Graham J. Smith. An infrared radiometer for millimeter astronomy. Master's thesis, University of Lethbridge, Lethbridge, Alberta, 2001.
- [2] I. M. Chapman. The atmosphere above Mauna Kea at mid-infrared wavelengths. Master's thesis, University of Lethbridge, Lethbridge, Alberta, 2003.
- [3] G. Sanders and TMT Project. The Thirty Meter Telescope (TMT) Project. In *Bulletin of the American Astronomical Society*, volume 36 of *Bulletin of the American Astronomical Society*, page 1476, December 2004.
- [4] M. Johns. The Giant Magellan Telescope (GMT). In *Society of Photo-Optical Instrumentation Engineers (SPIE) Conference Series*, volume 6986 of *Presented at the Society of Photo-Optical Instrumentation Engineers (SPIE) Conference*, May 2008.
- [5] R. Gilmozzi and J. Spyromilio. The European Extremely Large Telescope (E-ELT). *The Messenger*, 127:11, March 2007.
- [6] United States Committee on Extension to the Standard Atmosphere. U.S. Standard Atmosphere, 1976. Technical report, National Oceanic and Atmospheric Administration, National Aeronautics and Space Administration, United States Air Force, Washington D.C., U.S.A., 1976.
- [7] Hugh D. Young and Roger A. Freedman. *University Physics with Modern Physics*. Addison Wesley, San Francisco, California, U.S.A., 11th edition, 2004.
- [8] G. Tinetti, A. Vidal-Madjar, M.-C. Liang, J.-P. Beaulieu, Y. Yung, S. Carey, R. J. Barber, J. Tennyson, I. Ribas, N. Allard, G. E. Ballester, D. K. Sing, and F. Selsis. Water vapour in the atmosphere of a transiting extrasolar planet. *Nature*, 448:169–171, July 2007.
- [9] H. Shibai. AKARI (ASTRO-F): Flight performance and preliminary results. *Advances in Space Research*, 40:595–599, 2007.
- [10] G. L. Pilbratt, J. R. Riedinger, T. Passvogel, G. Crone, D. Doyle, U. Gageur, A. M. Heras, C. Jewell, L. Metcalfe, S. Ott, and M. Schmidt. Herschel Space Observatory - An ESA facility for far-infrared and submillimetre astronomy. *ArXiv e-prints*, May 2010.

## BIBLIOGRAPHY

---

- [11] T. Nakagawa. SPICA: space infrared telescope for cosmology and astrophysics. *Advances in Space Research*, 34:645–650, 2004.
- [12] M. W. Werner, T. L. Roellig, F. J. Low, G. H. Rieke, M. Rieke, W. F. Hoffmann, E. Young, J. R. Houck, B. Brandl, G. G. Fazio, J. L. Hora, R. D. Gehrz, G. Helou, B. T. Soifer, J. Stauffer, J. Keene, P. Eisenhardt, D. Gallagher, T. N. Gautier, W. Irace, C. R. Lawrence, L. Simmons, J. E. Van Cleve, M. Jura, E. L. Wright, and D. P. Cruikshank. The Spitzer Space Telescope Mission. *Astrophysical Journal, Supplement*, 154:1–9, September 2004.
- [13] Ian M. Chapman and David A. Naylor. Development of a Freely Distributed, Customizable Atmospheric Radiative Transfer Model. In *Fourier Transform Spectroscopy/Hyperspectral Imaging and Sounding of the Environment*. Technical Digest (CD), paper HTuD2, OSA, 2005.
- [14] H. J. P. Smith, D. J. Dube, M. E. Gardner, S. A. Clough, F. X. Kneizys, and L. S. Rothman. FASCODE: Fast Atmospheric Signature Code (Spectral Transmittance and Radiance). Technical Report Technical Report AFGL-TR-78-0081, Air Force Geophysics Laboratory, Hanscom AFB, Massachusetts, U.S.A., 1978.
- [15] L. S. Rothman, I. E. Gordon, A. Barbe, D. C. Benner, P. F. Bernath, M. Birk, V. Boudon, L. R. Brown, A. Campargue, J.-P. Champion, K. Chance, L. H. Coudert, V. Dana, V. M. Devi, S. Fally, J.-M. Flaud, R. R. Gamache, A. Goldman, D. Jacquemart, I. Kleiner, N. Lacome, W. J. Lafferty, J.-Y. Mandin, S. T. Massie, S. N. Mikhailenko, C. E. Miller, N. Moazzen-Ahmadi, O. V. Naumenko, A. V. Nikitin, J. Orphal, V. I. Perevalov, A. Perrin, A. Predoi-Cross, C. P. Rinsland, M. Rotger, M. Šimečková, M. A. H. Smith, K. Sung, S. A. Tashkun, J. Tennyson, R. A. Toth, A. C. Vandaele, and J. Vander Auwera. The HITRAN 2008 molecular spectroscopic database. *Journal of Quantitative Spectroscopy and Radiative Transfer*, 110:533–572, June 2009.
- [16] I. S. Schofield. The IRMA III control and communication system. Master’s thesis, University of Lethbridge, Lethbridge, Alberta, 2005.
- [17] Frederick K. Lutgens and Edward J. Tarbuck. *The Atmosphere: An Introduction to Meteorology*. Prentice Hall College Division, Prentice Hall, Paramus, NJ, U.S.A., 6th edition, 1995.
- [18] R. R. Querel. IRMA calibrations and data analysis for telescope site selection. Master’s thesis, University of Lethbridge, Lethbridge, Alberta, 2007.
- [19] D. A. Naylor, R. T. Boreiko, T. A. Clark, R. J. Emery, B. Fitton, and M. F. Kessler. Atmospheric emission in the 20-micron window from Mauna Kea. *PASP*, 96:167–173, February 1984.
- [20] M. Burton, D. K. Aitken, D. A. Allen, M. C. B. Ashley, M. G. Burton, R. D. Cannon, B. D. Carter, G. S. Da Costa, M. A. Dopita, M. L. Duldig, P. G. Edwards, P. R. Gillingham, P. J. Hall, A. R. Hyland, P. J. McGregor, J. R. Mould, R. P. Norris,

## BIBLIOGRAPHY

---

- E. M. Sadler, C. H. Smith, J. Spyromilio, and J. W. V. Storey. The scientific potential for astronomy from the Antarctic Plateau. *Proceedings of the Astronomical Society of Australia*, 11:127–150, August 1994.
- [21] Lord Rayleigh. On the light from the sky, its polarization and colour. *Phil. Mag*, 41:107–120,274–279, 1871.
- [22] S. Chandrasekhar. *Radiative Transfer*. Dover Publications, Inc., New York, U.S.A., 1st edition, 1960.
- [23] P.F. Bernath. *Spectra of Atoms and Molecules*. Oxford University Press, New York, U.S.A., 2nd edition, 1995.
- [24] J. Michael Hollas. *Modern Spectroscopy*. John Wiley & Sons, Ltd., Chichester, West Sussex, England, 4th edition, 2005.
- [25] David. J. Griffiths. *Introduction to Quantum Mechanics*. Addison-Wesley, Boston, MA, U.S.A., 2nd edition, 2004.
- [26] R. K. Pathria. *Statistical mechanics*. Butterworth-Heinemann, Linacre House, Jordan Hill, Oxford, U.K., 1st edition, 1972.
- [27] Vladimir I. Tikhonov and Alexander A. Volkov. Separation of Water into Its Ortho and Para Isomers. *Science*, 296(5577):2363–, 2002.
- [28] N. Jacquinet-Husson, N. A. Scott, A. Chédin, L. Crépeau, R. Armante, V. Capelle, J. Orphal, A. Coustenis, C. Boone, N. Poulet-Crovisier, A. Barbe, M. Birk, L. R. Brown, C. Camy-Peyret, C. Claveau, K. Chance, N. Christidis, C. Clerbaux, P. F. Coheur, V. Dana, L. Daumont, M. R. De Backer-Barilly, G. Di Lonardo, J. M. Flaud, A. Goldman, A. Hamdouni, M. Hess, M. D. Hurley, D. Jacquemart, I. Kleiner, P. Köpke, J. Y. Mandin, S. Massie, S. Mikhailenko, V. Nemtchinov, A. Nikitin, D. Newnham, A. Perrin, V. I. Perevalov, S. Pinnock, L. Régalia-Jarlot, C. P. Rinsland, A. Rublev, F. Schreier, L. Schult, K. M. Smith, S. A. Tashkun, J. L. Teffo, R. A. Toth, V. G. Tyuterev, J. Vander Auwera, P. Varanasi, and G. Wagner. The GEISA spectroscopic database: Current and future archive for Earth and planetary atmosphere studies. *Journal of Quantitative Spectroscopy and Radiative Transfer*, 109:1043–1059, April 2008.
- [29] Iouli E. Gordon, Laurence S. Rothman, Robert R. Gamache, David Jacquemart, Chris Boone, Peter F. Bernath, Mark W. Shephard, Jennifer S. Delamere, and Shepard A. Clough. Current updates of the water-vapor line list in HITRAN: A new “diet” for air-broadened half-widths. *Journal of Quantitative Spectroscopy and Radiative Transfer*, 108(3):389 – 402, 2007.
- [30] K. M. Menten, A. Lundgren, A. Belloche, S. Thorwirth, and M. J. Reid. A multi-transition submillimeter water maser study of evolved stars. Detection of a new line near 475 GHz. *Astronomy & Astrophysics*, 477:185–192, January 2008.

## BIBLIOGRAPHY

---

- [31] Allen M. Larar, William B. Cook, Dana C. Gould, Carl S. Mills, and Robert G. Parker. Airborne Imaging Fabry-Perot Interferometer System for Tropospheric Trace Species Detection. In *Earth Science Technology Conference - 2002*. Earth Science Technology Office, NASA, 2002.
- [32] Max Born. *Principles of Optics*. University Press, Cambridge, U.K., 7th edition, 2005.
- [33] Sumner P. Davis, Mark C. Abrams, and James W. Brault. *Fourier Transform Spectrometry*. Academic Press, 1st edition, 2001.
- [34] R. T. Boreiko, T. L. Smithson, T. A. Clark, and H. Wieser. Line strengths and positions of the submillimeter magnetic dipole transitions of O<sub>2</sub>. *Journal of Quantitative Spectroscopy and Radiative Transfer*, 32:109–117, August 1984.
- [35] Grant W. Petty. *A First Course in Atmospheric Radiation*. Sundog Publishing, 2004.
- [36] John T. Houghton. *The physics of atmospheres*. Cambridge University Press, University Press, Cambridge, U.K., 2nd edition, 1986.
- [37] K. N. Liou. *An Introduction to Atmospheric Radiation*. Academic Press, Burlington, MA, U.S.A., 2nd edition, 2002.
- [38] J. T. Houghton, F. W. Taylor, and C. D. Rodgers. *Remote sounding of atmospheres*. Cambridge University Press, University Press, Cambridge, U.K., 1st edition, 1984.
- [39] Barry Schwartz and Mark Govett. A hydrostatically consistent north american radiosonde data base at the forecast systems laboratory, 1946-present. Technical Report NOAA Technical Memorandum ERL FSL-4, Forecast Systems Laboratory, National Oceanic and Atmospheric Administration, Boulder, Colorado, U.S.A., August 1992.
- [40] Richard M. Goody and James C. G. Walker. *Atmospheres*. Prentice-Hall Inc., Englewood Cliffs, New Jersey, U.S.A., 1st edition, 1972.
- [41] David Bolton. The computation of equivalent potential temperature. *Monthly Weather Review*, 108:1046–1053, 1980.
- [42] R. R. Phillips, D. A. Naylor, J. di Francesco, and B. Gom. Initial results of field testing an infrared water vapor monitor for millimeter astronomy (IRMA III) on Mauna Kea. In J. M. Oschmann Jr., editor, *Society of Photo-Optical Instrumentation Engineers (SPIE) Conference Series*, volume 5489 of *Presented at the Society of Photo-Optical Instrumentation Engineers (SPIE) Conference*, pages 146–153, October 2004.
- [43] D. A. Naylor, R. R. Phillips, J. di Francesco, T. L. Bourke, R. R. Querel, and S. C. Jones. IRMA as a Potential Phase Correction Instrument: Results from the SMA Test Campaign. *International Journal of Infrared and Millimeter Waves*, 29:1196–1204, December 2008.
- [44] A. Otárola, T. Travouillon, M. Schöck, S. Els, R. Riddle, W. Skidmore, R. Dahl, D. Naylor, and R. Querel. Thirty Meter Telescope Site Testing X: Precipitable Water Vapor. *PASP*, 122:470–484, April 2010.

## BIBLIOGRAPHY

---

- [45] H. Kurlandczyk and M. Sarazin. Remote sensing of precipitable water vapour and cloud cover for site selection of the European Extremely Large Telescope (E-ELT) using MERIS. In *Society of Photo-Optical Instrumentation Engineers (SPIE) Conference Series*, volume 6745 of *Society of Photo-Optical Instrumentation Engineers (SPIE) Conference Series*, October 2007.
- [46] J. L. Bezy and M. Rast. The ESA Medium Resolution Imaging Spectrometer MERIS a review of the instrument and its mission. *International Journal of Remote Sensing*, 20:1681–1702, June 1999.
- [47] J. Fischer and R. Bennartz. Algorithm theoretical basis document: Retrieval of total water vapour content from meris measurements. Technical Report ESA Reference: PO-TN-MEL-GS-0005, ESA-ESTEC, Noordwijk, Netherlands, 1997.
- [48] Z. Li, J.-P. Muller, P. Cross, P. Albert, T. Hewison, R. Watson, J. Fisher, and R. Bennartz. Validation of MERIS Near IR Water Vapour Retrievals Using MWR and GPS Measurements. In *MERIS User Workshop*, volume 549 of *ESA Special Publication*, May 2004.
- [49] D. A. Erasmus and M. S. Sarazin. Forecasting precipitable water vapor and cirrus cloud cover for astronomical observatories: satellite image processing guided by synoptic model dissemination data. In J. E. Russell, K. Schaefer, & O. Lado-Bordowsky, editor, *Society of Photo-Optical Instrumentation Engineers (SPIE) Conference Series*, volume 4168 of *Presented at the Society of Photo-Optical Instrumentation Engineers (SPIE) Conference*, pages 317–328, January 2001.
- [50] B. J. Soden, D. D. Turner, B. M. Lesht, and L. M. Miloshevich. An analysis of satellite, radiosonde, and lidar observations of upper tropospheric water vapor from the Atmospheric Radiation Measurement Program. *Journal of Geophysical Research (Atmospheres)*, 109:4105, February 2004.
- [51] Erasmus D.A. Precipitable water vapour at SKA telescope candidate sites: Derivation from rawinsonde data and a discussion of alternative measurement methods. Technical Report SKA Memo 59, Square Kilometre Array, 2005.
- [52] D. Erasmus and M. Sarazin. Utilizing satellite data for evaluation and forecasting applications at astronomical sites. In J. Vernin, Z. Benkhaldoun, & C. Muñoz-Tuñón, editor, *Astronomical Site Evaluation in the Visible and Radio Range*, volume 266 of *Astronomical Society of the Pacific Conference Series*, page 310, 2002.
- [53] K. P. Rao. *Weather satellites: Systems, data and environmental applications*. 1990.
- [54] B. J. Soden and F. P. Bretherton. Upper tropospheric relative humidity from the GOES 6.7  $\mu\text{m}$  channel: Method and climatology for July 1987. *Journal of Geophysical Research*, 98:16669–16688, September 1993.
- [55] B. J. Soden and J. R. Lanzante. An Assessment of Satellite and Radiosonde Climatologies of Upper-Tropospheric Water Vapor. *Journal of Climate*, 9:1235–1250, June 1996.



## BIBLIOGRAPHY

---

- [56] J. Weinreb, J.X. Johnson, and D. Han. Conversion of GVAR Infrared Data to Scene Radiance or Temperature. Technical report, NOAA Technical Memorandum, NOAA NESDIS Office of Satellite Operations, 2009.
- [57] R. Bernstein, S. A. Shectman, S. M. Gunnels, S. Mochnacki, and A. E. Athey. MIKE: A Double Echelle Spectrograph for the Magellan Telescopes at Las Campanas Observatory. In M. Iye and A. F. M. Moorwood, editors, *Instrument Design and Performance for Optical/Infrared Ground-based Telescopes. Edited by Iye, Masanori; Moorwood, Alan F. M. Proceedings of the SPIE, Volume 4841, pp. 1694-1704 (2003).*, volume 4841 of *Presented at the Society of Photo-Optical Instrumentation Engineers (SPIE) Conference*, pages 1694–1704, March 2003.
- [58] J. W. Brault, J. S. Fender, and D. N. B. Hall. Absorption Coefficients of Selected Atmospheric Water Lines. *Journal of Quantitative Spectroscopy and Radiative Transfer*, 15:549–551, 1975.
- [59] J. Thomas-Osip, A. McWilliam, M. M. Phillips, N. Morrell, I. Thompson, T. Folkers, F. C. Adams, and M. Lopez-Morales. Calibration of the Relationship between Precipitable Water Vapor and 225 GHz Atmospheric Opacity via Optical Echelle Spectroscopy at Las Campanas Observatory. *PASP*, 119:697–708, June 2007.
- [60] C. B. Markwardt. Non-linear Least-squares Fitting in IDL with MPFIT. In D. A. Bohlender, D. Durand, & P. Dowler, editor, *Astronomical Society of the Pacific Conference Series*, volume 411 of *Astronomical Society of the Pacific Conference Series*, page 251, September 2009.
- [61] R. R. Querel, D. A. Naylor, J. Thomas-Osip, G. Prieto, and A. McWilliam. Comparison of precipitable water vapour measurements made with an optical echelle spectrograph and an infrared radiometer at Las Campanas Observatory. In *Society of Photo-Optical Instrumentation Engineers (SPIE) Conference Series*, volume 7014 of *Presented at the Society of Photo-Optical Instrumentation Engineers (SPIE) Conference*, August 2008.
- [62] J. Thomas-Osip, G. Prieto, A. McWilliam, M.W. Phillips, P. McCarthy, M. Johns, R.R. Querel, and D.A. Naylor. Giant Magellan Telescope Site Testing: PWV Statistics and Calibration. In *Society of Photo-Optical Instrumentation Engineers (SPIE) Conference Series*, volume 7733-169 of *Presented at the Society of Photo-Optical Instrumentation Engineers (SPIE) Conference*, June 2010.
- [63] Jorge J. Moré. *The Levenberg-Marquardt Algorithm: Implementation and Theory, in \*Numerical Analysis\*, Lecture Notes in Mathematics 630.* Springer-Verlag, 1977.
- [64] H.-U. Kaeuffl, P. Ballester, P. Biereichel, B. Delabre, R. Donaldson, R. Dorn, E. Fedrigo, G. Finger, G. Fischer, F. Franza, D. Gojak, G. Huster, Y. Jung, J.-L. Lizon, L. Mehrgan, M. Meyer, A. Moorwood, J.-F. Pirard, J. Paufigue, E. Pozna, R. Siebenmorgen, A. Silber, J. Stegmeier, and S. Wegerer. CRIRES: a high-resolution infrared spectrograph for ESO’s VLT. In A. F. M. Moorwood & M. Iye, editor, *Society of Photo-Optical Instrumentation Engineers (SPIE) Conference Series*, volume 5492 of

## BIBLIOGRAPHY

---

- Society of Photo-Optical Instrumentation Engineers (SPIE) Conference Series*, pages 1218–1227, September 2004.
- [65] P. O. Lagage, J. W. Pel, M. Authier, J. Belorgey, A. Claret, C. Doucet, D. Dubreuil, G. Durand, E. Elswijk, P. Girardot, H. U. Käufl, G. Kroes, M. Lortholary, Y. Lussignol, M. Marchesi, E. Pantin, R. Peletier, J.-F. Pirard, J. Pragt, Y. Rio, T. Schoenmaker, R. Siebenmorgen, A. Silber, A. Smette, M. Sterzik, and C. Veyssiere. Successful Commissioning of VISIR: The Mid-Infrared VLT Instrument. *The Messenger*, 117:12–16, September 2004.
- [66] A. Smette, H. Horst, and J. Navarette. Measuring the Amount of Precipitable Water Vapour with VISIR. In A. Kaufer and F. Kerber, editors, *The 2007 ESO Instrument Calibration Workshop: Proceedings of the ESO Workshop held in Garching, Germany, 23-26 January 2007, ESO Astrophysics Symposia European Southern Observatory, Volume . ISBN 978-3-540-76962-0. Springer-Verlag Berlin Heidelberg, 2008*, page 433. 2008.
- [67] A. Kaufer, O. Stahl, S. Tubbesing, P. Nørregaard, G. Avila, P. Francois, L. Pasquini, and A. Pizzella. Commissioning FEROS, the new high-resolution spectrograph at La-Silla. *The Messenger*, 95:8–12, March 1999.
- [68] H. Dekker, S. D’Odorico, A. Kaufer, B. Delabre, and H. Kotzlowski. Design, construction, and performance of UVES, the echelle spectrograph for the UT2 Kueyen Telescope at the ESO Paranal Observatory. In M. Iye & A. F. Moorwood, editor, *Society of Photo-Optical Instrumentation Engineers (SPIE) Conference Series*, volume 4008 of *Society of Photo-Optical Instrumentation Engineers (SPIE) Conference Series*, pages 534–545, August 2000.
- [69] G. Avila, V. Burwitz, C. Guirao, J. Rodriguez, R. Shida, and D. Baade. BACHES A Compact Light-Weight Echelle Spectrograph for Amateur Astronomy. *The Messenger*, 129:62–64, September 2007.
- [70] M. Mayor, F. Pepe, D. Queloz, F. Bouchy, G. Rupprecht, G. Lo Curto, G. Avila, W. Benz, J.-L. Bertaux, X. Bonfils, T. Dall, H. Dekker, B. Delabre, W. Eckert, M. Fleury, A. Gilliotte, D. Gojak, J. C. Guzman, D. Kohler, J.-L. Lizon, A. Longinotti, C. Lovis, D. Megevand, L. Pasquini, J. Reyes, J.-P. Sivan, D. Sosnowska, R. Soto, S. Udry, A. van Kesteren, L. Weber, and U. Weilenmann. Setting New Standards with HARPS. *The Messenger*, 114:20–24, December 2003.
- [71] S. D’Odorico, H. Dekker, R. Mazzoleni, J. Vernet, I. Guinouard, P. Groot, F. Hammer, P. K. Rasmussen, L. Kaper, R. Navarro, R. Pallavicini, C. Peroux, and F. M. Zerbi. X-shooter UV- to K-band intermediate-resolution high-efficiency spectrograph for the VLT: status report at the final design review. In *Society of Photo-Optical Instrumentation Engineers (SPIE) Conference Series*, volume 6269 of *Society of Photo-Optical Instrumentation Engineers (SPIE) Conference Series*, July 2006.
- [72] R.R. Querel, F. Kerber, G. Lo Curto, J. Thomas-Osip, G. Prieto, A. Chacón, O. Cuevas, D. Pozo, J. Marín, D.A. Naylor, M. Curé, M.S. Sarazin, C. Guirao, and

## BIBLIOGRAPHY

---

- G. Avila. Support for site testing of the European Extremely Large Telescope: precipitable water vapor over La Silla. volume 7733-155 of *Proc. SPIE*, June 2010.
- [73] A. Chacón, O. Cuevas, D. Pozo, J. Marín, A. Oyanadel, C. Dognac, L. Cortes, L. Illanes, M. Caneo, M. Curé, M.S. Sarazin, F. Kerber, A. Smette, D. Rabanus, R.R. Querel, and G. Tompkins. Measuring and forecasting of PWV above La Silla, APEX and Paranal Observatories. volume 7733-166 of *Proc. SPIE*, June 2010.
- [74] F. Kerber, R.R. Querel, R.W. Hanuschik, A. Chacón, M. Caneo, L. Cortes, M. Curé, L. Illanes, D.A. Naylor, A. Smette, M.S. Sarazin, D. Rabanus, and G. Tompkins. Support for site testing of the European Extremely Large Telescope: precipitable water vapor over Paranal. volume 7733-54 of *Proc. SPIE*, June 2010.
- [75] M. Schneider, P. M. Romero, F. Hase, T. Blumenstock, E. Cuevas, and R. Ramos. Continuous quality assessment of atmospheric water vapour measurement techniques: FTIR, Cimel, MFRSR, GPS, and Vaisala RS92. *Atmospheric Measurement Techniques*, 3:323–338, March 2010.
- [76] J. Wang, L. Zhang, A. Dai, T. Van Hove, and J. Van Baelen. A near-global, 2-hourly data set of atmospheric precipitable water from ground-based GPS measurements. *Journal of Geophysical Research (Atmospheres)*, 112:11107, June 2007.
- [77] M. McKinnon. Measurement of Atmospheric Opacity Due to Water Vapor at 225 GHz. Technical report, ALMA Memo, 1987.
- [78] A. Stirling, R. Hills, J. Richer, and J. Pardo. 183 GHz water vapour radiometers for ALMA: Estimation of phase errors under varying atmospheric conditions. Technical report, ALMA Memo, 2004.
- [79] K. J. Thome, B. M. Herman, and J. A. Reagan. Determination of Precipitable Water from Solar Transmission. *Journal of Applied Meteorology*, 31:157–165, February 1992.
- [80] K. J. Thome, M. W. Smith, J. M. Palmer, and J. A. Reagan. Three-channel solar radiometer for the determination of atmospheric columnar water vapor. *Applied Optics*, 33:5811–5819, Aug 1994.
- [81] J. R. Schott. *Remote sensing: the image chain approach*. Oxford University Press, Inc., 198 Madison Avenue, New York, New York, U.S.A., 2nd edition, 2007.
- [82] E. Hecht. *Optics 2nd edition*. Reading MA: Addison-Wesley Publishing Company, 1987.
- [83] E. Loewen, editor. *Diffraction Gratings Handbook 5th Edition*. Thermo RGL, Richardson Grating Laboratory, Rochester, New York, 2002.

---

## Appendix A

# Methods of Measuring Water Vapour: Lunar Absorption Spectrophotometer

### A.1 Overview

A novel instrument has been designed to measure the atmospheric water vapour column abundance by near-infrared absorption spectrophotometry of the moon. The instrument provides a simple, inexpensive, portable and effective means of measuring rapidly the water vapour content along the lunar line-of-sight. Moreover, the instrument is relatively insensitive to the atmospheric model used and has the potential to provide an effective, independent calibration for other measures of precipitable water vapour from both ground and space-based platforms.

### A.2 Introduction

Determination of atmospheric water vapour content is important to ground-based astronomy due to its strong absorption, and thus emission, characteristics in the infrared spectral region. In addition, the distribution of water vapour can be highly dynamic, varying dramatically, both spatially and temporally. Thus, any practical method for measuring and monitoring the water vapour abundance in real-time has direct applications in ground-based infrared astronomy and by extension in space-based terrestrial remote sensing.

The impetus behind the development of the lunar spectrophotometer was to provide an independent measurement of PWV in order to validate the calibration of an infrared radiometer, IRMA, which was developed by our group to determine PWV by measuring the emission of water vapour at  $20\ \mu\text{m}$  [19]. Its usefulness becomes particularly important at remote sites where alternate measures of PWV are not available. The lunar spectrophotometer, is a simple, compact and lightweight device, which measures the atmospheric water vapour content by absorption spectroscopy of the moon using four spectral bands centred around  $0.95\ \mu\text{m}$ . Two of these bands are carefully chosen to include transitions from atmospheric water vapour (on-band), while the other two bands measure the continuum at

### A.3. BACKGROUND

---

adjacent regions of the spectrum (off-band). The ratio of on-band to off-band radiance measurements can be used with an atmospheric model, BTRAM [2], to derive the PWV. Results from the prototype instrument are presented and their values compared with other, simultaneously available, measurements of PWV, including radiosondes launched at the observing site.

#### A.3 Background

Studies have shown that water vapour is the largest source of opacity in the infrared and severely limits ground-based infrared astronomy. Water vapour has a multitude of transitions from the visible into the far-infrared. While in the far-infrared, water vapour is the dominant source of opacity, a lesser but still significant amount of absorption occurs in the near-infrared region, around 0.95  $\mu\text{m}$ . The lunar spectrophotometer is designed to measure absorption in this region.

Several methods exist for estimating water vapour column abundance, including heterodyne receivers (183 and 225 GHz) [77, 78], emission measuring radiometers (IRMA) [1, 16, 18, 42, 43], solar reflectance-based satellite measurements [46], absorption-based estimates using high-resolution echelle spectrographs [57, 58, 59, 61], through to direct measurements with radiosonde instrumentation.

Calibration is a challenging problem for all radiometers and particularly for those operating in the thermal infrared. The lunar photometer, by virtue of the fact that it operates at a wavelength at which the atmosphere emits virtually no radiation, provides a robust calibration point, since the derived PWV values are relatively insensitive to the atmospheric profile used in the model.

IRMA, the Infrared Radiometer for Millimetre Astronomy, is based around a cryo-cooled, photoconductive HgCdTe detector. The detector has its maximum sensitivity at a wavelength of  $\sim 20 \mu\text{m}$ , which is near the peak of the Planck curve for typical atmospheric temperatures ( $\sim 260 \text{ K}$ ), and in a region that contains many strong transitions from atmospheric water vapour [19]. IRMA observes atmospheric emission in a spectral band on the order of  $\sim 2 \mu\text{m}$  centred at a wavelength of  $\sim 20 \mu\text{m}$ . The detected flux is converted to PWV by use of a sophisticated atmospheric radiative transfer model. Studies have shown that temperature and scale height of water vapour are dominant factors affecting the retrieved PWV in the atmospheric model [18]. Simultaneously, base pressure and adiabatic lapse rate are less important model parameters. Since it operates in the thermal-infrared region, however, IRMA is sensitive to any source of stray radiation from ambient temperature sources which may be in the field of view and thus requires careful calibration.

#### A.4 Lunar spectrophotometer

In contrast to the thermal-infrared, the atmosphere is mostly transparent at visible wavelengths. In the near-infrared (i.e. 700–1000 nm), however, there exist several absorption bands due to oxygen and water vapour. Since, in most cases, from high altitude sites, these transitions occur in the weak regime of radiative transfer, the absorption across these bands is directly proportional to the amount of water vapour in the simulated atmosphere.

## A.5. DESIGN

---

By measuring the reduction in transmission across bands selected to contain transitions from atmospheric water vapour, and by use of an atmospheric model, it is possible to derive the PWV.

The concept is illustrated in Figure A.1. Bands A and D are the so-called off-bands, while B spans a region of weaker water vapour transitions and could be used to probe high PWV amounts, whereas region C has strong transitions and would thus be limited to probing lower PWV amounts due to the early onset of line saturation.

As seen in Figure A.1, the principal water vapour absorption region that is employed in this scheme is centred near 950 nm, while the continuum measures are determined in bands centred at 850 nm and 1000 nm, respectively. The technique to derive water vapour from the absorption measurement is shown in Figure A.3.

This technique has been used extensively by instruments making day-time measurements of ozone, aerosols and water vapour abundance by using the sun as a source [79, 80]. In principle, the technique could be extended to use the light emitted from the photosphere from a star, but this would require a telescope with a large collecting area. An intermediate solution, and the one we have adopted, is to use the moon as a source and a small (diameter 100 mm) telescope aperture. Since the moon acts as a diffuse reflector of solar irradiance, it has a well defined spectrum. The continuum level corresponding to the zero absorption case,  $L'_C$  is determined from the off-band measurements. The ratio of the measured radiance,  $L_C$ , to  $L'_C$ , in combination with the atmospheric model, is used to yield PWV.

### A.5 Design

The detailed design of the lunar spectrophotometer will be presented elsewhere, but is summarised here. As depicted in Figure A.4, the instrument consists of a small, off-axis parabolic telescope, which directs light to a filter wheel containing four filters (shown as the coloured bands in Figure A.1), which is mounted immediately in front of a Silicon photodiode<sup>1</sup>. Since atmospheric water vapour varies on timescales of <1 s, and measurements of all four bands must occur within this time, a relatively fast detector was required; the photodiode, with its  $\sim 10$  ns rise/fall time, easily met this requirement. The fast time response also removed the requirement for active lunar tracking. Si photodiodes, which are sensitive over the range of interest, provide a simple and inexpensive detector solution. Moreover, they operate at room temperature, eliminating the need for complex cooling systems, such as those required for the IRMA HgCdTe detectors.

### A.6 Calibration and operation

The four filter transmission profiles (shown in Figure A.1) were measured using a grating spectrometer with three overlapping detector bands providing spectral coverage from the visible through to the near-infrared (350–2500 nm)<sup>2</sup> and a Tungsten Halogen

---

<sup>1</sup>FDS100 Silicon Photodiode. ThorLabs, Inc. <http://www.thorlabs.com/>

<sup>2</sup>FieldSpec 3 Hi-Res. ASD, Inc. <http://www.asdi.com/>

## A.6. CALIBRATION AND OPERATION

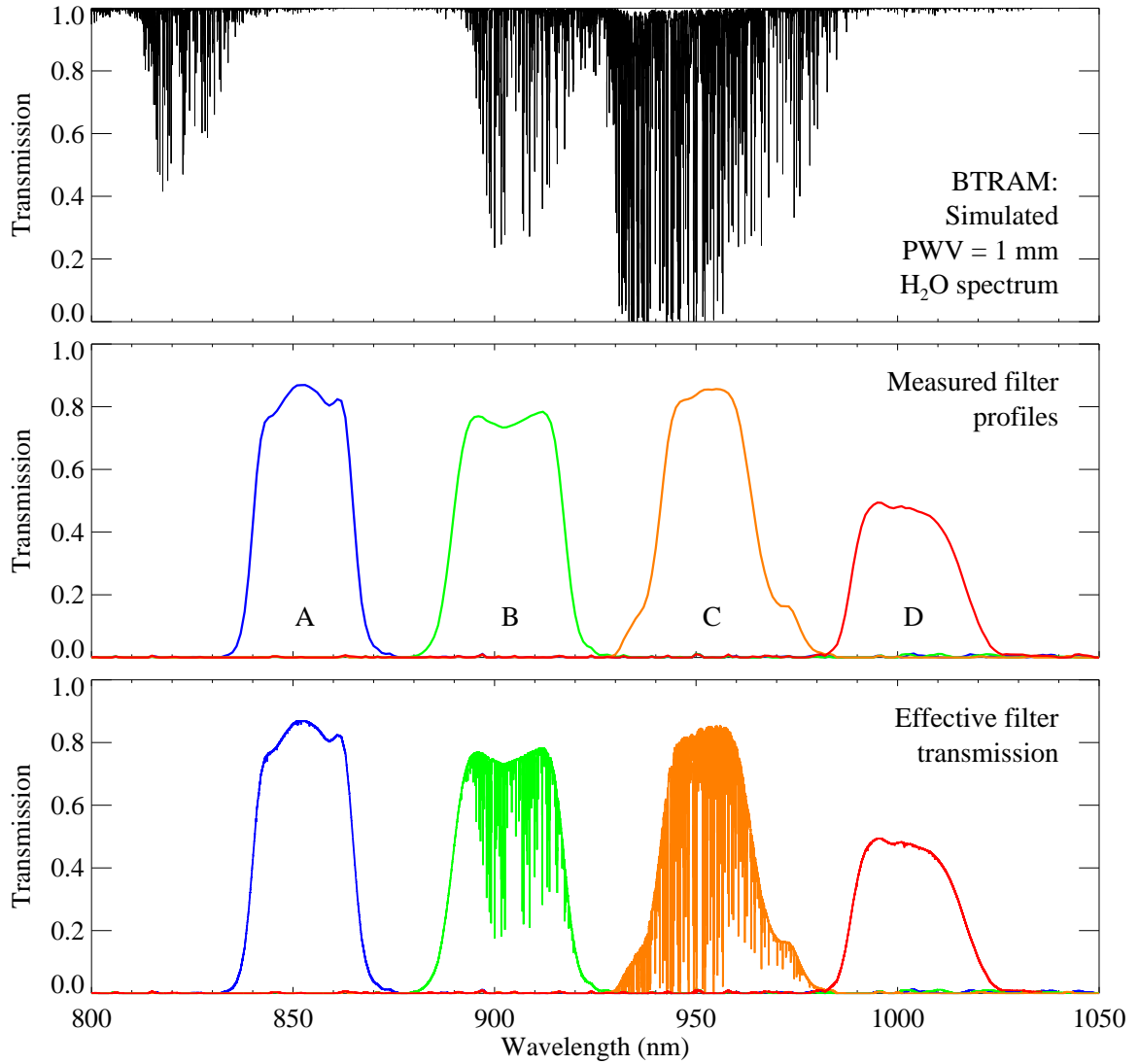


**Figure A.1:** The top window shows a simulated water vapour transmission spectrum for the atmosphere above the La Silla Paranal Observatory in Chile situated at an elevation of  $\sim 2400$  m. The simulated spectrum was calculated using the BTRAM software for a PWV of 1 mm at a spectral resolution of 0.001 nm. The middle window shows the measured transmission profiles for the four filters being used in the instrument. The bottom window shows the effective transmission through each of the four filtered spectral bands. Regions A and D have negligible absorption, whereas regions B and C exhibit weak and strong absorption, respectively.

## A.6. CALIBRATION AND OPERATION

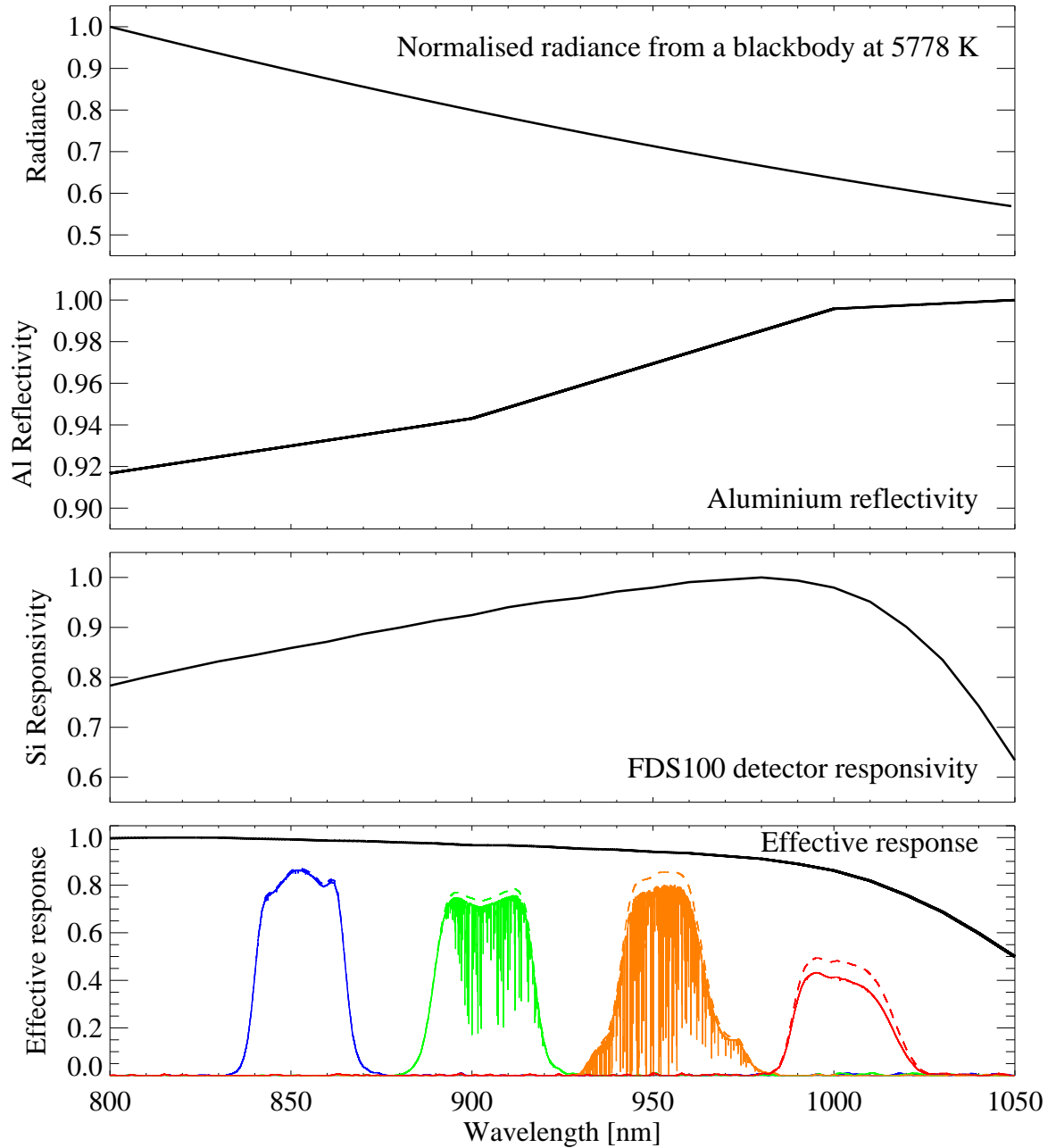


**Figure A.2:** All windows are normalised. The top window shows the Planck emission (normalised radiance per unit wavelength) from a blackbody at 5778 K, the assumption being that the continuum emission of the sun is reflected without the addition of any spectral features due to the lunar surface. The second window shows the reflectivity of aluminium. The third window shows the manufacturer's specifications for the response of the Silicon photodetector used in this system. In the bottom window the profiles from the top three windows are combined into an effective response of the lunar photometer. This is then applied to the filter transmissions from Figure A.1 and the resulting effective response of the lunar photometer is overplotted. The dotted curves represent the unaltered filter transmission profiles from the middle window of Figure A.1 for the sake of comparison.



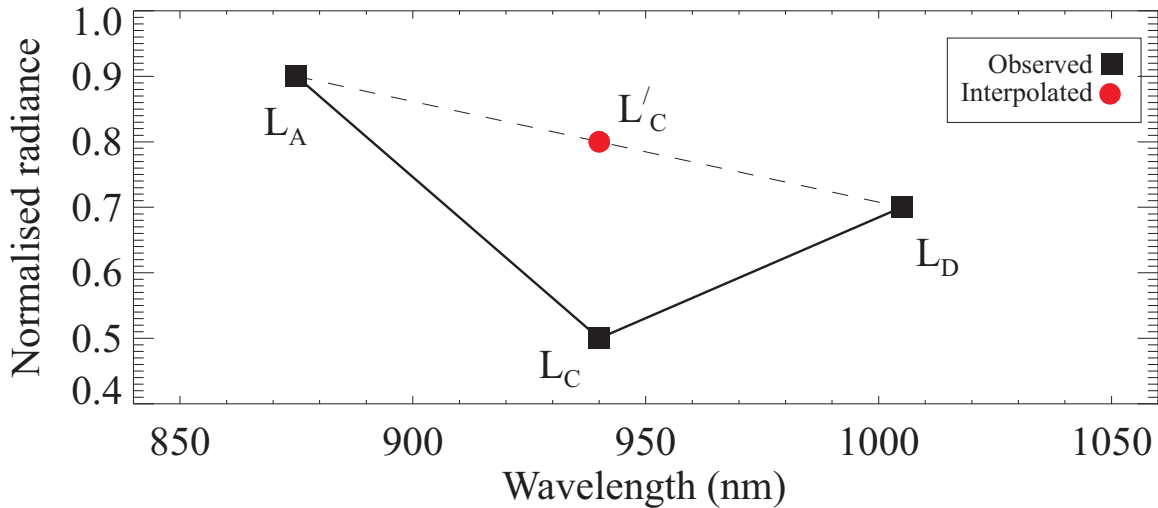


**Figure A.3:** Illustration of the technique used to determine absorber abundance through a sequence of on- and off-band measurements.  $L_A$  and  $L_D$  are the observed radiance within bands A and D (Figure A.1). These two measurements serve to establish the continuum radiance,  $L'_C$ . The ratio of the measured radiance,  $L_C$  to  $L'_C$ , yields a band transmission which is used to derive PWV [81].

broadband light source<sup>3</sup>.

To calibrate the detector and filter assembly, a compact grating spectrometer<sup>4</sup> was used in conjunction with an integrating sphere<sup>5</sup>. The combination of integrating sphere and its collimated light source were used to provide diffuse, uniform illumination. A fiber optic cable was mounted to the integrating sphere, and attached to the high resolution Universal Serial Bus (USB) spectrometer. This allowed us to measure the apparent spectrum of the halogen bulb/integrating sphere system. The detector, complete with filter wheel assembly, was positioned at an open port of the integrating sphere. Detector signal voltages were measured on a digital multimeter while the filter wheel was manually rotated between the four filters.

Once the relative sensitivity between adjacent channels was determined, the detector and filter wheel were integrated with the off-axis parabolic telescope mirror. A high-speed USB data acquisition board<sup>6</sup> was used to record the detector signal voltage. On May 10, 2009, when the moon was nearly full (to maximise the potential signal) several measurements, over all bands, were recorded, with one representative period shown in Figure A.6.

<sup>3</sup>LS-1 Tungsten Halogen Light Source. <http://www.oceanoptics.com/>

<sup>4</sup>USB4000-VIS-NIR Miniature Fiber Optic Spectrometer. <http://www.oceanoptics.com/>

<sup>5</sup>RTS-3ZC Integrating Sphere. ASD, Inc. <http://www.asdi.com/>

<sup>6</sup>Data Translation DT9822, <http://www.datatranslation.com/>

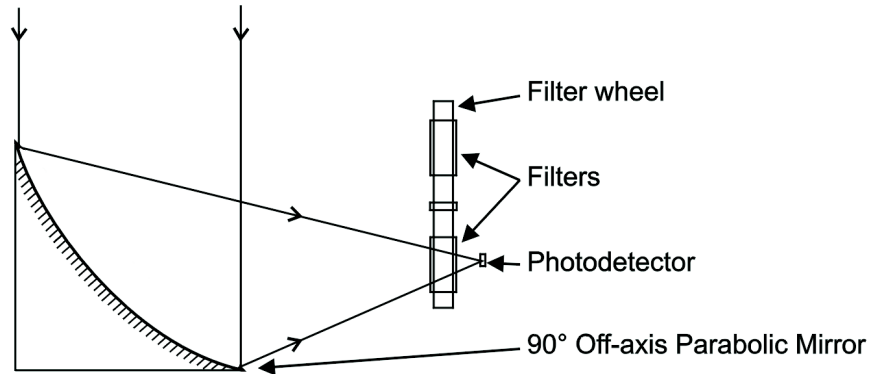


**Figure A.4:** Optical design schematic of the lunar spectrophotometer.

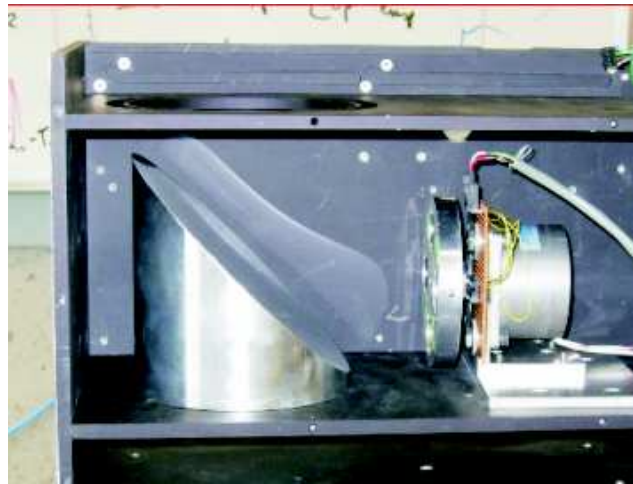


**Figure A.5:** Interior photo of the lunar spectrophotometer.

### A.7 Data processing

As mentioned previously, an atmospheric model developed by our group, BTRAM, was used to calculate the expected incident flux on the detector using the effective response of the system as shown in Figure A.2. To convert the lunar measurements shown in Figure A.6 into PWV, a model atmosphere is required. The measurements were performed in central and northern Chile, so a simulated spectrum was created using parameters applicable to that location, i.e., adiabatic lapse rate, elevation, local ambient temperature and pressure. This model was computed for 1 mm PWV. The transmission spectrum was multiplied by each of the filter profiles to compute the flux that would be expected on the detector, as seen in the three panels of Figure A.1. The integrated band flux was expressed as a mean band absorption. This process was repeated for PWV values from 1.1 – 20 mm. In each case, the 1 mm PWV spectrum was converted to opacity, linearly scaled, and then converted back

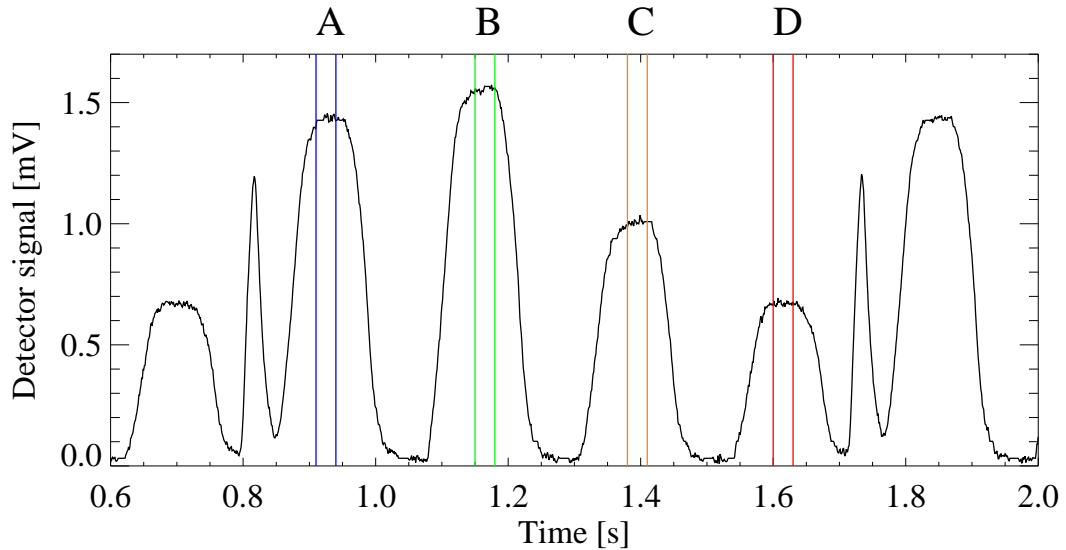


**Figure A.6:** Time-series data from the lunar spectrophotometer detector as recorded by a high-speed USB data acquisition board. One period of the filter bands (from Figure A.1) are delineated with the colour bars. A notch in the filter wheel used as a position check is marked by the violet bar at  $\sim 0.8$  s in this plot. The bands labels (A,B,C,D) are defined in Figure A.1.

to transmission. The relationship between opacity and transmission is given as  $T = e^{-\tau}$ , where  $\tau$  is opacity. As transmission in the water absorption band decreases with increasing PWV, flux is also expected to decrease, as shown by the dashed curve in Figure A.9.

## A.8 Results

As part of a PWV measurement campaign, observations with the lunar spectrophotometer were taken over the period from May 8–13, 2009, at La Silla and August 1–7 at the Paranal Observatory in central Chile. The instrument and installation at the ESO 1-m telescope at La Silla are shown in Figure A.8. *In situ* measurements of PWV were derived from radiosondes launched from the sites at 00, 06 and 12 UT. The ratio of the 850 nm and 950 nm band fluxes was associated to PWV from a contemporaneous radiosonde launch. These normalised band fluxes were plotted against PWV and compared to the theoretically expected values. The dashed line in Figure A.9 shows the theoretical curve with a gain applied. The agreement is quite good and suggests that with a larger set of measurements, it will be possible to validate the theoretical model, and finally invert it to allow for direct retrieval of PWV from a band flux ratio. The lunar spectrophotometer could then provide an effective, low-cost means of determining atmospheric water vapour columnar abundance.

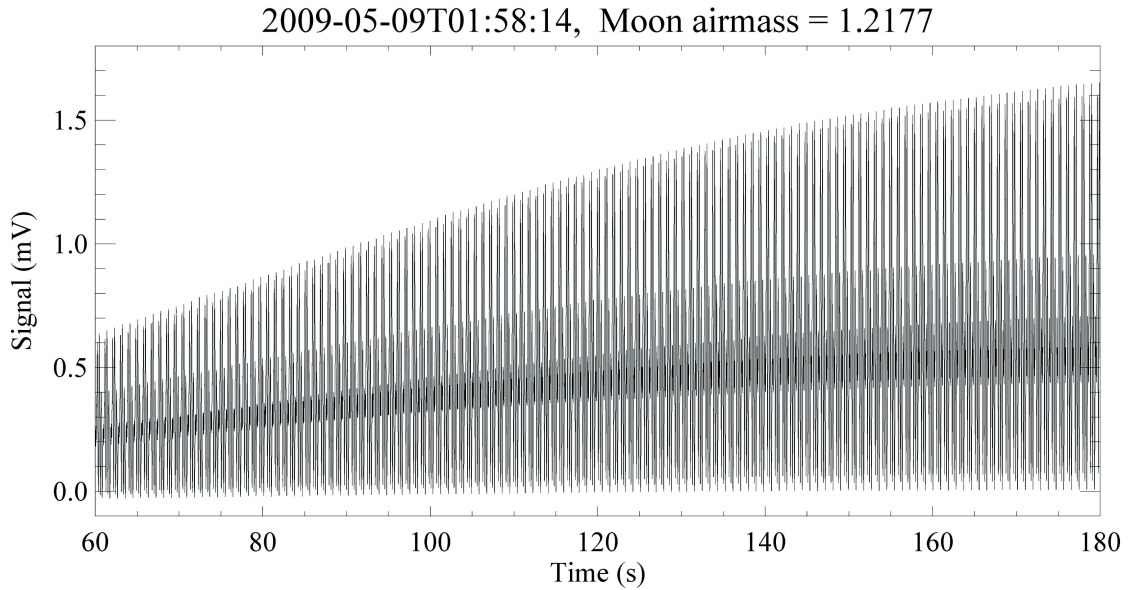


**Figure A.7:** Two minutes of signal from the detector clearly shows that a lunar tracking system would be beneficial.

### A.9 Further work

The lunar spectrophotometer and these proof-of-concept measurements have validated our main hypothesis and demonstrated the potential utility of this instrument. Much can be gained by the addition of a lunar tracking system, which would facilitate long integration times. The preliminary results indicate that once reasonably calibrated, with a sound theoretical model, the lunar spectrophotometer will provide a simple and effective means of determining the PWV along the lunar line-of-sight.

## A.9. FURTHER WORK

---

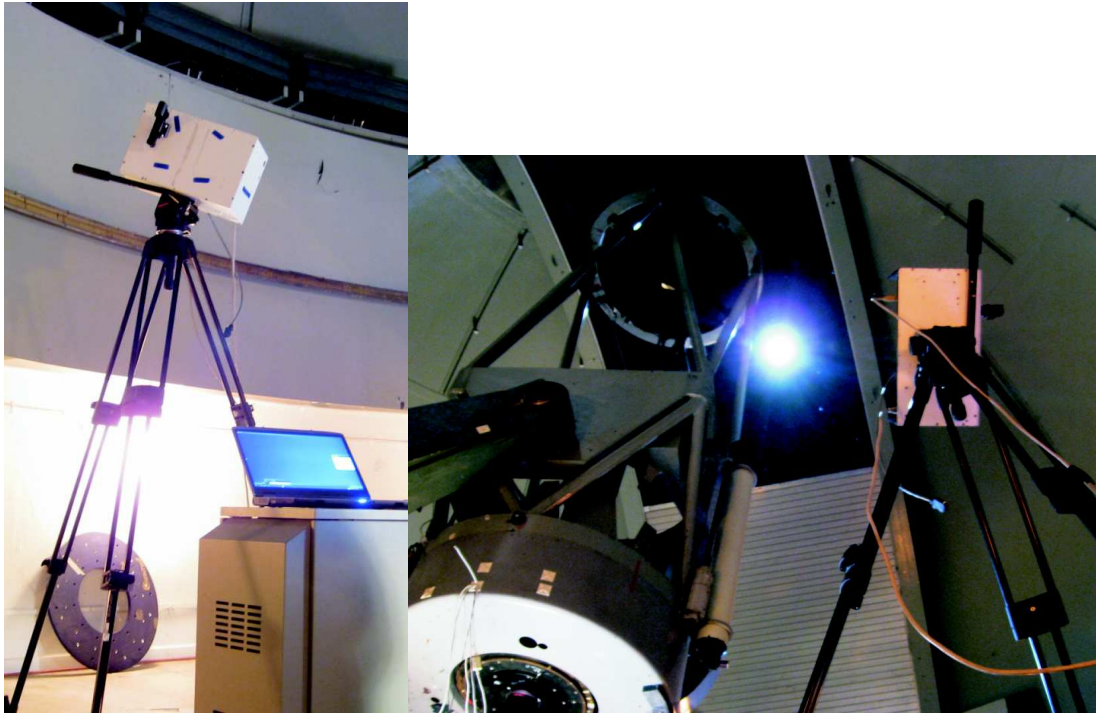


**Figure A.8:** The lunar spectrophotometer mounted on a tripod (left). The moon, as viewed through the open dome above the ESO, 1-meter telescope at La Silla Paranal Observatory, Chile (right).

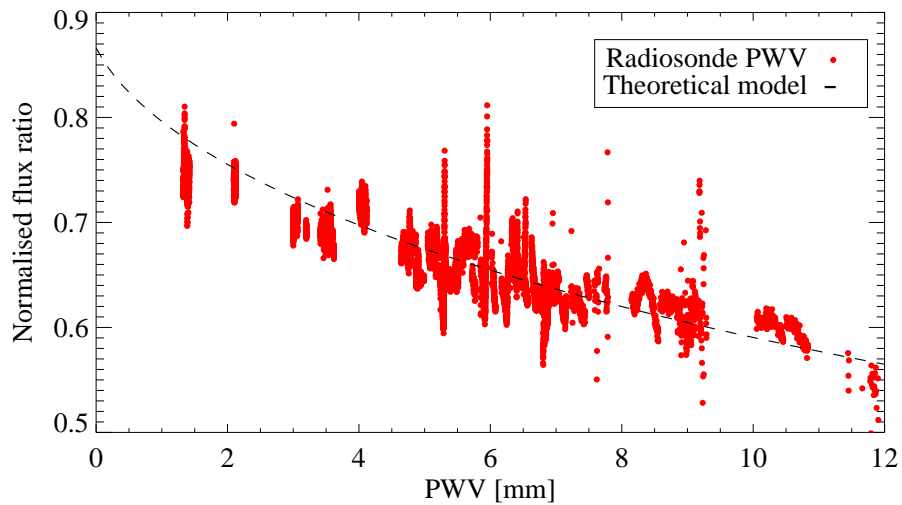


**Figure A.9:** Comparison between PWV and measured and theoretical expected flux ratio from the 850 and 950 nm lunar spectrometer bands. The measured flux ratios were associated with contemporaneous PWV values from radiosonde launches. As more data are acquired and the theoretical relationship is confirmed, it could be inverted to retrieve PWV from band flux ratios.

---

## Appendix B

# Fundamentals of Diffraction Grating Spectrometers

Since several of the instruments used in the PWV measurements campaigns are based upon the diffraction grating, I include a brief summary of the relevant physics.

### B.1 Spectrometers

A spectrometer is a device used to measure the intensity variation with wavelength of an astronomical source. A typical spectrometer contains fore-optics, a dispersive element (a prism or a grating), post-optics and a detector, shown schematically in Figure B.1. The fore-optics collimate the input radiation to illuminate uniformly the dispersive element. The post-optics subsequently focus the dispersed light onto the detector. The dispersive element results in a wavelength dependent change in direction of the incident radiation. In a prism this is accomplished by the wavelength dependent refractive index of the medium. In a diffraction grating this is accomplished by the resonance condition of the multiple beam interference of each of the facets in the grating. Finally, the detector converts the incident light into an electric signal that is amplified, digitised, and recorded by suitable electronics. The detector itself will in general have a non-uniform frequency response which must be taken into account when calibrating the spectrometer.

### B.2 Diffraction grating

MIKE [57] is a cross-dispersed, echelle, diffraction grating spectrometer, which exploits the principle of multiple beam interference [82]. The grating itself consists of a periodic set of slits or grooves that together act as diffracting elements. There are two types of diffraction gratings, transmission or reflecting, and their principle of operation is identical. The vast majority of research grade diffraction spectrometers utilise reflective gratings. The schematic of a reflective grating is shown in Figure B.2, where two parallel light rays are incident on adjacent facets of the grating, a distance  $d$  apart. The two rays are in phase at wavefront  $A$ . After diffraction at angle  $\beta$ , the rays will again be in phase at wavefront  $B$  if the difference in their path lengths,  $d \sin\alpha + d \sin\beta$ , is a multiple of the

## B.2. DIFFRACTION GRATING

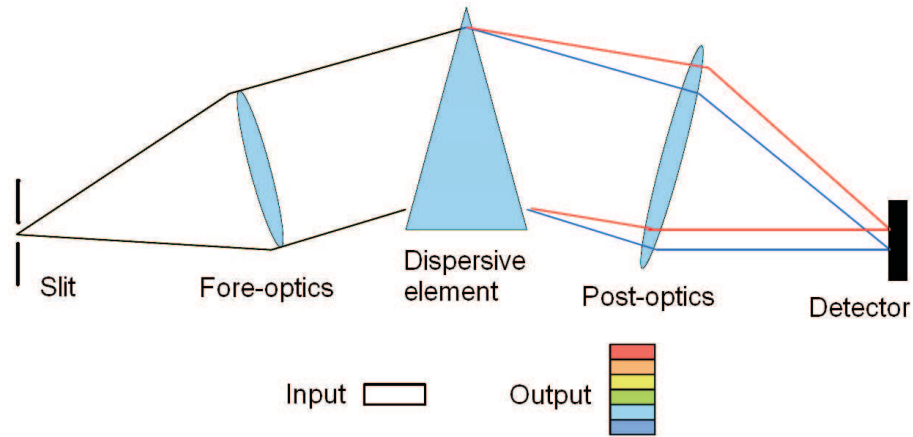


**Figure B.1:** A simple spectrograph consisted of (from left to right) a fore-optics, a dispersive element (shown here as a prism), post-optics and a detector.

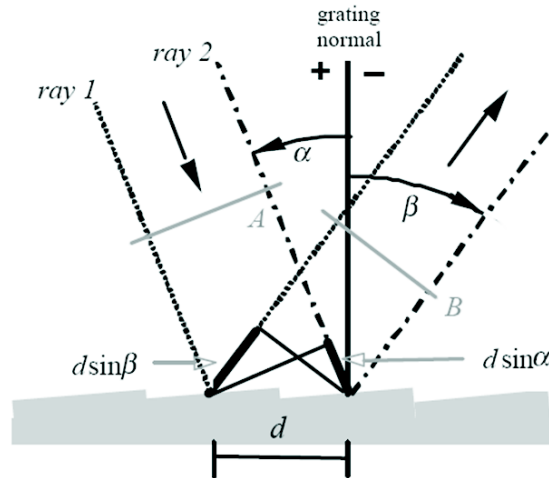


**Figure B.2:** Geometry of diffraction for planar wavefronts.

wavelength. This relationship can be expressed as:

$$m\lambda = d[\sin\alpha + \sin\beta] \quad (\text{B.1})$$

which is known as the grating equation. In this equation,  $m$  is the diffraction (or spectral) order of the grating,  $\lambda$  is the wavelength of refracted light,  $d$  is the groove spacing, and  $\alpha$  and  $\beta$  are the incident and reflected angles, respectively.

In the case where the geometry of the spectrometer is chosen such that the incident angle is equal to the reflected angle, i.e.  $\alpha = \beta = \theta$ , an incident light ray would reflect directly back upon itself; this design is known as the Littrow configuration and represents autocollimation, in which case the grating equation (Equation B.1) simplifies to:

$$m\lambda = 2d\sin(\theta). \quad (\text{B.2})$$

### B.3. ORDER

---

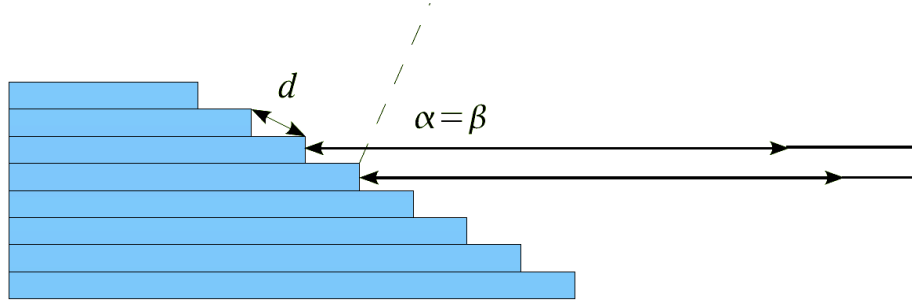


**Figure B.3:** Diagram of an echelle grating. The dotted line represents the grating normal.

For a given groove spacing,  $d$ , equation B.2 shows the relationship between wavelength,  $\lambda$ , order,  $m$ , and angle,  $\theta$ . It can readily be seen that the specific wavelength of radiation diffracted into a specific angle is not unique but depends also on the order. This characteristic of diffraction gratings is exploited with echelle gratings. The free spectral range of a grating is the measure of this overlap from adjacent orders, and is discussed below.

An echelle grating is a blazed grating (meaning its diffractive elements are shaped), used at high orders, where the incident light is approximately normal to the lower step of the blaze. This in effect makes the grating appear to the light ray as a stair-case, see Figure B.3. Quite appropriately, *echelle* is the French word for ladder. The concept of blazing is described below.

### B.3 Order

The diffraction or spectral order,  $m$ , is an integer variable which determines the angle into which a given wavelength will be diffracted. The 0<sup>th</sup> order represents specular reflection and is not useful for spectroscopy because all wavelengths are diffracted into the same angle, see Equation B.2. The diffraction order,  $m$ , can be a positive or negative integer depending on the side of the grating normal that the light emerges from.

### B.4 Dispersion

Dispersion, or more accurately, the angular dispersion, is the measure of angular separation between the diffracted light of different wavelengths, and is expressed as:

$$D = \frac{d\theta}{d\lambda} \quad [\text{radians} / \mu\text{m}], \quad (\text{B.3})$$

which is determined by the geometry of the grating and the orientation of its illumination. Equation B.3 can be re-expressed if we differentiate the grating equation as:

$$d\theta = \frac{m d\lambda}{d \cos\theta}, \quad (\text{B.4})$$

$D$  can be written as:

$$D = \frac{d\theta}{d\lambda} = \frac{m}{d \cos\theta} \left[ = \frac{2}{\lambda} \tan\theta \text{ in Littrow} \right]. \quad (\text{B.5})$$



## B.5. SPECTRAL RESOLUTION AND RESOLVING POWER

---

It is worth noting here that angular dispersion in the Littrow condition is independent of the groove spacing,  $d$ .

While angular dispersion of the grating is determined by the physical parameters of the grating and its illumination geometry, the linear dispersion of the grating spectrometer is determined by the post-optics. For post-optics having focal length  $f$ , the linear dispersion is:

$$f D = f \frac{d\theta}{d\lambda} = f \frac{m}{d \cos\theta} \quad [\text{m } \mu\text{m}^{-1}] . \quad (\text{B.6})$$

The above equation shows that linear dispersion is dependent upon the diffracted angle, and one result of this effect is that for a linear detector of uniform pixel size, as we move across the array of pixels, the range of wavelengths, and hence the spectral resolution, incident on each pixels varies as we move across the array. This must be taken into account when calibrating grating spectra.

### B.5 Spectral resolution and resolving power

The resolving power of a spectrometer is defined as its ability to separate two closely spaced spectral lines. There is a minimum angular separation required between their respective wavelengths for their peaks to not overlap and allow each to be uniquely identified. This, chromatic resolving power of a spectrometer is defined as:

$$R = \frac{\lambda}{(\Delta\lambda)_{min}} = m N, \quad (\text{B.7})$$

where  $(\Delta\lambda)_{min}$  is the limit of resolution, or least resolvable difference,  $\lambda$  is the mean wavelength of the measurement, or  $m$  is the diffraction order and  $N$  is the number of illuminated grooves on the grating surface. The resolving power is equal to the number of grooves  $N$  multiplied by the order number  $m$ . This last form of  $R$  can be recast by replacing  $m$  with the grating equation, as:

$$R = \frac{N d (\sin\alpha + \sin\beta)}{\lambda}. \quad (\text{B.8})$$

Since the maximal value from  $\sin\alpha + \sin\beta$  is 2, the maximum value for resolving power comes from the Littrow configuration and has a value of:

$$R_{\text{max}} = \frac{2 N d}{\lambda}. \quad (\text{B.9})$$

Lord Rayleigh's criterion for the resolution of nearby fringes requires that the first maximum of one fringe coincide with the first minimum of the next fringe [82], shown in Figure B.4. From this statement, at the limit of resolution, the angular separation will be equal to half of the linewidth. The angular width is given by  $\Delta\theta$ , expressed as:

$$\Delta\theta = \frac{2 \lambda}{N d \cos\theta_m} \quad (\text{B.10})$$

Thus if  $N$  is made very large, then  $\Delta\theta$  is very small, and the diffraction pattern consists of tightly packed fringes. This is the angular separation between two spectral lines differing in wavelength by  $\Delta\lambda$ .

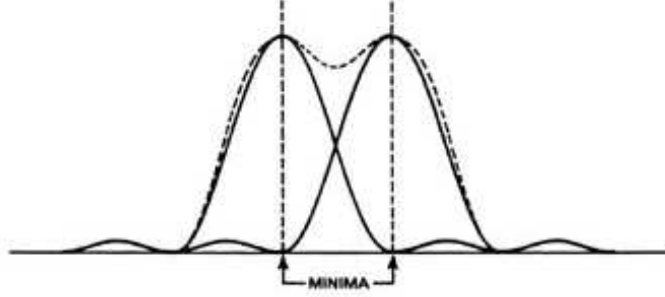


Figure B.4: Diagram of the Rayleigh criterion.

### B.6 Free spectral range

The range of wavelengths in a given spectral order, for which superposition of wavelengths from adjacent orders does not occur, is known as the free spectral range,  $F_\lambda$ . As mentioned above, overlapping orders require special attention when using a diffraction grating. If two lines at wavelengths  $\lambda$  and  $(\lambda + \Delta\lambda)$ , in adjacent spectral orders  $(m + 1)$  and  $m$ , just coincide, then:

$$a(\sin\theta_m - \sin\theta_i) = (m + 1)\lambda = m(\lambda + \Delta\lambda), \quad (\text{B.11})$$

where the precise wavelength difference,  $\Delta\lambda$ , is defined as the free spectral range:

$$(\Delta\lambda)_{\text{fsr}} = F_\lambda = \frac{\lambda}{m}. \quad (\text{B.12})$$

### B.7 Blazing

Under normal conditions, a large component of incident radiation is diffracted into the specular, or 0<sup>th</sup> order, which is not particularly useful since it overlays all wavelengths in a common direction, rendering the measurement of a single wavelength impossible. By modifying the shape or tilt of the diffractive elements it is possible to shift the diffracted energy from the specular order into higher orders [82]. This technique of shaping the diffractive elements is called blazing. Typical blazing takes the form of a sawtooth shape defined by a blaze angle which relates the longer edge of the sawtooth to the plane of the grating. The groove spacing  $d$  in a blazed grating still refers to one period of the shape. The shape of the blaze can also be defined by the step width ( $t$ ) and step height ( $s$ ). The aim is to set the blaze angle to equal the specular angle for a given order and wavelength [83].

I now consider the application of the above theory to the echelle spectrometer which provided data used in my thesis. The grating for the MIKE red channel is an R2 grating. This refers to the blaze angle through the following relationship:

$$\text{R number} = \tan^{-1}(\theta_B) = \frac{t}{s}, \quad (\text{B.13})$$

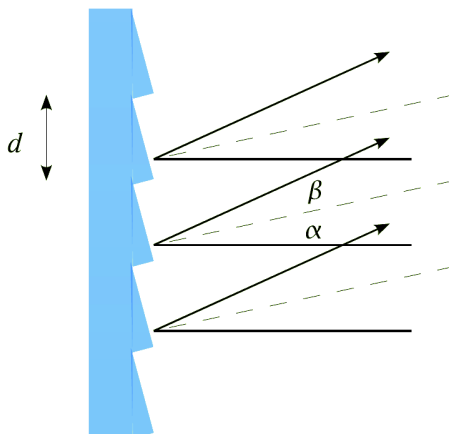


**Figure B.5:** Diagram of a blazed grating.

where  $\theta_B$  is the blaze angle of the grating,  $t$  is the width of one echelle step and  $s$  is the height of one echelle step. The normal to the  $s$  surface is facet normal.

From the equation for maximum resolving power under Littrow condition (Equation B.9), the quantity  $Nd$  is the ruled width of the grating, and can be represented with a  $W$ . If we assume that the total red-side grating is illuminated, in this case 12 inches or 305 mm, then  $R_{\max}$  becomes:

$$R_{\max} = \frac{2Nd}{\lambda} = \frac{2W}{\lambda} = \frac{0.610}{\lambda}, \quad (\text{B.14})$$

where  $\lambda$  is expressed in meters. From this we see that resolving power will vary inversely with wavelength. The lower wavelength orders will be able to achieve a higher resolving power than the orders of higher wavelength. At  $\lambda = 500 \text{ nm} = 5 \times 10^{-7} \text{ m}$ ,  $R_{\max} = 1,220,000$ , whereas at  $\lambda = 1000 \text{ nm} = 10^{-6} \text{ m}$ ,  $R_{\max} = 610,000$ . This is the maximum theoretical resolving power. MIKE operates close to the Littrow configuration [82] which results in the practical resolution being in the range  $R = 30000\text{--}40000$ .

## B.8 MIKE free spectral range

Equation B.12 describes free spectral range as the ratio of  $\lambda/m$ . Free spectral range is of particular importance to echelle gratings because they operate at very high spectral orders ( $m$ ) and therefore have small free spectral ranges. The potential for overlap between adjacent orders is high, and necessitates some form of order sorting to discriminate between adjacent orders. The MIKE red channel operates from  $m = 31$  to 73 (depending on the grating configuration). The following calculation table is for the configuration with orders 37 to 70. The lowest order, 37, corresponds to the highest wavelengths, largest spectral band and largest free spectral range. This means that order 37 has the lowest amount of overlap between adjacent orders, as can be seen from the wavelength limits of each order. The free spectral ranges at either end of the order range are detailed below.

## B.8. MIKE FREE SPECTRAL RANGE

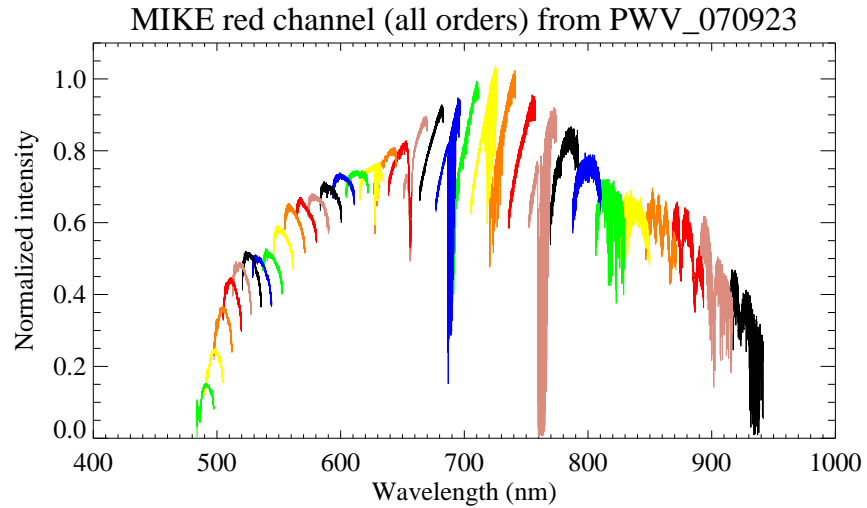


**Figure B.6:** MIKE red channel (all orders) from September 23, 2007. The lowest wavelength order is 70 and the highest wavelength order is 37.

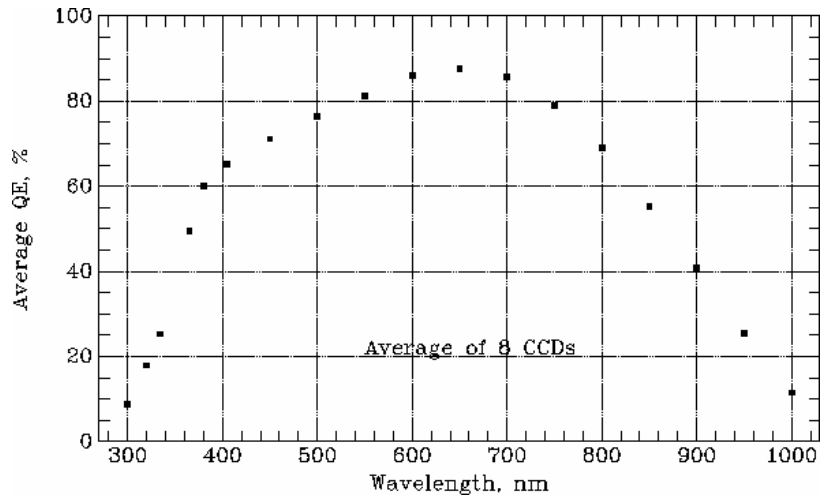


**Figure B.7:** Average quantum efficiency vs. wavelength of several CCDs similar to those installed in MIKE.

Order	[nm] Lambda-Min	[nm] Lambda-Max	[nm] Lambda-Band	[nm] Lambda-Mid	[nm] Free-Spectral-Range
37	915.2	941.8	26.5	928.5	25.1
38	891.1	917.0	25.8	904.1	23.8
39	868.3	893.4	25.2	880.9	22.6
...	...	...	...	...	...
68	497.6	512.1	14.5	504.8	7.4
69	490.4	504.6	14.3	497.5	7.2
70	483.8	497.4	13.6	490.6	7.0

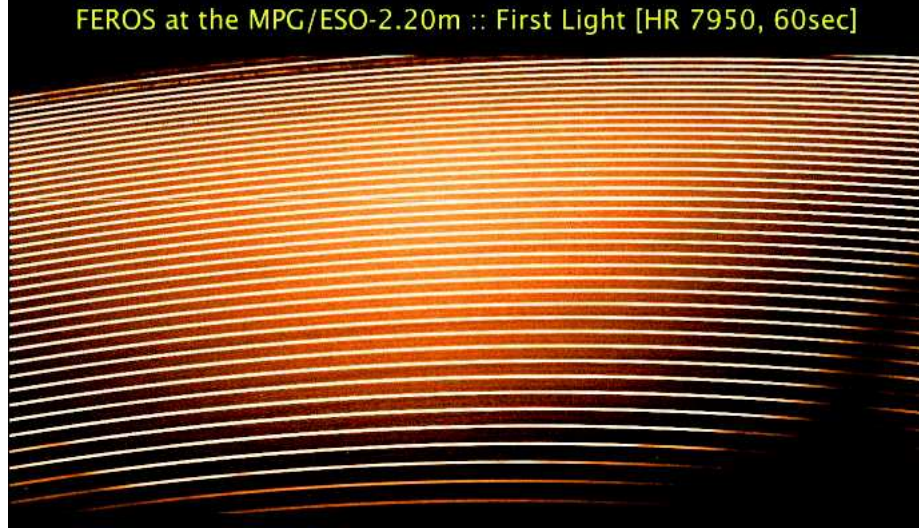


**Figure B.8:** First light of the FEROS spectrograph.  $\sim 40$  orders are visible in this image.

Figure B.6 shows a full data set from one measurement made with the MIKE red channel. The parabolic envelope to the entire set is due to the quantum efficiency of the MIKE CCDs, shown in Figure B.7. Each of the individual orders also has a parabolic shape. This is the curve that must be identified and eliminated when performing the spectral fitting described in Chapter 8.

To address the significant amount of overlap present in the higher orders, a second dispersive element must be employed. If a star is imaged through a slit at the entrance to the spectrometer, a one-dimensional spectral image of the object will be formed. This one dimensional line may then be dispersed a second time, with for example a prism. Spatially, this image will be along the long axis of the slit, while the spectral information is encoded in the orthogonal direction. The resulting two dimensional surface is ideally suited for use with a rectangular CCD detector. An example of this two-dimensional surface is shown in the image of FEROS data given in Figure B.8. With a knowledge of which curve represents which order, obtained through a suitable calibration scheme, the detected signal can be readily analysed to extract meaningful spectral information from the object being studied.

## B.9 Diffraction grating ILS

When the notion of single-slit diffraction is extended to multiple-slits and finally to diffraction by an arbitrary aperture, the resulting line shape becomes increasingly complicated. For example, the flux density distribution function for a set of rectangular slits is given as [82]:

$$I(\theta) = I_0 \left( \frac{\sin\beta}{\beta} \right)^2 \left( \frac{\sin N\alpha}{\alpha} \right)^2 \quad (\text{B.15})$$

where  $\beta = (kb/2) \sin \theta$ ,  $\alpha = (ka/2) \sin \theta$ ,  $b$  is the width of one slit,  $a$  is the separation between adjacent slit centres,  $k = 2\pi/\lambda$ ,  $N$  is the number of slits, and  $I_0$  is the flux density

in the  $\theta = 0$  direction emitted by any one of the slits and that  $I(0) = N^2 I_0$ . When the contributions from all slits are superimposed, the result is a multiple wave interference system modulated by the single-slit diffraction envelope [82]. Thus, the resulting ILS of a grating spectrometer would be both wavelength dependent and complex.

This appendix summarises some of the key points to consider when using a diffraction grating spectrometer. From the perspective of line fitting discussed in Chapter 8 it is clear that the ILS is both complex and varies nonlinearly with wavelength. While accommodating this function in any line fitting algorithm may appear challenging, to first order a wavelength dependent Gaussian function provides a realistic representation of the ILS and allows rapid computation in the fitting routine. The fact that the residuals of the fitted spectra show little structure (Figures 8.4, 8.8 and 8.9) justifies the use of the Gaussian ILS in the fitting of data acquired from the grating spectrometers used in this thesis.

---

## Appendix C

# Spectral Fitting Algorithm Source Code

This section contains the source code for the transmission spectrum fitting routines I used in this work. They were written in IDL<sup>®</sup> V.6 and V.7.

### `read_uves_raw_fits.pro`

This routine ingests raw .FITS files, deciphers the header information, determines the wavelength scale, and outputs the data as an IDL binary save file. Other information about the spectrum, i.e. Date, slit width, target name, temperature and air mass are stored in the output filename.

### `fit_continuum_UVES_peak_find.pro`

This code reads in an IDL binary save file of measured data and a simulated spectrum file in order to correct any wavelength offsets and to normalise the continuum in the measurement. One peak is identified in both the simulated and the measured spectrum. The simulated spectrum is shifted in wavelength to match the measured data. Then the simulated spectrum is analysed to determine where transmission is greater than 0.9985. Those wavelengths are tagged as *continuum* in the measured data. A second-order polynomial is fit to the subset of *continuum* measured data. The polynomial parameters are stored in a spectrum-specific data file for use in the next routine.

### `make_UVES_plot_archive.pro`

This routine performs the fit between the measured data and the simulated spectrum. The measured data are wavelength shifted, normalized and have their continua removed using the parameters determined by the previous routine. The fit is performed with MPFIT [60], a non-linear least-squares fitting package that uses the Levenberg-Marquardt algorithm, which finds the best set of model parameters that match the data by minimising the sum of the weighted squared differences between the model and data [63]. The fit involves four parameters: wavelength shift (this is mostly corrected above), a gain, PWV and a Gaussian function halfwidth. The simulated spectrum is iteratively modified and compared to the measured data. When the fitting routine has found a minimum it reports the fitting pa-

---

rameters. In some instances this will be a local minimum, in which case the fit parameters must be fitted to in sequence rather than all at once. The simulated transmission spectrum is converted into opacity where it can be linearly scaled by the PWV parameter. It is then converted back to transmission for comparison. Through this method, only one spectrum need ever be generated for a given site with constant temperature and pressure. The Gaussian halfwidth parameter is used in a function that performs a Gaussian convolution on the simulated spectrum to approximate the instrumental effects on the spectrum. Once the fitting routine has returned its fit parameters, a number of files are generated including a postscript spectrum, an IDL binary save file of the fit and measured data, and a text file with the date, fit parameters and resulting PWV.

`parse_uves_params_file.pro`

This code ingests the text file outputs from the previous step in order to produce an airmass corrected postscript plot of the data as well as a text file containing date, modified Julian date and airmass corrected PWV.



read\_uves\_raw\_fits.pro

**PRO read\_UVES\_raw\_fits**

```
inputDir = 'C:\UVES\'

files = DIALOG_PICKFILE(path = inputDir, filter = '*REDL*.fits', /READ,$
    /MULTIPLE_FILES)

outputDir = 'C:\UVES\SAV'

FOR i = 0, N_ELEMENTS(files)-1 DO BEGIN

    PRINT, STRING(i) + ' of ' + STRING(N_ELEMENTS(files)-1) + ' ' +files[i]

    data = mrdfits(files[i], 0, header)

    index = WHERE(STRMATCH(header, 'CRVAL1*'))
    wave_start = 0
    IF (index NE -1) THEN BEGIN
        result = STRSPLIT(header[index], '=', /EXTRACT)
        wave_start = DOUBLE(result[1])
    ENDIF

    result = STRSPLIT(header[WHERE(STRMATCH(header, 'CDELTA1*'))], '=', /EXTRACT)
    wave_res = DOUBLE(result[1])

    dateTime = (STRSPLIT(header[WHERE(STRMATCH(header, 'DATE-OBS*'))], " ", $
        /EXTRACT))[1]
    dateTime = STRJOIN(STRSPLIT(dateTime, ':', /EXTRACT), '_')

    wave = (DINDGEN(N_ELEMENTS(data)) * wave_res) + wave_start
    wave = wave/10.0

    result = (STRSPLIT(header[WHERE(STRMATCH(header, '*SLIT3 WID*', $
        /FOLD_CASE))], '=/', /EXTRACT))[1]
    slitW = STRTRIM(STRING(result, format='(f04.1)'), 2)

    result = STRSPLIT(header[WHERE(STRMATCH(header, 'BUNIT*', /FOLD_CASE))], $
        "'=' ", /EXTRACT)
    BUNIT = result[1]

    result = STRSPLIT(header[WHERE(STRMATCH(header, '*TARG NAME*'))], "'='/", $
        /EXTRACT)
    TARGET = STRTRIM(result[2], 2)

    result = STRSPLIT(header[WHERE(STRMATCH(header, '*TEMP4 MEAN*'))], '=/', $
        /EXTRACT)
    TEMPERATURE = FLOAT(result[1]) + 273.15
```

read\_uves\_raw\_fits.pro

```
result = STRSPLIT(header[WHERE(STRMATCH(header, '*AIRM START*'))], "'=/", $
/EXTRACT)
AIRMASS = STRTRIM(result[1], 2)

outFilename = outputDir + '\'+ dateTime + '_' + STRING(AIRMASS, $
FORMAT='(d05.3)')+ '_' + STRING(TEMPERATURE, FORMAT='(d05.1)')+ $
'_'+TARGET+'_'+BUNIT+'_'+slitW+'.sav'

PRINT, outFilename

SAVE, filename = outFilename, wave, data, header

ENDFOR

END
```

fit\_continuum\_UVES\_peak\_find.pro

**PRO rrq\_fit\_continuum\_UVES\_peak\_find**

**SET\_PLOT**, 'win'

files = **DIALOG\_PICKFILE**(PATH = 'C:\UVES\SAV\' , FILTER = '\*\_10.0.sav' , \$  
/READ, /MULTIPLE\_FILES)

filedirectory = 'C:\UVES\SAV\PROCESSED\'

xlimits = [717, 719]  
xlimits\_peak = [718.15, 718.65]

filebase = **FILE\_BASENAME**(files)  
outFilename = filedirectory + 'fits\fit\_params\_' + **STRING**(xlimits[0], \$  
FORMAT='(f5.1)') + '\_' + **STRING**(xlimits[1], \$  
FORMAT='(f5.1)') + '\_' + filebase

**read\_spc**, 'BTRAM\_715-730nm\_765mBar\_285K\_1mm\_LCO.spc', x1mm\_raw, y1mm\_raw

x1mm\_full = x1mm\_raw  
y1mm\_full = y1mm\_raw

xOffset = 0  
x1mm\_full = x1mm\_raw + xOffset

;Determine where the BTRAM spec is ~ 1 (continuum)

smallerIndex = **WHERE**(x1mm\_full **GT** xlimits[0] **AND** x1mm\_full **LT** xlimits[1])  
smallerIndex\_Peak = **WHERE**(x1mm\_full **GT** xlimits\_Peak[0] **AND** x1mm\_full **LT** \$  
xlimits\_Peak[1])

x1mm = x1mm\_full[smallerIndex]  
y1mm = y1mm\_full[smallerIndex]

cont\_index = **WHERE**(y1mm **GT** 0.9985)

**WINDOW**,0

**PLOT**, x1mm, y1mm, xrange=xlimits

**OPLOT**, x1mm[cont\_index], y1mm[cont\_index], color=2, psym=2

**WINDOW**,1

**FOR** filesIndex = 0, **N\_ELEMENTS**(files)-1 **DO BEGIN**

**RESTORE**, files[filesIndex]

!P.**MULTI**=[0]

**PLOT**, x1mm\_full[smallerIndex\_Peak], y1mm\_full[smallerIndex\_Peak], \$

fit\_continuum\_UVES\_peak\_find.pro

```
xrange=xlimits_peak, color=2

rawIndex_Peak = WHERE(wave GT xlimits_Peak[0] AND wave LT xlimits_Peak[1])

PLOT, wave[rawIndex_Peak], data[rawIndex_Peak], xrange=xlimits_peak,$
/NOERASE

SPEC_wl = DOUBLE((wave[rawIndex_Peak]))$
  [WHERE(data[rawIndex_Peak] EQ MIN(data[rawIndex_Peak]))])
BTRAM_wl = DOUBLE((x1mm_full[smallerIndex_Peak]))$
  [WHERE(y1mm_full[smallerIndex_Peak] EQ $
  MIN(y1mm_full[smallerIndex_Peak]))])

xOffset = XOffset + SPEC_wl-BTRAM_wl

xOffset = xOffset[0]
x1mm_full = x1mm_raw + xOffset

smallerIndex = WHERE(x1mm_full GT xlimits[0] AND x1mm_full LT xlimits[1])
smallerIndex_Peak = WHERE(x1mm_full GT xlimits_Peak[0] AND $
  x1mm_full LT xlimits_Peak[1])

x1mm = x1mm_full[smallerIndex]
y1mm = y1mm_full[smallerIndex]

cont_index = WHERE(y1mm GT 0.9985)

x = wave
y = data

smallerIndex = WHERE(x GT xlimits[0] AND x LT xlimits[1])
x = x[smallerIndex]
y = y[smallerIndex]

x_reduced = x*0

j_start = 0L

FOR i=0L,N_ELEMENTS(cont_index)-1 DO BEGIN

  match=0
  FOR j=j_start,N_ELEMENTS(x)-1 DO BEGIN
    upper = x1mm[cont_index[i]] * 1.000001
    lower = x1mm[cont_index[i]] * 0.999999

    IF ((upper GT x[j]) AND (lower LT x[j])) THEN BEGIN
      x_reduced[j] = 1
      j_start = j+1
      BREAK
    ENDIF
  ENDFOR
ENDFOR
```

```
fit_continuum_UVES_peak_find.pro
```

```
x_r_index = WHERE(x_reduced EQ 1)

index = WHERE(x GE xlimits[0] AND x LE xlimits[1])
mp_x=x[index]

newX = x[x_r_index]
newY = y[x_r_index]

FOR i=0,N_ELEMENTS(newY) - 1 DO BEGIN
  poly_fit_result = poly_fit(newX,newY, 1, yfit=yfit, sigma=sigma)
  distance = ABS(newY - yfit)
  maxIndex = WHERE(distance EQ MAX(distance))
  newY[maxIndex] = yfit[maxIndex]
ENDFOR

y_cont = interpol(yfit, x[x_r_index], x)

SAVE, filename=outFilename[filesIndex], poly_fit_result, xoffset

ENDFOR

END
```

make\_UVES\_plot\_archive.pro

**PRO** rrq\_make\_UVES\_plot\_archive

**COMMON** share, xTemp, yTemp

**read\_spc**, 'BTRAM\_715-730nm\_765mBar\_285K\_1mm\_LCO.spc', x1mm, y1mm

xlimits = [717,719]

files = **DIALOG\_PICKFILE**(PATH = 'C:\UVES\SAV\' , FILTER = '\*.sav' , \$  
/READ, /MULTIPLE\_FILES)

filedirectory = 'C:\UVES\SAV\PROCESSED\'

filebase = **FILE\_BASENAME**(files)

epsFilename = filedirectory + 'eps\eps\_' + **STRING**(xlimits[0], \$  
FORMAT='(d05.1)')+ '\_' + **STRING**(xlimits[1], FORMAT='(d05.1)')+ '\_' \$  
+ filebase + '.eps'

fitFilename = filedirectory + 'fits\fit\_params\_' + **STRING**(xlimits[0], \$  
FORMAT='(d05.1)')+ '\_' + **STRING**(xlimits[1], FORMAT='(d05.1)')+ '\_' + filebase

txtFilename = filedirectory + 'params\_' + **STRING**(xlimits[0], \$  
FORMAT='(d05.1)')+ '\_' + **STRING**(xlimits[1], FORMAT='(d05.1)')+ '.txt'

dataFilename = filedirectory + 'data\data\_' + **STRING**(xlimits[0], \$  
FORMAT='(d05.1)')+ '\_' + **STRING**(xlimits[1], FORMAT='(d05.1)')+ '\_' + filebase

**GET\_LUN**, Unit

**OPENW**, Unit, txtFilename

**PRINTF**, Unit, **STRTRIM**(**STRING**(xlimits[0]),2)+'-' + **STRTRIM**(**STRING**(xlimits[1]),2)

**FOR** filesIndex = 0, **N\_ELEMENTS**(files)-1 **DO BEGIN**

**FOR** runThrough = 0,1 **DO BEGIN**

**IF** ~runThrough **THEN** MIKEgain = 1

**RESTORE**, files[filesIndex]

**RESTORE**, fitFilename[filesIndex]

        x=wave-xOffset

        y=data

        index = **WHERE**(x **GE** xlimits[0]-1 **AND** x **LE** xlimits[1]+1)

        mp\_x=x[index]

        mike\_continuum = poly\_fit\_result[0] + poly\_fit\_result[1] \* x[index]

**IF** runthrough **THEN** mike\_continuum = mike\_continuum / MIKEgain

        mp\_y=y[index] / mike\_continuum

        index = **WHERE**(x1mm **GE** xlimits[0]-1 **AND** x1mm **LE** xlimits[1]+1)

        xTemp = x1mm[index]

make\_UVES\_plot\_archive.pro

```
yTemp = y1mm[index]

;;*****MP_FITFUNC SETUP*****
measure_errors = (mp_y)*0d;+1d
measure_errors = measure_errors + 1d

yfit=FLTARR(N_ELEMENTS(mp_x)) ;this will hold the returned fit array
maxiter=500 ;maximum number of iterations

parinfo = REPLICATE({value:0.D, fixed:0, limited:[0,0], limits:[0.,0.]}, 4)
;Fit parameters
;0 xOffset = 0.015
;1 yGain = 2.6E4
;2 PWV = 5
;3 GaussianOneSigmaWidth = 0.11

parinfo(0).fixed = [0]
parinfo(0).limited= [1,1]
parinfo(0).limits = [-0.2d,+0.2d]

;GAIN
parinfo(1).fixed = [runThrough]
parinfo(1).limited= [1,1]
parinfo(1).limits = [0.1d,2d]

parinfo(2).fixed = [0]
parinfo(2).limited= [1,1]
parinfo(2).limits = [0.1d,20.0d]

parinfo(3).fixed = [1]
parinfo(3).limited= [1,1]
parinfo(3).limits = [0.0001d,.5d]

parinfo(*).value = [-0.003d, 1d, 5d, 0.0035d] ;initial guesses

result = mpfitfun('RRQ_func', mp_x, mp_y, measure_errors, yfit=yfit, $
    maxiter=maxiter, perror=perror, niter=niter, status=stat, $
    parinfo=parinfo, bestnorm=bestnorm, dof=dof, /quiet)

MIKEgain = result[1]

ps_plot = 1

IF ps_plot THEN BEGIN
    SET_PLOT, 'ps'
    DEVICE, file=epsFilename[filesIndex], /encapsulated, /inches, $
        /color, /portrait
ENDIF

PRINT, epsFilename[filesIndex]
PRINT, result

set_font

PLOT, mp_x, mp_y, yrange=[-0.1,1.1], xrange=[xlimits[0],xlimits[1]], $
```

make\_UVES\_plot\_archive.pro

```
charthick=1, xcharsize=1.0, ycharsize=1.0, xthick=2, ythick=2, $
thick=2, xtitle='Wavelength (nm)', ytitle='Transmission', psym=0,$
xmargin=[10,8], ymargin=[5,5], title = STRING(filebase[filesIndex])
OPLOT, mp_x, yfit-0.0, color=2, thick=2
OPLOT, mp_x, mp_y-yfit, thick=2

legend, psym=[0,0], ['UVES data', 'BTRAM fit'], color=[0,2], $
margin=0.5, charthick=2, charsize=1.5, pspacing=1, thick=2, $
pos=[xlimits[0]+0.2,0.25]

XYOUTS, xlimits[0]+.2,0.3, STRTRIM(STRING(result[2],format='(F5.2)')$
,2)+' mm PWV'

IF ps_plot THEN BEGIN
    DEVICE, /CLOSE
    SET_PLOT, 'win'
ENDIF

SAVE, filename=dataFilename[filesIndex], mp_x, mp_y, yfit

PRINTF, Unit, STRTRIM(STRING(filebase[filesIndex]),2)+' '+ $
    STRTRIM(STRING(result[0]),2)+' '+ $
    STRTRIM(STRING(result[1]),2)+' '+ $
    STRTRIM(STRING(result[2]),2)+' '+ $
    STRTRIM(STRING(result[3]),2)

ENDFOR

ENDFOR

CLOSE, Unit
FREE_LUN, Unit

END

FUNCTION RRQ_FUNC, data, val

COMMON share, xTemp, yTemp

xOffset                = val[0]
yGain                  = val[1]
PWV                    = val[2]
GaussianHalfWidth     = val[3]

;Scale the PWV
y_sim = EXP(PWV*ALOG(yTemp)); + alog(Tau_Dry))

out = rrq_convolve_gaussian(GaussianHalfWidth,0.001,y_sim)
```



```
make_UVES_plot_archive.pro
```

```
out = out / MAX(out)  
out_i = interpol(out, xTemp, data+xOffset)
```

```
guess = out_i * yGain
```

```
RETURN, guess
```

```
END
```

parse\_uves\_params\_file.pro

**PRO** rrq\_parse\_UVES\_params\_file

filedirectory = 'C:\UVES\SAV\PROCESSED\'

txtFilename = filedirectory + 'params\_717.0\_719.0.txt'

**RESTORE**, 'param\_template.sav'

param\_data = **READ\_ASCII**( txtFilename, TEMPLATE=param\_template , /VERBOSE )

index = **WHERE**(param\_data.GAIN EQ 1.0)

header = param\_data.HEADER[index]

pwv = param\_data.PWV[index]

airmass = pwv\*0.0

am\_corrected\_pwv = pwv\*0.0

datetime = **STRARR**(N\_ELEMENTS(header))

iso\_datetime = **STRARR**(N\_ELEMENTS(header))

jul\_datetime = **DBLARR**(N\_ELEMENTS(header))

**FOR** i=0, N\_ELEMENTS(header)-1 **DO BEGIN**

result = **STRSPLIT**(header[i], '\_', /EXTRACT)

temp\_result = **STRMID**(result[3], 0, 5)

airmass[i] = **FLOAT**(temp\_result)

t\_date = result[0]

t\_time0 = result[1]

t\_time1 = result[2]

iso\_datetime[i] = t\_date + ':' + t\_time0 + ':' + t\_time1

jul\_datetime[i] = **iso8901\_to\_julday**(iso\_datetime[i])

am\_corrected\_pwv[i] = pwv[i] / airmass[i]

**ENDFOR**

ps\_plot = 1

**IF** ps\_plot **THEN BEGIN**

**SET\_PLOT**, 'ps'

**DEVICE**, file='C:\UVES\UVES\_PWV.eps', /encapsulated, \$

/inches, /color, /portrait

**ENDIF**

**set\_font**

**PLOT**, (jul\_datetime-FLOOR(jul\_datetime[0])-0.5)\*24.0, am\_corrected\_pwv, \$

parse\_uves\_params\_file.pro

```
psym=4, xtitle='[Hours]', ytitle = 'PWV [mm]', $  
title = 'UVES [fit at 717-719 nm]', yrange=[0,5]
```

```
IF ps_plot THEN BEGIN
```

```
  DEVICE, /CLOSE
```

```
  SET_PLOT, 'win'
```

```
ENDIF
```

```
OPENW, Unit, 'C:\UVES\UVES_PWV.txt', /GET_LUN
```

```
PRINTF, Unit, $
```

```
  '# ISO8901 Datetime,      Modified Julian,      Airmass corrected PWV [mm]'
```

```
FOR i=0, N_ELEMENTS(pwv)-1 DO BEGIN
```

```
  PRINTF, Unit, STRTRIM(STRING(iso_datetime[i]),2)+' ', $
```

```
    + STRTRIM(STRING(jul_datetime[i]-2400000.5, FORMAT='(F11.5)'),2) $
```

```
    + ',      '+ STRTRIM(STRING(am_corrected_pwv[i]),2)
```

```
ENDFOR
```

```
CLOSE, Unit
```

```
FREE_LUN, Unit
```

```
END
```